Advanced Design and Optimization of High-Efficiency Semiconductor Luminescent Solar Concentrators

By

Junyu Wang

B.S., Chemistry, Southeast University, 2015

M.S., Material Science and Engineering, University of Florida. 2017

M.A, Chemistry, Brown University, 2019

A Dissertation Submitted in Partial Fulfillment of the
Requirements for the Degree of Doctor of Philosophy in the
Department of Chemistry at Brown University

Providence, Rhode Island
May 2023

This dissertation by Junyu Wang is accepted in its present form by the Department of Chemistry as satisfying the dissertation requirement for the degree of Doctor of Philosophy.

Date_____ _____

Ou Chen, Advisor

Recommended to the Graduate Council by

Date_____ _____

Shouheng Sun, Reader

Date_____ _____

Vicki L. Colvin, Reader

Approved by the Graduate Council

Date_____ _____

Thomas A. Lewis,

Interim Dean of the Graduate School

CURRICULUM VITAE

Junyu Wang began his journey at Tianjin No.1 High School in Tianjin, China, where he graduated in 2011. He then pursued his undergraduate degree in Chemistry at Southeast University's School of Chemistry and Chemical Engineering in Jiangsu, China. During his time there, from 2012 to 2013, he was involved in Professor Hong Yang's research group, where he focused on liquid crystal materials and functional polymeric materials. After earning his bachelor's degree in chemistry, Junyu moved on to the University of Florida in 2015, where he pursued a master's degree in Material Science and Engineering. In 2016, he joined Professor Peng Jiang's research group as a research assistant, concentrating on photonic crystal structures, shape memory polymers, and pressure-sensitive membranes. In 2017, Junyu began his Ph.D. research at Brown University's Chemistry Department, working under the guidance of Professor Ou Chen. His research centered around "Advanced Design and Optimization of High-Efficiency Semiconductor Luminescent Solar Concentrators." He demonstrated exceptional proficiency in solar managing device fabrication, material characterizations, and device performance simulation. His primary focus was on improving the performance limitations of luminescent solar concentrators using novel high-luminescent nanomaterials and innovative fabrication techniques. Junyu's academic accomplishments include 12 published papers, with three first-author articles in peer-reviewed journals. Additionally, he has presented his research findings at various conferences, including four oral presentations and one poster presentation at ACS and MRS meetings.

PUBLICATIONS

(In reverse chronological order, * corresponding author)

14. **J. Wang**, T. Cai, Z. Liu and O. Chen*. High-Performance Mixing Design Luminescent Solar Concentrators Based on Quantum Dots and Perovskite Nanocrystals. ***in preparation.***
13. **J. Wang**, M. Li, J. Bae and O. Chen*. Optimized Quinary Ink Formulation for Ultrasonic Spray Coating in the Fabrication of High-Performance Luminescent Solar Concentrators. ***in preparation.***
12. **J. Wang**, T. Cai and O. Chen*. Cesium Copper Halide Perovskite Nanocrystals Based Photon-Managing Devices with Enhanced Ultraviolet Photon Harvesting. ***submitted to Nano Lett.***
11. **J. Wang,** Y. Yuan, J. Schneider, W. Zhou, H. Zhu, T. Cai, and O. Chen*. Quantum Dot-Based Luminescent Solar Concentrators Fabricated through the Ultrasonic Spray-Coating Method. ***ACS Applied Materials & Interfaces*** 2022, 14, 41013-41021.
10. K. Hills-Kimball, I. Lovelace, I. Peng, **J. Wang**, H. Garces, M. Rios, O. Chen, and L-Q. Wang*. New Insights to the Interactions between Amorphous Georgite Pigment and Linseed Oil Binder that Lead to a Drastic Color Change. ***Colorants*** 2022, 1, 376–387.
9. Peng, K. Hills-Kimball, I. Lovelace, **J. Wang**, M. Rios, O. Chen, and L-Q. Wang*. Exploring the Colors of Copper-Containing Pigments, Copper (II) Oxide and Malachite, and Their Origins in Ceramic Glazes. **Inorganica Chimica Acta** 2022, 529 120661.
8. Z. Liu, H. Yang, **J. Wang**, Y. Yuan, K. Hills-Kimball, T. Cai, P. Wang, A. Tang*, and O. Chen*. Synthesis of Lead-Free Cs2AgBiX6 (X = Cl, Br, I) Double Perovskite Nanoplatelets and Their Application in CO2 Photocatalytic Reduction. ***Nano Lett.*** 2021, 21, 1620-1627.
7. K. Hills-Kimball, H. Yang, T. Cai, **J. Wang**, Recent Advances in Ligand Design

and Engineering in Lead Halide Perovskite Nanocrystals. ***Advanced Science*** 2020.

6. T. Cai, W. Shi, S. Hwang, K. Kobbekaduwa, Y. Nagaoka, H. Yang, K. Hills-Kimball, H. Zhu, **J. Wang**, Z. Wang, Y. Liu, D. Su, J. Gao and O. Chen*. Lead-Free Cs4CuSb2Cl12 Layered Double Perovskite Nanocrystals. ***J. Am. Chem. Soc.*** 2020, 142, 11927-11936
5. T. Cai, **J. Wang**, W. Li, K. Hills-Kimball, H. Yang, Y. Nagaoka, Y. Yuan, R. Zia and O. Chen*. Mn2+/Yb3+ Codoped CsPbCl3 Perovskite Nanocrystals with Triple-Wavelength Emission for Luminescent Solar Concentrators. ***Advanced Science*** 2020, 2001317.
4. **J. Wang**, Y. Yuan, H. Zhu, T. Cai, Y. Fang and O. Chen*. Three-Dimensional Macroporous Photonic Crystal Enhanced Photon Collection for Quantum Dot-Based Luminescent Solar Concentrator. ***Nano Energy*** 2020, 67, 104217.
3. C. Yu, X. Guo, Z. Yin, Z. Zhao, X. Li, J. Robinson, M. Muzzio, C. Barbosa, M. Shen, Y. Yuan, **J. Wang**, J. Antolik, G. Lu, D. Su, O. Chen, P. Guduru, C. Seto* and S. Sun*. Highly Efficient AuPd Nanoparticle Catalyst for Synthesizing Polybenzoxazole with Controlled Polymerization. ***Matter*** 2019, 1, 1-13.

Before Brown University

2. Y. Fang, S. Leo, Y. Ni, **J. Wang**, B. Wang, L. Yu, Z. Dong, Y. Dai, V. Basile, C. Taylor, P. Jiang*, Reconfigurable Photonic Crystals Enabled by Multi-StimuliResponsive Shape Memory Polymers Possessing Unconventional Room Temperature Shape Processability. ***ACS Appl. Mater. Interfaces*** 2017, 9, 5457–5467.
1. H. Yang*, M. Xu, L. Guo, H. Ji, **J. Wang,** B. Lin*, X. Zhang and Y. Sun, Organocatalysis in polysiloxane gels: a magnetic-stir-bar encapsulated catalyst system prepared by thiol–ene photo-click immobilization. ***RSC Advance***, 2015, 5, 7304-7310.

Conferences

(In reverse chronological order)

5. **J. Wang** and O. Chen, “Highly Luminescent Lead-free Cesium Copper Halide Perovskite Nanoplatelets for Luminescent Solar Concentrator Application” Materials Research Society (MRS) meeting, Apr. 2023, San Francisco, CA.
4. **J. Wang**, Y. Yuan and O. Chen, “Quantum Dot Based Luminescent Solar Concentrators Fabricated Through Ultrasonic Spray-coating Method” American Chemical Society (ACS) meeting, Apr. 2022, San Diego, CA.
3. **J. Wang**, Y. Yuan and O. Chen, “Innovative Coating Method for Luminescent Solar Concentrator Fabrication” American Chemical Society (ACS) meeting, Aug. 2021, Atlanta, GA.
2. **J. Wang** and O. Chen, “Photonic Crystal Enhanced Photon Collection for Quantum Dot-Based Luminescent Solar Concentrator” Materials Research Society (MRS) meeting, Nov. 2020, Virtual.
1. **J. Wang**, Y. Yuan, M. Li, Y. Fang and O. Chen, “Optimization Method of Polymer & Inorganic Nanoparticles Composite: Luminescent Solar Concentrator” American Chemical Society (ACS) meeting, Apr. 2019, Orlando, FL.

ACKNOWLEDGEMENTS

Life is like a boat; it can face tumultuous waters that challenge my ability to navigate. However, amidst the difficulties, it is essential to be grateful for those who help me stay afloat. During my 6 years in Brown, these people are my advisor, professors, colleagues, classmates, friends, who offer a helping hand or a listening ear. By expressing my appreciation, I not only show gratitude but also strengthen the bonds that keep us connected. Like a captain who knows the importance of the voyage ahead, I will never forget the people who guide me in my journey of life and be grateful for their presence.

Firstly, I cannot express enough gratitude for the unwavering support and mentorship that my PhD advisor, Ou Chen, has provided me. Throughout my research, Ou's insightful feedback and constructive criticism have helped me grow as a scholar, challenging me to push beyond my limits and reach new heights in my work. I am grateful for the countless hours spent discussing ideas, offering guidance, and providing unwavering support through my academic and personal struggles. More than a mentor, Ou has become the one who is always there to listen, offer advice, and inspire me to be my best self. It is an honor to have had the opportunity to work under such an outstanding and supportive advisor, and I will always cherish the memories and lessons learned under his guidance.

Secondly, I would like to thank for my PhD committee members, Prof. Shouheng Sun and Prof. Vicki L. Colvin, for their guidance and support throughout my doctoral journey. Their feedback has been critical in shaping my research and pushing me to think deeply about my work. Their expertise, generosity, and dedication to my success have been invaluable, and I feel incredibly fortunate to have had the opportunity to work with such outstanding scholars. I am confident that the knowledge and guidance they have imparted will stay with me throughout my career.

Thirdly, I am grateful for all the collaborators (Prof. Fang Yin, Prof. Angus Kingon, Prof. Jing Zhao, Prof. Nitin Padture, Prof. Jinhye Bae, Dr. Li-Qiong Wang, Dr. Zhenghong Dai, Dr. Seunghyun Kim, Minghao Li, Nyiera Hawi, Iris Peng and Isabela Lovelace) who have supported and contributed to my PhD research. Working with people from diverse backgrounds has enriched my work and helped me achieve my academic goals. Their expertise and dedication have inspired me to push beyond my limits and strive for excellence. I appreciate their support and the friendships we have built throughout our collaborations. I cannot thank them enough for their contribution to my PhD career, and I look forward to continued collaborations in the future.

Fourthly, I am extremely grateful for all Chen group members (Dr. Yasutaka Nagaoka, Dr. Wenwu Shi, Dr. Hanjun Yang, Dr. Katie Hills-Kimball, Dr. Hua Zhu, Dr. Yucheng Yuan, Dr. Tong Cai, Na Jin, Lacie Dube, Jeremy Schneider, Peter Saghy, Rongzhen Wu, Yejing Liu, Ken Hong, Spencer Yang, Prof. Ping Wang, Dr. Zhenyang Liu, Dr. Meidan Que, Dr. Na Chen), who have been an integral part of my PhD journey. Their support, encouragement, and camaraderie have made the long hours in the lab more enjoyable and productive. Their unique perspectives, diverse experiences, and scientific expertise have challenged and inspired me to grow as a researcher. They have been a source of motivation, and their enthusiasm and dedication to science have pushed me to work harder and pursue my research goals. I appreciate the friendships we have built, and I am grateful for the memories and experiences we have shared. I cannot imagine my PhD journey without them, and I am thankful for their presence in my life.

I would also like to express my gratitude to all the professors, staff, classmates, and friends that I had the pleasure of meeting at Brown. Your support and companionship have been invaluable during my Chemistry journey, and I cannot thank you enough. I enjoyed every moment of working alongside you at Brown, and I appreciate the knowledge and experiences that you have shared with me. It has been an honor to be a

part of this community, and I will cherish the memories and friendships that I have made here. Thank you for making my time at Brown a truly unforgettable experience.

I am so grateful for the love and support from my girlfriend and family. They've always encouraged and helped me, even in my academic pursuits. They inspire me and keep me strong when times are tough. I appreciate everything they've done for me, including their sacrifices, emotional support, and faith in me. Their love and guidance have helped shape who I am, and I can't imagine life without them. I feel very lucky to have them in my life, and I love you forever!

Abstract of “Advanced Design and Optimization of High-Efficiency Semiconductor Luminescent Solar Concentrators” By Junyu Wang, Ph.D., Brown University, May 2023

Luminescent Solar Concentrators (LSCs) consist of a thin slab of luminescent composite that absorbs sunlight and re-emits it at a lower energy level, subsequently directing it towards the device's edges, where solar cells collect it. Boasting low-cost, flexibility, and functionality in low-light conditions, LSCs hold the potential to enhance solar cell efficiency by decreasing the necessary amount of semiconductor material. However, LSCs are still in the preliminary stages of development and have not yet reached widespread commercialization due to factors such as manufacturing restrictions, performance limitation, and size constraints. Despite these challenges, LSCs show promise as a potentially significant technology for boosting efficiency and reducing solar power costs. In this thesis, the primary focus lies on optimizing LSCs from various angles. Building on the working principle of the LSC device, optimization efforts target aspects such as coating techniques, surface structure, emitter composition, and innovative geometries. By integrating these optimization strategies with simulation studies, enhanced LSC performance can be achieved, paving the way for exploring future developments in the field.

Chapter 1 provides a comprehensive introduction to LSCs, encompassing the rationale for their necessity, their optical characteristics, and potential applications. Additionally, this chapter elucidates the fundamental operating principles of LSCs and offers an overview of the field's developments. Furthermore, it identifies the prevailing limitations and challenges within the domain and outlines potential strategies for addressing these issues, which will be discussed further in the following chapters.

Chapter 2 introduces an ultrasonic spray coating technique for creating high-quality QD-LSCs with smooth, customizable layers. This adaptable method reduces QD aggregation and works with various substrates. By adjusting the QD-ink solution, we

can fine-tune photon capture, transparency, and solar energy harvesting for QD-LSC devices. This study marks a significant step toward integrating programmable, high-performance LSC devices in diverse applications.

Chapter 3 presents a 3D macroporous-structured photonic crystal (PC) coated QD-based LSC (PC-LSC) device, effectively reducing escape cone photon loss. The PC-LSC's light-trapping efficiency increases by ~30% compared to conventional LSCs. Results show significant improvements in external quantum efficiency and concentration factor for large-area PC-LSC devices under sunlight, highlighting their potential in practical solar energy conversion systems with enhanced energy harvesting capabilities.

Chapter 4 describes a lead-free $Cs_3Cu_2Cl_5$ perovskite nanodisks (NDs) with high PL QY (84.2%) and a large Stoke shift (1.43 eV). Incorporating these NDs into LSC and LDS devices using an ultrasonic spray coating method, we achieved high visible light transmission, low photon scattering, and superior UV photon harvesting and energy conversion with Si-PV cells. Our research highlights the potential of these unique photon-managing devices for spacecraft photon collection or multifunctional energy collection hulls with increased specific power, paving the way for lead-free perovskite nanomaterials in space-based solar power systems.

Chapter 5 demonstrates a mixed-design LSC incorporating high PLQY quantum cutting perovskite Yb-doped $CsPbCl_3$ nanocrystals and Stokes-shift engineered $CuInS_2/ZnS$ quantum dots, achieving high η_{ext} performance for large-scale LSC devices through experimental and computational methods. This mixed design LSC reduces re-absorption losses and scattering attenuation compared to tandem-design LSCs. Our simulations show that the mixed LSC-PV system can significantly reduce energy generation costs, enhancing energy gain in NZEB buildings compared to stand-alone roof-mounted PV panels. This study advances the design and fabrication of LSCs and building-integrated solar windows.

In conclusion, Chapter 6 summarizes the whole projects through my PhD studies on LSCs and offers my perspective on the future direction of LSC developments across various aspects. These include potential avenues to improve performance limitations and the exploration of future LSC applications within the solar energy field.

Table of Contents

List of Abbreviations

Key Abbreviation	Definition
LSC	Luminescent solar concentrator
LDS	Luminescent down-shifting layer
η_{ext}	External optical efficiencies
η_{int}	Internal optical efficiencies
η_{abs}	Absorption ratio/absorption efficiencies
η_{trap}	Light trapping efficiency
n	Refractive index
QD	Quantum dots
NC	Nanocrystal
ND	Nanodisks
PL	Photoluminescence
PL QY	Photoluminescence quantum yield
PLE	Photoluminescence excitation
XRD	X-ray diffraction
OA	Oleic acid
OAm	Oleylamine
OAc	acetate
TEM	Transmission electron microscopy
HR	High-resolution
UV	Ultraviolet

NIR	Near-infrared
PDMS	Polydimethylsiloxane
PMMA	Poly (methyl methacrylate)
PLMA	Poly (lauryl methacrylate)
TET	Trimethylolpropane ethoxylate triacrylate
PEGDA	Poly (ethylene glycol) diacrylate
ODPA	Octadecylphosphonic acid
TOPO	Trioctylphosphine oxide
TOP	Trioctylphosphine
DDT	1-dodecanethiol
Si-PV	Silica photovoltaic
EQE	External quantum efficiency
TIR	Total internal reflection
0D, 1D, 2D, 3D	Zero, one, two, three-dimensional
FWHM	Full width at half-maximum
SEM	Scanning electron microscopy
AFM	Atomic force microscopy
AVT	Average visible transmittance
VLT	Visible light transmittance
CDF	Cumulative distribution functions
PC	Photonic crystal
IEA	International Energy Agency

PV	Photovoltaic
CSP	Concentrated, solar heating systems and solar power
NZEBs	Net-zero energy buildings
DLS	Dynamic light scattering
Ra	Arithmetic average roughness
CLC	Cholesteric liquid crystal
STE	Self-trapping exciton
RT	Room temperature
J-V	Current density-voltage
GHI	Global horizontal irradiance
DNI	Direct normal irradiance
GRI	Ground reflected irradiance
EF	Enhancement factor

List of Figures

List of Tables

Chapter 1

Introduction

1.1 Why we need luminescent solar concentrators

Given the current global energy consumption demands of the humanity, the expeditious development of solar energy is imperative due to its innovative, environmentally friendly, and economically viable nature as a renewable energy source. In comparison to conventional energy sources like fossil fuels, solar energy exhibits a significant advantage as a clean, sustainable energy source. The potential capacity of solar energy is vast and virtually limitless. The amount of energy that the Earth receives from the sun in just one hour is enough to power the entire world for a year. According to the International Energy Agency (IEA), the technical potential of solar energy has experienced a significant increase, surging by more than 30 times in the past decade (from 32.2 TWh in 2010 to 1002.9 TWh in 2021). Projections suggest that this upward trend will continue, with solar energy potential expected to grow over 7 times in the next 10 years, reaching 7431.9 TWh by 2030 (**Figure 1.1**).[1-4]

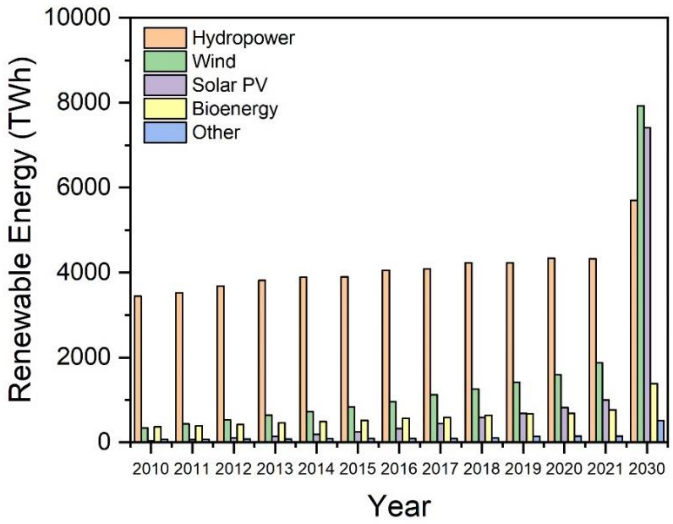

Figure 1.1. Renewable power generation by technology in the Net Zero Scenario, 2010-2030

The development of solar energy involves harnessing the sun's incident energy and converting it into useful forms of energy like electricity or heat. Various technologies can be employed to capture solar energy, including photovoltaic (PV) panels (**Figure 1.2a**)[5, 6], PV panels directly transform sunlight into electricity, while solar heating systems employ the sun's energy to heat water or air, which can be utilized for space heating or hot water purposes (**Figure 1.2b**)[7], and concentrated, solar heating systems and solar power (CSP). CSP systems use physical or chemical method to focus sunlight onto a central receiver to produce heat or electricity. Luminescent solar concentrators (LSCs), a type of CSP system, have the ability to enhance PV energy output efficiency by serving as attachment devices (**Figure 1.2c**).[8]

The roots of LSCs can be traced back to the 1970s when conventional solar cells were cost-prohibitive and inefficient, precluding their widespread adoption.[9, 10] This drove the scientific community to explore novel technologies that could increase the efficiency of solar energy conversion while reducing associated costs. During this time, the use of fluorescent materials to concentrate sunlight onto a solar cell emerged as a promising solution. The approach relied on the absorption of sunlight by a fluorescent material, which would then re-emit the energy at a wavelength suitable for photovoltaic (PV) capture. The re-emitted energy would be confined within the material through total internal reflection (TIR) and then transported to a solar cell to improve its efficiency. This method offered numerous benefits over traditional solar cells, including

the ability to capture light from different angles and wavelengths, the capacity to boost PV performance, and the potential for reduced manufacturing costs.[11]

The emergence of LSCs underscores the significance of research and exploration in advancing solar energy. After decades of experimentation and innovation, scientists have developed a novel solar technology with the potential to revolutionize energy generation and utilization. As we confront pressing challenges such as climate change and energy security, the continual progression of LSCs and other solar technologies will play a crucial role in facilitating a cleaner and more sustainable future.

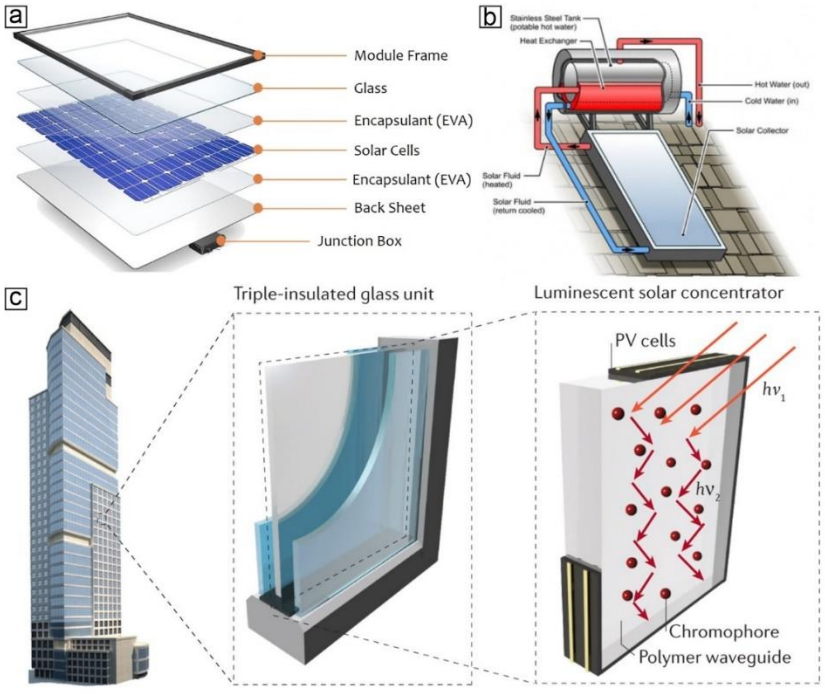

Figure 1.2. The scheme of a **(a)** photovoltaic (PV) modules (b) Solar Hot Water and Heating Systems **(c)** LSC, a type of CSP systems in building integrated solar energy system application.

1.2 Working principle of luminescent solar concentrators

LSCs are transparent composites commonly fabricated from polymers or glass as a matrix, which contain embedded or coated luminescent moieties. The luminescent molecules absorb incident sunlight, followed by re-emitting photons at a specific wavelength. The re-emitted light is then confined within the substrate through TIR, ultimately directing it towards the PV cells affixed to the periphery of the substrate. The working principle of the LSC can be described in the following steps (**Figure 1.3a**):

Absorption: The LSC is made up of a transparent waveguide material that contains luminescent emitters. When sunlight enters the LSC, the emitters absorb some portion of the incident photons and become excited.

Photoluminescence: The excited emitters re-emit the absorbed photons in the form of lower energy photons that travel through the waveguide. According to Snell's law, the difference in refractive index between the LSC and the surrounding medium will trap the emitted photons into the, which is described as TIR effect.

Edge Emission: The LSCs is designed in such a way that it has a large surface area to capture sunlight and a small cross-sectional area to concentrate the emitted photons at the edges of the device. At the edges of the waveguide, the concentrated photons are collected by PVs or other energy conversion devices and converted into electricity or other forms of energy.

Meanwhile, the loss of efficiency in LSC devices can occur through several mechanisms, including (**Figure 1.3b**):

Emitter quenching: Fluorescence quenching is a phenomenon characterized by the suppression or reduction of the fluorescence emission from a fluorescent molecule or material due to several mechanism, such as Förster resonance energy transfer, Dexter electron transfer, exciplex, static quenching, and collisional quenching. The occurrence of different quenching processes varies depending on the type of emitter material used, leading to a decrease in luminescent solar concentrator (LSC) efficiency.

Escape-cone loss: It is a phenomenon that occurs when a portion of the emitted light from a luminescent solar concentrator (LSC) is directed outside the acceptance angle, which is defined by Snell's law. When a photon hits the top or bottom surface of the LSC beyond the acceptance angle, total internal reflection (TIR) cannot trap the photon, and it is eventually transmitted through the LSC, resulting in its loss.

Reabsorption loss: It occurs in LSCs when emitted photons are reabsorbed by the emitters and subsequently re-emitted, rather than being directed towards the solar cell for electricity conversion. This process results in quenching effect during the re-absorption and re-emitting process.

Scattering loss: It occurs due to the presence of impurities, defects, aggregation, or surface roughness in the LSC material, which can scatter the emitted light in various directions. The amount of scattering loss depends on the scattering properties of the material and the size of the scattering centers.

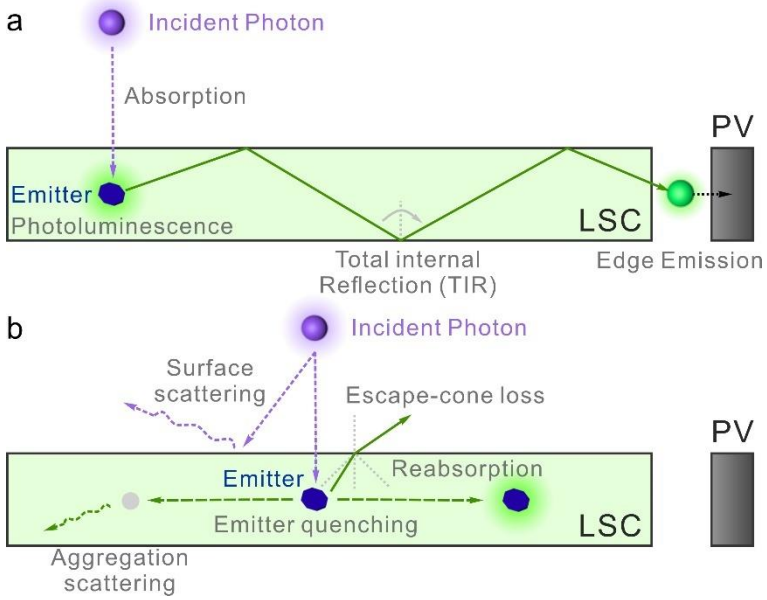

Figure 1.3 (a) Working process of the LSC. **(b)** Lossing process of the LSC

1.3 The development of luminescent solar concentrators

The concept of LSCs was first proposed in the 1970s, but the development of efficient LSCs took several decades of research and development. In the 1970s, Weber et al., proposed the concept of using fluorescent dyes to capture and concentrate sunlight (**Figure 1.4a**).[12] At that time, conventional solar cells were still relatively expensive and inefficient, and researchers were exploring new ways to harness the energy of sunlight.[13] They suggested that the dye molecules could absorb light in the visible and ultraviolet regions, and then re-emit the light at a longer wavelength in the infrared region.[9, 10, 14]

The first experimental LSCs were developed in the early 1981 by Batchelder et al., They used a plastic slab containing coumarin and rhodamine as emitter to concentrate sunlight onto a small silicon solar cell. However, the efficiency of these early LSCs was quite low, at only 1.9%, and there were significant losses due to reabsorption of the emitted light.[15]

One of the key developments in this period was the use of rare earth ions, such as erbium and ytterbium, as the fluorescent emitters.[10, 16] The Levitt et al., already claimed the idea in 1977 the use of neodymium (Nd^{3+})-doped glasses as materials for LSCs.[10] These ions have unique electronic properties that allow them to absorb a wide range of sunlight wavelengths and emit the light at a longer wavelength with high efficiency. The major advantages of using rare earth ions in LSCs is that they can emit light in the

near-infrared range, which is not easily absorbed by conventional silicon solar cells (**Figure 1.4b**). By using rare earth ions in LSCs, researchers were able to convert a larger fraction of the sunlight spectrum into usable energy, making LSCs a potentially promising technology for solar energy conversion.[17-20]

Another significant advancement in the field of Luminescent Solar Concentrators (LSCs) has been the implementation of wavelength-selective mirrors, such as photonic layer and Bragg reflectors, which enhance their efficiency by minimizing energy loss during the light propagation process. By incorporating full, narrow-band reflecting cholesterics on the top surface of the LSCs containing, up to 30% of the light that had previously escaped the surface was converted into edge emission. This innovative approach resulted in a 12% improvement in LSC output using designed reflectors (**Figure 1.4c**).[21-23]

In recent years, researchers have continued to refine and improve LSC technology. For example, they have explored using different types of fluorescent emitters, such as quantum dots and perovskites, which could potentially offer even higher efficiencies. They have also investigated new ways to integrate LSCs into buildings, such as by using them as windows or cladding materials.

Quantum dots (QDs) are semiconductor nano particles, typically a few nanometers in size, that have unique electronic and optical properties. They are made of

semiconductor materials, such as CdSe, ZnS, and PbS, that can be tuned to emit light of different colors depending on their size and composition. The development of QDs began in the early 1980s, when researchers discovered that nanoscale crystals of semiconductors exhibited size-dependent optical properties (quantum confinement).[24-29]

In the early 2000s, researchers began to investigate the use of quantum dots (QDs) as the luminescent material for LSCs.[30] The demonstration of a QD-based LSC was reported in 2007. This initial study showed that QD LSCs could be used to efficiently collect and concentrate sunlight, with an efficiency enhancement of 58% to a reference LSC made by organic dye. Since then, numerous studies have been carried out to improve the efficiency and stability of QD LSCs, as well as to explore new types of QDs and LSC designs.[31, 32]

In recent years, the advancement of QD LSCs has seen significant progress, with novel designs featuring core-shell engineered QDs or the integration of QDs with other luminescent materials. Klimov and Meinardi have made substantial contributions to the development of QD-based LSCs by significantly enhancing the PL QY of the QDs as emitters and seamlessly incorporating them with polymer matrices. Building on previous research involving CdSe/CdS core-shell QDs[33], thick-shell CdSe/$Cd_{1-x}Zn_xS$ QDs[34], heavy-metal-free $CuInSe_xS_{2-x}$/ZnS QDs[35], and earth-abundant silicon QDs[36], they have extensively investigated the application of QDs in the LSC field. Additionally,

they have introduced an innovative characterization system for LSCs, which is expected to greatly benefit future research (**Figure 1.4d-f**).[34, 37-39]

The use of perovskite materials in luminescent solar concentrators (LSCs) was first reported in 2017, when researchers showcased a $CsPb(Br_xI_{1-x})$ perovskite LSC that exhibited an external optical efficiency of 2.0% and maintained long-term air stability without any noticeable change in photoluminescence (PL) intensity.[40] Subsequently, doping perovskite was introduced to the LSC to create a nearly zero-reabsorption emitter, significantly improving the LSC's performance, particularly for large-scale devices. Meinardi was the first to introduce Mn^{2+}-doped $CsPbCl_3$ LSCs, which exhibited a significantly reduced reabsorption effect from the matrix material (less than 1.0% reabsorption) (**Figure 1.4g**).[41] To further minimize reabsorption, a co-doping system was developed that reduced the bandgap emission of the perovskite through the introduction of doping ions. Tong and I designed a Mn^{2+} and Yb^{3+} co-doped $CsPbCl_3$ LSC, which showed a considerable improvement in energy conversion efficiency compared to the Mn^{2+}-doped LSC.[42] On the other hand, researchers have developed layered $CsPbBr_3$ perovskite nanoplatelets (PNPLs) as unique emitters for LSCs. The ultrafast energy transfer between these nanoplatelets generates a large Stokes shift (quantum well), resulting in minimal or no reabsorption properties.[43] Multiple studies have demonstrated the mechanism behind this and have led to the development of more layered perovskite LSCs. The narrowband exciton routing strategy offers a simple and scalable approach to the field of low-loss LSCs (**Figure 1.4h**).[44, 45]

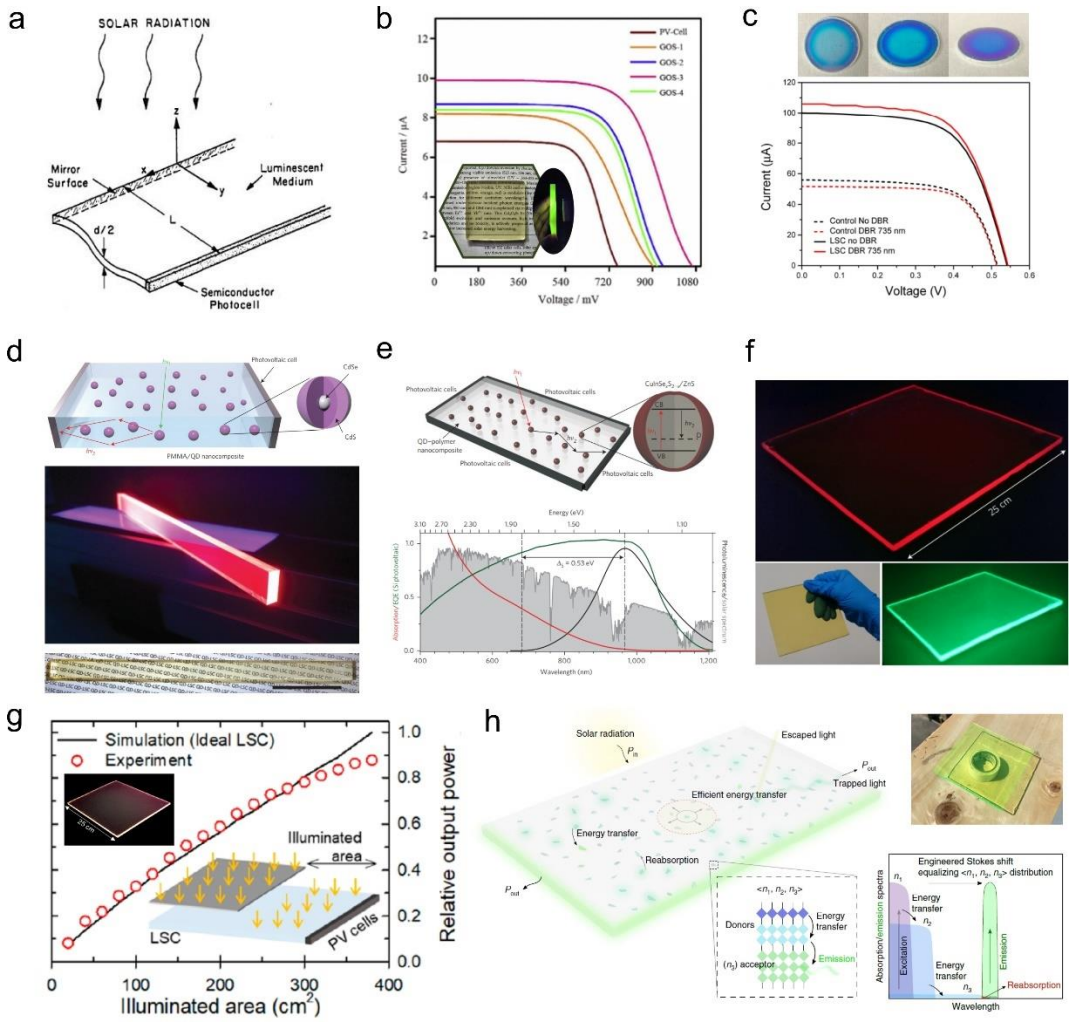

Figure 1.4. (a) The first illustration scheme for the concept of LSC **(b)** Rare earth doping LSC **(c)** Bragg reflector LSC **(d)** CdSe/CdS QD-LSC **(e)** $CuInSe_xS_{2-x}/ZnS$ QDs-LSC **(f)** Si QD-LSC **(g)** Mn^{2+} doping $CsPbCl_3$ LSC **(h)** $CsPbBr_3$ PNPLs LSC

1.4 Current problems and strategies

While Luminescent Solar Concentrators (LSCs) offer a promising solution for low-cost and efficient solar energy harvesting, but there are still some challenges that need to be addressed. One of the main challenges facing LSCs is the limitation of their scalability and cost-effectiveness during the fabrication process. Currently, the dimensions of LSCs are limited to the laboratory scale, making it essential to develop a scalable fabrication approach that enables large-scale industrial production while minimizing the overall production cost. To address this challenge, novel fabrication strategies are required that are appropriate for industry-scale manufacturing. Solution-based deposition techniques, such as Doctor Blade coating or spray coating, offer a promising avenue to achieve the scalable fabrication of LSCs while minimizing the production cost. The development of innovative fabrication methods that effectively upscale LSCs while addressing economic constraints is crucial in overcoming the limitations associated with LSC scalability and cost-effectiveness. Such advancements are pivotal in promoting the commercial deployment of LSCs, which have the potential to become a cost-effective and efficient solution for solar energy harvesting.

Another challenge is the energy conversion efficiency of LSCs, which is affected by factors such as the escape cone losses, reabsorption effect of the LSCs, the not unity photoluminescent quantum yield (PLQY) of the luminescent emitters and multiple types of LSC designs.

To minimize the escape cone losses in LSCs, using a material with a high refractive index as the waveguide layer is a commonly employed method. This waveguide layer, also known as the LSC matrix, plays a crucial role in trapping and guiding the light towards the solar cell. By opting for a high refractive index material, the light can be tightly confined within the waveguide layer, leading to a reduction in the amount of light escaping from the concentrator. Another promising method to tackle escape cone losses is to incorporate a photon crystal reflective layer on the top or bottom surface of the LSC. This reflective layer is designed to reflect the light that travels through the escape cone back into the LSC, where it can be guided towards the edge and converted into electricity by the solar cell. This approach can be highly effective in reducing the escape cone losses and improving the overall efficiency of the LSC.

Reabsorption losses are another challenge that needs to be addressed in LSCs. Reabsorption occurs when some of the photons generated by the emitters are absorbed by the surrounding emitters, rather than being directed towards the solar cell. This reduces the efficiency of the LSC, especially the LSC with large dimension. To overcome reabsorption losses is to develop the emitters that have a large Stokes shift. The Stokes shift is the difference between the energy of the absorbed and emitted photons, and emitters with a large Stokes shift can emit light at a lower energy than they absorb. This reduces the chance of reabsorption, as the emitted light is of a lower energy than the absorbed light and is less likely to be absorbed by the surrounding. Introducing core/shell structure quantum dots and doping system perovskite as the

luminescent emitters for LSCs is an innovative approach recently. Meanwhile, these types of the emitters exhibit high PLQY and a narrow absorption and emission spectra. This makes them more efficient at converting the absorbed light into lower-energy light that can be guided towards the solar cell, while also reducing the chance of reabsorption.

Another approach to optimize the design of LSCs and enhance their sunlight absorption efficiency is to integrate multiple types of LSCs into an LSC-photovoltaic (PV) system. Tandem design LSCs are a common method for addressing the limitations of LSCs, where multiple layers of luminescent emitters with different spectral properties are incorporated to absorb and re-emit light in specific wavelength ranges. The stacked layers enable tandem LSCs to capture a broader range of sunlight wavelengths and reduce reabsorption losses, ultimately leading to increased overall efficiency. However, as the development of emitter materials progresses, the need for other LSC geometry designs may arise.

My PhD research has focused on optimizing the design of luminescent solar concentrators (LSCs) by addressing current challenges and implementing strategies for improvement. In chapter 2, I will discuss an ultrasonic spray coating method for highly efficient, large-scale, and cost-effective LSC fabrication. In Chapter 3, I will present a three-dimensional macroporous photonic crystal layer that significantly reduces escape cone losses from the LSC device. Chapter 4 will focus on the application of cesium copper halide perovskite nanocrystals with zero-reabsorption and high PLQY in LSCs

and luminescent downshifting (LDS) layers for space applications, along with another co-doping perovskite nanocrystals suitable for LSC applications. In Chapter 5, I will introduce the mixing design LSC, which offers a high energy conversion efficiency and easy fabrication compared to normal tandem LSCs. Through building energy consumption simulation studies, I will demonstrate the potential of the mixing design LSC in constructing net-zero energy buildings (NZEBs). Finally, I will summarize the project I have completed and provide an outlook for future LSC studies.

Reference

1. Gross, R.; Leach, M.; Bauen, A., Progress in renewable energy. *Environ Int* **2003,** *29* (1), 105-22.
2. Yildirim, E.; Saraç, Ş.; Aslan, A., Energy consumption and economic growth in the USA: Evidence from renewable energy. *Renewable and Sustainable Energy Reviews* **2012,** *16* (9), 6770-6774.
3. Ahmed, R.; Sreeram, V.; Mishra, Y.; Arif, M. D., A review and evaluation of the state-of-the-art in PV solar power forecasting: Techniques and optimization. *Renewable and Sustainable Energy Reviews* **2020,** *124*.
4. Sebestyén, V., Renewable and Sustainable Energy Reviews: Environmental impact networks of renewable energy power plants. *Renewable and Sustainable Energy Reviews* **2021,** *151*.
5. Gregg, B. A.; Hanna, M. C., Comparing organic to inorganic photovoltaic cells: Theory, experiment, and simulation. *J Appl Phys* **2003,** *93* (6), 3605-3614.
6. Tu, Y.; Wu, J.; Xu, G.; Yang, X.; Cai, R.; Gong, Q.; Zhu, R.; Huang, W., Perovskite Solar Cells for Space Applications: Progress and Challenges. *Adv Mater* **2021,** *33* (21), e2006545.
7. Schoeneberger, C. A.; McMillan, C. A.; Kurup, P.; Akar, S.; Margolis, R.; Masanet, E., Solar for industrial process heat: A review of technologies, analysis approaches, and potential applications in the United States. *Energy* **2020,** *206*.
8. Meinardi, F.; Bruni, F.; Brovelli, S., Luminescent solar concentrators for building-integrated photovoltaics. *Nature Reviews Materials* **2017,** *2* (12).
9. Goetzberger, A.; Greubel, W., Solar-Energy Conversion with Fluorescent Collectors. *Appl Phys* **1977,** *14* (2), 123-139.
10. Levitt, J. A.; Weber, W. H., Materials for luminescent greenhouse solar collectors. *Appl Opt* **1977,** *16* (10), 2684-9.
11. Aste, N.; Tagliabue, L. C.; Del Pero, C.; Testa, D.; Fusco, R., Performance analysis of a large-area luminescent solar concentrator module. *Renewable Energy* **2015,** *76*, 330-337.
12. Weber, W. H.; Lambe, J., Luminescent greenhouse collector for solar radiation. *Appl Opt* **1976,** *15* (10), 2299-300.
13. Halmann, M., Photoelectrochemical Reduction of Aqueous Carbon-Dioxide on P-Type Gallium-Phosphide in Liquid Junction Solar-Cells. *Nature* **1978,** *275* (5676), 115-116.
14. Goetzberger, A., Fluorescent Solar-Energy Collectors - Operating-Conditions with Diffuse Light. *Appl Phys* **1978,** *16* (4), 399-404.
15. Batchelder, J. S.; Zewail, A. H.; Cole, T., Luminescent Solar Concentrators .2. Experimental and Theoretical-Analysis of Their Possible Efficiencies. *Appl Optics* **1981,** *20* (21), 3733-3754.
16. Reisfeld, R.; Kalisky, Y., Nd-3+ and Yb-3+ Germanate and Tellurite Glasses for Fluorescent Solar-Energy Collectors. *Chem Phys Lett* **1981,** *80* (1), 178-183.
17. Lurin, C.; Parent, C.; Leflem, G.; Hagenmuller, P., Energy-Transfer in a Nd-3+-Yb-3+ Borate Glass. *J Phys Chem Solids* **1985,** *46* (9), 1083-1092.

18. Reisfeld, R., Industrial Applications of Rare-Earths in Fiber Optics, Luminescent Solar Concentrators and Lasers. *Inorg Chim Acta* **1987,** *140* (1-2), 345-350.
19. Wang, T.; Zhang, J.; Ma, W.; Luo, Y.; Wang, L.; Hu, Z.; Wu, W.; Wang, X.; Zou, G.; Zhang, Q., Luminescent solar concentrator employing rare earth complex with zero self-absorption loss. *Solar Energy* **2011,** *85* (11), 2571-2579.
20. Kataria, V.; Mehta, D. S., Multispectral harvesting rare-earth oxysulphide based highly efficient transparent luminescent solar concentrator. *Journal of Rare Earths* **2022,** *40* (1), 41-48.
21. Bronstein, N. D.; Yao, Y.; Xu, L.; O'Brien, E.; Powers, A. S.; Ferry, V. E.; Alivisatos, A. P.; Nuzzo, R. G., Quantum Dot Luminescent Concentrator Cavity Exhibiting 30-fold Concentration. *ACS Photonics* **2015,** *2* (11), 1576-1583.
22. Wang, J.; Yuan, Y.; Zhu, H.; Cai, T.; Fang, Y.; Chen, O., Three-dimensional macroporous photonic crystal enhanced photon collection for quantum dot-based luminescent solar concentrator. *Nano Energy* **2020,** *67*.
23. Bauser, H. C.; Bukowsky, C. R.; Phelan, M.; Weigand, W.; Needell, D. R.; Holman, Z. C.; Atwater, H. A., Photonic Crystal Waveguides for >90% Light Trapping Efficiency in Luminescent Solar Concentrators. *ACS Photonics* **2020,** *7* (8), 2122-2131.
24. Coropceanu, I.; Bawendi, M. G., Core/shell quantum dot based luminescent solar concentrators with reduced reabsorption and enhanced efficiency. *Nano Lett* **2014,** *14* (7), 4097-101.
25. Park, J.; Kim, S.-W., CuInS2/ZnS core/shell quantum dots by cation exchange and their blue-shifted photoluminescence. *Journal of Materials Chemistry* **2011,** *21* (11).
26. Geyer, S. M.; Scherer, J. M.; Moloto, N.; Jaworski, F. B.; Bawendi, M. G., Efficient luminescent down-shifting detectors based on colloidal quantum dots for dual-band detection applications. *ACS Nano* **2011,** *5* (7), 5566-71.
27. Colvin, V. L.; Schlamp, M. C.; Alivisatos, A. P., Light-Emitting-Diodes Made from Cadmium Selenide Nanocrystals and a Semiconducting Polymer. *Nature* **1994,** *370* (6488), 354-357.
28. Chen, O.; Zhao, J.; Chauhan, V. P.; Cui, J.; Wong, C.; Harris, D. K.; Wei, H.; Han, H. S.; Fukumura, D.; Jain, R. K.; Bawendi, M. G., Compact high-quality CdSe-CdS core-shell nanocrystals with narrow emission linewidths and suppressed blinking. *Nat Mater* **2013,** *12* (5), 445-51.
29. Shcherbatyuk, G. V.; Inman, R. H.; Wang, C.; Winston, R.; Ghosh, S., Viability of using near infrared PbS quantum dots as active materials in luminescent solar concentrators. *Applied Physics Letters* **2010,** *96* (19).
30. Barnham, K.; Marques, J. L.; Hassard, J.; O'Brien, P., Quantum-dot concentrator and thermodynamic model for the global redshift. *Applied Physics Letters* **2000,** *76* (9), 1197-1199.
31. Hyldahl, M. G.; Bailey, S. T.; Wittmershaus, B. P., Photo-stability and performance of CdSe/ZnS quantum dots in luminescent solar concentrators. *Solar Energy* **2009,** *83* (4), 566-573.
32. Gallagher, S. J.; Norton, B.; Eames, P. C., Quantum dot solar concentrators: Electrical conversion efficiencies and comparative concentrating factors of fabricated devices. *Solar Energy* **2007,** *81* (6), 813-821.

33. Meinardi, F.; Colombo, A.; Velizhanin, K. A.; Simonutti, R.; Lorenzon, M.; Beverina, L.; Viswanatha, R.; Klimov, V. I.; Brovelli, S., Large-area luminescent solar concentrators based on 'Stokes-shift-engineered' nanocrystals in a mass-polymerized PMMA matrix. *Nature Photonics* **2014,** *8* (5), 392-399.
34. Li, H.; Wu, K.; Lim, J.; Song, H.-J.; Klimov, V. I., Doctor-blade deposition of quantum dots onto standard window glass for low-loss large-area luminescent solar concentrators. *Nature Energy* **2016,** *1* (12).
35. Meinardi, F.; McDaniel, H.; Carulli, F.; Colombo, A.; Velizhanin, K. A.; Makarov, N. S.; Simonutti, R.; Klimov, V. I.; Brovelli, S., Highly efficient large-area colourless luminescent solar concentrators using heavy-metal-free colloidal quantum dots. *Nat Nanotechnol* **2015,** *10* (10), 878-85.
36. Meinardi, F.; Ehrenberg, S.; Dhamo, L.; Carulli, F.; Mauri, M.; Bruni, F.; Simonutti, R.; Kortshagen, U.; Brovelli, S., Highly efficient luminescent solar concentrators based on earth-abundant indirect-bandgap silicon quantum dots. *Nature Photonics* **2017,** *11* (3), 177-185.
37. Song, H. J.; Jeong, B. G.; Lim, J.; Lee, D. C.; Bae, W. K.; Klimov, V. I., Performance Limits of Luminescent Solar Concentrators Tested with Seed/Quantum-Well Quantum Dots in a Selective-Reflector-Based Optical Cavity. *Nano Lett* **2018,** *18* (1), 395-404.
38. Wu, K.; Li, H.; Klimov, V. I., Tandem luminescent solar concentrators based on engineered quantum dots. *Nature Photonics* **2018,** *12* (2), 105-110.
39. Gungor, K.; Du, J.; Klimov, V. I., General Trends in the Performance of Quantum Dot Luminescent Solar Concentrators (LSCs) Revealed Using the "Effective LSC Quality Factor". *ACS Energy Letters* **2022,** *7* (5), 1741-1749.
40. Zhao, H.; Zhou, Y.; Benetti, D.; Ma, D.; Rosei, F., Perovskite quantum dots integrated in large-area luminescent solar concentrators. *Nano Energy* **2017,** *37*, 214-223.
41. Meinardi, F.; Akkerman, Q. A.; Bruni, F.; Park, S.; Mauri, M.; Dang, Z.; Manna, L.; Brovelli, S., Doped Halide Perovskite Nanocrystals for Reabsorption-Free Luminescent Solar Concentrators. *ACS Energy Lett* **2017,** *2* (10), 2368-2377.
42. Cai, T.; Wang, J.; Li, W.; Hills-Kimball, K.; Yang, H.; Nagaoka, Y.; Yuan, Y.; Zia, R.; Chen, O., Mn(2+)/Yb(3+) Codoped CsPbCl(3) Perovskite Nanocrystals with Triple-Wavelength Emission for Luminescent Solar Concentrators. *Adv Sci (Weinh)* **2020,** *7* (18), 2001317.
43. Wei, M.; de Arquer, F. P. G.; Walters, G.; Yang, Z.; Quan, L. N.; Kim, Y.; Sabatini, R.; Quintero-Bermudez, R.; Gao, L.; Fan, J. Z.; Fan, F.; Gold-Parker, A.; Toney, M. F.; Sargent, E. H., Ultrafast narrowband exciton routing within layered perovskite nanoplatelets enables low-loss luminescent solar concentrators. *Nature Energy* **2019,** *4* (3), 197-205.
44. Li, Z.; Johnston, A.; Wei, M.; Saidaminov, M. I.; Martins de Pina, J.; Zheng, X.; Liu, J.; Liu, Y.; Bakr, O. M.; Sargent, E. H., Solvent-Solute Coordination Engineering for Efficient Perovskite Luminescent Solar Concentrators. *Joule* **2020,** *4* (3), 631-643.

45. Wei, T.; Lian, K.; Tao, J.; Zhang, H.; Xu, D.; Han, J.; Fan, C.; Zhang, Z.; Bi, W.; Sun, C., Mn-Doped Multiple Quantum Well Perovskites for Efficient Large-Area Luminescent Solar Concentrators. *ACS Appl Mater Interfaces* **2022,** *14* (39), 44572-44580.

Chapter 2

Quantum Dot-Based Luminescent Solar Concentrators Fabricated through Ultrasonic Spray-Coating Method

J. Wang, Y. Yuan, J. Schneider, W. Zhou, H. Zhu, T. Cai, and O. Chen*. Quantum Dot-Based Luminescent Solar Concentrators Fabricated through the Ultrasonic Spray-Coating Method. *ACS Applied Materials & Interfaces* **2022**, 14, 41013-41021.

2.1 Introduction

Moving global energy consumption away from fossil fuels requires innovative, clean, and cost-effective renewable energy technologies.[1-5] Among all the sustainable energy sources, solar power conversion through photovoltaics (PVs) holds the highest potential capacity (~ 80TW/yr).[6-10] In particular, rapid development of PV technology in recent decades makes the realization of net zero-energy buildings (NZEBs), which produce as much energy as they consume over the course of a year through on-site renewable energy generation, increasingly achievable.[11-14] The conventional method for integrating rigid and opaque PV panels to buildings is through mounting on the building rooftop as a solar power farm.[16, 17] However, this installation constraint limits the on-site solar power generation capacity, which is typically insufficient to meet the building total energy demand, especially for multi-floor, high-rise architectures. Therefore, developing innovative means to readily allow the implementation of additional power generation units on-site has been a pressing need. In this context, transparent or semi-transparent luminescent solar concentrators (LSC), light-management devices that can serve as low-cost large-area sunlight collectors for PV cells,[15, 18-21] provide an effective way to transform building facades into power generation units.[11-15, 22-29] An LSC consists of a slab of transparent materials, *e.g.*, glass or polymer, containing highly emissive fluorophores, which are responsible for absorbing and down-converting solar photons for PV usage. In particular, colloidal semiconductor quantum dots (QDs) have been identified as one promising class of emitters for the LSC application, owing to their solution processability, high chemical/physical stability, superior optical

performances including tunable absorption and emission spectral profiles, and high photoluminescence quantum yields (PL QYs).[30-37] Currently, there are two major approaches to fabricate QD-based LSC (QD-LSC) devices. The first approach is to directly incorporate QDs into a polymer matrix, e.g., polydimethylsiloxane (PDMS), poly (methyl methacrylate) (PMMA) or poly (lauryl methacrylate) (PLMA).[18, 19, 22, 38-44] One potential challenge of this approach is the aggregation and thus quenching phenomena of QD emitters during the inevitable polymerization process,[41, 45-50] which leads to performance drop of the obtained LSC devices. Moreover, the QD aggregation-caused refractive index fluctuations may induce significant and undesired scattering events,[47, 51] resulting in device transparency reduction as well as photon/energy loss.[47] The second approach is to cast QD emitters on the surface of a substrate, *e.g.*, glass slide or polymer slab, commonly through coating a thin layer of QD-polymer film.[25, 27, 43, 52-60] This approach can greatly alleviate the negative quenching effects of QDs and LSC composite scattering effect. However, the adaptability and coating-layer controllability of this approach have been largely limited by common coating techniques, such as spin coating process, or Doctor-blade method.[52, 61]

In this work, we report an ultrasonic nebulization assisted spray-deposition technique to fabricate high quality QD-LSCs. Comparing to other coating methods, *e.g.*, conventional spray coating or Doctor blade coating techniques, the ultrasonic spray coating method provides a smooth and artifact-free QD-thin-film layer with programmable optical performance. Meanwhile, the micro-droplets produced by the

ultrasonic nebulizer can significantly reduce the QD aggregation upon QD-film formation. Moreover, this ultrasonic spray coating method can be easily adapted to substrates with different size, geometry, and materials, making it highly adaptable in various applications. Furthermore, by controlling the concentration and volume of QD-ink solution, we demonstrate that it is possible to delicately program the photon capture ability, transparency, and solar energy harvesting and conversion (coupled to PV devices) of the resulting QD-LSC devices through both experimental results and simulation studies. This study shows an important step toward future integration of programable high-performance LSC devices in diverse application setups.

2.2 The fabrication technique for luminescent solar concentrators utilizing ultrasonic spray-coating method

High-quality colloidal CdSe/CdS core/shell QDs were synthesized following a previously reported method (**Figure 2.1**).[30, 33] The energy diagram for the band structural alignment of the core-shell QD depicts strongly confined holes (localized hole wavefunction inside the core) and weakly confined electrons (delocalized electron wavefunction in both core and shell) that are photo-generated in QDs (**Figure 2.1a**). TEM images show that the particles are spherical in shape and highly uniform in size with an average diameter of 11.1 ± 0.6 nm (**Figure 2.1b**). High resolution TEM images show clear cross-fringes of hexagonal atomic lattices, indicating high crystallinity of the sample with a Wurtzite crystal structure (**Figure 2.1b, 2.2**). The high morphological uniformity and particle crystallinity of the QDs impart a narrow PL peak centered at 623 nm (full width at half-maximum: ~ 80 meV), and a high PL QY of 79.5%.

Importantly, due to the presence of the CdS shell dominating the absorption event, photon reabsorption processes of the QDs can be largely reduced because of the significantly minimized spectral overlap between the absorption and PL profiles (also referred as 'Stokes-shift-engineered' QDs, **Figure 2.1c**).[33-35] After dispersing into the hexane/PDMS mixture to form a QD-coating ink, both the absorption and PL spectra remained intact (**Figure 2.1c**), indicating preservation of QD integrity inside the coating ink.

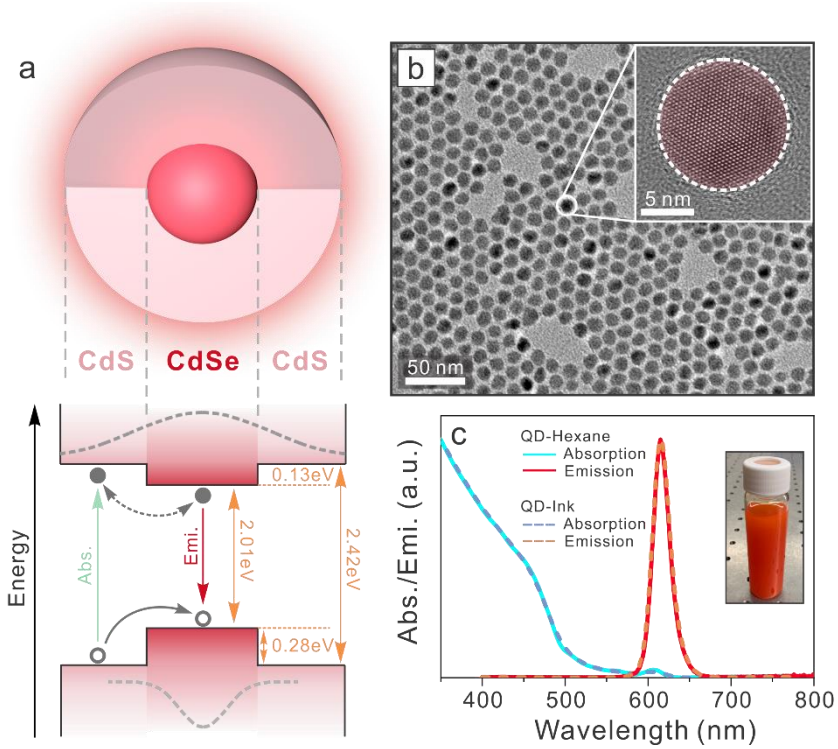

Figure 2.1. (a) Schematic representation of the CdSe/CdS core-shell QDs (top) and the corresponding quasi-Type-II band structural alignment (bottom). **(b)** Typical TEM image of the CdSe/CdS core-shell QDs. Inset: High Resolution TEM image of one representative core-shell QD. **(c)** Absorption and emission spectra of the CdSe/CdS QDs in hexane solution (solid lines) and in QD-PDMS-ink solution (dashed lines). Inset: Photograph of the QD-ink solution.

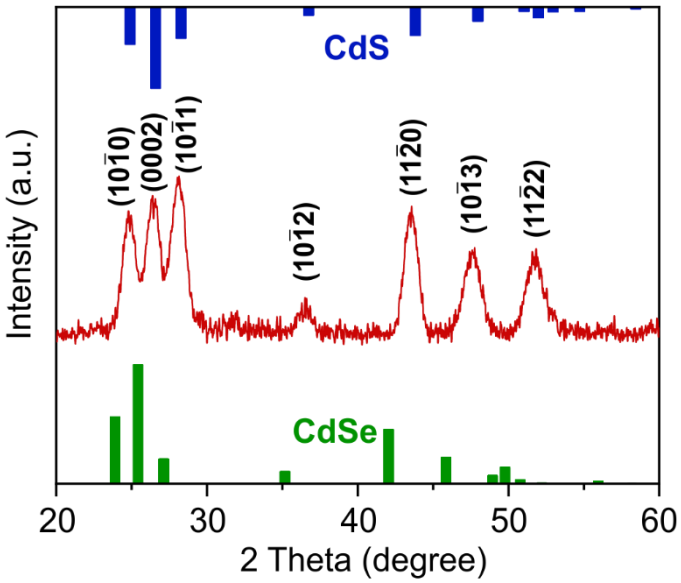

Figure 2.2: X-ray powder diffraction pattern of the CdSe/CdS core/shell QDs. The stick patterns show the standard peak positions of bulk wurtzite CdSe (bottom green sticks) and CdS (top blue sticks).

The fabrication process of QD-containing PDMS thin films using an ultrasonic nebulizer (*Gülife*, model: GP002) is shown in **Figure 2.3** (see **Method** for the detailed procedure). Briefly, hexane/PDMS solution (volume ratio of 10:1) with well-dispersed CdSe/CdS core/shell QDs (2.0-12.0 wt% with respect to PDMS in the ink solution) was prepared as the QD-ink solution for ultrasonic spray. The QD-ink solution was then converted to micro-droplets through the built-in high frequency ultrasonic vibration generator (**Figure 2.3a, b**). After mixing with air through the air channel, a homogeneous aerosol flow in the form of fine mist was created and deposited onto a heated substrate (either a PDMS film or a glass substrate, preheated to 80 °C) with fixed nozzle-substrate distance of 10 cm and a flow rate of 1.0 mL/min (**Figure 2.3b**). After hexane evaporation, the QD-PDMS composite film was cured onto the substrate by annealing at 60 °C for 30 min to obtain the final QD-LSC (**Figure 2.3c**). Scanning electron microscopy (SEM) measurements show the smooth surface of the obtained

QD-LSC devices (**Figure 2.3d-e**) with a low arithmetical mean height (Sa = 15) determined by surface roughness measurement (see **Method** for details). In contrast, a film with significantly increased roughness (Sa = 5347) and uneven surface was obtained when coating with the same QD-ink using a regular spray nozzle following an identical coating procedure (**Figure 2.4, 2.5**). This result demonstrates that the fine mist of aerosol flow created by the ultrasonic nebulizer is crucial to obtaining high-quality QD-LSC devices with a smooth QD thin-film emitting layer.

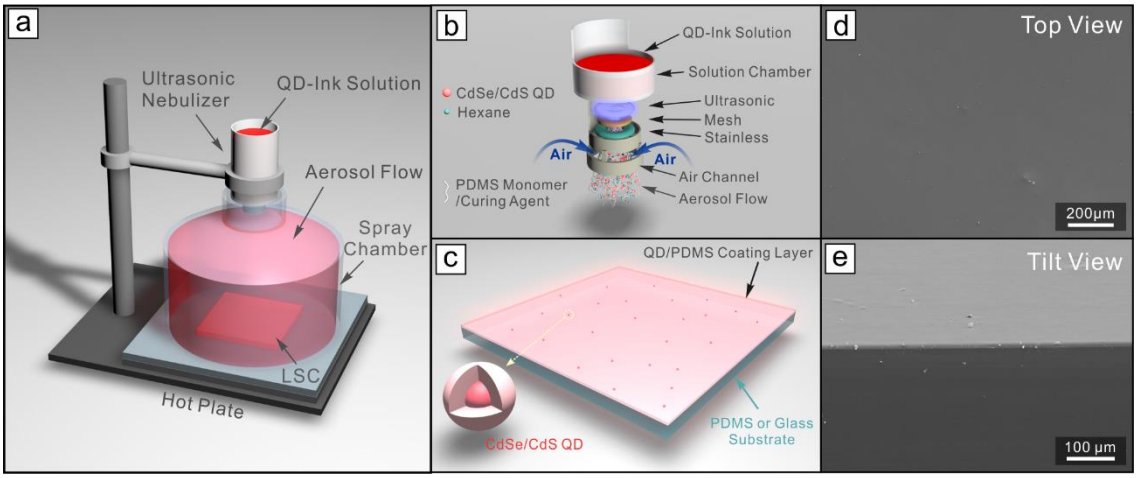

Figure 2.3. (a) Schematic representation of the LSC fabrication process using an ultrasonic nebulization assisted spray-deposition technique. **(b)** Zoomed-in working principle of the ultrasonic nebulizer. **(c)** Schematic of the fabricated QD-LSC device. SEM images for the **(d)** top view and **(e)** 45° tilting view of the ultrasonic-spray coated QD-LSC device surface.

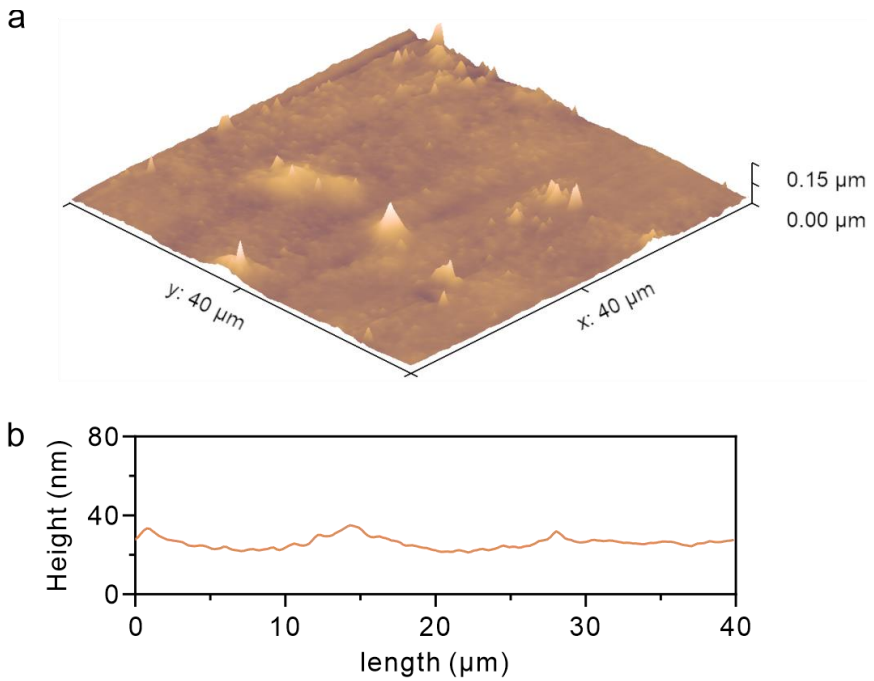

Figure 2.4. (a) 3D and **(b)** 2D height profiles of the QD-LSC surface fabricated through the ultrasonic spray coating method.

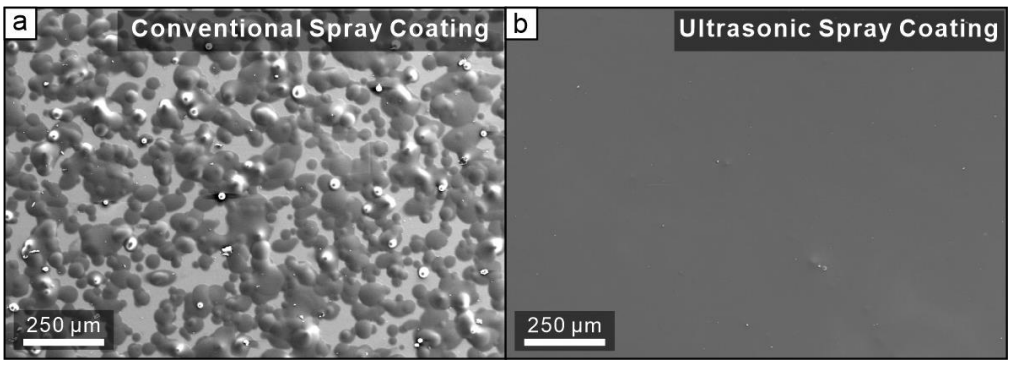

Figure 2.5. SEM images of the coating surface through **(a)** normal spray method, and **(b)** ultrasonic spray-coating method using the same QD-ink solution.

2.3 Ultrasonic spray-coating film characterization

To demonstrate the scalability of the ultrasonic spray method, we fabricated a large scale QD-LSC through ultrasonic spray coating of 25 mL QD-ink solution (1.0 wt%) on a glass substrate with dimensions of 20 cm × 20 cm × 0.2 cm (geometric factor, G = 25, see **Method** for coating details). G factor is defined as the ratio of the areas of top surfaces and device edges (G = L/4d, L: square device edge length; d: device thickness).

The obtained QD-LSC device showed a high average visible transparency (AVT: 79.7%, **Figure 2.6a**) and a strong light concentrating effect with the PL signal dominantly emitted from the edge windows of the device (**Figure 2.6b**). To further demonstrate the adaptivity of the coating method, we also ultrasonic spray coated the QD-ink solution (2.0 wt%, 1.0 mL) on curved PDMS substrates (both concave and convex shapes) with different curvature levels. **Figure 2.6c, d** show photographs of the obtained convex and concave QD-LSC devices with the curvatures of 0.15 cm^{-1}, 0.34 cm^{-1} and 0.42 cm^{-1}. All the devices show smooth and uniform coatings with concentrated emitted light at the edges of each device under UV illumination (**Figure 2.6c, d**, right panels). The QD-coating film thickness can be characterized using fluorescent microscopy. For example, **Figure 2.6e, f, g** shows cross-section fluorescent images of a convex QD-LSC device (convex curvature of 0.34 cm^{-1}) at three different measuring spots (indicated in the middle right panel of **Figure 2.6c**). Nearly identical QD emitting layer thicknesses (~ 5 μm) were observed, demonstrating the coating uniformity on the curved substrates using the ultrasonic spray method, consistent with the ultrasonic nebulized spray pyrolysis process.[62-64] The light concentrating effect was quantitatively determined by measuring the emission profiles of the same device (the QD-LSC with a convex curvature of 0.34 cm^{-1}). The area-integrated emission spectra showed that about 80.9% of the total QD emitted photons propagated to the edge windows, while only 19.1% photons escaped through the top and bottom surfaces of the QD-LSC device (**Figure 2.6h**).

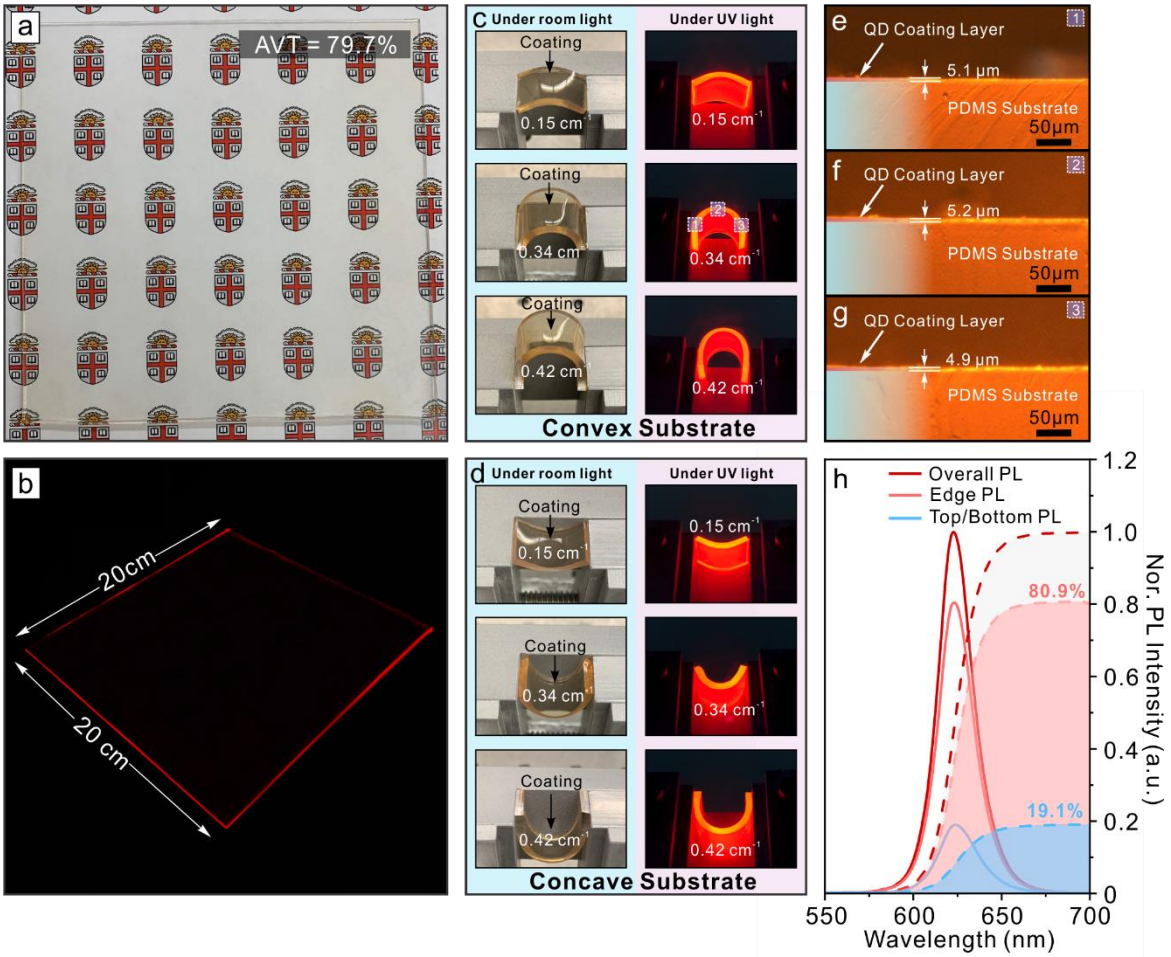

Figure 2.6. Photographs of the large scale QD-LSC device under **(a)** ambient light and **(b)** 365 nm UV light illumination. **(c)** QD-LSC devices with a convex geometry and different curvature levels under room light (left) and 365 nm UV light (right). **(d)** QD-LSC devices with a concave geometry and different curvature levels under room light (left) and 365 nm UV light (right). **(e-g)** Microscopic fluorescence images of the QD-LSC device with a convex curvature of 0.34 cm^{-1} at spots 1 **(e)**, 2 **(f)** and 3 **(g)** as labeled in the panel (c). **(h)** PL spectra measured from the overall device (dark red), and top/bottom (light red) and edge (blue) windows for the convex QD-LSC device (curvature of 0.34 cm^{-1}). Dashed lines represent the integrated emission peak areas normalized to the overall device emission peak area.

To program the QD-LSC device performances, we fabricated a series of LSC devices under the same ultrasonic spray coating conditions but altering the QD-ink solution concentration (see details in **Method**). While maintaining the QD-ink solution volume (*i.e.*, 1.0 mL), we fabricated four LSC devices with PDMS substrates (dimension: 4.0

cm × 4.0 cm × 0.2 cm; G = 5) using QD-ink solutions with different QD concentrations of 2.0 wt%, 4.0 wt%, 8.0 wt% and 12.0 wt%. We found that in all cases, continuous and smooth QD-coating layers can be obtained with a consistent thickness of ~ 4.5 μm **(Figure 2.7a-e**). Cross-section fluorescent images of the devices showed that the coating layer exhibited uniform fluorescence signal from the embedded QD emitters, indicating homogeneity of the QD-coating layer (**Figure 2.7a-d**). Moreover, we measured the emission peak intensities at 10 random spots (spot size of 50×50 μm^2) on the QD-coating layer of each device. As shown in **Figure 2.7f**, all the four QD-LSC devices exhibited stable PL peak intensities with minimal fluctuations. Meanwhile, the overall PL intensity of the QD-LSC devices showed a proportional dependence on the concentration (from 2.0 wt% to 12.0 wt%) of the utilized QD-ink solution (**Figure 2.7g**), indicating a comparable coating quality with marginal photon scattering effects (induced by surface roughness).[65, 66] All these results validated the high quality coating of QD emissive layer and showed versatility of the ultrasonic nebulization assisted spray coating method for fabrications of QD-LSCs with tunable optical properties.

Then, optical performances of the obtained QD-LSC devices were characterized by measuring the device transmission, absorption, and emission spectral profiles. All the devices show superior device transparency with relatively high AVT values of > 70% (**Figure 2.7h**), revealing their high adaptability for transparent or semitransparent surface integrations, such as building facades, shade covers, and car windows.[11] With increasing QD concentration from 2.0 wt% to 12.0 wt%, the AVT value exhibited a

linear decrease from 83.6 % to 73.2% (**Figure 2.7h, inset**). The absorption measurements for the QD-LSC devices coated with 2.0 wt%, 4.0 wt% and 8.0 wt% QD-ink solutions revealed a high consistency with the absorption profiles of the starting dilute QD hexane solution (**Figure 2.1c**), indicating a solid-solution nature of the fabricated QD-coating film (**Figure 2.7i**). Whereas the absorption spectrum of the LSC device coated with 12.0 wt% QD-ink solution showed a slight photon scattering signal (**Figure 2.7i**), which can be attributed to a low level of QD aggregation induced by the high QD concertation (*i.e.*, 12.0 wt%) during the film curing process.[47] The PL spectral profiles of all the devices showed single narrow emission peaks with the peak position at 631 nm (**Figure 2.7j**), consistent with the emission spectrum of the dilute QD hexane solution, further proving the low level of particle aggregation even using a high concentration (*i.e.*, 12.0 wt%) QD-ink solution. In addition, we also applied this ultrasonic spray coating method to produce QD-LSCs by spraying different volumes of the same QD-ink solution (from 0.5 mL to 3.0 mL, **Figure 2.8, 2.9**), or using QD-ink solutions containing different types of QDs (*i.e.*, $CsPbBr_3$ perovskite QDs and $CuInS_2$/ZnS core/shell QDs). Similar levels of optical performance can be obtained for the fabricated QD- LSC devices (**Figure 2.10**), suggesting a high versatility of this coating method.

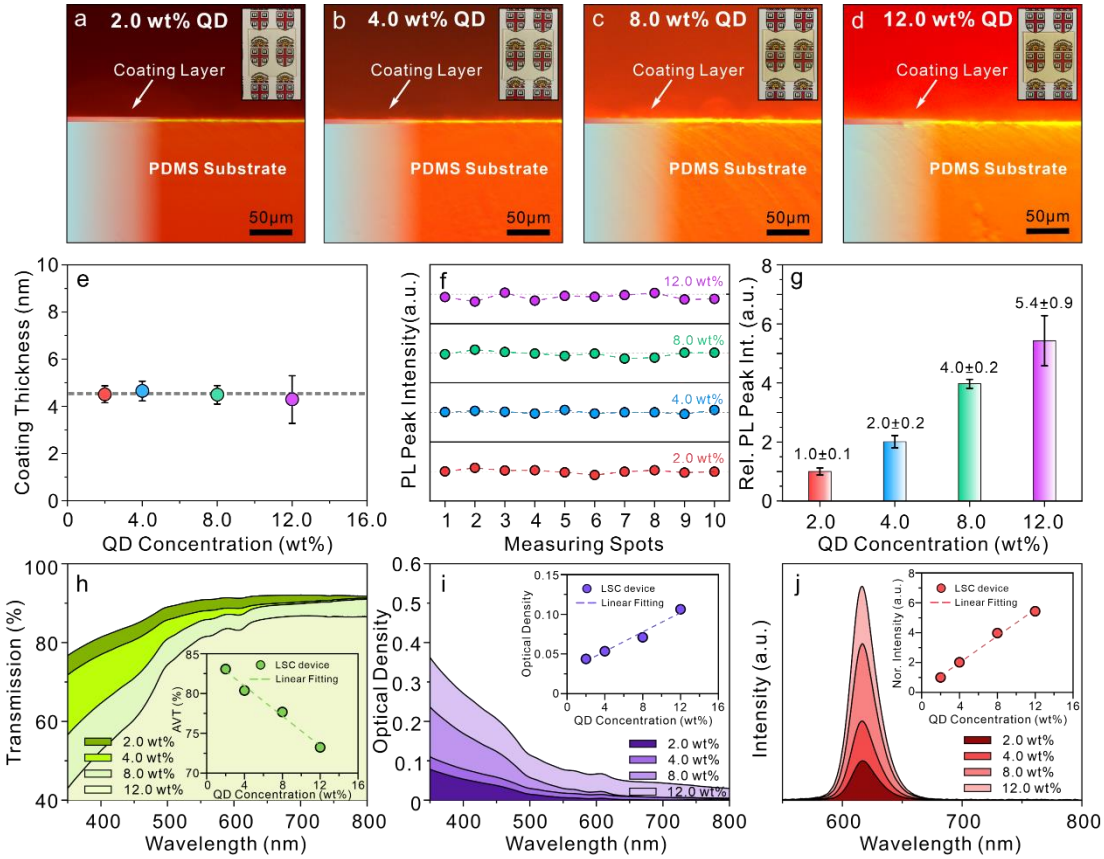

Figure 2.7. Microscopic fluorescence images of the ultrasonic spray-coated LSC devices using 1.0 mL QD-ink with a QD concentration of **(a)** 2.0 wt%, **(b)** 4.0 wt%, **(c)** 8.0 wt% and **(d)** 12.0 wt%. Insets: photographs of the corresponding prototype QD-LSC devices. **(e)** The average QD-film thickness for the LSC devices fabricated using different QD-ink concentrations. **(f)** Normalized PL peak intensity of 10 random measuring spots on 2.0 wt% (red), 4.0 wt% (blue), 8.0 wt% (green) and 12.0 wt% (purple) LSC devices. **(g)** The corresponding relative (rel.) overall PL peak intensities (int.) of the four LSC devices. **(h)** Transmission, **(i)** absorption, and **(j)** emission spectra of the four LSCs with different QD-ink concentration. Insets: AVT (h), optical density at 612 nm (i), and relative emission peak intensity (j) as a function of QD-ink concentration.

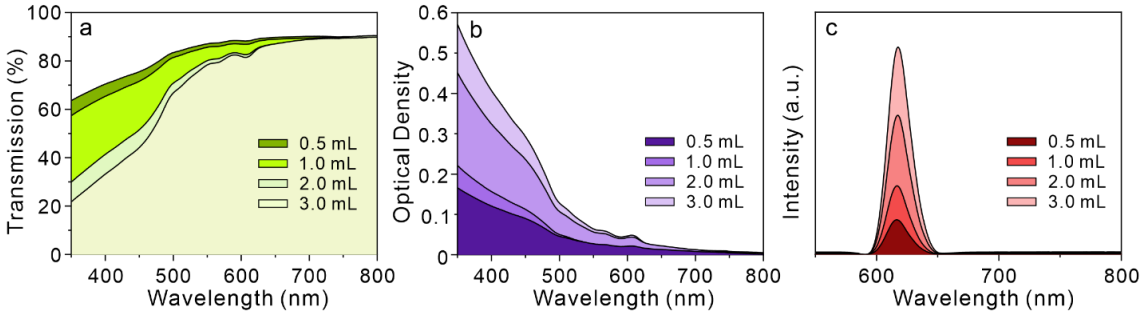

Figure 2.8. (a) Transmission, **(b)** absorption, and **(c)** PL spectra of the four QD-LSCs fabricated using the CdSe/CdS QD-ink solution (8.0 wt%) with different QD-ink solution volume.

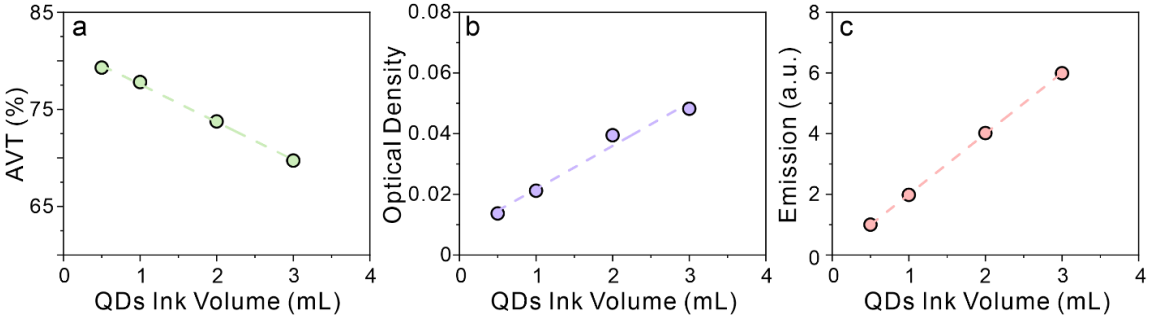

Figure 2.9. (a)AVT, **(b)** optical density at 612 nm, and **(c)** relative PL peak intensity of the four QD-LSCs fabricated using the CdSe/CdS QD-ink solution (8.0 wt%) with different QD-ink solution volume.

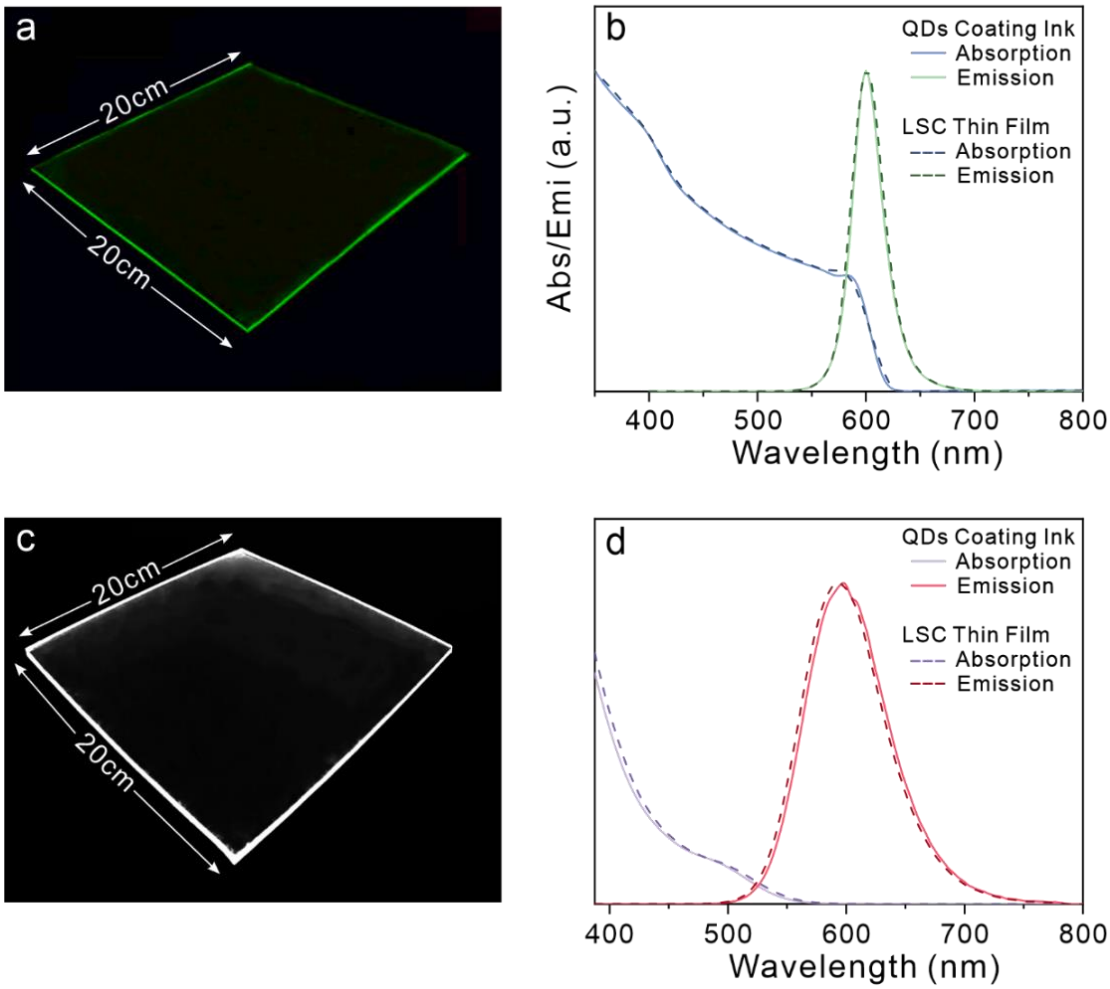

Figure 2.10. (a) A large scale (20 cm × 20 cm × 0.2 cm, G = 25) LSC device fabricated through the ultrasonic spray-coating with a $CsPbBr_3$ QD-ink solution (QD concentration: 1.0 wt%, and volume: 25 mL). The photo was taken under 365nm UV light illumination. **(b)** Absorption and emission spectra of the $CsPbBr_3$ QD-ink solution (solid lines) and the fabricated LSC thin film (dashed lines). **(c)** A large scale (20 cm × 20 cm × 0.2 cm, G = 25) LSC device fabricated through the ultrasonic spray-coating with a $CuInS_2/ZnS$ QD-ink solution (QD concentration: 1.0 wt%, and volume: 25 mL). The photo was taken by NIR camera under 365nm UV light illumination. **(d)** Absorption and emission spectra of the $CuInS_2/ZnS$ QD-ink solution (solid lines) and LSC thin film (dashed lines).

2.4 Luminescent solar concentrators simulation

Monte Carlo (MC) ray-tracing simulations were carried out to evaluate the light concentrating performance of the QD-LSC devices fabricated through the ultrasonic spray method. The detailed logic flow of the MC simulation is shown in the supporting information (see **Method**, **Scheme 2.2**). To obtain meaningful results, 10,000 incident photons (at 365 nm) were set to hit the top surface of each LSC device. In the simulation, we considered a cuboid substrate slab with a dimension of 4.0 cm × 4.0 cm × 0.2 cm (G = 5, refractive index: n = 1.4, adopted from the refractive index number of PDMS). A QD-coating layer (thickness of 6.0 μm) on the top surface of the device was considered in the MC simulation. The input optical profiles were based on the experimentally measured device absorption spectra for the QD-LSCs fabricated using an 8.0 wt% QD-ink solution with four different coating volumes (*i.e.*, 0.5 mL, 1.0 mL, 2.0 mL, to 3.0 mL) (see the experimental data in **Method**, **Figure 2.8b**). When the coating volume increased from 0.5 mL to 3.0 mL, the edge-emitted photons (labeled in red arrows) increased from 7.08%, 9.22%, 14.47% and 17.70% of the total incident photons, respectively (**Figure 2.11a-d**). We quantitatively analyzed the incident photon behaviors based on the MC mode photon tracking counters for the four LSC devices. The analysis results showed that the fraction of transmitted photons gradually decreased from 81.5% to 57.6% of the total incident photons when the coating ink volume increased from 0.5 mL to 3.0 mL (**Figure 2.11e-h**). Meanwhile, the corresponding fraction of absorbed photons increased from 16.3% to 39.9%. Importantly, for all the simulated samples, the fraction of surface reflected/scattered photons stayed in a nearly

constant range (*i.e.*, 2.2-2.5%) (**Figure 2.11e-h**), in line with the consistent coating film quality as we observed experimentally. The fates of QD absorbed and emitted photons were also quantitatively analyzed from the simulation. The fractions of the edge-emitted, escaped (through top/bottom surfaces), and lost (through reabsorption and attenuation) photons were maintained at similar levels for all devices (**Figure 2.11i-l**). Around 42-44% of the QD captured photons can be emitted (down-converted by QDs), trapped, and concentrated to the LSC edge windows (**Figure 2.11i-l**), suggesting a stable and high light trapping performance for all devices studied here.

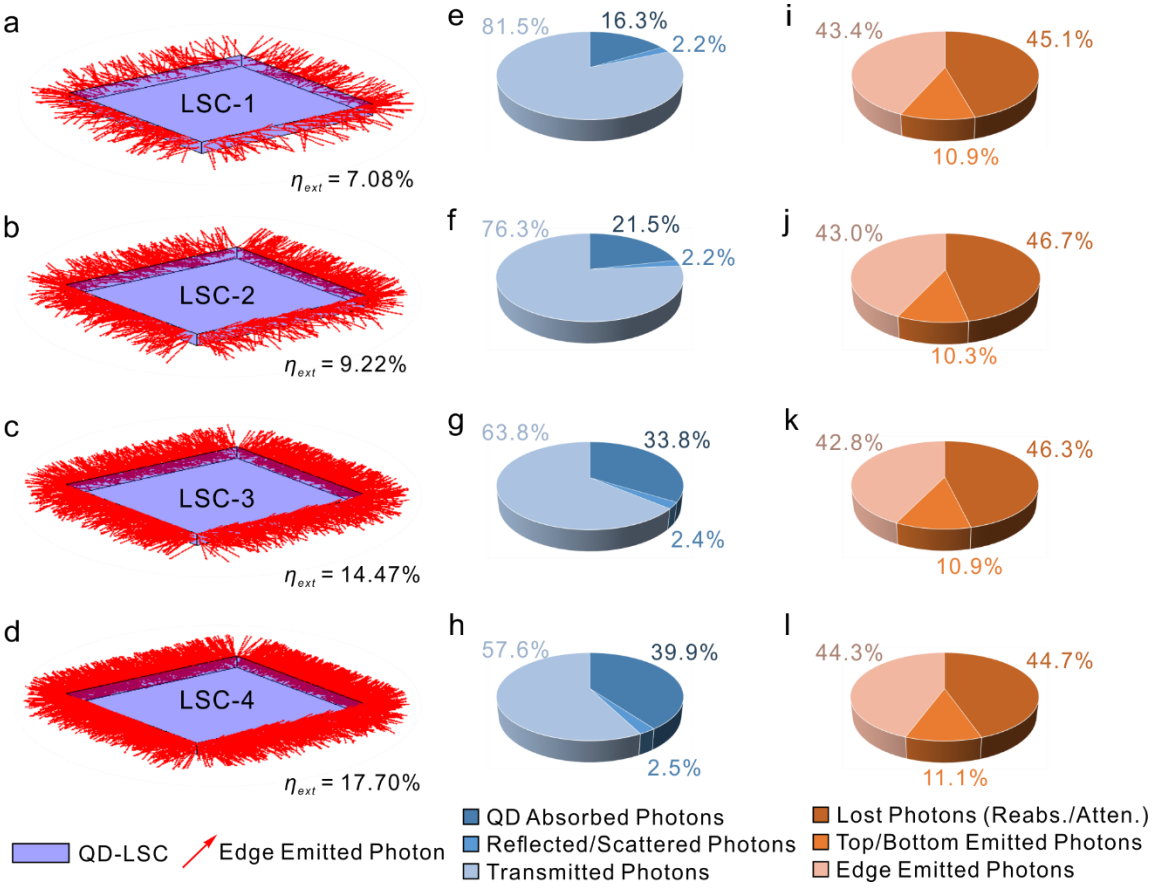

Figure 2.11. Visualization of the Monte-Carlo ray-tracing simulation for the LSC devices fabricated through ultrasonic spray-coating method using 8.0 wt% QD-ink solution with different volumes: 0.5 mL for LSC-1 **(a)**, 1.0 mL for LSC-2 **(b)**, 2.0 mL for LSC-3 **(c)**, and 3.0 mL for LSC-4 **(d)**. **(e-h)**: Pie charts of incident photon fractions

after hitting the surface of the devices of LSC-1 **(e)**, LSC-2 **(f)**, LSC-3 **(g)**, and LSC-4 **(h)**. **(i-l)** Pie charts of the fate of absorbed photons for the devices of LSC-1 **(i)**, LSC-2 **(j)**, LSC-3 **(k)**, and LSC-4 **(l)**.

2.5 Luminescent solar concentrators performance characterization

Finally, we evaluated device performances of the QD-LSCs fabricated through the ultrasonic spray coating by characterizing the optical and electro-optical properties of the LSC devices (4.0 cm × 4.0 cm × 0.2 cm, G = 5) coated with 8.0 wt% QD-ink with different volumes (*i.e.*, 0.5 mL, 1.0 mL, 2.0 mL, and 3.0 mL, denoted as LSC-1, LSC-2, LSC-3, and LSC-4, respectively). The internal optical efficiencies (η_{int}, defined as the ratio of the edge-collected photon flux and the total absorbed photon flux) under 365 nm light excitation were experimentally determined to be 42.2 ± 2.5% (LSC-1), 44.0 ± 2.1% (LSC-2), 43.2 ± 1.9% (LSC-3), and 44.1 ± 2.3% (LSC-4) for the four devices (**Figure 2.12a**). The η_{int} values were highly consistent with the analytical simulation (an analytical approach to evaluate the performance of LSCs) results for the devices with the same G factor (**Figure 2.12a**),[67, 68] as well as the MC simulation results (**Figure 2.11i-l**). The relatively stable η_{int} of the devices, insensitive to the QD-coating layer thickness, was in good agreement with relatively large Stokes shift with minimal photon reabsorption loss of the applied QD emitters (**Figure 2.1c**). The external optical efficiency (η_{ext}, defined as the ratio of the edge-collected photon flux and the total incident photon flux) of the four QD-LSC devices were measured to be 7.5 ± 1.8% (LSC-1), 9.5 ± 0.8% (LSC-2), 14.7 ± 0.9% (LSC-3), and 17.5 ± 1.2% (LSC-4), in accordance with the values determined by the analytical simulation (**Figure 2.12b**).

Taking both η_{ext} and G factor into consideration, we calculated the C factor (defined as the ratio between output and input photon flux densities, C = η_{ext} × G) evolution as a function of G factor (**Figure 2.12c**). For the four samples with the same G factor of 5, a continuous increase of C factor from 0.37 (0.38) to 0.88 (0.89) was obtained from experiments (simulations) upon increasing the coating volume of QD-ink solution from 0.5 mL to 3.0 mL. In addition, the analytical simulation showed that C factor can be further increased by increasing the device G factor (**Figure 2.12c**).

To characterize the performance of the integrated QD-LSC-PV systems in converting solar energy, we coupled a silicon PV cell to one edge of each QD-LSC device (the other three edges were blocked by black tape, see **Scheme 2.1**). Under the simulated solar illumination using a sunlight simulator (1.5 AM Global), we measured the *J-V* curves of the four QD-LSC-PV systems, showing a positive dependency with respect to the QD-ink coating volume (**Figure 2.12d**). This result was in good agreement with the device optical properties and η_{ext} characterizations, as well as the simulation prediction (**Figure 2.12a-c**). The η_{ext} values under sunlight irradiation were experimentally determined by integrating the obtained device *J-V* curves and compared with the analytical simulation results (**Figure 2.12e, 2.13**). Specially, the experimental (simulated) η_{ext} under sunlight illumination increased from 3.2 ± 0.7% (3.6%), 4.5 ± 0.3% (4.4%), 6.8 ± 0.8% (6.6%) to 7.6 ± 0.5% (7.4%), respectively for the QD-LSC devices coated with 0.5 mL, 1.0 mL, 2.0 mL, and 3.0 mL of 8.0 wt% QD-ink solution. Furthermore, the spectral dependent external quantum efficiency (EQE) curves for each

QD-LSC-PV systems were also measured and showed consistency with the absorption profiles of the devices (**Figure 2.12f, 2.14**), validating the reliable performances in solar energy conversion of the QD-LSC devices fabricated through the ultrasonic spray coating method.

In this study, we present an ultrasonic nebulization assisted spray-deposition method to fabricate high-quality QD-LSC devices with uniform and homogenous QD layer surface coatings and low photon scatterings. Importantly, this method shows a high adaptability and can be easily applied to fabrications of QD-LSC devices with various substrates (with different dimensions and geometries including highly curved surfaces) and using different QD-ink solutions (with different QD type, concentration, and solution volume). By adjusting the QD concentration and ink solution volume, we have successfully fabricated a series of QD-LSC devices with high visible light transparency and superior performances in sunlight energy harvesting and power conversion. The experimental results were strongly supported by both MC ray-tracing and analytical simulations developed in this study. We anticipate this ultrasonic spray coating method can be widely employed to productions of various LSC devices using different type of emitters including and beyond QDs. Our study demonstrates an important step towards fabrications of high-quality LSC devices that can be effectively integrated into windows, shades, and/or other types of architectural façades, thus transforming them into on-site power-generation units.

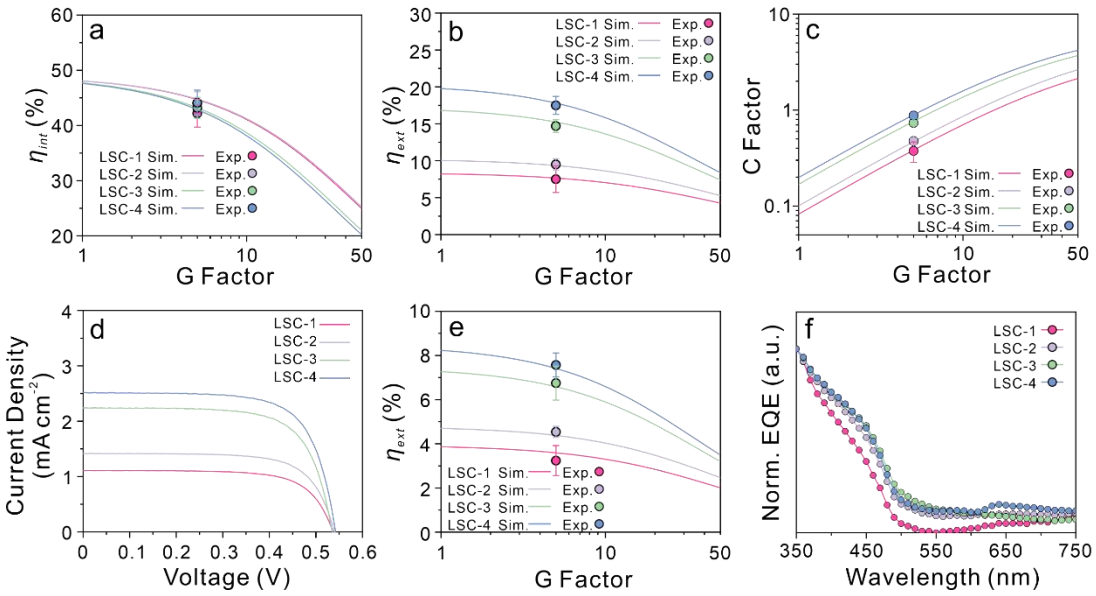

Figure 2.12. (a-c) Simulated (solid lines) and experimentally obtained (dots) η_{int} **(a)**, η_{ext} **(b)** and C factor **(c)** as a function of G-factor under 365 nm light excitation for the QD-LSC devices fabricated using 8.0 wt% QD-ink with different volumes of 0.5 mL (LSC-1, pink), 1.0 mL (LSC-2, purple), 2.0 mL (LSC-3, green) and 3.0 mL (LSC-4, blue). **(d)** Experimentally measured *J-V* curves of the LSC devices under sunlight (1.5 AM Global) illumination. **(e)** Simulated (solid lines) and experimentally obtained (dots) η_{ext} as a function of G-factor under sunlight (1.5 AM Global) illumination. **(f)** Normalized spectrally resolved EQE values for the four LSC devices under sunlight (1.5 AM Global) illumination.

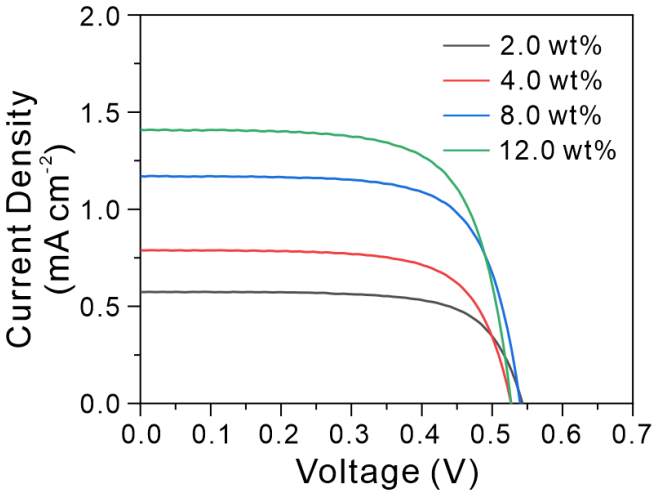

Figure 2.13. *J-V* curve of the QD-LSC-PV fabricated using the QD-ink solutions (1.0 mL) with different QD concentrations: 2.0 wt% (grey), 4.0 wt% (red), 8.0 wt% (blue) and 12.0 wt% (green).

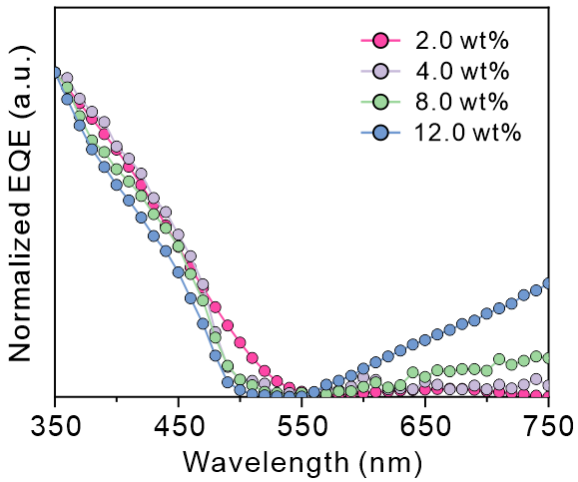

Figure 2.14. Normalized EQE spectra under sunlight (1.5 AM Global) illumination for the four QD-LSC-PV systems. The QD-LSCs were fabricated using the QD-ink solution (1.0 mL) with different QD concentrations: 2.0 wt% (pink), 4.0 wt% (purple), 8.0 wt% (green) and 12.0 wt% (blue).

2.6 Ultrasonic spray-coating method optimization

Then we focus on optimizing ink solution components to enhance the ultrasonic spray-coating process, taking inspiration from the ternary solvent ink strategy used in inkjet printing.[69] This method showcases exceptional printability and film-forming abilities, resulting in high-quality emissive thin films with fewer surface defects. We evolve the quinary ink into a quaternary solvent system, consisting of naphthene, n-tridecane, n-nonane, hexane, and PDMS. By maintaining the component ratio of the quinary coating solution system, we successfully integrate the ink into the ultrasonic spray-coating process. The quinary coating solution system outshines the binary hexane/PDMS

component, providing lower surface tension and accommodating higher concentrations of perovskite emitters.

Using low surface tension solutions in ultrasonic spray-coating presents several advantages. First, these solutions ensure improved coverage by allowing materials to spread smoothly across the substrate, resulting in even coating and reducing uncovered or inadequately coated areas. Second, low surface tension solutions enhance wetting, fostering better adhesion to the substrate and decreasing the chances of material separation over time or under stress. Lastly, these solutions minimize surface defects, such as pinholes or cracks, by spreading more readily and adhering more effectively to the substrate, yielding a sleek, seamless coating.[70-72]

Incorporating high concentration solutions in spray-coating offers numerous benefits, including increased efficiency, enhanced control, and shortened processing time. First, high concentration solutions augment the coating process's efficiency by depositing a larger amount of material onto the substrate in less time, minimizing waste and boosting overall performance. Second, these solutions provide greater control over coating thickness and uniformity, as precise adjustments can be made to the solution's concentration, resulting in a more consistent coating. Lastly, high concentration solutions facilitate faster coating deposition rates, which shortens processing time and becomes essential for applications that demand extensive coverage or high throughput.

To develop an ideal ultrasonic spray coating ink that avoids agglomeration and precipitation behaviors, it is crucial to prioritize dispersity, orthogonality, and printability. Initially, we examine the coating ink recipe without considering the emitter component to simplify the problem. The inclusion of nanoparticles may cause additional agglomeration due to the ligand, which could impact the selection of the ink recipe.

Based on previous studies, obtaining an ultrasonic coating ink requires reducing the solution viscosity to a certain level, ensuring that the solution can be atomized by the high-frequency ultrasonic vibration generator without clogging the nozzle. Nonane, tridecane, and naphthalene all exhibit relatively high viscosity, so it is necessary to ensure that the solution system contains at least 50 wt% hexane. The hexane solution effectively reduces viscosity and evaporates immediately upon contact with the hot plate, thus not significantly affecting the coating film formation process. PDMS serves as the final film formation component. To guarantee film thickness and uniformity, the PDMS concentration is set to approximately 4 wt%.

The working principle of the coating solution is as follows: First, the solution is atomized by the ultrasonic nebulizer. After mixing with air through the air channel, a homogeneous aerosol flow in the form of a fine mist is created and deposited onto a heated substrate. As the heating plate temperature is much higher than its boiling point, the hexane evaporates immediately from the substrate, and the PDMS (with a volume

ratio of monomer:initiator = 1:1) begins to cure. During the drying process, nonane, tridecane, and naphthalene start to evaporate. The boiling point gradient of the ternary solution system compresses the coffee-ring effect through the inward Marangoni flow with low surface tension, resulting in significantly improved coating thin films. In this process, nonane, which has the lowest boiling point, helps generate the Marangoni flow and reduces the final evaporation time. To ensure the presence of Marangoni flow, the concentration of nonane is set to be approximately 37%.

Generally, the surface tension, viscosity, and inertia properties of inks govern the rheological behaviors of stable microscale liquid jets and droplets formation, which can be primarily assessed by the Kosower Z value of the solvents. The Z value offers a simple, fast, and precise parameter for measuring solvent polarity on a molecular level. According to reported literature, Z values ranging from 4 to 14 are considered suitable for stable coating inks. Naphthalene and tridecane serve as Z value coordinators for the solution system, and their addition results in better solubility for the emitter. To find the most appropriate recipe component, we created five groups of coating ink solutions (**Table 2.1**). Our study indicates that tridecane and naphthalene provide a relatively high degree of freedom, as adjusting the components of these two compounds does not significantly affect the final coating film quality.

To examine the coating ink quality, we use contact angle and surface tension measurements to quantitatively evaluate the ink properties. As low surface tension

indicates better surface coverage, wetting abilities, and fewer surface defects, the optimized coating ink solution should minimize surface tension as much as possible by adjusting the ratio of tridecane and naphthalene. The captive bubble method measures the wetting contact angle at a solid-liquid interface. From the optical image, the equilibrium Young's law contact angle of the sessile droplet for reference water and coating ink is shown in **Figure 2.16 (a-f)**. The contact angle of the reference water droplet is used to calculate the surface tension. From **Figure 2.16 (b-f)**, coating inks 1-5 (corresponding to Inks 1-5 in Table 2.1) display a lower contact angle compared to the reference water droplet, indicating better wetting ability for the coating ink. **Figure 2.16 (g)** presents the average contact angle data corresponding to different naphthalene and tridecane volumes, revealing that Ink 4 (containing 0.25mL tridecane and 0.15mL naphthalene) has the lowest contact angle of 29.64°. According to Young's Law, the surface tension of the coating ink solution can be expressed as follows:

$$\gamma_l = \frac{\gamma_{water}(1+cos(\theta_{water}))^2}{(1+cos(\theta_l))^2} \quad (1)$$

Where γ_l and γ_{water} is the surface tension of the ink and reference water drop accordingly, θ_l and θ_{water} is the contract angle of the ink and the reference water drop accordingly. Utilizing this equation, we can determine the surface tension of the coating ink as depicted in **Figure 2.16 (h)**. Following the same trend observed in the contact angle plot, Ink 4 exhibits the lowest surface tension at 38.52 mN/m, making it the most suitable ink for ultrasonic spray-coating.

Ink	**Component**				
	PDMS	**Hexane**	**Nonane**	**Tridecane**	**Naphthalene**

1	100 mg	2 mL	1.4 mL	0.1 mL	0.3 mL
2	100 mg	2 mL	1.4 mL	0.15 mL	0.25 mL
3	100 mg	2 mL	1.4 mL	0.2 mL	0.2 mL
4	100 mg	2 mL	1.4 mL	0.25 mL	0.15 mL
5	100 mg	2 mL	1.4 mL	0.3 mL	0.1 mL

Table 2.1 The component of different coating ink.

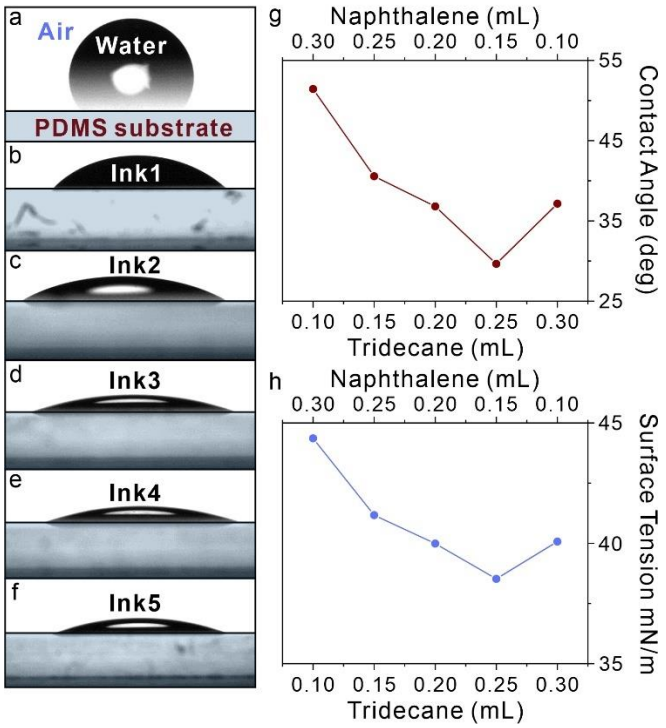

Figure 2.15. (a-f) Captive bubble configuration for measuring the contact angle of **(a)** reference water drop, **(b)** coating ink 1, **(c)** coating ink 2, **(d)** coating ink 3, **(e)** coating ink 4, and **(f)** coating ink 5 on PDMS substrate. **(g)** Contact angles of the coating ink with different naphthalene and tridecane volume. **(h)** Surface tension of the coating ink with different naphthalene and tridecane volume.

In order to determine the optimal emitter loading concentration for the coating ink, we measure the viscosity and perform dynamic light scattering (DLS) measurements on

Ink 4 with different concentrations of emitters. In this study, we use $CsPbBr_3$ QDs as the emitter due to its potential application in LSC research. The viscosity plot is shown in **Figure 2.17 (a)**, where the viscosity displays varying values under different shear speeds. The viscosity at low shear rates is considerably higher than at high shear rates under all concentration conditions, indicating that the coating solution is a shear-thinning fluid. As $CsPbBr_3$ QDs are added, the viscosity changes at low shear rates and stabilizes at a certain value, as illustrated in **Figure 2.17(b)**. This effect suggests that when the $CsPbBr_3$ QDs concentration increases up to 30 wt%, the nanoparticles begin to aggregate and increase the viscosity. When the shear rate rises to 100 1/s, the viscosity is only influenced by the solution, demonstrating an almost unchanged value among the various $CsPbBr_3$ QD concentrations. Therefore, an optimal $CsPbBr_3$ QD concentration of around 20 wt% should result in minimal aggregation and low viscosity at low speeds. To validate this conclusion, we also conduct DLS measurements to assess the $CsPbBr_3$ QDs' condition in the solution. As shown in **Figure 2.17 (c)**, when the $CsPbBr_3$ QDs are at concentrations of 10 wt% and 20 wt%, significant peak signals are observed around 10 nm^3, indicating that the individual $CsPbBr_3$ QDs are well dispersed in the solution system. Another small peak is present around 1000 nm^3, suggesting minor aggregation of the $CsPbBr_3$ QDs. However, when the concentration increases to 30 wt%, no peak appears around 10 nm^3. The peak is only observed at around 1000 nm^3, implying that most of the $CsPbBr_3$ QDs are aggregated in the solution system, rendering it unsuitable for the coating ink.

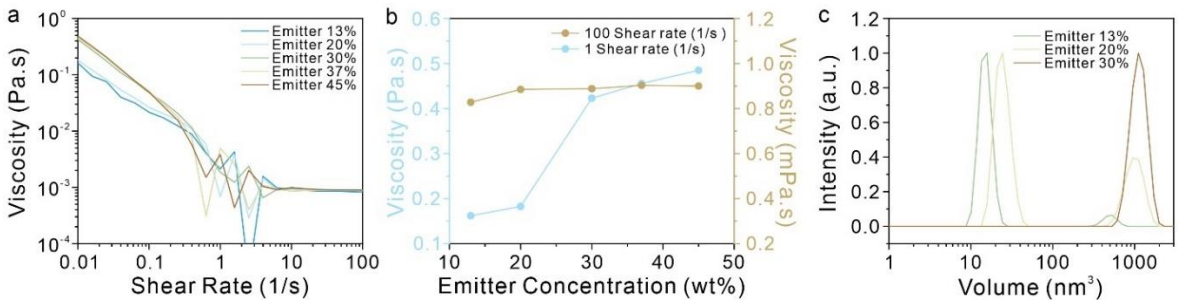

Figure 2.16. (a) Viscosity plot of the ink 4 loading different concentration of $CsPbBr_3$ QD. **(b)** The viscosity value under 100 1/s shear rate (khaki) and 1/s shear rate. (cyan) with ink 4 loading different concentration of $CsPbBr_3$ QDs. **(c)** DLS measurement of the ink 4 loading different concentration of $CsPbBr_3$ QDs.

The fabrication process of QD-containing PDMS thin films using an ultrasonic nebulizer (*Gülife*, model: GP002) is described in **Method**. Briefly, the prepared Ink 4 with well-dispersed $CsPbBr_3$ QDs (13-45 wt% relative to PDMS in the ink solution) was used as the solution for ultrasonic spraying. The coating ink solution was transformed into micro-droplets through the built-in high-frequency ultrasonic vibration generator. After mixing with air in the air channel, a homogeneous aerosol flow in the form of fine mist was produced and deposited onto a heated PDMS substrate (preheated to 80 °C) with a fixed nozzle-substrate distance of 10 cm and a flow rate of 1.0 mL/min. Ultrasonic spray-coating of alternating layers of $CsPbBr_3$ QDs/PDMS (250µL for $CsPbBr_3$ QDs layer, 500µL for PDMS layer, and 30min curing with N_2 blowing) was performed. Following the coating process, the substrate was annealed at 60 °C for 48 hours to obtain the final QD-LSC. Scanning electron microscopy (SEM) measurements reveal the smooth surface of the resulting 13wt% and 20wt% QD-LSC devices (**Figure 2.18 a, b**) with low arithmetic average roughness (Ra = 78 and 80,

respectively) as determined by surface roughness measurements (**Figure 2.19**). In contrast, a film with significantly increased roughness (Ra = 152 and 163, respectively) and an uneven surface was obtained when coating with the 30wt% and 45wt% QD-ink (**Figure 2.18 c, d**). This result indicates that the optimal concentration of $CsPbBr_3$ QDs is around 20 wt% in order to achieve high-loading and high-quality QD-LSC devices with a smooth QD thin-film emitting layer.

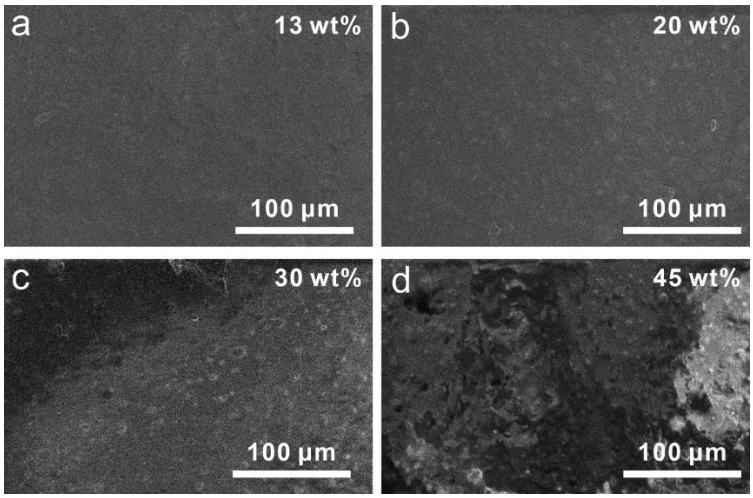

Figure 2.17. SEM images of the coating film surface through ultrasonic spray-coating method using the ink 4 loading different **(a)** 13 wt%, **(b)** 20 wt%, **(c)** 30 wt%, **(d)** 45 wt% of $CsPbBr_3$ QD.

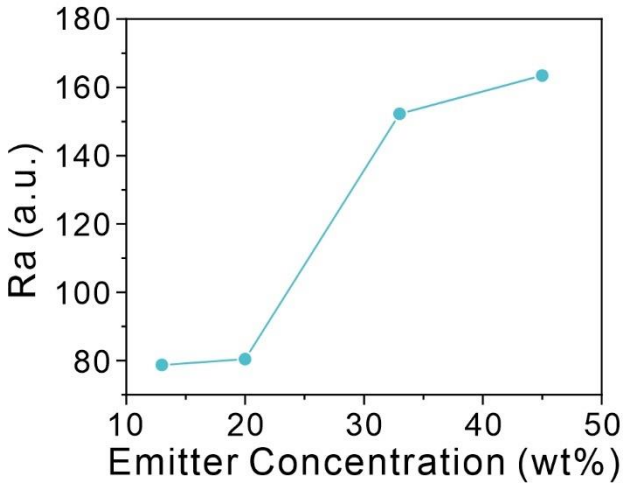

Figure 2.18. Arithmetic average roughness (Ra) of the coating film surface with ink 4 loading different concentration of $CsPbBr_3$ QD.

After incorporating $CsPbBr_3$ QDs into Ink 4 to create a QD-coating ink, both the absorption and PL spectra remained intact (**Figure 2.20 a**), signifying that the QD integrity was maintained within the coating ink. We employed the analytical mode simulation (see **Method** for details) to predict the device's external quantum efficiency (η_{ext}) performance. The simulation results revealed an optimal point for achieving the best η_{ext} performance in LSC under 365 nm light excitation. To reach that point, we needed to adjust the coating volume to deposit a specific amount of $CsPbBr_3$ QDs onto the substrate. The simulated absorption spectra for the optimal performance QD-LSC are displayed in **Figure 2.20 b**.

Based on the simulation results, we coated 13.5 mL of 20 wt% $CsPbBr_3$ QDs Ink 4 onto the PDMS substrate to fabricate the LSC devices (4.0 cm × 4.0 cm × 0.2 cm, G = 5). The actual device absorption spectra are also presented in **Figure 2.20 b**, with the absorption plot partially overlapping, suggesting that with the assistance of the simulation result and the optimal coating ink recipe, we can achieve a high emitter loading LSC. Furthermore, we measured the emission peak intensities at five random spots (spot size of 50×50 μm^2) on the QD-coating layer of the device. As depicted in **Figure 2.20 c**, the QD-LSC device exhibited stable PL peak intensities with minimal fluctuations. In addition, the η_{ext} of the best-performing device was measured to be 39.7 ± 2.0%, consistent with the values determined by the analytical simulation. The η_{abs}

was calculated to be 93.7% under 365 nm single-wavelength excitation, which closely aligns with the optimal η_{abs} point according to the simulation results.

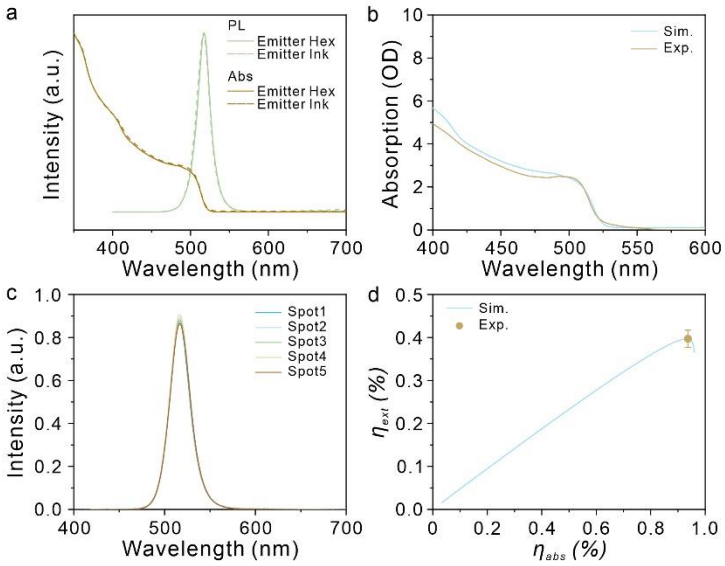

Figure 2.19. (a) Absorption and emission spectra of the $CsPbBr_3$ QD emitter in hexane solution (solid lines) and coating ink solution (dashed lines). **(b)** Absorption spectra of the best performance fabricated LSC thin film and the corresponding simulated LSC thin film **(c)** PL spectra of 5 random measuring spots the fabricated LSC thin film. **(d)** Simulated (solid lines) and experimentally obtained (dots) η_{ext} as a function of η_{abs} under 365 nm light excitation for the LSC devices fabricated using 20.0 wt% $CsPbBr_3$-QD-ink 4.

In this study, we successfully optimized the ultrasonic-spray deposition method's coating recipe to create high-loading and high-efficiency QD-LSC devices. Through surface tension measurements, viscosity tests, and DLS measurements, we developed the optimal recipe components and the highest applicable emitter concentration for the ink. Furthermore, by integrating the analytical mode simulation, we fabricated the optimal QD-LSC devices with outstanding η_{abs} and η_{ext} performance (the best-performing device) for UV energy harvesting and power conversion.

Method

Chemicals

Cadmium oxide (CdO, 99.998%), octadecylphosphonic acid (ODPA, 97%), trioctylphosphine oxide (TOPO, 99%), trioctylphosphine (TOP, 97%), selenium powder (99.999%), cesium carbonate (Cs_2CO_3, 99.9%), lead bromide ($PbBr_2$, 99.999%), Zinc acetate (Zn(OAc)2, 99.9%), oleic acid (OA, 90%) 1-octadecene (ODE, 90%), oleylamine (OAm, 70%), cadmium nitrate tetrahydrate ($Cd(NO_3)_2 \cdot 4H_2O$, 99.99%), 1-octanethiol (> 98.5%), 1-dodecanethiol (DDT, 98%), nonane (> 99%), tridecane (> 99%), naphthalene (99%), ethanol and toluene were purchased from Sigma-Aldrich. Sygrad 184 Polydimethylsiloxane (PDMS) was purchased by Gelest Inc. All chemicals were used without further purification.

Synthesis of CdSe cores:

Wurtzite-CdSe (W-CdSe) cores were synthesized according to the literature method.[30,31] 60 mg CdO, 280 mg octadecylphosphonic acid (ODPA) and 3 g trioctylphosphine oxide (TOPO) were added to a 50 mL flask. The mixture was heated to 150 °C and degassed under vacuum for 1 hour. Under nitrogen flow, the reaction mixture was heated to 320 °C to form a colorless clear solution. After adding 1.0 mL trioctylphosphine (TOP) to the solution, the temperature was brought up to 380 °C, at which point Se/TOP (60 mg Se in 0.5 mL TOP) solution was swiftly injected into the flask. When the CdSe cores reached the desired size, the reaction was terminated by removing the heat. The resulting CdSe particles were precipitated by adding acetone and dispersed in hexane as a stock solution.

Synthesis of CdSe/CdS core/shell quantum dots (QDs):

As-prepared CdSe QDs were loaded in a mixture of 1-octadecene (ODE, 3 mL) and oleylamine (OAm, 3 mL). The reaction solution was degassed under vacuum at room temperature for 1 hour and 120 °C for 20 min to completely remove the hexane, water and oxygen inside the reaction solution. Then, the reaction solution was heated up to

310 °C with a heating rate of 18 °C/min under nitrogen flow and magnetic stirring. During the heating, when the temperature reached 240 °C, a desired amount of cadmium (II) oleate (Cd-oleate, diluted in 6 mL ODE) and 1-octanethiol (1.2 equivalent amounts relative to Cd-oleate, diluted in 6 mL ODE) began to be injected dropwise into the growth solution at a rate of 3 mL/hr using a syringe pump. After finishing precursor injection, 1 mL oleic acid was quickly injected and the solution was further annealed at 310 °C for 60 min. The resulting CdSe/CdS core/shell QDs were precipitated by adding acetone, and then redispersed in hexane. The particles were further purified by precipitation-redispersion for two more rounds and finally suspended in ~2 ml toluene solution.

Preparation of Cs-oleate:

814 mg Cs_2CO_3 was loaded into 100mL 3-neck flask along with 40 mL ODE and 2.5 mL oleic acid, dired under vaccum for 1 h at 120 ℃, then heated under N_2 to 150 ℃ for another 1 h until all Cs_2CO_3 reacted with OA. The Cs-oleate solution should be preheated to 100 ℃ before further use.[73]

Synthesis of $CsPbBr_3$ perovskite QDs:

5 mL ODE and 69 mg $PbBr_2$ were loaded into 25 mL 3-neck flask and dried under vacuum for 1h at 120 ºC. 0.5 mL OA and 0.5 mL OAm were injected at 120 ºC under N_2. After complete solubilisation of a $PbBr_2$ salt, the temperature was raised to 160 ºC and 0.4 mL as-prepared Cs-oleate solution was quickly injected. And 5s later, the reaction mixture was cooled by the ice-water bath. The solution was centrifuged at 6000 rpm for 5 min. Collect the precipitated and redispersed into hexane solution.[73]

Synthesis of Zink stock solution

734 mg $Zn(OAc)_2$ were mixed with 8 mL OA and 2 mL DDT in a 50 mL flask. After being purged with N_2 flow for 10 min, the solution was heated up to 200 ℃ under N_2 flow protection.[74]

Synthesis of $CuInS_2$/ZnS core/shell QDs

191 mg CuI, 292 mg $In(OAc)_3$ and 5 mL DDT were loaded into a 25 mL 3-necked flask and purged with N_2 gas for 10 min. Next, the solution was heated up to 230 ℃ and maintain at this temperature for 30 min. After that, 5 mL as-prepared Zink stock solution were quickly injected into the reaction solution. After 30 min, remove the heating mental and cool down the solution to room temperature. 10 mL ethanol was added into the solution and centrifuged at 8000 rpm for 5 min to form the precipitated. Collect the solid sample and then dispersed in hexane.[74]

Fabrication of ultrasonic spray-coated luminescent solar concentrators (LSCs):

The purified CdSe/CdS core-shell QDs were desolved in toluene solution and added into a mixture with Sygrad 184 PDMS viscus oligomer and Sygrad 184 curing agent with a weight ratio of 1:1. The degased mixture was stirred and vacummed for 1h to form a clear and homogeneous solution and dissolved into hexane with a PDMS/hexane volume ratio of 1:10. The QD concentration in the final mixtures were adjusted from 2.0 wt% to 12.0 wt% (QD/PDMS). The different QD inks were ultrasonic sprayed onto the heated PDMS substrate. The distance between ultrasonic spray nozzle and substrate was set to 10 cm. The surface temperature of the substrate was set at 80 °C. After 5 min, the coated device was annealed at 60 °C for 30 min.

For large scale LSC fabrication, the coating ink recipe is the same. The PDMS substrate was placed into a polyvinyl alcohol (PVA) chamber. The distance between ultrasonic spray nozzle and the substrate was set to 20 cm. The substrate was preheated in the oven at 80 °C and immediately coated with 1.0 mL 1.0 wt% QD-ink solution. When the aerosol flow was fully deposited, the substrate was put back into the oven at 80 °C for 30 min. Then another 1.0 mL QD-ink solution was coated onto the subtrate. The procedure was repeated until 25 mL QD-ink solution was coated. After coating, the substrate was put into the oven to cure for overnight at 60 °C. All the LSC devices were cut into desire dimension after the final annealing process.

For the optimized method, the purified $CsPbBr_3$ QDs were desolved in hexane solution and added into a mixture with Sygrad 184 PDMS viscus oligomer and Sygrad 184 curing agent with a weight ratio of 1:1. The degased mixture was stirred and vacummed for 1h to form a clear and homogeneous solution and dissolved into a solution system with different ratio of PDMS/hexane/nonane/tridecane/naphthalene. The QD concentration in the final mixtures were adjusted from 10 wt% to 45 wt% (QD/PDMS). The distance between ultrasonic spray nozzle and substrate was set to 10 cm and a flow rate of 1.0 mL/min. The surface temperature of the substrate was set at 80 °C. The substrate was deposited by 250 μL $CsPbBr_3$ QDs ink solution and 500 μL PDMS protection layer alternatively with the N_2 blowing. After the coating process, the substrate was annealing at 60 °C for 48 h to obtain the final QD-LSC.

UV-Vis absorption and transmission measurements

UV-Vis absorption spectra and transmission spectra were performed using an Agilent Technologies Cary 5000 UV-Vis-NIR Spectrophotometer. The LSC devices were placed onto the solid film holder for the measurement.

Photoluminescence (PL) and PL quantum yield (PL QY) measurements

The PL spectra and PL QY measurements were measured using an Edinburgh Instruments Fluorescence Spectrometer FS5. The PL QYs were measured by FS5 Spectrometers with a built-in integrating sphere. The LSC samples were placed onto a solid sample holder.

X-ray Diffraction (XRD) measurements of CdSe/CdS core-shell QDs

XRD pattern was acquired using a Bruker D8 Discovery 2D X-ray Diffractometer equipped with a Vantec 500 2D area detector operating with Cu Kα radiation (λ = 1.541 Å). The CdSe/CdS core-shell QD sample in a hexane solution was drop-casted on glass slides and evaporated at ambient conditions.

Current density-voltage (J-V) curve characterization

The *J-V* characteristics were measured using a 2400 source meter (Keithley, USA) under simulated 1-sun illumination (AM1.5G, 100 mW·cm^{-2}) which is generated by an Oriel Sol3A Class AAA solar simulator (Newport, USA) in air. The procedure of single junction LSC devices follows a literature approach[57]: we used a polycrystalline silicon (c-Si) mini cell (Sunnytech Mini Small Solar Panel) coupled with the edge regions of the LSC devices by using NOA 68 polymer adhesive. Black tape was applied to cover the excess area of the solar cell. The *J–V* curves of the coupled LSC-PVs and the standalone PV were obtained using a voltage source meter (Keithley 236) in the range of −0.1 V to 12 V with a voltage step of 0.1 V. In all LSC-PV measurements, after attaching solar cells to the LSC, the excess edge areas were masked with total absorbing black tape to stabilize the set-up. (**Scheme 2.1**)

External quantum efficiency (EQE) measurement

The external quantum efficiency (EQE) of the PSCs was measured using an internal quantum efficiency system (IQE200B, Newport, USA) under the irradiation by a 100 W xenon lamp. The LSC-PV set-up was the same as the *J-V* curve characterization (see Scheme 2.1 below).

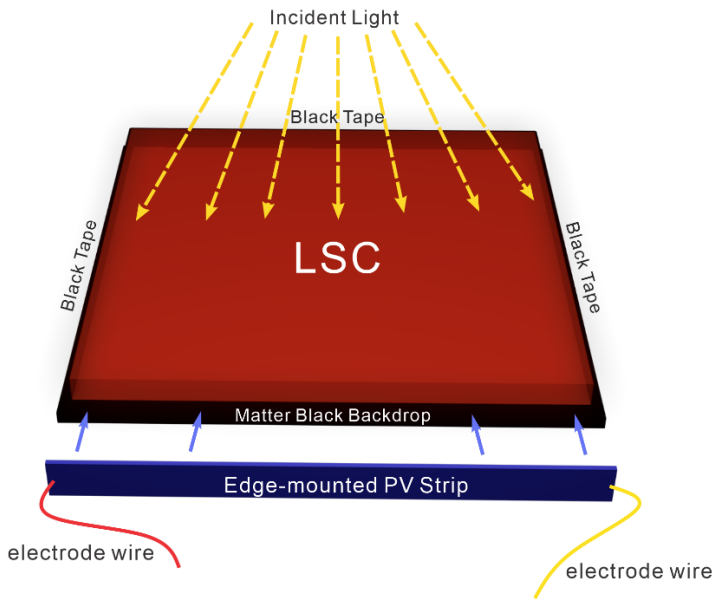

Scheme 2.1: Schematic illustrating the PV-LSC system set-up for *J-V* curve and EQE

measurement.

Scanning electron microscope (SEM) measurements and surface roughness measurement

SEM measurements were carried out on Thermo Scientific Quattro S ESEM operated at 5kV on a solid-sample holder. A thin layer of gold (~2 nm) was sputtered onto the samples prior to the measurements. The surface roughness measurements were carried by using a *ImageJ* plugin surfcharj_1q.

Atomic force microscopy (AFM) measurements.

The AFM images were collected on a MFP3D (Asylum research) atomic force microscope.

Internal (η_{int}) and External optical efficiency (η_{ext}) of LSCs from optical measurements

Due to the size limitation of the built-in integrating sphere, we applied optical measurements to determine the external optical efficiency of the small size LSC device (4.0 cm × 4.0 cm × 0.2 cm, G = 5). We first measured the PL QY of the edge emitted LSC device. This value was definited as the internal optical efficiency (η_{int}) of the LSC device, which is the ratio of the edge photon flux and the total absorbed incident photon. Further, we defined η_{ext} as the ratio of the edge-collected photon flux and the total incident photon flux, which is described by following equation:

$$\eta_{ext} = \eta_{int} \times \eta_{abs} \quad (2)$$

In this equation, η_{abs} is the absorption ratio of LSC device, which is the ratio of the LSC captured photon and the total incident photon, described as:

$$\eta_{abs} = (1 - T)(1 - R) = (1 - R)(1 - e^{-\alpha_1 d}) \quad (3)$$

where, T is the transmission of the overall LSC device, α_1 is the absorption coefficient of the LSC device, d is the thickness of the LSC deivce, and R is the reflection coefficient of LSC surface.[52]

η_{ext} of LSCs from electro-optical measurements

The electro-optical measurements for the large scale LSCs were applied based on the previous work.[57] The relationship between the power conversion efficiencies (PCEs) of a single photovoltaic (η_{PV}) and a LSC coupled LSC-PV junction device ($\eta_{LSC\text{-}PV}$) can be expressed as follows:

$$\eta_{LSC-PV} = \frac{\langle Q_{PL} \rangle}{\langle Q_S \rangle} \eta_{s,abs} \eta_{int} \eta_{PV} \quad (4)$$

$\langle Q_S \rangle$ and $\langle Q_{PL} \rangle$ are the averaged external quantum efficiencies (EQEs) of the PV devices over the sunlight incident wavelength range and the LSC emission wavelength range, respectively. $\eta_{s,abs}$ is the abosrption ratio under the sunlight radiation. Following this equation, the η_{int} and η_{ext} of the LSC in LSC-PV junction devices can be expressed by the following equations:

$$\eta_{int} = \frac{\eta_{LSC-PV}\langle Q_S \rangle}{\eta_{s,abs}\eta_{PV}\langle Q_{PL} \rangle} = \frac{J_{SC,LSC-PV}\langle Q_S \rangle}{J_{SC}\eta_{s,abs}G\langle Q_{PL} \rangle} \quad (5)$$

$$\eta_{ext} = \frac{J_{SC,LSC-PV}\langle Q_S \rangle}{J_{SC}G\langle Q_{PL} \rangle} \quad (6)$$

J_{SC} and $J_{SC,LSC-PV}$ are the short-circuit current densities of the standalone PV and LSC-PV, respectively.

Average visible transmittance (AVT) calculation

The average visible transmittance (AVT) of an LSC device is expressed by the following equations:[57, 75]

$$AVT = \frac{\int T(\lambda)P(\lambda)S(\lambda)d\lambda}{\int P(\lambda)S(\lambda)d\lambda} \quad (7)$$

Where λ is the light wavelength, T(λ) is the transmittance of the LSC, *P(λ)* is the photopic response function of the human eye (photonic vision)[76], S(λ) is the normalized AM 1.5 solar spectrum. The AVT is calculated by taking the ratio of the integrated area of the convoluted curve with the integrated area of the photopic response of the eye.

Monte Carlo ray-tracing simulation (MC simulation)

Firstly, the input parameters for the Monte Carlo ray-tracing simulation mode include the total number of incident photons (*i.e.*, 10,000); the dimension of the LSC substrate and coating layer (length, width, thickness); refractive index of the LSC's substrate and coating layer material; the absorption coefficient of CdSe/CdS core/shell QDs, cumulative distribution functions (CDF) plot for PL spectra and PL QY of the CdSe/CdS core/shell QDs.

After that, we assign random x and y coordinates as initial position parameters for each photon and collect all the position data to generate a photon database. Next, we randomly delete a certain number of input photons from the database, representing the scattering effect from the LSC surface according to Fresnel Law. Then, we release a non-scattered photon into the main loop of the coating layer; CdSe/CdS QDs absorption coefficient spectra and CdSe/CdS QDs concentration data can determine if the coating layer absorbs this photon. For the absorbed photon, we determine if this photon will be absorbed and emitted by the CdSe/CdS QDs (according to the emission CDF plot and PL QY data). If not, the photon runs through the non-radiative decay channels of the CdSe/CdS QDs. If the photon is emitted, we further determine if the newly released photon will hit the surface of the LSC. If it does not hit the surface, the photon is back to the initial emission determination step. If it hits the surface, the photons will be updated with a new set of location vector parameters and proceed to the next step. We can determine which surface the photons hit (top/bottom or edge of the QD coating layer) according to the new photon location data.

According to the location vector, the refractive index of the coating layer material, and substrate material, we can determine whether the photons are reflected through the total internal reflection (TIR). If so, the simulation procedure moves back to the initial emission determination step. If the photon goes through the coating layer top or edge region, this photon is transmitted through the edge, close one photon tracing loop, and record the transmitted positions. After that, we release another photon into the main loop from the database.

If the photon transmits through the bottom surface of the LSC, we can further determine if the TIR occurs on the substrate surface. If so, we keep tracing the photon until it transmits through the surface. If the photon transmits through the top surface, the traced photon moves back to the initial emission determination step in the coating layer. If the photon transmits through the bottom or edge surface, record the transmitted photon positions and release another photon into the main loop from the database.

The main loop keeps repeating until all the photons in the database are traced.

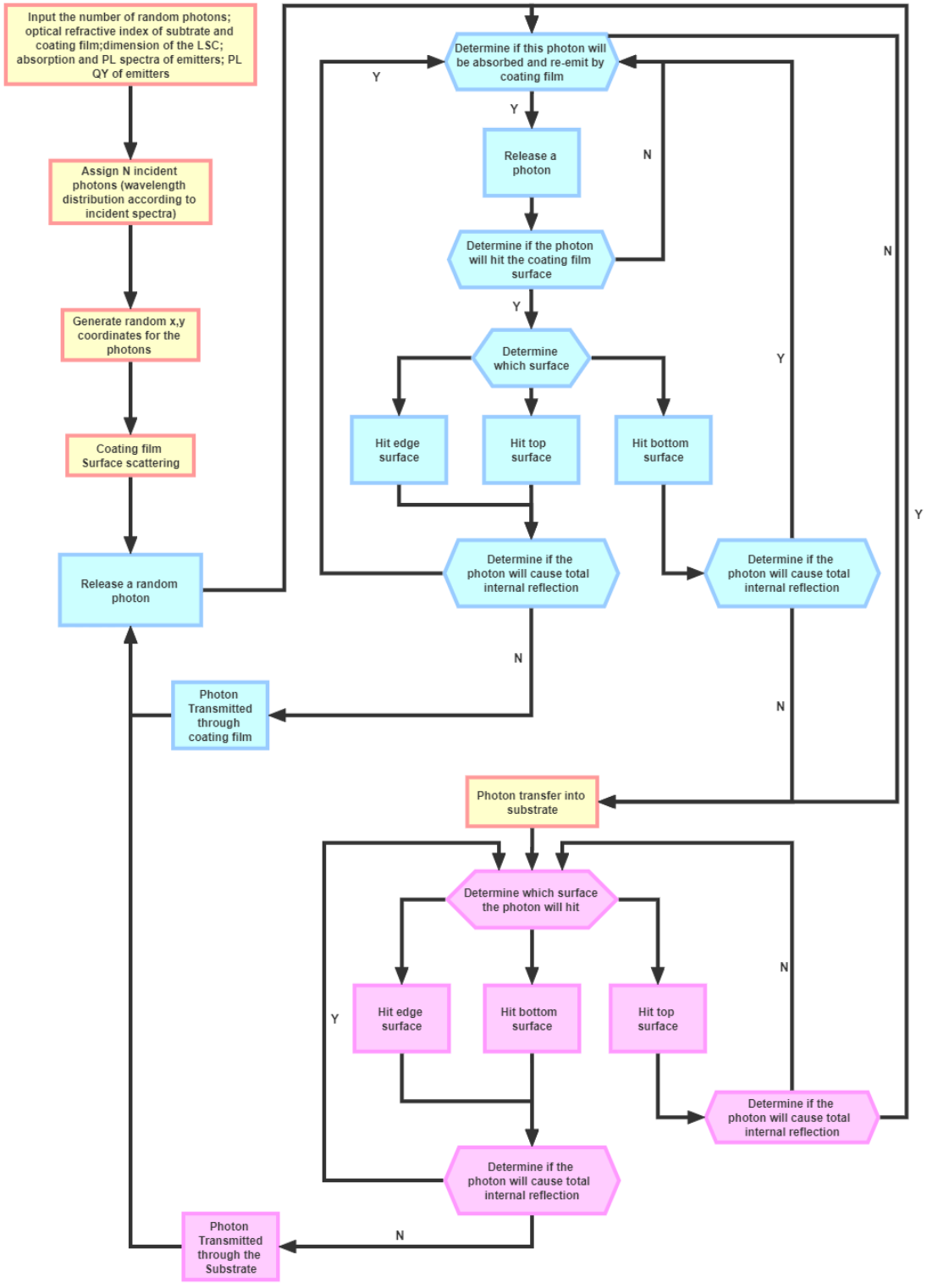

Scheme 2.2: Logic flow chart of the MC ray-tracing simulation for the LSC device through ultrasonic spray coating method. The blue blocks are the main loop region for the coating layer and the pink blocks are the main loop region for the substrate, where individual photons are traced.

Analytical mode simulation

The analytical mode simulation is developed based on previous published methods.[25,67] Following the procedure decribed in the literature, we determine the following parameters as:

$$< \alpha_1 >= -\frac{1}{d} ln \left(\frac{\int_{E_g}^{\infty} S_{in}(\lambda) e^{-\alpha(\lambda) d} d\lambda}{\int_{E_g}^{\infty} S_{in}(\lambda) d\lambda} \right) \quad (8)$$

Where $< \alpha_1 >$ is the average absorption coefficient among the incident light wavelength range. The obtained value can apply for the α_1. α is the absorption coefficient of the QDs. λ is the wavelength. d is the thickness of the LCS. E_g is the bandgap of QDs. S_{in} is the spectral shape of incident light.

α_2 is the absorption coefficient at the wavelength of the emitted light, which can be replaced by the average value of $< \alpha_2 >$ defined as:

$$< \alpha_2 >= \frac{\int S_{PL}(\lambda) \alpha(\lambda) d\lambda}{\int S_{PL}(\lambda) d\lambda} \quad (9)$$

Where S_{PL} is the spectral shape of the QD emission, and α is the absorption coefficient of the QDs. λ is the wavelength.

η_{trap} is the efficiency of light trapping into the LSC device, which is determined by the refrative index of the LSC matrix, which is:

$$\eta_{trap} = \sqrt{1 - n^{-2}} = cos\theta_{esc} \quad (10)$$

For β value determination, the initial value can be calculated based on the following equation:[7]

$$\beta = 1.4 + 0.5 \left(\frac{L}{150} \right)^{0.5} \quad (11)$$

Where L is the edge length for square shape LSCs. This equation is relatively reliable for L = 0-2000 cm. Then, the β value is further corrected based on multiple tests from MC simulation. The final β value is determined as 1.408 for all the analytical mode simulations in this study.

Overall, the external optical quantum efficiencies of the LSC device can be expreseed as:

$$\eta_{ext} = (1-R)(1-T) \times \eta_{int} = \frac{(1-R)\left(1-e^{-\alpha_1 d}\right)\eta_{PL}\eta_{trap}}{1+\beta\alpha_2(1-\eta_{PL}\eta_{trap})} \quad (12)$$

Where, η_{PL} is the PL QY of the emitters; R is the reflection coefficient of LSC surfaces; T is the transmission of the overall LSC device.

Reference

1. Wang, Y.; Chhowalla, M., Making Clean Electrical Contacts on 2D Transition Metal Dichalcogenides. *Nature Reviews Physics* **2021,** *4* (2), 101-112.
2. Tabor, D. P.; Roch, L. M.; Saikin, S. K.; Kreisbeck, C.; Sheberla, D.; Montoya, J. H.; Dwaraknath, S.; Aykol, M.; Ortiz, C.; Tribukait, H.; Amador-Bedolla, C.; Brabec, C. J.; Maruyama, B.; Persson, K. A.; Aspuru-Guzik, A., Accelerating the Discovery of Materials for Clean Energy in the Era of Smart Automation. *Nature Reviews Materials* **2018,** *3* (5), 5-20.
3. Carley, S.; Konisky, D. M., The Justice and Equity Implications of the Clean Energy Transition. *Nature Energy* **2020,** *5* (8), 569-577.
4. Driscoll, C. T.; Buonocore, J. J.; Levy, J. I.; Lambert, K. F.; Burtraw, D.; Reid, S. B.; Fakhraei, H.; Schwartz, J., US Power Plant Carbon Standards and Clean Air and Health Co-benefits. *Nature Climate Change* **2015,** *5* (6), 535-540.
5. Kamat, P. V., Meeting the Clean Energy Demand: Nanostructure Architectures for Solar Energy Conversion. *J Phys Chem C* **2007,** *111* (7), 2834-2860.
6. Cheng, P.; Li, G.; Zhan, X.; Yang, Y., Next-generation Organic Photovoltaics Based on Non-fullerene Acceptors. *Nature Photonics* **2018,** *12* (3), 131-142.
7. Chu, S.; Majumdar, A., Opportunities and Challenges for a Sustainable Energy Future. *Nature* **2012,** *488* (7411), 294-303.
8. Yang, H.; Zhang, Y.; Hills-Kimball, K.; Zhou, Y.; Chen, O., Building Bridges Between Halide Perovskite Nanocrystals and Thin-film Solar Cells. *Sustainable Energy & Fuels* **2018,** *2* (11), 2381-2397.
9. Zhang, Y.; Yang, H.; Chen, M.; Padture, N. P.; Chen, O.; Zhou, Y., Fusing Nanowires into Thin Films: Fabrication of Graded-Heterojunction Perovskite Solar Cells with Enhanced Performance. *Advanced Energy Materials* **2019,** *9* (22), 19900243.
10. Que, M.; Dai, Z.; Yang, H.; Zhu, H.; Zong, Y.; Que, W.; Padture, N. P.; Zhou, Y.; Chen, O., Quantum-Dot-Induced Cesium-Rich Surface Imparts

Enhanced Stability to Formamidinium Lead Iodide Perovskite Solar Cells. *ACS Energy Letters* **2019,** *4* (8), 1970-1975.

11. Petter Jelle, B.; Breivik, C.; Drolsum Røkenes, H., Building Integrated Photovoltaic Products: A State-of-the-art Review and Future Research Opportunities. *Solar Energy Materials and Solar Cells* **2012,** *100*, 69-96.
12. Meinardi, F.; Bruni, F.; Brovelli, S., Luminescent Solar Concentrators for Building-integrated Photovoltaics. *Nature Reviews Materials* **2017,** *2* (12), 17072.
13. Mohamed, A.; Hasan, A.; Sirén, K., Fulfillment of Net-zero Energy Building (NZEB) with Four Metrics in a Single Family House with Different Heating Alternatives. *Applied Energy* **2014,** *114*, 385-399.
14. Svetozarevic, B.; Begle, M.; Jayathissa, P.; Caranovic, S.; Shepherd, R. F.; Nagy, Z.; Hischier, I.; Hofer, J.; Schlueter, A., Dynamic Photovoltaic Building Envelopes for Adaptive Energy and Comfort Management. *Nature Energy* **2019,** *4* (8), 671-682.
15. Meinardi, F.; Akkerman, Q. A.; Bruni, F.; Park, S.; Mauri, M.; Dang, Z.; Manna, L.; Brovelli, S., Doped Halide Perovskite Nanocrystals for Reabsorption-Free Luminescent Solar Concentrators. *ACS Energy Lett* **2017,** *2* (10), 2368-2377.
16. Dunnett, S.; Sorichetta, A.; Taylor, G.; Eigenbrod, F., Harmonised Global Datasets of Wind and Solar Farm Locations and Power. *Sci Data* **2020,** *7* (1), 130.
17. Varma, R. K.; Khadkikar, V.; Seethapathy, R., Nighttime Application of PV Solar Farm as STATCOM to Regulate Grid Voltage. *IEEE Transactions on Energy Conversion* **2009,** *24* (4), 983-985.
18. Bradshaw, L. R.; Knowles, K. E.; McDowall, S.; Gamelin, D. R., Nanocrystals for Luminescent Solar Concentrators. *Nano Lett* **2015,** *15* (2), 1315-23.
19. Erickson, C. S.; Bradshaw, L. R.; McDowall, S.; Gilbertson, J. D.; Gamelin, D. R.; Patrick, D. L., Zero-reabsorption Doped-nanocrystal Luminescent Solar Concentrators. *ACS Nano* **2014,** *8* (4), 3461-7.
20. van Sark, W. G.; Barnham, K. W.; Slooff, L. H.; Chatten, A. J.; Buchtemann, A.; Meyer, A.; McCormack, S. J.; Koole, R.; Farrell, D. J.; Bose, R.; Bende, E. E.; Burgers, A. R.; Budel, T.; Quilitz, J.; Kennedy,

M.; Meyer, T.; Donega Cde, M.; Meijerink, A.; Vanmaekelbergh, D., Luminescent Solar Concentrators--a Review of Recent Results. *Opt Express* **2008,** *16* (26), 21773-92.

21. Wang, J.; Yuan, Y.; Zhu, H.; Cai, T.; Fang, Y.; Chen, O., Three-dimensional Macroporous Photonic Crystal Enhanced Photon Collection for Quantum Dot-based Luminescent Solar Concentrator. *Nano Energy* **2020,** *67*, 104217.
22. Meinardi, F.; McDaniel, H.; Carulli, F.; Colombo, A.; Velizhanin, K. A.; Makarov, N. S.; Simonutti, R.; Klimov, V. I.; Brovelli, S., Highly Efficient Large-area Colourless Luminescent Solar Concentrators Using Heavy-metal-free Colloidal Quantum Dots. *Nat Nanotechnol* **2015,** *10* (10), 878-85.
23. Zhao, H.; Sun, R.; Wang, Z.; Fu, K.; Hu, X.; Zhang, Y., Zero-Dimensional Perovskite Nanocrystals for Efficient Luminescent Solar Concentrators. *Advanced Functional Materials* **2019,** *29* (30), 1902262.
24. Zhao, H.; Benetti, D.; Tong, X.; Zhang, H.; Zhou, Y.; Liu, G.; Ma, D.; Sun, S.; Wang, Z. M.; Wang, Y.; Rosei, F., Efficient and Stable Tandem Luminescent Solar Concentrators Based on Carbon Dots and Perovskite Quantum Dots. *Nano Energy* **2018,** *50*, 756-765.
25. Song, H. J.; Jeong, B. G.; Lim, J.; Lee, D. C.; Bae, W. K.; Klimov, V. I., Performance Limits of Luminescent Solar Concentrators Tested with Seed/Quantum-Well Quantum Dots in a Selective-Reflector-Based Optical Cavity. *Nano Lett* **2018,** *18* (1), 395-404.
26. Sadeq, R. M.; Abdelraziq, I.; Abu-Jafar, M. S.; Bilous, O., The Behavior of Sound Absorption Coefficient for Binary Mixture Nitroethane-isooctane Above Critical Temperature and Concentration. *AIP Advances* **2018,** *8* (11).
27. Meinardi, F.; Ehrenberg, S.; Dhamo, L.; Carulli, F.; Mauri, M.; Bruni, F.; Simonutti, R.; Kortshagen, U.; Brovelli, S., Highly Efficient Luminescent Solar Concentrators Based on Earth-abundant Indirect-bandgap Silicon Quantum Dots. *Nature Photonics* **2017,** *11* (3), 177-185.

28. Nikolaidou, K.; Sarang, S.; Hoffman, C.; Mendewala, B.; Ishihara, H.; Lu, J. Q.; Ilan, B.; Tung, V.; Ghosh, S., Hybrid Perovskite Thin Films as Highly Efficient Luminescent Solar Concentrators. *Advanced Optical Materials* **2016,** *4* (12), 2126-2132.
29. Zhou, Y.; Benetti, D.; Fan, Z.; Zhao, H.; Ma, D.; Govorov, A. O.; Vomiero, A.; Rosei, F., Near Infrared, Highly Efficient Luminescent Solar Concentrators. *Advanced Energy Materials* **2016,** *6* (11), 150191.
30. Chen, O.; Zhao, J.; Chauhan, V. P.; Cui, J.; Wong, C.; Harris, D. K.; Wei, H.; Han, H. S.; Fukumura, D.; Jain, R. K.; Bawendi, M. G., Compact High-quality CdSe-CdS Core-Shell Nanocrystals with Narrow Emission Linewidths and Suppressed Blinking. *Nat Mater* **2013,** *12* (5), 445-51.
31. Chen, O.; Wei, H.; Maurice, A.; Bawendi, M.; Reiss, P., Pure Colors From Core–shell Quantum Dots. *MRS Bulletin* **2013,** *38* (9), 696-702.
32. Yuan, Y.; Zhu, H.; Wang, X.; Cui, D.; Gao, Z.; Su, D.; Zhao, J.; Chen, O., Cu-Catalyzed Synthesis of CdZnSe–CdZnS Alloy Quantum Dots with Highly Tunable Emission. *Chemistry of Materials* **2019,** *31* (7), 2635-2643.
33. Tan, R.; Yuan, Y.; Nagaoka, Y.; Eggert, D.; Wang, X.; Thota, S.; Guo, P.; Yang, H.; Zhao, J.; Chen, O., Monodisperse Hexagonal Pyramidal and Bipyramidal Wurtzite CdSe-CdS Core–Shell Nanocrystals. *Chemistry of Materials* **2017,** *29* (9), 4097-4108.
34. Chen, Y.; Vela, J.; Htoon, H.; Casson, J. L.; Werder, D. J.; Bussian, D. A.; Klimov, V. I.; Hollingsworth, J. A., "Giant" Multishell CdSe Nanocrystal Quantum Dots with Suppressed Blinking. *Journal of the American Chemical Society* **2008,** *130* (15), 5026-5027.
35. Wang, X.; Ren, X.; Kahen, K.; Hahn, M. A.; Rajeswaran, M.; Maccagnano-Zacher, S.; Silcox, J.; Cragg, G. E.; Efros, A. L.; Krauss, T. D., Non-blinking Semiconductor Nanocrystals. *Nature* **2009,** *459* (7247), 686-9.
36. Chen, D.; Lei, H.; Zhu, C.; Chen, X.; Tian, H.; Fang, W.; Qin, H.; Peng, X., Epitaxial Integration of Multiple CdSe Quantum Dots in a Colloidal CdS Nanoplatelet. *J Am Chem Soc* **2022,** *144* (19), 8444-8448.

37. Reiss, P.; Protiere, M.; Li, L., Core/Shell Semiconductor Nanocrystals. *Small* **2009,** *5* (2), 154-68.
38. Meinardi, F.; Colombo, A.; Velizhanin, K. A.; Simonutti, R.; Lorenzon, M.; Beverina, L.; Viswanatha, R.; Klimov, V. I.; Brovelli, S., Large-area Luminescent Solar Concentrators Based on 'Stokes-shift-engineered' Nanocrystals in a Mass-polymerized PMMA Matrix. *Nature Photonics* **2014,** *8* (5), 392-399.
39. Knowles, K. E.; Kilburn, T. B.; Alzate, D. G.; McDowall, S.; Gamelin, D. R., Bright $CuInS_2$/CdS Nanocrystal Phosphors for High-gain Full-spectrum Luminescent Solar Concentrators. *Chem Commun (Camb)* **2015,** *51* (44), 9129-32.
40. Coropceanu, I.; Bawendi, M. G., Core/shell Quantum Dot Based Luminescent Solar Concentrators with Reduced Reabsorption and Enhanced Efficiency. *Nano Lett* **2014,** *14* (7), 4097-101.
41. Zhao, Y.; Lunt, R. R., Transparent Luminescent Solar Concentrators for Large-Area Solar Windows Enabled by Massive Stokes-Shift Nanocluster Phosphors. *Advanced Energy Materials* **2013,** *3* (9), 1143-1148.
42. Slooff, L. H.; Bende, E. E.; Burgers, A. R.; Budel, T.; Pravettoni, M.; Kenny, R. P.; Dunlop, E. D.; Büchtemann, A., A Luminescent Solar Concentrator with 7.1% Power Conversion Efficiency. *physica status solidi (RRL) - Rapid Research Letters* **2008,** *2* (6), 257-259.
43. Corsini, F.; Tatsi, E.; Colombo, A.; Dragonetti, C.; Botta, C.; Turri, S.; Griffini, G., Highly Emissive Fluorescent Silica-based Core/Shell Nanoparticles for Efficient and Stable Luminescent Solar Concentrators. *Nano Energy* **2021,** *80*, 105551.
44. Cai, T.; Wang, J.; Li, W.; Hills-Kimball, K.; Yang, H.; Nagaoka, Y.; Yuan, Y.; Zia, R.; Chen, O., Mn^{2+}/Yb^{3+} Codoped $CsPbCl_3$ Perovskite Nanocrystals with Triple-Wavelength Emission for Luminescent Solar Concentrators. *Adv Sci (Weinh)* **2020,** *7* (18), 2001317.
45. Koch, K. C.; Korus, D.; Doyle, J.; Plummer, M.; Boxx, M.; Win-Piazza, H.; McDowall, S.; Patrick, D. L.; Rider, D. A., Quantum Dot–Block

Copolymer Hybrids for Low Scattering Luminescent Solar Concentrators. *ACS Applied Polymer Materials* **2022,** *4* (5), 3283-3293.

46. Koerner, H.; Drummy, L. F.; Benicewicz, B.; Li, Y.; Vaia, R. A., Nonisotropic Self-Organization of Single-Component Hairy Nanoparticle Assemblies. *ACS Macro Letters* **2013,** *2* (8), 670-676.
47. Sumner, R.; Eiselt, S.; Kilburn, T. B.; Erickson, C.; Carlson, B.; Gamelin, D. R.; McDowall, S.; Patrick, D. L., Analysis of Optical Losses in High-Efficiency $CuInS_2$-Based Nanocrystal Luminescent Solar Concentrators: Balancing Absorption versus Scattering. *The Journal of Physical Chemistry C* **2017,** *121* (6), 3252-3260.
48. Gong, X.; Jiang, H.; Cao, M.; Rao, Z.; Zhao, X.; Vomiero, A., Eu-doped ZnO Quantum Dots with Solid-state Fluorescence and Dual Emission for High-performance Luminescent Solar Concentrators. *Materials Chemistry Frontiers* **2021,** *5* (12), 4746-4755.
49. Wu, J.; Xin, W.; Wu, Y.; Zhan, Y.; Li, J.; Wang, J.; Huang, S.; Wang, X., Solid-state Photoluminescent Silicone-carbon Dots/Dendrimer Composites for Highly Efficient Luminescent Solar Concentrators. *Chemical Engineering Journal* **2021,** *422* (15), 130158.
50. Talite, M. J.; Huang, H. Y.; Wu, Y. H.; Sena, P. G.; Cai, K. B.; Lin, T. N.; Shen, J. L.; Chou, W. C.; Yuan, C. T., Greener Luminescent Solar Concentrators with High Loading Contents Based on in Situ Cross-Linked Carbon Nanodots for Enhancing Solar Energy Harvesting and Resisting Concentration-Induced Quenching. *ACS Appl Mater Interfaces* **2018,** *10* (40), 34184-34192.
51. Liu, H.; Li, S.; Chen, W.; Wang, D.; Li, C.; Wu, D.; Hao, J.; Zhou, Z.; Wang, X.; Wang, K., Scattering Enhanced Quantum Dots Based Luminescent Solar Concentrators by Silica Microparticles. *Solar Energy Materials and Solar Cells* **2018,** *179*, 380-385.
52. Li, H.; Wu, K.; Lim, J.; Song, H.-J.; Klimov, V. I., Doctor-blade Deposition of Quantum Dots onto Standard Window Glass for Low-loss Large-area Luminescent Solar Concentrators. *Nature Energy* **2016,** *1* (12).

53. Liu, Y.; Li, N.; Sun, R.; Zheng, W.; Liu, T.; Li, H.; Chen, Y.; Liu, G.; Zhao, H.; Liu, H.; Zhang, Y., Stable Metal-halide Perovskites for Luminescent Solar Concentrators of Real-device Integration. *Nano Energy* **2021,** *85*, 105960.
54. ZdraZil, L.; Kalytchuk, S.; Hola, K.; Petr, M.; Zmeskal, O.; Kment, S.; Rogach, A. L.; Zboril, R., A Carbon Dot-based Tandem Luminescent Solar Concentrator. *Nanoscale* **2020,** *12* (12), 6664-6672.
55. Cohen, T. A.; Milstein, T. J.; Kroupa, D. M.; MacKenzie, J. D.; Luscombe, C. K.; Gamelin, D. R., Quantum-cutting Yb^{3+}-doped Perovskite Nanocrystals for Monolithic Bilayer Luminescent Solar Concentrators. *Journal of Materials Chemistry A* **2019,** *7* (15), 9279-9288.
56. Luo, X.; Ding, T.; Liu, X.; Liu, Y.; Wu, K. F., Quantum-Cutting Luminescent Solar Concentrators Using Ytterbium-Doped Perovskite Nanocrystals. *Nano Letters* **2019,** *19* (1), 338-341.
57. Wu, K.; Li, H.; Klimov, V. I., Tandem Luminescent Solar Concentrators Based on Engineered Quantum Dots. *Nature Photonics* **2018,** *12* (2), 105-110.
58. Yang, C.; Moemeni, M.; Bates, M.; Sheng, W.; Borhan, B.; Lunt, R. R., High-Performance Near-Infrared Harvesting Transparent Luminescent Solar Concentrators. *Advanced Optical Materials* **2020,** *8* (8), 1901536.
59. Chen, J.; Zhao, H.; Li, Z.; Zhao, X.; Gong, X., Highly Efficient Tandem Luminescent Solar Concentrators Based on Eco-friendly Copper Iodide Based Hybrid Nanoparticles and Carbon Dots. *Energy & Environmental Science* **2022,** *15* (2), 799-805.
60. Liu, X.; Benetti, D.; Rosei, F., Semi-transparent Luminescent Solar Concentrators Based on Plasmon-enhanced Carbon Dots. *Journal of Materials Chemistry A* **2021,** *9* (41), 23345-23352.
61. Freitas, V. T.; Fu, L.; Cojocariu, A. M.; Cattoen, X.; Bartlett, J. R.; Le Parc, R.; Bantignies, J. L.; Man, M. W.; Andre, P. S.; Ferreira, R. A.; Carlos, L. D., Eu^{3+}-based Bridged Silsesquioxanes for Transparent Luminescent Solar Concentrators. *ACS Appl Mater Interfaces* **2015,** *7* (16), 8770-8.

62. Mwakikunga, B. W., Progress in Ultrasonic Spray Pyrolysis for Condensed Matter Sciences Developed From Ultrasonic Nebulization Theories Since Michael Faraday. *Critical Reviews in Solid State and Materials Sciences* **2013,** *39* (1), 46-80.
63. Tadeo, I. J.; Mukhokosi, E. P.; Krupanidhi, S. B.; Umarji, A. M., Low-cost VO_2(M1) Thin Films Synthesized by Ultrasonic Nebulized Spray Pyrolysis of an Aqueous Combustion Mixture for IR Photodetection. *RSC Adv* **2019,** *9* (18), 9983-9992.
64. Bharathi, R.; Naorem, R.; Umarji, A. M., Metal–insulator Transition Characteristics of Vanadium Dioxide Thin Films Synthesized by Ultrasonic Nebulized Spray Pyrolysis of an Aqueous Combustion Mixture. *Journal of Physics D: Applied Physics* **2015,** *48* (30), 305103.
65. Debije, M. G.; Verbunt, P. P. C., Thirty Years of Luminescent Solar Concentrator Research: Solar Energy for the Built Environment. *Advanced Energy Materials* **2012,** *2* (1), 12-35.
66. Breukers, R. D.; Smith, G. J.; Stirrat, H. L.; Swanson, A. J.; Smith, T. A.; Ghiggino, K. P.; Raymond, S. G.; Winch, N. M.; Clarke, D. J.; Kay, A. J., Light Losses from Scattering in Luminescent Solar Concentrator Waveguides. *Appl Opt* **2017,** *56* (10), 2630-2635.
67. Klimov, V. I.; Baker, T. A.; Lim, J.; Velizhanin, K. A.; McDaniel, H., Quality Factor of Luminescent Solar Concentrators and Practical Concentration Limits Attainable with Semiconductor Quantum Dots. *ACS Photonics* **2016,** *3* (6), 1138-1148.
68. Gungor, K.; Du, J.; Klimov, V. I., General Trends in the Performance of Quantum Dot Luminescent Solar Concentrators (LSCs) Revealed Using the "Effective LSC Quality Factor". *ACS Energy Letters* **2022,** *7* (5), 1741-1749.
69. Wei, C.; Su, W.; Li, J.; Xu, B.; Shan, Q.; Wu, Y.; Zhang, F.; Luo, M.; Xiang, H.; Cui, Z.; Zeng, H., A Universal Ternary-Solvent-Ink Strategy toward Efficient Inkjet-Printed Perovskite Quantum Dot Light-Emitting Diodes. *Adv Mater* **2022**, 34 (10), e2107798.

70. Pan, S.; Guo, R.; Bjornmalm, M.; Richardson, J. J.; Li, L.; Peng, C.; Bertleff-Zieschang, N.; Xu, W.; Jiang, J.; Caruso, F., Coatings super-repellent to ultralow surface tension liquids. *Nat Mater* **2018**, 17 (11), 1040-1047.

71. 48. Rykaczewski, K.; Paxson, A. T.; Staymates, M.; Walker, M. L.; Sun, X.; Anand, S.; Srinivasan, S.; McKinley, G. H.; Chinn, J.; Scott, J. H.; Varanasi, K. K., Dropwise condensation of low surface tension fluids on omniphobic surfaces. *Sci Rep* **2014**, 4, 4158.

72. 49. Zhang, H.; Ji, X.; Liu, L.; Ren, J.; Tao, F.; Qiao, C., Versatile, mechanochemically robust, sprayed superomniphobic coating enabling low surface tension and high viscous organic liquid bouncing. *Chemical Engineering Journal* **2020**, 402.

73. Protesescu, L.; Yakunin, S.; Bodnarchuk, M. I.; Krieg, F.; Caputo, R.; Hendon, C. H.; Yang, R. X.; Walsh, A.; Kovalenko, M. V., Nanocrystals of Cesium Lead Halide Perovskites (CsPbX(3), X = Cl, Br, and I): Novel Optoelectronic Materials Showing Bright Emission with Wide Color Gamut. *Nano Lett* **2015,** *15* (6), 3692-6.

74. Liu, Z.; Guan, Z.; Li, X.; Tang, A.; Teng, F., Rational Design and Synthesis of Highly Luminescent Multinary Cu-In-Zn-S Semiconductor Nanocrystals with Tailored Nanostructures. *Advanced Optical Materials* **2020,** *8* (6).

75. Bergren, M. R.; Makarov, N. S.; Ramasamy, K.; Jackson, A.; Guglielmetti, R.; McDaniel, H., High-Performance CuInS2 Quantum Dot Laminated Glass Luminescent Solar Concentrators for Windows. *ACS Energy Letters* **2018,** *3* (3), 520-525.

76. Hamilton, R.; Bees, M. A.; Chaplin, C. A.; McCulloch, D. L., The luminance-response function of the human photopic electroretinogram: a mathematical model. *Vision Res* **2007,** *47* (23), 2968-72.

Chapter 3

Three-dimensional Macroporous Photonic Crystal Enhanced Photon Collection for Quantum Dot-based Luminescent Solar Concentrator

J. Wang, Y. Yuan, H. Zhu, T. Cai, Y. Fang and O. Chen*. Three-Dimensional Macroporous Photonic Crystal Enhanced Photon Collection for Quantum Dot-Based Luminescent Solar Concentrator. *Nano Energy* **2020**, 67, 104217.

3.1 Introduction

Moving global energy consumption away from fossil fuels requires innovative, clean and cost-effective renewable energy technologies.[1-4] In this concern, solar power is the most abundant of all sustainable sources on our planet and harvesting solar energy utilizing photovoltaics (PVs) hold the highest potential capacity (~80 TW) among all renewable energy sources.[5-12] To this end, luminescent solar concentrators (LSCs) are innovative, cost-effective and large-area light collecting and concentrating devices that can be coupled to PVs for solar energy harvesting and conversion.[13-17] Depending on the utilized fluorophores, the LSCs can focus the broad range of wavelengths from sunlight into a confined wavelength range, then direct them to a smaller region of the device (light concentrating effect) for PV utilization.[13, 18] Although the original idea for LSCs was initiated in the 1970s, significant developments have been recently demonstrated due to the advances of various high-quality emitters, especially semiconductor quantum dots (QDs).[17-29] As a result of the geometric design and high refractive index of matrix materials utilized (e.g., glass, polymer), the emitted photons can be largely trapped inside of the LSC through total internal reflection (TIR) as defined by Snell's law followed by further propagation to the edges of the LSC device.[30-33] In this light concentrating process, the energy output efficiency of LSCs is mainly limited by three major events: (1) The reabsorption process caused by partial overlap between absorption and emission spectra of the applied fluorophores; (2) energy loss through non-radiative decay channels due to the sub-unity photoluminescence quantum yield (PL QY) of the fluorophores; (3) photon loss

through the escape cone of LSC devices. While the first two events can be greatly regulated by improving the absorption and emission qualities of the applied emitters,[19-24, 34, 35] the escape cone photon loss has been recognized as an intrinsic limitation of LSCs.[30-46] Even for an ideal emitter with zero reabsorption behavior and unity PL QY, the escape cone photon loss of the LSC is still inevitable and invariant. Recent efforts in reducing this escape cone photon loss include coating the LSC with organic cholesteric mirrors,[37-39] two-dimensional (2D) photonic crystal (PC) distributed Bragg reflectors,[28, 33, 36, 40] silver and aluminum metal films,[36, 43] and rugate filters .[44-46] However, most of these reported Bragg filters possess non-selective broad reflection bands, and/or sophisticated fabrication processes not ideal for large-scale production, thus limiting their potentials in practical applications.[47]

Herein, we introduce a 3D macroporous-structured PC coated QD-based LSC (PC-LSC) device as an alternative means to effectively reduce escape cone photon loss. We demonstrate that the stopband of PC layer can be programmed to serve as a highly selective wavelength reflector in order to perfectly match the emission profile of the applied emitters (e.g., QDs). After PC coating on both the top and bottom of the LSC surfaces, light trapping efficiency of the PC-LSC can be dramatically increased by ~30% as compared to the conventional LSC without PC coating (PC-free LSC). Both experimental and simulation results reveal that this enhanced photon trapping capability leads to significant improvements for both the external quantum efficiency (η_{ext}) and the concentration factor (C factor) of the resulting PC-LSC devices. Both η_{ext} and C

factor can be nearly doubled by the PC coating for large-area LSC devices under sunlight illumination, demonstrating their potentials for practical integration into solar energy conversion systems with enhanced energy harvesting capabilities.

3.2 Working principle of PC-LSC devices.

The escape cone photon loss is associated with an internal light beam angle that is smaller than the critical angle of LSC surface (shown in Figure 1a, right). According to the LSC's refractive index (n), the trapping efficiency (η_{trap}) is defined as:[30]

$$\eta_{trap} = \sqrt{1 - n^{-2}} = cos\theta_{esc} \quad (1)$$

where, θ_{esc} is the escape cone angle, which is defined by Snell's law as $\theta_{esc} = \arcsin(\frac{1}{n})$. For a typical polymer matrix with *e.g.* n = 1.5, the η_{trap} is ~ 74.5% and θ_{esc} is 41.8º. This means ~ 25.5% of the emitted photons inside an LSC will be lost to the top/bottom surfaces through the escape cone, dramatically diminishing the light harvesting and concentrating capabilities of the LSC. To minimize this photon loss, we have designed a 3D macroporous PC layer that covers both top and bottom surfaces of the QD-based LSC device (**Figure 3.1a**). This PC coating can efficiently recycle the photons otherwise lost through the escape cone, trap and subsequently concentrate them to the edge windows of the LSC device (**Figure 3.1a**).

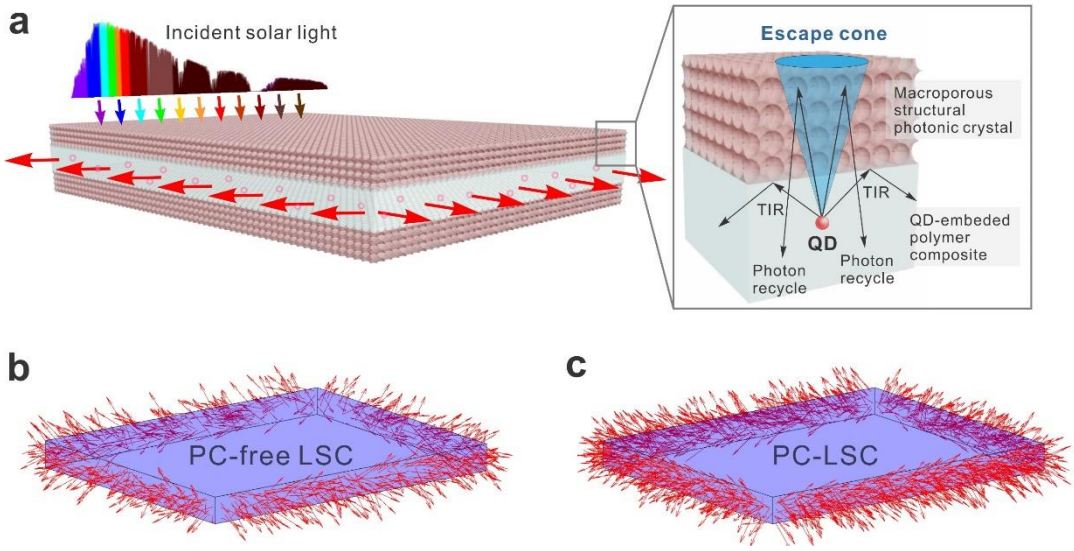

Figure 3.1. (a) Schematic representation of the QD-based PC-LSC device (left), and the zoomed-in schematic illustration of the top PC surface and the associated photon trapping mechanism (right). **(b, c)** Visualization of Monte-Carlo ray-tracing simulation for PC-free LSC device **(b)** and PC-LSC device **(c)**. The red arrows represent the photon output from the edge region of the LSC devices.

To demonstrate the enhanced photon trapping effect of the PC coating, we have carried out the Monte Carlo ray-tracing model (MC model) simulation for the LSC devices with and without PC coating.[48] Based on Fresnel Law, we can track the photon propagation of both designs by using a set of vector and location functions. By monitoring a large number of photons, the photon concentrating performances can be evaluated. In order to obtain meaningful comparisons, 30,000 photons (at 365 nm) were set to hit the LSC device normal to the top surface. In the simulation, we considered a cuboid LSC slab with dimensions of 2.8 cm × 1.5 cm × 0.1 cm, and a refractive index (n) of 1.47 (estimated based on the trimethylolpropane ethoxylate triacrylate (TET) and poly (ethylene glycol) diacrylate (PEGDA) copolymer matrix used in the experiments).

When 0.2 wt% (with respect to the co-polymer matrix) of QDs was applied to the MC simulation (see simulation details in **Method**), a drastically increased number of edge-escaped photons (labeled in red arrows) can be directly visualized after PC coating (**Figure 3.1b, c**). Quantitatively, 9.1% of the incident photons can be concentrated to the edge region for the PC-free LSC, whereas this value increased to 17.6% for the PC-LSC device with the same dimensions and similar amount of the absorbed photons (absorbed ~12800, 42.7% of the total incident photons). Only a slight increase in initially scattered photons (increased by ~360, 1.2% of the total incident photons) after PC coating was simulated, indicating minimal interference between the PC layer and incident photons (outside of the PC stopband), thus the absorption event of the QD emitters inside PC-LSC.

3.3 Band structure and characterizations of CdSe/CdS core-shell QDs

To test the performance of the PC-LSC design in real devices, colloidal CdSe/CdS core-shell QDs with a CdSe core diameter of 3.0 ± 0.2 nm and a CdS shell thickness of 3.8 nm were synthesized following a previously reported method (**Figure 3.2**).[49-51] The energy diagram for the band structural alignment of the core-shell QD depicts strongly confined hole (localized hole wavefunction inside the core) and weakly confined electron (delocalized electron wavefunction in both core and shell) that are photo-generated in QDs (**Figure 3.2a**).[52, 53] TEM measurements showed that the particles were highly uniform in size and shape with an average diameter of 10.6 ± 0.6 nm (**Figure 3.2b and Figure 3.3**). High resolution TEM images showed clear cross-fringes

of hexagonal atomic lattices, indicating high crystallinity of the sample with a Wurtzite crystal structure, consistent with x-ray powder diffraction measurements (**Figures 3.2b, inset, and Figure 3.4**). The high morphological uniformity and particle crystallinity of the QDs impart a narrow PL peak centered at 636 nm with a linewidth (full width at half maximum, FWHM) of 85.6 meV (~ 27.9 nm, **Figure 3.2c**), and a high PL QY of 71% determined by an integrating-sphere. Importantly, due to the presence of a thick CdS shell dominating the absorption event, photon reabsorption processes of the QDs can be largely reduced because of the significantly minimized spectral overlap between the absorption and PL profiles (also referred as 'Stokes-shift-engineered' QDs, **Figure 3.2c**).[19-24, 33-34, 54, 55] After incorporating into the TET/PEGDA copolymer slab (QD/polymer, 0.2 wt%), both the absorption and PL spectra remained intact (**Figure 3.2c**), indicating the preservation of QD integrity inside the copolymer matrix and the formation of a QD-polymer solid solution.

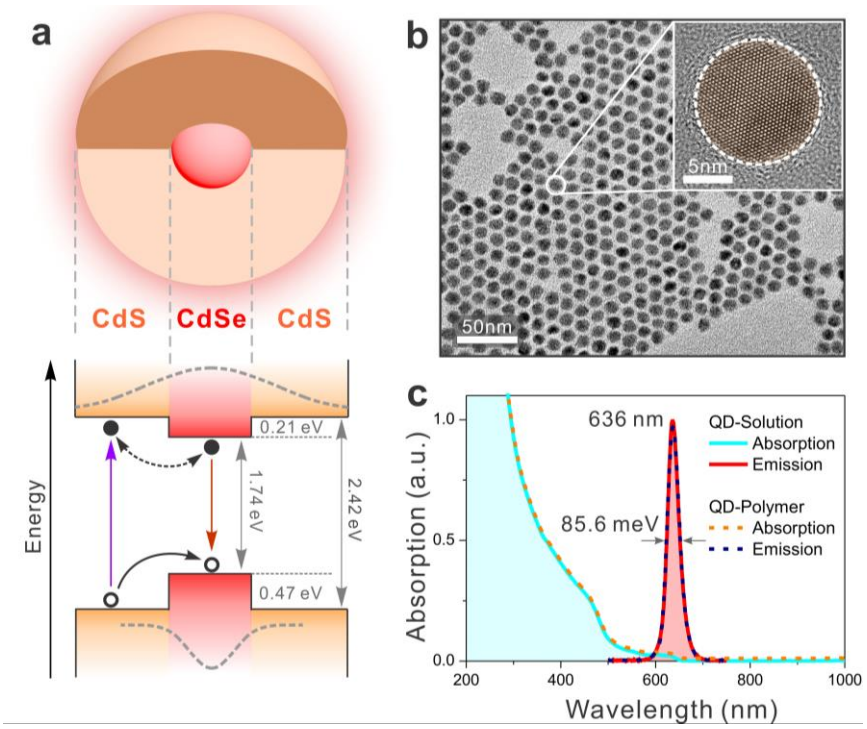

Figure 3.2. (a) Schematic representation of the CdSe/CdS core-shell QDs (top) and the corresponding quasi-Type-II band structural alignment (bottom). **(b)** Typical TEM image of the CdSe/CdS core-shell QDs. Inset: HR-TEM image of one representative core-shell QD. **(c)** Absorption and emission spectra of the CdSe/CdS QDs in hexane solution (solid lines) and in polymer matrix (dashed lines).

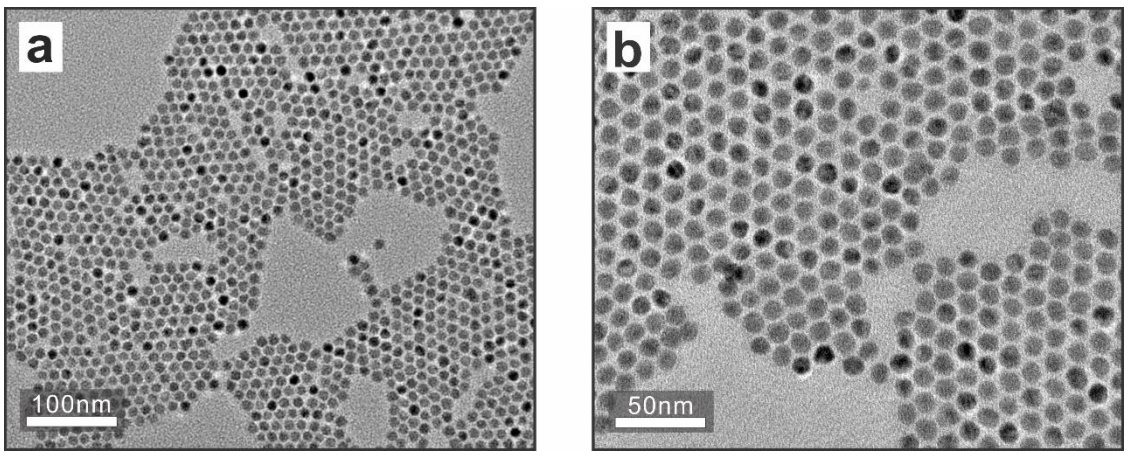

Figure 3.3. TEM images of the CdSe/CdS core-shell QDs at different magnifications.

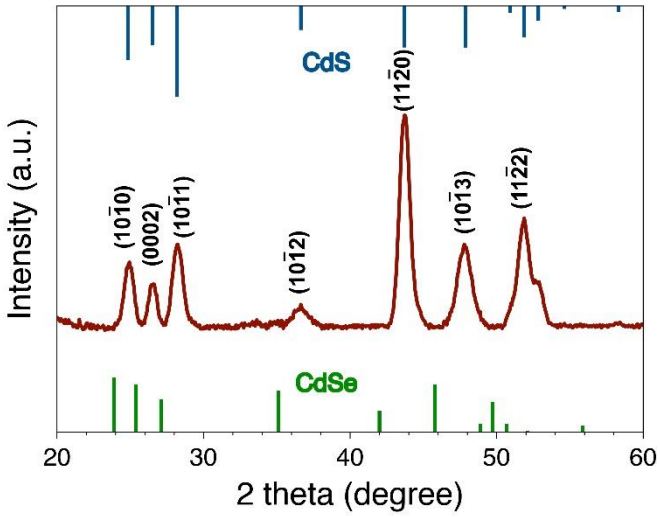

Figure 3.4. X-ray powder diffraction pattern of the CdSe-CdS core-shell QDs. The stick patterns show the standard peak positions of bulk CdSe (bottom green sticks) and CdS (top blue sticks).

3.4 Fabrication and light-trapping performance of PC-LSCs.

To fabricate PC-LSC devices, two PC filters consisting of 3D arrays of macropores were coated on the top and bottom surfaces of a QD-embedded LSC copolymer slab (**Figure 3.5**). The fabrication procedure is illustrated in **Figure 3.5a** (see **Method** for fabrication details). Briefly, a PC filter was first fabricated on a glass substrate by crystallizing colloidal silica spheres through a convective self- assembly process (**Figure 3a**).[56-58] In order to form a double-sided PC coating, a sandwich structure formed from two pieces of PC-coated glass substrates was constructed (**Figure 3.5a, I**), and then filled with a toluene solution of the two mixed monomers (*i.e.*, TET and PEGDA monomers) and the CdSe/CdS QDs (0.2 wt%) (**Figure 3.5a, II**). The entire sandwich structure was photo-polymerized (**Figure 3.5a, III**) at room temperature and then immersed into 2% hydrofluoric acid for 20 seconds to etch away the silica spheres,

resulting in an array of macropores on both sides of the device (**Figure 3.5a, IV**). After triggering with acetone vapor, all the macropores can be fully opened up to form a 3D ordered PC structure with a narrow dielectric photonic stopband (**Figure 3.6 and Table 3.1**).[57] It is worth to mention that the PC reflection band may have a blue shift while maintaining the narrow band width when the incident light angle varies from 0° (normal to the surface of PC-LSC) to 90° (parallel to the surface of PC-LSC).[59] However, given by the wide absorption profile of the QDs (**Figure 3.2c**), we do not expect a significant influence on the overall performance of the PC-LSC device. We also estimated the materials cost for industrial level large-scale production of this PC coating layer to be \$0.1575/m^2 (**Table 3.2**), representing the low-cost nature of this PC coating method.

One advantage of this PC-LSC system is that the PC stopband position can be easily controlled by tuning the size of macropores,[60] allowing for a spectral match with the PL profile of the applied emitters (**Figure 3.6**). This reflection-emission spectral match allows optimal photon trapping efficiency, thus light concentrating performance of the PC-LSC device. In our case, when using the silica spheres with an average diameter of ~ 400 nm, cross-section scanning electron microscopy (SEM) measurements showed a uniform thickness of the PC layer (~ 3.0 μm, ~ 12 monolayers of macropores) with an average pore size of ~375 nm (**Figures 3.5b and 3.7**). The resulting PC stopband with maximal reflectivity of 96% was centered at ~ 650 nm with a FWHM of ~ 220 meV (~ 87 nm), covering the entire emission spectral region of the embedded QDs in the LSC device (**Figure 3.8a**). The well-defined Fabry-Perot fringes at both sides of the major

reflection band demonstrate a high crystallinity of the assembled macroporous structure **(Figure 3.8a)**,[53] consistent with the SEM measurements (**Figure 3.5b and 3.7**). Also, except the reflection and Fabry-Perot fringes region, the PC layer showed a high transparency (~90%) which indicated a low light scattering effect caused by the PC layer (**Figure 3.9**). When photons reach the top and bottom surfaces of the LSC within the escape cone (incident angle smaller than the TIR angle), most of them can be recycled by the PC reflector and trapped inside the LSC. The photographs of a PC-LSC device under ambient and 365nm UV light illumination show a clear light concentrating effect with light dominantly emitted from the edge windows rather than from the top/bottom surfaces of the PC-LSC device (**Figure 3.5c, d**). Quantitative photon-output measurements using an integrating sphere showed that 95.3% of the total collected photons were contributed from the four edges, leaving only 4.7% emitted from the top/bottom surfaces (**Figure 3.8b**), in line with the direct visualization (**Figure 3.5c, d**). As a comparison, only 71.2% of the photons escape from the edges for the conventional PC-free LSC device (**Figure 3.10**), indicating a 33.8% enhancement in the photon concentrating effect caused by the PC coating.

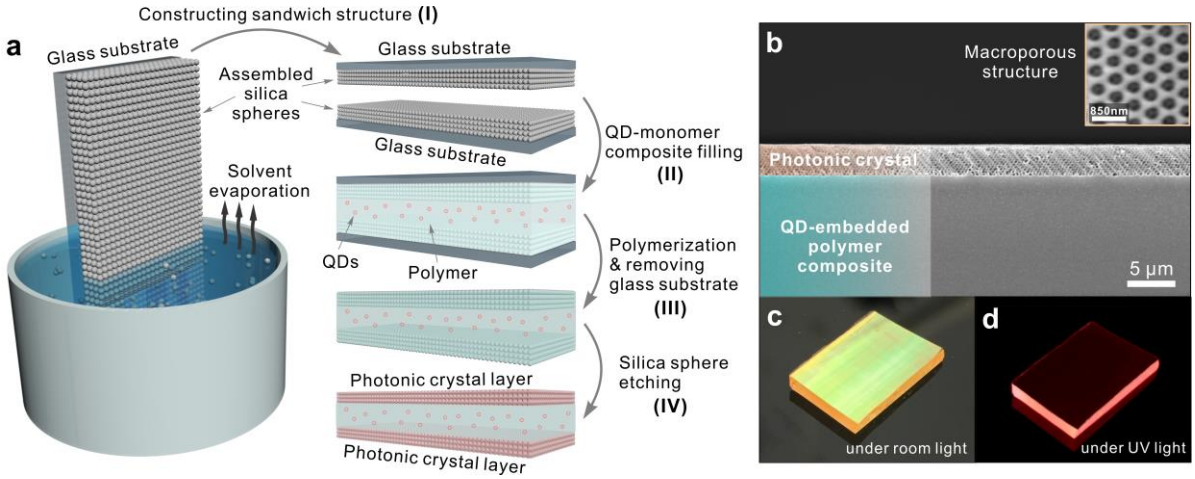

Figure 3.5 (a) Schematics of fabrication process for macroporous PC coated QD-based LSC copolymer slab. **(b)** Cross-section SEM image of a PC-LSC device. The zoomed-in top-view of the macroporous structure is shown in the right corner. **(c, d)** Photographs of a PC-LSC device (dimensions: 2.8 cm × 1.5 cm × 0.1 cm) illuminated under room light (c) and ultraviolet (UV) light at 365 nm (d).

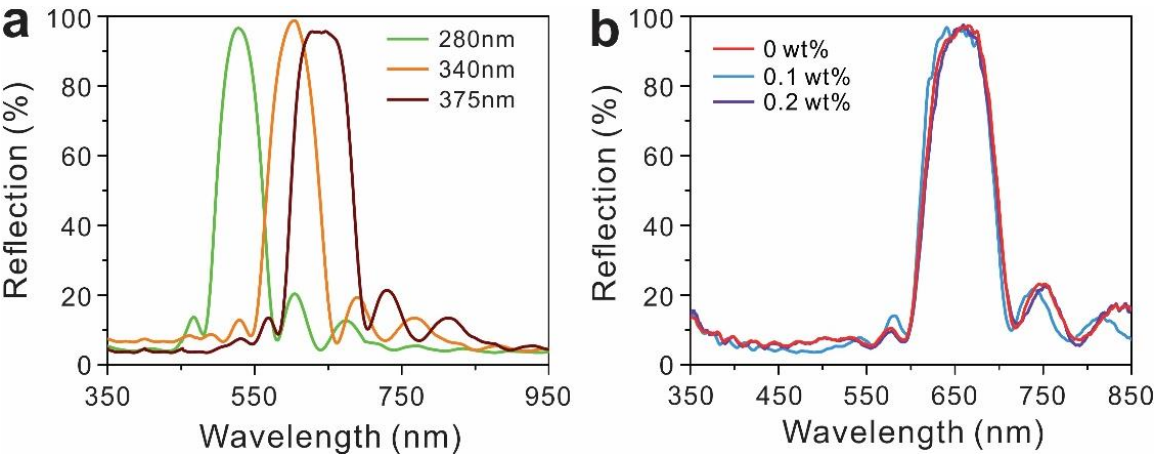

Figure 3.6. (a) The reflection spectra of the PC layers with different macropore sizes showing tunable PC reflection bands. **(b)** The reflection spectra of PC-LSCs with different weight concentrations of CdSe-CdS core-shell QDs.

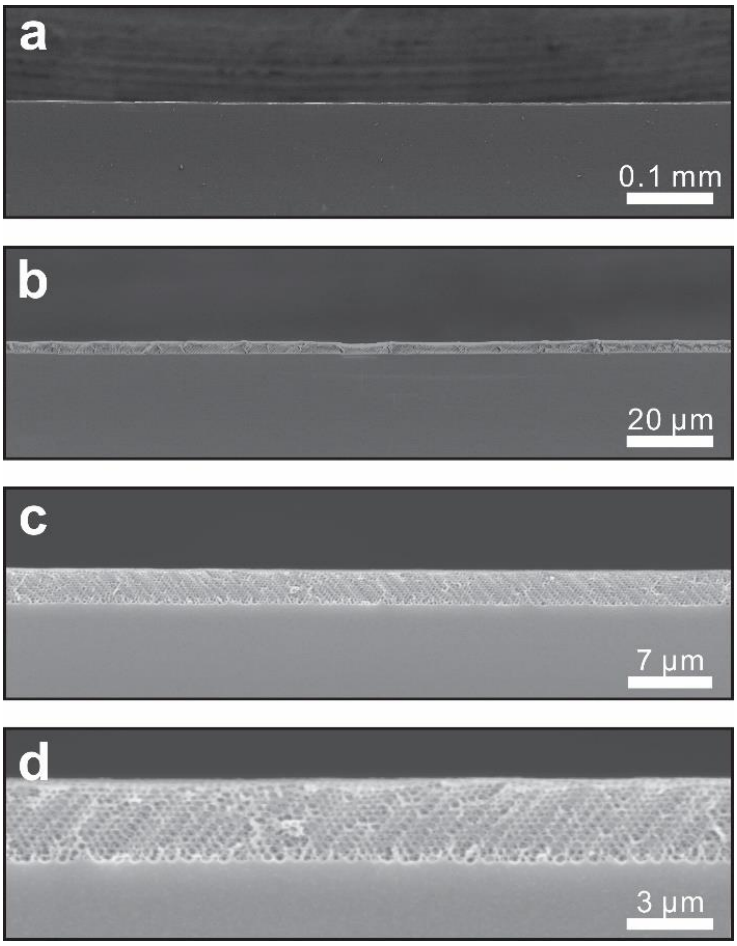

Figure 3.7. Cross-section SEM images of the PC-LSC at different magnifications.

Reference	Filter Type	Band width (FWHM)
***Appl. Opt.* 2005, *44 (26)*, 5415-5421.**	Porous silicon-based rugate filters	~ 300 nm
***Appl. Phys. Lett.* 2006, *89 (24)*, 241116.**	Silver (Ag) and double-layered cholesteric liquid crystal (CLC) mirrors	~ 100 nm
***Appl. Opt.* 2010, *49 (4)*, 745-751.**	Organic wavelength-selective mirrors	~ 90 nm
***Opt. Express* 2012, *20 (S3)*, A395-A405.**	Broad-band cholesteric filters	~ 120 nm
***ACS Photonics* 2015, *2 (11)*, 1576-1583.**	Dielectric mirror fabricated by Optical Filter Source, LLC	~ 300 nm
***ACS Photonics* 2016, *3 (2)*, 278-285.**	Alternating layers of SiO_2 and SnO_2	~ 140 nm
***Nano Lett* 2018, *18 (1)*, 395-404.**	1. 50 nm Ag coating 2. Bragg mirror	1. > 600 nm 2. > 400 nm
This work	3D macroporous-structured PC	~ 87 nm

Table 3.1. Summary of the band width for different Bragg filters used for LSCs.

Chemicals & Supplies	Price per g or mL	Usage	Industrial Cost (per m^2)	Source link
Silica nanoparticles	$0.004/g	12 g	$0.048	*https://www.alibaba.com/product-detail/chemical-product-silica-nanoparticles-silicon-dioxide_62127835316.html?spm=a2700.7724838.2017115.1.3d2f4b8b3xyrjR&s=p*
Glass slide[1]	$1/$m^2$	1 m^2 (recycle 100 times)	$0.01	*https://www.alibaba.com/product-detail/Low-Iron-Clear-Tempered-Glass-Crystal_60758708065.html?spm=a2700.galleryofferlist.normalList.87.47be1e57Wotk61*
Hydrofluoric acid (HF)[2]	$0.00104/mL	50 mL	$0.052	*https://www.alibaba.com/product-detail/Factory-Wholesale-High-Quality-Industrial-Hydrofluoric_62240019047.html?spm=a2700.7724838.2017115.1.2eed24f54bOBI1*
Ethanol (EtOH)[2]	$0.00095/mL	50 mL	$0.0475	*https://www.alibaba.com/product-detail/Pure-Ethanol-95-96-99-5_62003808876.html?spm=a2700.7724838.2017115.80.6b392386GCOW8U*
Cost for PC layer fabrication			$0.1575	

1. Both sides of the glass slide can be used for the fabrication of PC-LSCs, we consider each glass slide can be used for one hundred times of fabrication.
2. Considering both the HF and EtOH are recyclable, we estimate the chemical cost by considering the solvent loss (loss of 50 mL for each solvent) during each fabrication process.

Table 3.2. Cost estimation of chemicals and supplies for the industrial level PC layer fabrication.

3.4 Simulation and device-performance of PC-LSCs.

To compare the device performances between the conventional PC-free LSC and PC-LSC devices, we have developed an analytical model simulation based on a previously reported method.[34, 57] In our model, we considered the solar concentrator waveguide as a square shape LSC slab with four equal edge windows. Without PC coating, the internal quantum efficiency (η_{int}, defined as the ratio of the edge-collected photon flux and the total absorbed solar flux) and external quantum efficiency (η_{ext}, defined as the ratio of the edge-collected photon flux and the total incident photon flux) can be expressed as the following equations: [61]

$$\eta_{int} = \frac{\eta_{PL}\eta_{trap}}{1+\beta\alpha_2(1-\eta_{PL}\eta_{trap})} \quad (2)$$

$$\eta_{ext} = (1-R)(1-T) \times \eta_{int} = \frac{(1-R)\left(1-e^{-\alpha_1 d}\right)\eta_{PL}\eta_{trap}}{1+\beta\alpha_2(1-\eta_{PL}\eta_{trap})} \quad (3)$$

Where, η_{PL} is the PL QY of the emitters; η_{trap} is the efficiency of light trapping into the LSC device; R is the reflection coefficient of LSC surfaces; T is the transmission of the overall LSC device; α_1 is the absorption coefficient at the wavelength of incident light; α_2 is reabsorption coefficient at the wavelength of the emitted light; d is the thickness of LSC device, β is a correction factor for elongation of photon light path in a 3D LSC mode versus a 1D mode. In this study, the β value was derived to be 1.8 after MC modelling correction (see **Method** for details).[36, 61]

For the PC-free LSC, η_{trap} is determined solely by TIR, so, $\eta_{trap} = \cos[\arcsin\left(\frac{1}{n}\right)]$.[31, 35, 61] However, for the PC-LSC, we need to consider additional reflection processes

caused by the top and bottom PC filter coatings. Thus, the $\eta_{trap,PC-LSC}$ needs to be modified as:

$$\eta_{trap,PC-LSC} = \cos\left[\arcsin\left(\frac{1}{n}\right)\right] + \left\{1 - \cos\left[\arcsin\left(\frac{1}{n}\right)\right]\right\} < R > \quad (4)$$

Where, <R> is the reflection factor integrated over the emission profile, which can be expressed as:

$$< R >= \frac{\int S_{PL}(\lambda) R_{PC}(\lambda) d\lambda}{\int S_{PL}(\lambda) d\lambda} \quad (5)$$

The <R> value was calculated to be 0.815 for the PC-LSC device based on experimentally acquired PC reflection and QD emission spectra (**Figure 3.8a**). Therefore, the calculated light trapping efficiency ($\eta_{trap,PC-LSC}$) increased from 73.3% for the PC-free LSC to 95.1% for the PC-LSC and agreed well with the experimentally obtained value of 95.3% (**Figure 3.8b**).

Overall, these equations provide accurate descriptions for both IQE (η_{int}) and EQE (η_{ext}). To clearly demonstrate the enhancement effect caused by the PC coating, we further define an enhancement factor (E factor) for the PC-LSC device as compared to PC-free LSC, expressed as:

$$E = \frac{\eta_{ext,PC-LSC}}{\eta_{ext,LSC}} \quad (6)$$

The simulation results showed that when increasing the geometry gain factor (G, defined as the ratio of the areas of top/bottom surfaces and device edges, G = L/2d, L: square device edge length; *d*: device thickness) from 1 to 10 while maintaining the device thickness, *i.e.* 1 mm, the η_{ext} for the PC-free LSC and PC-LSC devices decreased from 36.2% to 10.3%, and 51.5% to 17.9%, respectively under 365 nm light

illumination (**Figure 3.8c**). These EQE decreases of both PC-free LSC and PC-LSC were mainly attributed to the increased number of reabsorption events, thus the non-radiative decay energy loss of the QDs. Experimental data from measuring the η_{ext} of the fabricated PC-free LSC and PC-LSC devices matched well with the simulation results (**Figure 3.8c**, see **Method** for details). The E factor calculation, however, showed a continuous increase from 1.43 to 1.74, resulting in a positive correlation in regard to device dimension (**Figure 3.8c**). This E factor increase was also consistent with the improved light trapping efficiency (η_{trap} increased from 73.3% to 95.1%) of the PC-LSC, in line with the MC simulation (**Figure 3.1**). Taking both EQE and G factor into consideration for the overall photon concentrating performances, we calculated the C factor (defined as the ratio of the output and the input photon flux densities, C = η_{ext} × G) evolution as a function of G factor. As shown in **Figure 3.8d**, a continuous increase of C factor from 0.52 (0.36) to 1.79 (1.03) was obtained for the PC-LSC (PC-free LSC) upon increasing the G value from 1 to 10. **Figures 3.8e** and **3.8f** show the simulated evolutions of η_{ext}, C factor, and their associated E factor under sunlight (1.5 AM Global) illumination, all of which show similar trends as those under 365 nm light illumination (**Figure 3.8c, d**). To validate these theoretical modelling and simulated results, we have performed optoelectronic studies by integrating silicon-based PVs to the edge of our LSCs. The η_{ext} and C factor were then measured through measuring the *I-V* curve of the integrated LSC-PV devices under simulated solar light irradiation (see **Method** for details). Excellent consistencies between the experimentally obtained η_{ext} and C factors and our theoretically simulated results were

obtained (**Figure 3.8e, f**). An E factor of ~ 1.8 for both EQE and C factor (at G=10) was obtained in the LSC-PV systems and agreed well with the simulated value of 1.74. Our results demonstrated a reliable enhancement of device performance by the PC coating for the LSCs for all geometry designs under real device working conditions.

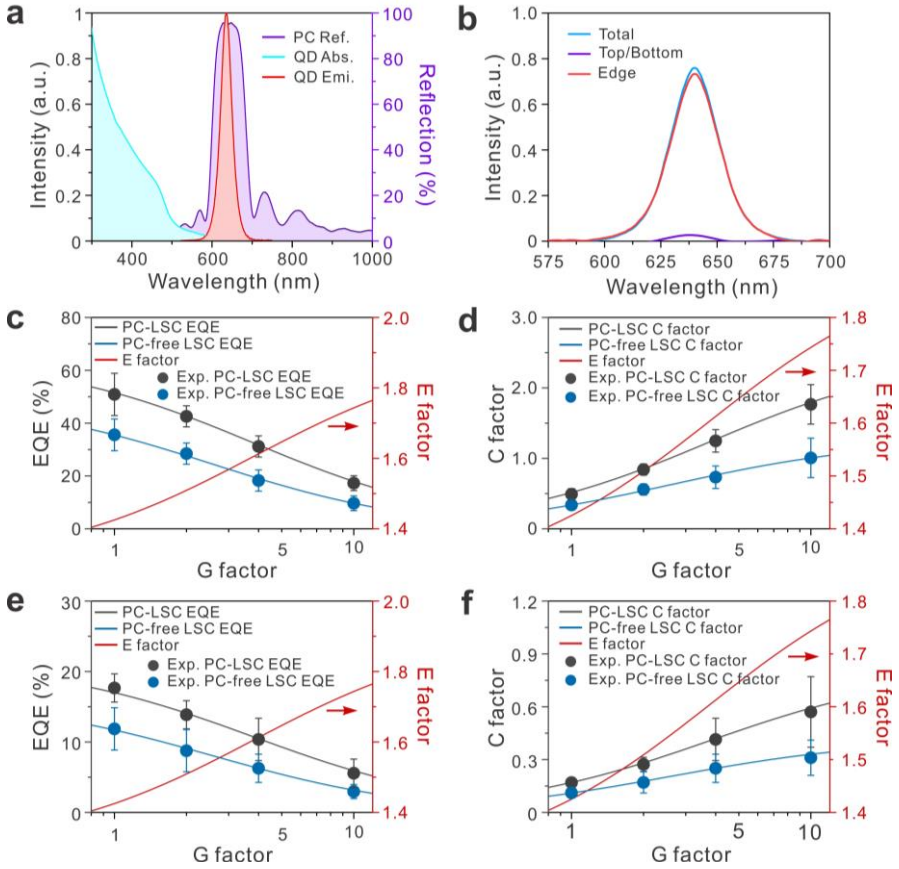

Figure 3.8. (a) Reflection (Ref.) spectrum (purple) of the PC reflector as compared with the absorption (Abs., light blue) and emission (Emi., red) spectra of CdSe/CdS core-shell QDs. **(b)** Emission spectra of total PC-LSC (light blue), edge-covered top/bottom (purple) and the edge emission (red). The dimension of the PC-LSC is 2.8 cm × 1.5 cm × 0.1 cm. **(c-f)** Simulated EQE (c, e) and C factor (d, f) for PC-free LSC (blue lines) and PC-LSC (black lines) evolutions as a function of G factor under 365 nm single wavelength excitation (c, d) and sunlight illumination (e, f).

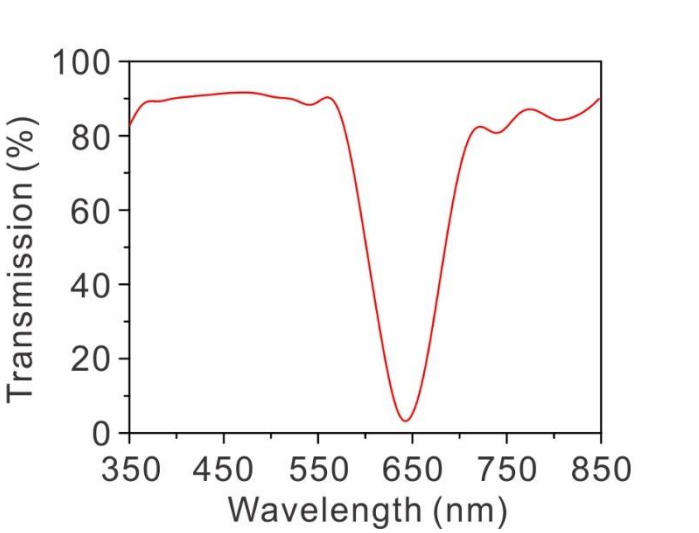

Figure 3.9. Transmission spectrum of the photonic crystal matrix without the incorporation of CdSe-CdS core-shell QDs.

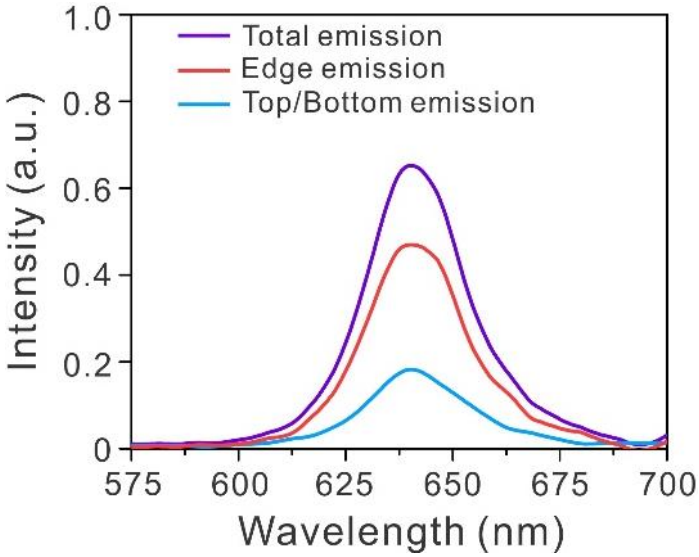

Figure 3.10. The PL spectra of total emission (purple line), top/bottom emission (light blue line) and edge emission (red line) for the PC-free LSC. The dimension of the PC-free LSC is 2.8 cm × 1.5 cm × 0.1 cm, the same as the PC-LSC used in Figure 4b.

3.4 Simulation study of G-factor and enhancement factor of PC-LSCs

In previous studies, G factor has been generally considered as the major geometrical parameter that may affect the LSC quantum efficiencies (both η_{int} and η_{ext}).[34, 36, 54, 61, 62]

However, during the simulation study, we found that by altering the total volume of the LSC device while maintaining the same G factor (*i.e.*, simultaneously scaling three dimensions of the LSC), the η_{ext} of the device could be significantly altered. The instability of the η_{ext} for the LSC with different total volumes but constant G factors can be attributed to the absorption/reabsorption events of the emitters during light propagation inside the LSCs. In other words, a larger device (with a large thickness, *d*, of the LSC) allows increased absorption of incident photons by embedded emitters before reaching device absorption saturation. In this case, more emitted photons will be concentrated by the LSC, and contribute to an enhancement of the η_{ext} of the device. On the other hand, in a larger device, the emitted photons need to travel a longer propagation path than that for a smaller device before reaching edge windows. As a result, the photons will have a higher probability of being reabsorbed by another emitter (*i.e.*, QD), and then lost through *e.g.* non-radiative events (due to sub-unity PL QY), thus contributing to a decrease the η_{ext} of the LSC. When considering these two competing effects, the existence of an optimal device volume (*i.e.* device thickness) with the highest η_{ext} value for an LSC device of fixed G factor should be anticipated. By applying our simulation model, we mapped out the optimal device thickness (*d*) for LSCs with varying G factors under either 365nm light or sunlight (1.5 AM Global) illumination (**Figures 3.11a-f**, **3.12 and 3.13**). Note that, in these simulations, we decreased the QD concentration to 0.1 wt% in order to achieve a wider simulation range for the device thickness before saturating the light absorption. The simulation result confirmed the existence of an optimal device thickness (device volume) with the

highest η_{ext} for PC-free LSC and PC-LSC devices. Moreover, different optimal device thickness (d) and EQE (η_{ext}) were also observed for different given G factors (**Figure 3.11a-c and 3.12**). For example, when G = 20 and under 365 nm light excitation, an optimal d of 14 mm was calculated with the highest η_{ext} of 25.8% for a conventional PC-free LSC. These values shifted to 16 mm and 38.3% for the corresponding PC-LSC (**Figure 3.11b**). Similarly, we have also investigated the C factor behavior under 365 nm light and sunlight illuminations. When the G factor was kept constant at 100, the C factor for the PC-free LSC device was calculated to be 3.97 at an optimal thickness of 12 mm (**Figure 3.11f**). However, for the PC-LSC device, the optimal device thickness shifted to 14 mm and the C factor showed a 59.2% enhancement reaching to a maximal value of 6.32 (**Figure 3.11f**). Our simulation results reveal that, in order to achieve the best light concentrating performance, specific geometric design and optimization processes of the LSC device need to be carried out before integration into a solar energy harvesting system.

Our simulation results unambiguously confirmed the enhancement of device performance caused by applying a PC reflector to conventional LSCs (**Figures 3.8 and 3.11**). For clear visualization of this enhancement effect, we constructed 3D plots of the enhancement factor (E) as functions of G factor and device thickness (d) under sunlight (1.5 AM Global) illumination (**Figure 3.11g**). Upon increasing both the G factor and d, the E factor continuously increased and plateaued at ~ 1.9 as the G factor and thickness reached large values of *e.g.* ~1000 and ~1000 mm, respectively. Nearly the same device

enhancement effects can be gained under 365 nm light illumination (**Figure 3.14**), indicating stable enhancement of device performance independent of the types of incident light. Moreover, we noticed that the E factor is highly sensitive to the quality of the emitters and the PC reflector. This can be attributed to a negative (positive) correlation between the escape photon loss and the <R> value (G factor) of the PC-LSC with a defined device thickness (**Figure 3.15**). When a unity value for the PL QY of the emitter and 0.9 for the <R> of the PC reflector coating were applied in our simulation model, the E factor was significantly boosted up to 11.5 (at G = 1000, d = 1 mm), indicating more than an order of magnitude enhancements for both EQE and C factor of the LSC devices (**Figure 3.16**). The E factor could be further elevated above 13 upon further geometrical optimizations (e.g., increasing the device thickness, **Figure 3.17**).

In conclusion, we demonstrate a 3D macroporous PC filter coating on QD-based LSC devices with enhanced light concentrating performance through both experimental studies and computer simulations. We show that the narrow PC reflection band can be tuned to perfectly cover the emission profile of the applied QDs in the LSCs. Compared with the conventional PC-free LSC devices, the PC-LSC shows significant enhancements for both EQE and C factor at different G factors. According to the simulation study, we demonstrate a basic principle for LSC and PC-LSC geometrical design. Furthermore, the tunable reflection window of the 3D macroporous PC with narrow reflection band offers the possibility for creating tandem LSCs consisting of

multi-type emitters with optimized reflection-emission matched PC coatings. Our study sheds light on the future design and fabrication of the LSCs with optimal light concentrating capabilities well-beyond conventional escape cone-limited LSCs.

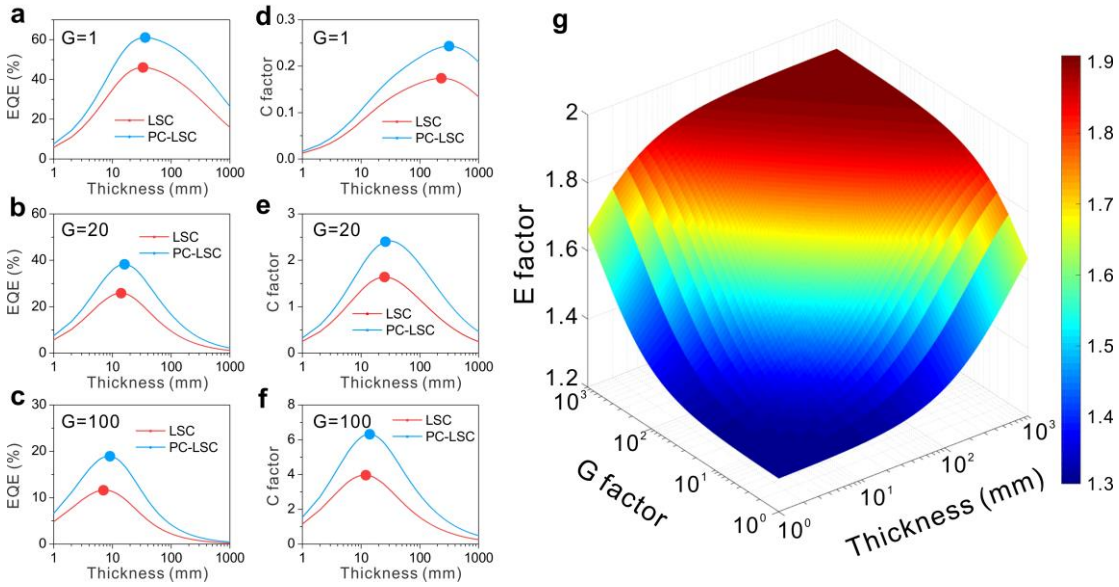

Figure 3.11. (a-c) External quantum efficiency (EQE) of the PC-free LSC (red line) and PC-LSC (blue line) as a function of device thickness under 365 nm light excitation at G factor values of 1 (a, d), 20 (b, e) and 100 (c, f). **(d-f)** Concentration factor (C factor) of the LSC (red line) and PC-LSC (blue line) as a function of device thickness under sunlight (1.5 AM Global) illumination at G factor values of 1 (d), 20 (e) and 100 (f). The blue and red dots in (a-f) indicate the maximal point of the EQE (a-c) and C factor (d-f). **(g)** 3D plot of the enhancement factor (E factor) evolution under sunlight (1.5 AM Global) illumination as functions of G factor and device thickness. The QD emitter concentration is set as 0.1 wt% in all simulations.

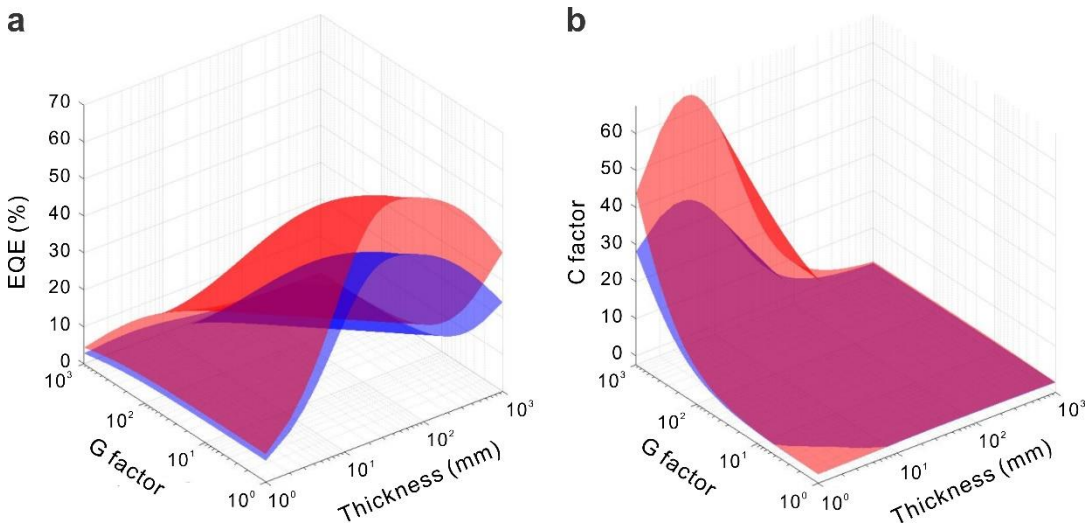

Figure 3.12. 3D plots of **(a)** EQE and **(b)** C factor evolutions as functions of G factor and PC-LSC/LSC thickness under 365 nm single wavelength excitation. The red shades in both figures represent the simulation results for PC-LSC devices. The dark blue shades represent the simulation results for PC-free LSC device. The QD emitter concentration is set as 0.1 wt% in all simulations.

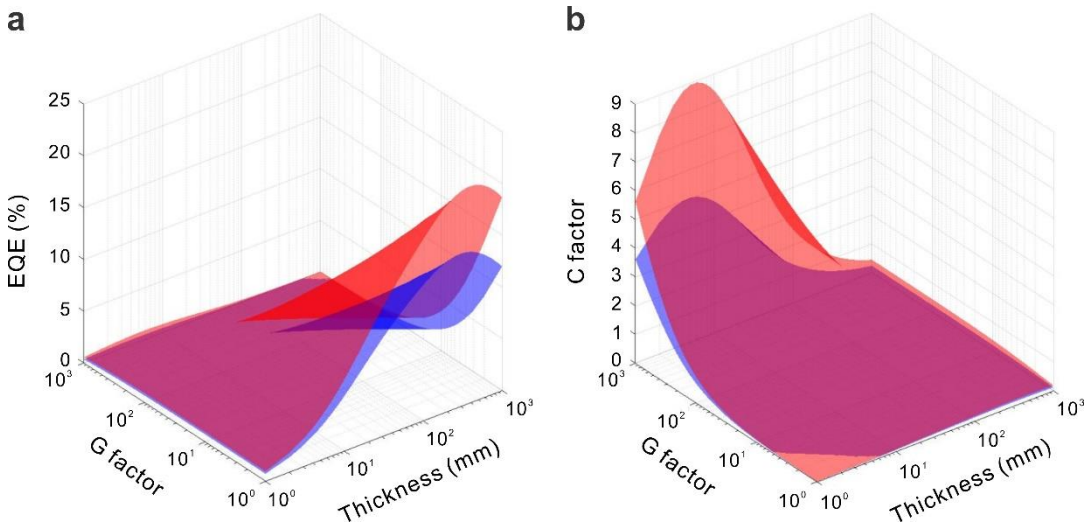

Figure 3.13. Figure S8. 3D plots of **(a)** EQE and **(b)** C factor evolutions as functions of G factor and PC-LSC/LSC device thickness (*d*) under sunlight (1.5 AM Global) illumination. The red shades in both figures represent the simulation results for PC-LSC devices. The dark blue shades represent the simulation results for PC-free LSC device. The QD emitter concentration is set as 0.1 wt% in all simulations.

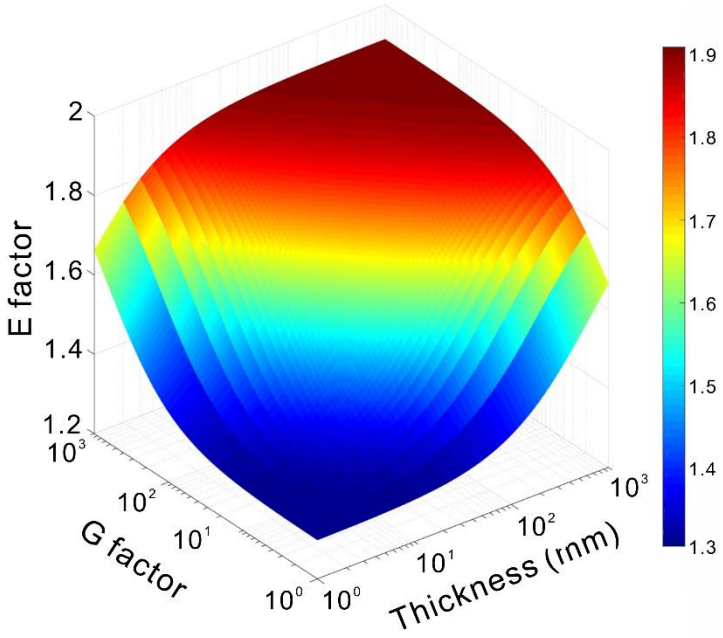

Figure 3.14. 3D plot of the enhancement factor (E factor) evolution as functions of G factor and device thickness (*d*) under 365nm single wavelength excitation. The QD emitter concentration is set as 0.1 wt%.

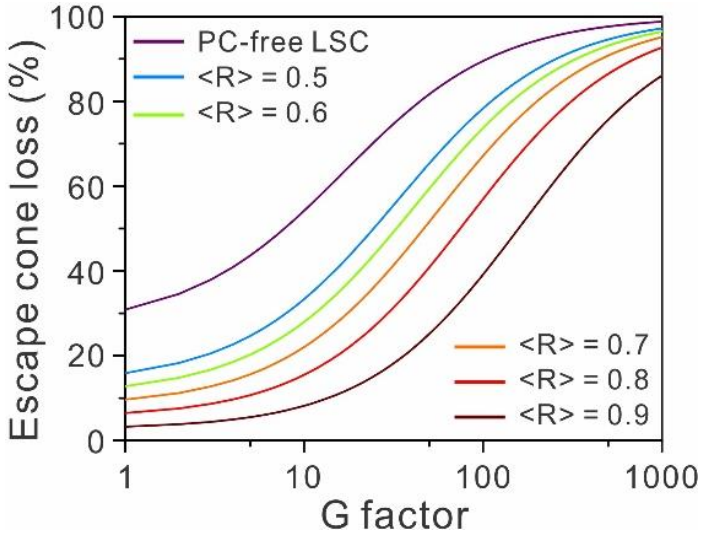

Figure 3.15. Escape cone photon loss of PC-free LSC (purple line), PC-LSC with <R> = 0.5 (blue line), 0.6 (green line), 0.7 (orange line), 0.8 (red line), and 0.9 (brown line). This indicates the G-factor dependent escape cone loss is due to the emitter reabsorption/re-emission processes. Note: we set the device thickness (*d*) as 0.1 cm, and the PL QY = 100% for the emitters to remove any non-radiative photon losses. The QD emitter concentration is set as 0.1 wt%.

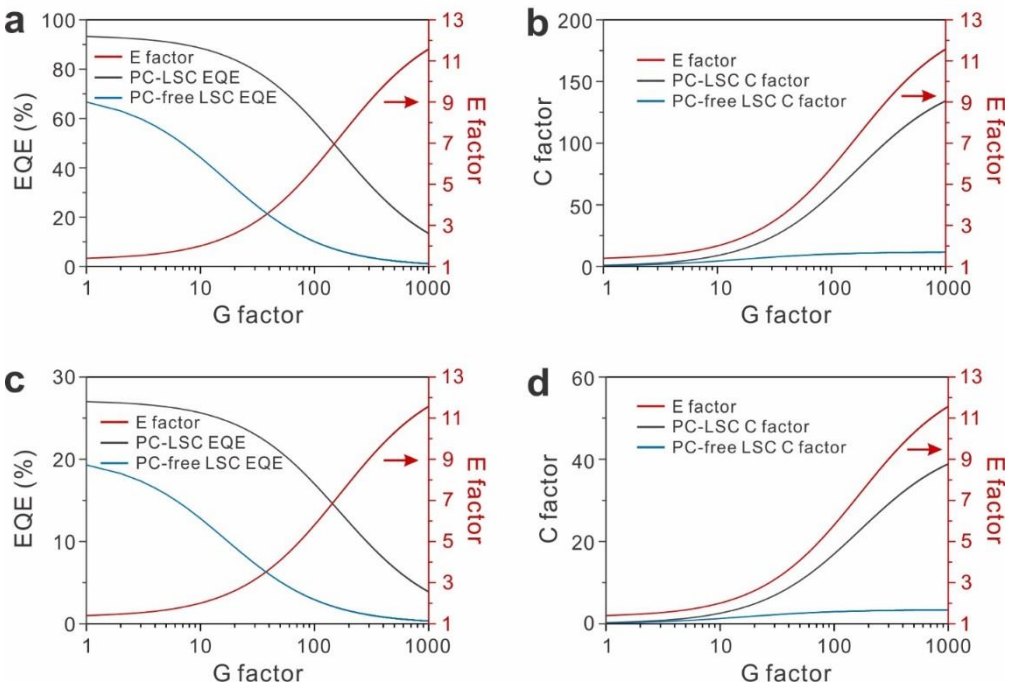

Figure 3.16. Simulation results for EQE and C factor as a function of G factor for PC-LSC (grey lines) and PC-free LSC (blue lines) with PL QY = 100% and <R> = 0.9. The red lines are the corresponding E factor evolutions. **(a)** EQE and **(b)** C factor data under 365nm single wavelength excitation. **(c)** EQE and **(d)** C factor data under sunlight (1.5 AM global) illumination. The QD emitter concentration is set as 0.1 wt%.

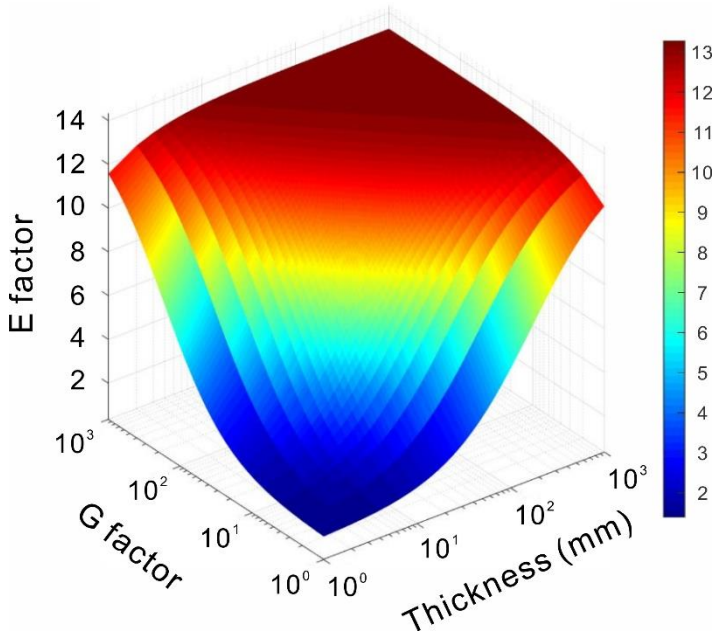

Figure 3.17. 3D plot of the enhancement factor (E factor) evolution under sunlight (1.5 AM Global) illumination as functions of G factor and device thickness (*d*) for a more ideal PC-LSC (PL QY = 100% for QDs, <R> = 0.9 for PC reflector). The QD emitter concentration is set as 0.1 wt%.

Method

Chemicals

Cadmium oxide (CdO, 99.998%), octadecylphosphonic acid (ODPA, 97%), trioctylphosphine oxide (TOPO, 99%), trioctylphosphine (TOP, 97%), selenium powder (99.999%), 1-octadecene (ODE, 90%), oleylamine (OAm, 70%), cadmium nitrate tetrahydrate ($Cd(NO_3)_2 \cdot 4H_2O$, 99.99%), 1-octanethiol (> 98.5%), trimethylolpropane ethoxylate triacrylate (TET, MW ~912), poly (ethylene glycol) diacrylate (PEGDA, MW ~575), 2-hydroxy-2-methylpropiophenone (97%), hydrofluoric acid (48 wt.% in H_2O, ≥ 99.99%) were purchased from Sigma-Aldrich. 400 nm monodispersed silica spheres were purchased from Layne Howell Particle Solutions, LLC. All chemicals were used without further purification.

Synthesis of CdSe cores:

Wurtzite-CdSe (W-CdSe) cores were synthesized according to the literature method.[49, 50] 60 mg CdO, 280 mg octadecylphosphonic acid (ODPA) and 3 g trioctylphosphine oxide (TOPO) were added to a 50 mL flask. The mixture was heated to 150 °C and degassed under vacuum for 1 hour. Under nitrogen flow, the reaction mixture was heated to 320 °C to form a colorless clear solution. After adding 1.0 mL trioctylphosphine (TOP) to the solution, the temperature was brought up to 380 °C, at which point Se/TOP (60 mg Se in 0.5 mL TOP) solution was swiftly injected into the flask. When the CdSe cores reached the desired size, the reaction was terminated by removing the heat. The resulting CdSe particles were precipitated by adding acetone

and dispersed in hexane as a stock solution.[49]

Synthesis of CdSe-CdS core-shell quantum dots (QDs):

As-prepared CdSe QDs were loaded in a mixture of 1-octadecene (ODE, 3 mL) and oleylamine (OAm, 3 mL). The reaction solution was degassed under vacuum at room temperature for 1 hour and 120 °C for 20 min to completely remove the hexane, water and oxygen inside the reaction solution. Then, the reaction solution was heated up to 310 °C with a heating rate of 18 °C/min under nitrogen flow and magnetic stirring. During the heating, when the temperature reached 240 °C, a desired amount of cadmium (II) oleate (Cd-oleate, diluted in 6 mL ODE) and 1-octanethiol (1.2 equivalent amounts refer to Cd-oleate, diluted in 6 mL ODE) began to be injected dropwise into the growth solution at a rate of 3 mL/hr using a syringe pump. After finishing precursor injection, 1 mL oleic acid was quickly injected and the solution was further annealed at 310 °C for 60 min. The resulting CdSe-CdS core-shell QDs were precipitated by adding acetone, and then redispersed in hexane. The particles were further purified by precipitation-redispersion for two more rounds and finally suspended in ~2 ml toluene solution.[2]

Fabrication of photonic crystal coated luminsecent solar concentrators (PC-LSCs):

The 400 nm silica spheres were purified in ethanol by centrifugating for six times (5900 rpmm, 15min) and then redispersed by sonication (4.5 MHz for 3min). The purified

silica spheres were assembled into 3D ordered crystalline structures on glass substrate by using the convective self-assembly method.[56] Then, we constructed a sandwich structure which consisted of two silica-sphere-coated glass substrates with an internal empty space (1 mm between two glass substrates) in between. The internal space was filled through capillary forces with viscous oligomer mixtures containing of TET and PEGDA (weight ratio of 1:3) and the CdSe-CdS core-shell QDs in 0.5 mL toluene solution (CdSe-CdS core-shell QDs with a weight ratio of 0.2% with respect to co-polymer matrix). 2-hydroxy-2-methylpropiophenone (1 wt%) was added into oligomer to serve as a photo initiator. The reaction system was polymerized under 365nm UV lamp for 120min. The glass substractes were removed afterwards and the co-polymer matrix was soaked into a 2 vol.% hydrofluoric acid aqueous solution for 20 seconds to form the macroporous photonic crystal (PC) coating. The final PC-LSC device was washed by acetone or ethanol solution to fully open the macropores.

UV-Vis absorption and transmission measurements

UV-Vis absorption spectra were measured using an Agilent Technologies Cary 5000 UV-Vis-NIR Spectrophotometer. The CdSe-CdS core-shell QDs samples were dissolved in anhydrous toluene and the LSC devices were placed onto film holder accessory for the absorption measurement.

Reflection measurements

Normal-incidence optical reflection spectra were obtained using the Ocean Optics

HR4000 high-resolution vis–NIR spectrometer with the QR200-7-UV-VIS reflection probe and a broadband 360 - 2600 nm light source (Model: SLS201L from Thorlabs).

Photoluminescence (PL) and PL quantum yield (PL QY) measurements

The PL spectra and PL QY measurements were performed using an Edinburgh Instruments Fluorescence Spectrometer FS5. The CdSe-CdS core-shell QDs samples were dissolved in anhydrous toluene for both measurements. The PC-free LSC and PC-LSC samples were placed onto a solid sample holder. The PL QYs were measured by FS5 Spectrometers with a built-in integrating sphere.

Scanning electron microscope (SEM) measurements

SEM measurements were carried out on LEO 1530 and Thermo Scientific Quattro S ESEM operate at 10kV on a cross-section holder. A thin layer of gold (~2nm) was sputtered onto the samples prior to the measurements.

***J-V* characteristics of the reference PC-free LCS and PC-LSC samples**

We used polyscrystalline silicon (c-Si) mini cell (Solar Made 0.5cm × 2.5cm) coupled with the edge regions of LSCs by using NOA 68 polymer adhesive. The black tape was applied to cover the excess area of the cell. Then, we measured the *J-V* curves for the whole system. The *J–V* characteristics of the mini cells, PC-free LSCs and PC-LSCs were measured using the 2400 SourceMeter under simulated 1-sun AM1.5G 100

mA·cm^{-2} intensity (Sol3A Class AAA, Oriel, Newport; USA) at ambient conditions, using both reverse (from V_{OC} to J_{SC}) and forward (from J_{SC} to V_{OC}) scans with a step size of 0.015 V and a delay time of 100 ms.

Transmission electron microscopy (TEM) measurements of CdSe-CdS core-shell QDs

TEM measurements were performed on a JEOL 2100F operated at 200 kV. The CdSe-CdS core-shell QD sample in a toluene solution (~10 μL) was dropped onto a 300-mesh copper TEM grid and dried at ambient conditions.

X-ray Diffraction (XRD) measurements of CdSe-CdS core-shell QDs

XRD pattern was acquired using a Bruker D8 Discovery 2D X-ray Diffractometer equipped with a Vantec 500 2D area detector operating with Cu Kα radiation (λ = 1.541 Å). The CdSe-CdS core-shell QD sample in a hexane solution was drop-casted on glass slides and evaporated at ambient conditions.

Derivation of the external quantum efficiency (EQE) of LSCs from optical measurements

EQE (η_{ext}) is defined as the ratio of the edge-collected photon flux and the total incident photon flux, which can be described by following equation:

$$\eta_{ext} = \eta_{int} \times \eta_{abs} \tag{7}$$

In this equation, η_{int} is the internal quantum efficiency (IQE) which is defined as the

ratio of the edge-collected photon flux and the total absorbed solar flux. η_{int} can be measured by measuring the edge emission PL QY. η_{abs} is the absorption ratio of LSC device, described as:

$$\eta_{abs} = (1 - T)(1 - R) = (1 - R)(1 - e^{-\alpha_1 d}) \quad (8)$$

where, T is the transmission of the overall LSC device, α_1 is the absorption coefficient of the LSC device, R is the reflection coefficient of LSC surface.[5]

Derivation of the EQE of LSCs from electro-optical measurements

The relationship between the power conversion efficiencies (PCEs) of the photovoltaic (PVs) without coupling to the LSC (η_{PV}) and with coupling to the LSC ($\eta_{LSC\text{-}PV}$) can be expressed as:[54, 55]

$$\eta_{LSC-PV} = \frac{\langle Q_{PL} \rangle}{\langle Q_S \rangle} \eta_{s,abs} \eta_{int} \eta_{PV} \quad (9)$$

$\langle Q_S \rangle$ and $\langle Q_{PL} \rangle$ are the averaged EQEs of the PVs over the solar incident wavelength range and the emission spectrum of the LSC, respectively. Then, the η_{int} and η_{ext} of the LSC coupled PV (LSC-PV) can be expressed by the following equations:

$$\eta_{int} = \frac{\eta_{LSC-PV} \langle Q_S \rangle}{\eta_{s,abs} \eta_{PV} \langle Q_{PL} \rangle} = \frac{J_{SC,LSC-PV} \langle Q_S \rangle}{J_{SC} \eta_{s,abs} G \langle Q_{PL} \rangle} \quad (10)$$

$$\eta_{ext} = \frac{J_{SC,LSC-PV} \langle Q_S \rangle}{J_{SC} \eta_{s,abs} G \langle Q_{PL} \rangle} \quad (11)$$

J_{SC} and $J_{SC,LSC-PV}$ are the short-circuit current densities of the standalone PV and LSC-PV, respectively.[54, 55]

Monte Carlo ray-tracing simulation (MC simulation)

The optical efficiency of the PC-LSC was performed via MC ray-tracing simulation.

The propagation behaviour of a photon into LSC can be modeled as a set of vector and location functions, which according to Fresnel Law (discribes the refraction and reflection at air/PC-LSC interfaces). By tracking a number of photons, we can perdict an overall trend of photon progagation and evaluate the photon concentrating performances of LSC devices. The logic flow of the PC-LSC is described in the following paragraph and shown in the logic flow chart below.

Firstly, the inputs for the MC simulation include the total number of photon (i.e., 30,000), the geometry parameter (length, width, height of the LSC) and refractive index of polymer material, the reflection spectrum of PC-LSC, the emission and absorption spectra and PL QY of the CdSe-CdS core-shell QDs. Next, we calculate how many of the inputed 30,000 rondom photons will be absorbed by PC-LSC according to reflection spectrum, absorption spectrum and Fresnel Law. For each absorbed photon, random x and y coordinates are assigned for its initial position.

Then, we determine whether this photon will be absorbed and emitted by the QDs (according to the emission spectrum of PC-LSC and PL QY of the applied CdSe-CdS core-shell QDs). If not, the photon is lost through the non-radiative decay channels of the QDs. If the photon is emitted by the QD, we further determine if the photon will hit the surface of LSC. If not hitting the surface, the photon will be considered back to the initial emission determination step. If hitting the LSC surface, the photon will be updated with a new set of location vectors and proceed to the next step. According to

the new photon location, we can determine which surface the photon hits (top/bottom or edge of the LSC).

If the photon hits the edge surface of the LSC, according to the location vector and refractive index of the polymer matrix, we can determine whether the photon will be reflected through the total internal reflection (TIR). If so, the simulation procedure moves back to the inital emission determination step. If not, this photon will transmit from the edge surface and close one photon tracing loop. After that, the next random photon can be released into the main ray-tracing loop.

If the photon hits top/bottom surface of the LSC, again we can determine if the TIR occurrs. If so, the simulation returns back to the initial emission determination step. If not, the photon is further determined whether it is reflected by the PC reflector according to the reflection spectrum of the PC-LSC. If so, the photon will be reflected back to the LSC, the simulation returns back to the initial emission determination step. If not, the photon is lost through escaping from the top/bottom surface of the PC-LSC. Then, the next photon can ben released into main ray-tracing loop.

The main loop will be repeated until all the photons are traced.

The main uncertainty of the parameters that are inputed in the model are concluded as fellows: the measured reflection and absorption spectra of PC-SLC, the estimated

refractive index of 1.47 for the co-polymer matrix based on the refractive indexes of TET (1.471) and PEGDA (1.467). The standard deviation of ± 1% for the PL QY of thick shell CdSe-CdS core-shell QDs. Overall, the upper limit of the EQE and IQE uncertainties in our simulation is within 5%, which is a tolerable error.

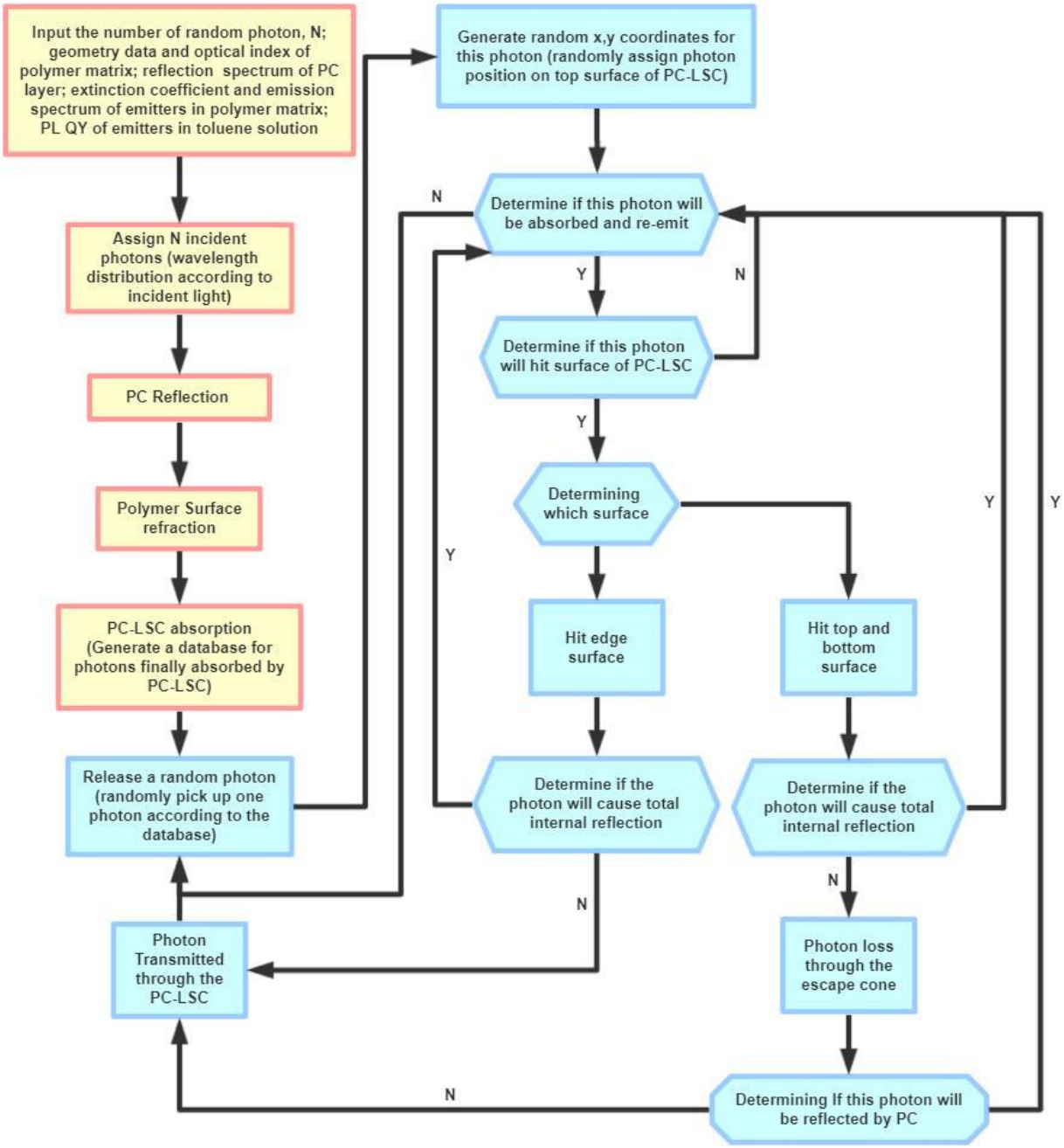

Scheme 3.1: Logic flow chart of the MC ray-tracing simulation for the PC-LSC device. The blue blocks are the main loop region, where individual photons are traced.

Analytical mode simulation

The analytical mode simulation is developed based on previous published methods.[36, 55, 61] The optical quantum efficiencies (i.e., IQE and EQE) are showed in the main text equation (2) and (3).

In the analytical model, we assume that the LSC photon losses are only caused by reabsorption process that are followed by either non-radiative recombination or escape cone loss. This model does not concern any scattering losses. To correct this error, a constant α_2 ~1.05 is introduced into the model to adjust the scattering losses. Based on Weber and Lambe analysis,[9] the calculation can be approximated by LSC efficiency function shown below.

$$\eta_{wg}^{1} = \frac{1}{1+\beta\alpha_2 L} \tag{12}$$

Here, η_{wg}^{1} is the first-time reabsorption loss fraction, β is a geometry correction constant (see below, equation (S12) and MC model correction). Then, the collection efficiency (η_{col}^{1}) of the first generation of emitted photon can be represented as:

$$\eta_{col}^{1} = \eta_{wg}^{1}\eta_{PL}\eta_{trap} \tag{13}$$

η_{PL} is the PL QY of emitters, η_{trap} is the light trapping efficiency (discussed in main text).

The reemission processes following reabsorption of the first generation of emitted photons in LSC device will enhance the overall photon collection efficiency and can be

accounted for by summing the contributions from the second, third, etc., reemission events. To account for the collection efficiency (η_{col}^{2}) of the second-generation of reemitted photons, the function can be expressed as follow:

$$\eta_{col}^{2} = \eta_{PL}\eta_{trap}(1-\eta_{wg}^{1})\eta_{col}^{1} \tag{14}$$

Thus, each reemission process term represents a member of a geometric progression. The total collection efficiency (η_{col}) can be expressed as a sum of contributions due to all photon generations.

$$\eta_{col} = \sum_{i=1}^{\infty}\eta_{col}^{i} \tag{15}$$

Therefore, the IQE (η_{int}) and EQE (η_{ext}) expressions can be obtained and shown in main text equation (2) and (3).

Following the procedure decribed in the literature, [36, 55, 61] we determine the following parameters as:

$$< \alpha_1 >= -\frac{1}{d} ln\left(\frac{\int_{E_g}^{\infty} S_{in}(\lambda)e^{-\alpha(\lambda)d}d\lambda}{\int_{E_g}^{\infty} S_{in}(\lambda)d\lambda}\right) \tag{16}$$

Where $< \alpha_1 >$ is the average absorption coefficient among the incident light wavelength range. The obtained value can apply for the α_1 in the equation (3) shown in the main text. α is the absorption coefficient of the QDs. λis the wavelength. *d* is the thickness of the LCS. E_g is the bandgap of QDs. S_{in} is the spectral shape of incident light.

In equations (2) and (3) in the main text, α_2 is the absorption coefficient at the wavelength of the emitted light, which can be replaced by the average value of $< \alpha_2 >$

defined as:

$$< \alpha_2 > = \frac{\int S_{PL}(\lambda)\alpha(\lambda)d\lambda}{\int S_{PL}(\lambda)d\lambda} \quad (17)$$

Where S_{PL} is the spectral shape of the QD emission, and α is the absorption coefficient of the QDs. λis the wavelength.

For β value determination, the initial value can be calculated based on the following equation:[61]

$$\beta = 1.4 + 0.5\left(\frac{L}{150}\right)^{0.5} \quad (18)$$

Where L is the edge length for square shape LSCs. This equation is relatively reliable for L = 0-2000 cm. Then, the β value is further corrected based on multiple tests from MC simulation. The final β value is determined as 1.8 for all the analytical mode simulations in this study.[7]

Reference

1. Erickson, P.; Lazarus, M.; Piggot, G., Limiting fossil fuel production as the next big step in climate policy. *Nat. Clim. Change* **2018,** *8* (12), 1037-1043.
2. Van de Graaf, T.; Colgan, J., Global energy governance: a review and research agenda. *Palgrave Commun* **2016,** *2* (1), 1-12.
3. Zheng, J.; Suh, S., Strategies to reduce the global carbon footprint of plastics. *Nat. Clim. Change* **2019,** *9* (5), 374-378.
4. Sgouridis, S.; Carbajales-Dale, M.; Csala, D.; Chiesa, M.; Bardi, U., Comparative net energy analysis of renewable electricity and carbon capture and storage. *Nat Energy* **2019**.
5. Cheng, P.; Li, G.; Zhan, X.; Yang, Y., Next-generation organic photovoltaics based on non-fullerene acceptors. *Nat Photonics* **2018,** *12* (3), 131-142.
6. Chu, S.; Majumdar, A., Opportunities and challenges for a sustainable energy future. *Nature* **2012,** *488* (7411), 294-303.
7. Gross, R.; Hanna, R., Path dependency in provision of domestic heating. *Nat Energy* **2019,** 4, 358–364.
8. Fei Guo, C.; Sun, T.; Cao, F.; Liu, Q.; Ren, Z., Metallic nanostructures for light trapping in energy-harvesting devices. *Light Sci Appl* **2014,** *3* (4), e161.
9. Kumar, M.; Kumar, S., Liquid crystals in photovoltaics: a new generation of organic photovoltaics. *Polym J* **2016,** *49* (1), 85-111.
10. Guo, X.; Yi, P.; Yang, Y.; Cui, J.; Xiao, S.; Wang, W., Effects of surfactants on agarose-based magnetic polymer electrolyte for dye-sensitized solar cells. *Electrochim. Acta* **2013,** *90*, 524-529.
11. Niehaus, F.; Williams, J., Studies of different energy strategies in terms of their effects on the atmospheric CO2concentration. *J. Geophys. Res.* **1979,** *84* (C6), 3123-3129.
12. Zhu, K.; Neale, N. R.; Miedaner, A.; Frank, A. J., Enhanced charge-collection efficiencies and light scattering in dye-sensitized solar cells using oriented TiO2 nanotubes arrays. *Nano Lett* **2007,** *7* (1), 69-74.

13. Batchelder, J. S.; Zewail, A. H.; Cole, T., Luminescent solar concentrators. 1: Theory of operation and techniques for performance evaluation. *Appl Opt* **1979,** *18* (18), 3090-110.
14. van Sark, W. G.; Barnham, K. W.; Slooff, L. H.; Chatten, A. J.; Buchtemann, A.; Meyer, A.; McCormack, S. J.; Koole, R.; Farrell, D. J.; Bose, R.; Bende, E. E.; Burgers, A. R.; Budel, T.; Quilitz, J.; Kennedy, M.; Meyer, T.; Donega Cde, M.; Meijerink, A.; Vanmaekelbergh, D., Luminescent Solar Concentrators--e. *Opt Express* **2008,** *16* (26), 21773-21792.
15. Meinardi, F.; Bruni, F.; Brovelli, S., Luminescent solar concentrators for building-integrated photovoltaics. *Nat Rev Mater* **2017,** *2* (12), 17072.
16. Debije, M.; Verbunt, P., Thirty Years of Luminescent Solar Concentrator Research: Solar Energy for the Built Environment. *Adv Energy Mater* **2012,** 2 (1), 12-35.
17. Evans, R.; Mckenna, B., Towards Efficient Spectral Converters through Materials Design for Luminescent Solar Devices. *Adv Matter* **2017,** 29 (28), 1606491.
18. Weber, W. H.; Lambe, J., Luminescent greenhouse collector for solar radiation. *Appl Opt* **1976,** *15* (10), 2299-2300.
19. Meinardi, F.; Colombo, A.; Velizhanin, K. A.; Simonutti, R.; Lorenzon, M.; Beverina, L.; Viswanatha, R.; Klimov, V. I.; Brovelli, S., Large-area luminescent solar concentrators based on 'Stokes-shift-engineered' nanocrystals in a mass-polymerized PMMA matrix. *Nat Photonics* **2014,** *8* (5), 392-399.
20. Luo, X.; Ding, T.; Liu, X.; Liu, Y.; Wu, K., Quantum Cutting Luminescent Solar Concentrators Using Ytterbium Doped Perovskite Nanocrystals. *Nano Lett* **2018,** 19(1), 338-34.
21. Coropceanu, I.; Bawendi, M. G., Core/shell quantum dot based luminescent solar concentrators with reduced reabsorption and enhanced efficiency. *Nano Lett* **2014,** *14* (7), 4097-4101.
22. Li, C.; Chen, W.; Wu, D.; Quan, D.; Zhou, Z.; Hao, J.; Qin, J.; Li, Y.; He, Z.; Wang, K., Large Stokes Shift and High Efficiency Luminescent Solar Concentrator Incorporated with CuInS2/ZnS Quantum Dots. *Sci Rep* **2015,** *5*, 17777.

23. Knowles, K. E.; Kilburn, T. B.; Alzate, D. G.; McDowall, S.; Gamelin, D. R., Bright CuInS2/CdS nanocrystal phosphors for high-gain full-spectrum luminescent solar concentrators. *Chem Commun (Camb)* **2015,** *51* (44), 9129-9132.
24. Meinardi, F.; McDaniel, H.; Carulli, F.; Colombo, A.; Velizhanin, K. A.; Makarov, N. S.; Simonutti, R.; Klimov, V. I.; Brovelli, S., Highly efficient large-area colourless luminescent solar concentrators using heavy-metal-free colloidal quantum dots. *Nat Nanotechnol* **2015,** *10* (10), 878-885.
25. Sun, K.; Vasudev, M.; Jung, H.-S.; Yang, J.; Kar, A.; Li, Y.; Reinhardt, K.; Snee, P.; Stroscio, M. A.; Dutta, M., Applications of colloidal quantum dots. *Microelectronics J* **2009,** *40* (3), 644-649.
26. Bradshaw, L. R.; Knowles, K. E.; McDowall, S.; Gamelin, D. R., Nanocrystals for luminescent solar concentrators. *Nano Lett* **2015,** *15* (2), 1315-23.
27. Zhou, Y.; Benetti, D.; Tong, X.; Jin, L.; Wang, Z. M.; Ma, D.; Zhao, H.; Rosei, F., Colloidal carbon dots based highly stable luminescent solar concentrators. *Nano Energy* **2018,** *44*, 378-387.
28. Liu, G.; Mazzaro, R.; Wang, Y.; Zhao, H.; Vomiero, A., High efficiency sandwich structure luminescent solar concentrators based on colloidal quantum dots. *Nano Energy* **2019,** *60*, 119-126.
29. Zhao, H.; Zhou, Y.; Benetti, D.; Ma, D.; Rosei, F., Perovskite quantum dots integrated in large-area luminescent solar concentrators. *Nano Energy* **2017,** *37*, 214-223.
30. McDowall, S.; Butler, T.; Bain, E.; Scharnhorst, K.; Patrick, D., Comprehensive analysis of escape-cone losses from luminescent waveguides. *Appl Opt* **2013,** *52* (6), 1230-1239.
31. Debije, M.; Verbunt, P.; Rowan, B.; Richards, B.; Hoeks J., Measured surface loss from luminescent solar concentrator waveguides. *Appl Opt* **2008,** 47 (36), 6763-6768.
32. Xu, L.; Yao, Y.; Bronstein, N. D.; Li, L.; Alivisatos, A. P.; Nuzzo, R. G., Enhanced Photon Collection in Luminescent Solar Concentrators with Distributed Bragg Reflectors. *ACS Photonics* **2016,** *3* (2), 278-285.

33. Bronstein, N. D.; Yao, Y.; Xu, L.; O'Brien, E.; Powers, A. S.; Ferry, V. E.; Alivisatos, A. P.; Nuzzo, R. G., Quantum Dot Luminescent Concentrator Cavity Exhibiting 30-fold Concentration. *ACS Photonics* **2015,** *2* (11), 1576-1583.
34. Sharma, M.; Gungor, K.; Yeltik, A.; Olutas, M.; Guzelturk, B.; Kelestemur, Y.; Erdem, T.; Delikanli, S.; McBride, J. R.; Demir, H. V., Near-Unity Emitting Copper-Doped Colloidal Semiconductor Quantum Wells for Luminescent Solar Concentrators. *Adv Mater* **2017,** *29* (30), 1700821
35. Erickson, C. S.; Bradshaw, L. R.; McDowall, S.; Gilbertson, J. D.; Gamelin, D. R.; Patrick, D. L., Zero-reabsorption doped-nanocrystal luminescent solar concentrators. *ACS Nano* **2014,** *8* (4), 3461-7.
36. Song, H. J.; Jeong, B. G.; Lim, J.; Lee, D. C.; Bae, W. K.; Klimov, V. I., Performance Limits of Luminescent Solar Concentrators Tested with Seed/Quantum-Well Quantum Dots in a Selective-Reflector-Based Optical Cavity. *Nano Lett* **2018,** *18* (1), 395-404.
37. Jeong, S. M.; Sonoyama, K.; Takanishi, Y.; Ishikawa, K.; Takezoe, H.; Nishimura, S.; Suzaki, G.; Song, M. H., Optical cavity with a double-layered cholesteric liquid crystal mirror and its prospective application to solid state laser. *Appl Phys Lett* **2006,** *89* (24), 241116.
38. Debije, M. G.; Van, M. P.; Verbunt, P. P.; Kastelijn, M. J.; van der Blom, R. H.; Broer, D. J.; Bastiaansen, C. W., Effect on the output of a luminescent solar concentrator on application of organic wavelength-selective mirrors. *Appl Opt* **2010,** *49* (4), 745-751.
39. Boer D.; Broer D.; Debije M.; Keur W.; Meijerink A.; Ronda C.; Verbunt P., Progress in phosphors and filters for luminescent solar concentrators. *Opt. Express* **2012,** 20 (S3), A395-A405.
40. M. Peters.; J. C. Goldschmidt.; P. Löper.; B. Bläsi.; A. Gombert., The effect of photonic structures on the light guiding efficiency of fluorescent concentrators. *J Appl Phys* **2009,** 105 (1), 014909.
41. Ng, H. M.; Moustakas, T. D.; Chu, S. N. G., High reflectivity and broad bandwidth AlN/GaN distributed Bragg reflectors grown by molecular-beam epitaxy. *Appl Phys Lett* **2000,** *76* (20), 2818-2820.

42. Nolte, A. J.; Rubner, M. F.; Cohen, R. E., Creating effective refractive index gradients within polyelectrolyte multilayer films: Molecularly assembled rugate filters. *Langmuir* **2004,** *20* (8), 3304-3310.
43. Lee, C. C.; Tang, C. J.; Wu, J. Y., Rugate filter made with composite thin films by ion-beam sputtering. *Appl Opt* **2006,** *45* (7), 1333-1337.
44. Pina-Hernandez, C.; Koshelev, A.; Dhuey, S.; Sassolini, S.; Sainato, M.; Cabrini, S.; Munechika, K., Nanoimprinted High-Refractive Index Active Photonic Nanostructures Based on Quantum Dots for Visible Light. *Sci Rep* **2017,** *7* (1), 17645.
45. Lorenzo, E.; Oton, C. J.; Capuj, N. E.; Ghulinyan, M.; Navarro-Urrios, D.; Gaburro, Z.; Pavesi, L., Porous silicon-based rugate filters. *Appl Opt* **2005,** *44* (26), 5415-5421.
46. Abusafia, H. A.; Alsharif, A. I.; Abualjarayesh, I. O., Rugate Filter Sidelobe Suppression Using Half-Apodization. *Appl Opt* **1993,** *32* (25), 4831-4835.
47. Aoki, K.; Guimard, G.; Nishioka, M.; Nomura, M.; Iwamoto, S.; Arakawa, Y., Coupling of quantum-dot light emission with a three-dimensional photonic-crystal nanocavity. *Nat Photonics* **2008**, *2*, 688–692.
48. Hu, X.; Kang, R.; Zhang, Y.; Deng, L.; Zhong, H.; Zou, B.; Shi, L. J., Ray-trace simulation of CuInS(Se)(2) quantum dot based luminescent solar concentrators. *Opt Express* **2015,** *23* (15), A858-A867.
49. Chen, O.; Zhao, J.; Chauhan, V. P.; Cui, J.; Wong, C.; Harris, D. K.; Wei, H.; Han, H. S.; Fukumura, D.; Jain, R. K.; Bawendi, M. G., Compact high-quality CdSe-CdS core-shell nanocrystals with narrow emission linewidths and suppressed blinking. *Nat Mater* **2013,** *12* (5), 445-451.
50. Tan, R.; Yuan, Y.; Nagaoka, Y.; Eggert, D.; Wang, X.; Thota, S.; Guo, P.; Yang, H.; Zhao, J.; Chen, O., Monodisperse Hexagonal Pyramidal and Bipyramidal Wurtzite CdSe-CdS Core–Shell Nanocrystals. *Chem Mater* **2017,** *29* (9), 4097-4108.
51. Li, B.; Bian, K.; Zhou, X.; Lu, P.; Liu, S.; Brener, I.; Sinclair, M.; Luk, T.; Schunk, H.; Alarid, L.; Clem, P. G.; Wang, Z.; Fan, H., Pressure compression of CdSe nanoparticles into luminescent nanowires. *Sci Adv* **2017,** *3* (5), e1602916.
52. Reiss, P.; Protiere, M.; Li, L., Core/Shell semiconductor nanocrystals. *Small* **2009,** *5* (2), 154-168.

53. McElroy, N.; Page, R. C.; Espinbarro-Valazquez, D.; Lewis, E.; Haigh, S.; O'Brien, P.; Binks, D. J., Comparison of solar cells sensitised by CdTe/CdSe and CdSe/CdTe core/shell colloidal quantum dots with and without a CdS outer layer. *Thin Solid Films* **2014,** *560*, 65-70.
54. Li, H.; Wu, K.; Lim, J.; Song, H.-J.; Klimov, V. I., Doctor-blade deposition of quantum dots onto standard window glass for low-loss large-area luminescent solar concentrators. *Nat Energy* **2016,** *1* (12), 16157.
55. Wu, K.; Li, H.; Klimov, V. I., Tandem luminescent solar concentrators based on engineered quantum dots. *Nat Photonics* **2018,** *12* (2), 105-110.
56. Jiang, P.; Bertone, J. F.; Hwang, K. S.; Colvin, V. L., Single-Crystal Colloidal Multilayers of Controlled Thickness. *Chem Mater* **1999,** *11* (8), 2132-2140.
57. Fang, Y.; Ni, Y.; Choi, B.; Leo, S. Y.; Gao, J.; Ge, B.; Taylor, C.; Basile, V.; Jiang, P., Chromogenic Photonic Crystals Enabled by Novel Vapor-Responsive Shape-Memory Polymers. *Adv Mater* **2015,** *27* (24), 3696-3704.
58. Ni, Y.; Zhang, Y.; Leo, S.-Y.; Fang, Y.; Zhao, M.; Yu, L.; Schulze, K. D.; Sawyer, W. G.; Angelini, T. E.; Jiang, P.; Taylor, C. R., Unconventional Shape Memory Mechanisms of Nanoporous Polymer Photonic Crystals: Implications for Nano-Optical Coatings and Devices. *ACS Appl Nano Mater* **2018,** *1* (11), 6081-6090.
59. Gaulding, E.; Liu, G.; Chen, C.; Lobbert, L.; Li, A.; Segev, G.; Eichhorn, J.; Aloni, S.; Schwatzberg, A.; Sharp, I.; Toma, F., Fabrication and optical characterization of polystyrene opal templates for the synthesis of scalable, nanoporous (photo)electrocatalytic materials by electrodeposition. *J. Mater. Chem. A,* **2017,** 5, 11601-11614.
60. Jiang, P., McFarland, M., *J. Am. Chem. Soc.*, **2004**, *126* (42), 13778-13786
61. Klimov, V. I.; Baker, T. A.; Lim, J.; Velizhanin, K. A.; McDaniel, H., Quality Factor of Luminescent Solar Concentrators and Practical Concentration Limits Attainable with Semiconductor Quantum Dots. *ACS Photonics* **2016,** *3* (6), 1138-1148.
62. Zhao, H.; Benetti, D.; Tong, X.; Zhang, H.; Zhou, Y.; Liu, G.; Ma, D.; Sun, S.; Wang, Z. M.; Wang, Y.; Rosei, F., Efficient and stable tandem luminescent solar

concentrators based on carbon dots and perovskite quantum dots. *Nano Energy* **2018,** *50*, 756-765.

Chapter 4

Cesium Copper Halide Perovskite Nanocrystals Based Photon-Managing Devices for Enhanced Ultraviolet Photon Harvesting

4.1 Introduction

Ever since the discovery of crystalline silicon wafer in the early 1950s, researchers have been considering integrating photovoltaic (PV) systems with aerospace satellites to harvest solar energies in space.[1-5] With this idea in mind, researchers have recently proposed a space-based solar power system which is composed of a spacecraft carrying an array of utility-scale PVs into geostationary orbit for efficient solar energy harvesting in space (Scheme 4.1).[6-8] The generated electricity can be radiated through an antenna system mounted on the spacecraft and collected by the receiving stations placed on earth (Scheme 4.1).[8-10] Practically, the solar harvesting system needs to reach a high level of specific power (defined as the power produced per mass of the mounted PV cell, unit of kW/kg) for sufficient solar photon to electricity conversion.[7] Theoretically, the space-based solar panels can generate 2,000 GW of power constantly, which is ~ 40 times more energy than on earth due to the continuous generation of electricity under direct solar irradiance.[11-14] However, for the standalone PV system, it is difficult to exceed a specific power of 1kW/kg,[15] which is the minimal requirement for a solar energy generation station.[7] This is mainly due to the dimension limitation of the mounted PV cells and their low efficiency for the high-energy UV photon collection and conversion.[6, 7, 16] In particular, the solar radiation in space consists of ~7% UV light of the total solar spectrum, *i.e.*, 0.45 % UVC (100-280nm), 1.12% UVB (280-315nm), and 5.43 % UVA (315-400nm) photons, which is ~2.5 times more than the total UV radiation on the earth surface (due to the strong UV absorption and scatting effects by ozone layer).[17, 18] Therefore, desirable light-weight photon-managing devices are

pressingly needed to boost the specific power, especially by more efficiently harvesting high-energy UV photons through aerospace satellite systems. In this regard, luminescent solar concentrator (LSC) is a dielectric device that can harvest, direct and concentrate incoming photons to small areas for the use of energy conversion by the attached PV cells.[19-24] And the luminescent down-shifting (LDS) layer can be directly attached to PV top surface to improve the short-wavelength response of PV modules by down-converting high-energy photons to longer wavelength range.[25-29] The integration of LSC or LDS devices has been proposed as a potential solution for boosting the solar energy harvesting and increasing the specific power of space-based solar panels.[16, 30-32]

Halide perovskite nanocrystals (NCs) are promising emitters for LSC and LDS layer integrations due to their tunable optical bandgap, narrow emission peak, and high photoluminescent quantum yield (PL QY).[16, 33-37] In particular, a new family of lead-free copper(I)-based metal halide (*i.e.*, $Cs_3Cu_2X_5$, X = Cl, Br, and I) perovskite NCs has recently been synthesized with multiple merits, *i.e.*, strong UV photon absorption, high transparency in visible spectral region, green/blue emissions with high PL QYs (> 80%), and large Stokes shift with non-reabsorption feature, making them ideal for LSC and LDS integrations in PV cells, especially for space-based solar panels.[38-40] However, to our best knowledge, the copper(I)-based metal halide perovskite NCs have not yet been demonstrated in LSC or LDS device applications.

Here in, we synthesized lead-free $Cs_3Cu_2Cl_5$ perovskite NDs with a high PL QY of 84.2% and a large Stoke shift of 1.43 eV. By incorporating these NDs into LSC and LDS devices using an ultrasonic spray coating method, we achieved high visible light transmission, low photon scattering, and superior UV photon harvesting and energy conversion when integrated with Si-PV cells. Our study demonstrates the potential of using these unique photon-managing devices for spacecraft photon collection or as multifunctional energy collection hulls with increased specific power. This opens new possibilities for applying lead-free perovskite nanomaterials to enhance high-energy photon utilization in space-based solar power systems.

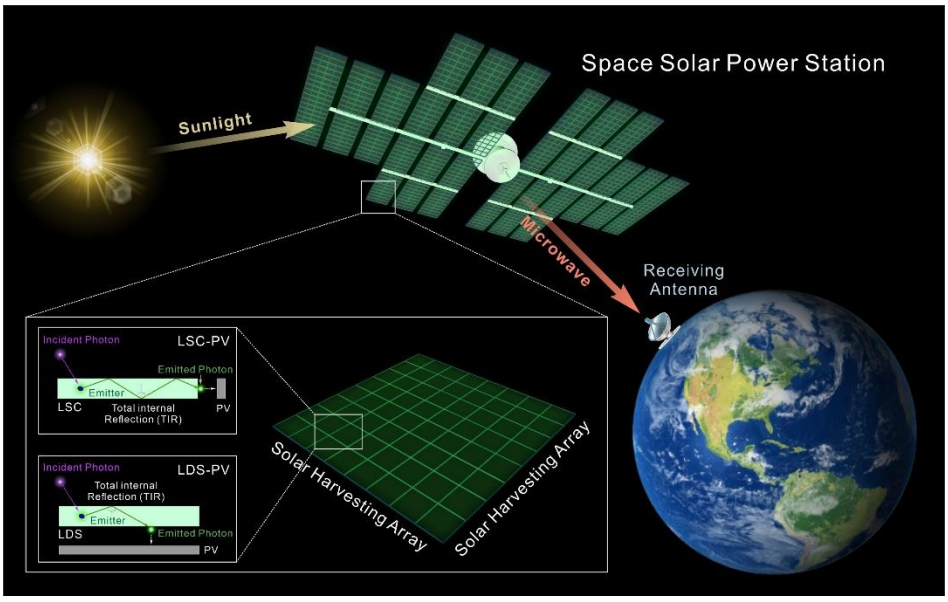

Scheme 4.1. Schematic demonstration for the working principle of space-based solar power station integrated with either LSC-PV or LDS-PV device systems.

4.2 Synthesis and characterization of $Cs_3Cu_2Cl_5$ NDs

Colloidal lead-free $Cs_3Cu_2Cl_5$ perovskite NDs were synthesized following a literature method.[41, 42] Briefly, oleylamine hydrochloride precursor was injected into 1-

octadecene solution containing cupric acetate, cesium carbonate and oleic acid at 120 °C to initiate the particle formation reaction. Transmission electron microscopy (TEM) measurements showed that the average lateral size of the as-prepared $Cs_3Cu_2Cl_5$ NDs is 20.7 ± 3.1 nm (**Figure 4.1a, Figure 4.2**). A high-resolution TEM (HR-TEM) image of individual ND showed clear lattice fringes with a *d*-spacing of 2.5 Å, which can be assigned to the interplanar distance of (330) planes in the orthorhombic phase of $Cs_3Cu_2Cl_5$ perovskite NDs (**Figure 4.1a, inset**).[38, 41-43] The X-ray diffraction (XRD) pattern of the sample confirmed the orthorhombic crystal structure with all the major Bragg diffraction peaks assigned to the simulated $Cs_3Cu_2Cl_5$ perovskite peak positions (**Figure 4.1b**). The unit cell structure of $Cs_3Cu_2Cl_5$ perovskite is shown in **Figure 4.1c**, which adopts an orthorhombic structure in the space group of *Pnma* with isolated $[Cu_2Cl_5]^{3-}$ dimers.[39-42, 44, 45] Absorption and PL (under 295nm excitation) spectroscopic measurements revealed that the NDs showed a strong UVC and UVB absorbance with the first absorption peak at 294 nm, corresponding to the Cu *d*-*d* electronic transition.[41, 43] Importantly, the sample exhibited a large Stokes shift of 1.43 eV with a strong self-trapping exciton (STE) emission peak centered at 524 nm (full width at half maximum, FWHM: ~ 470 meV) (**Figure 4.1e**). A high PL QY of the synthesized $Cs_3Cu_2Cl_5$ perovskite NDs was determined to be 84.2%. Time-resolved PL spectroscopy measurements (under 295nm excitation) revealed a PL decay lifetime of 115 μs (**Figure 4.1f**), in agreement with the STE emission character as well as previously reported values.[41, 45, 46]

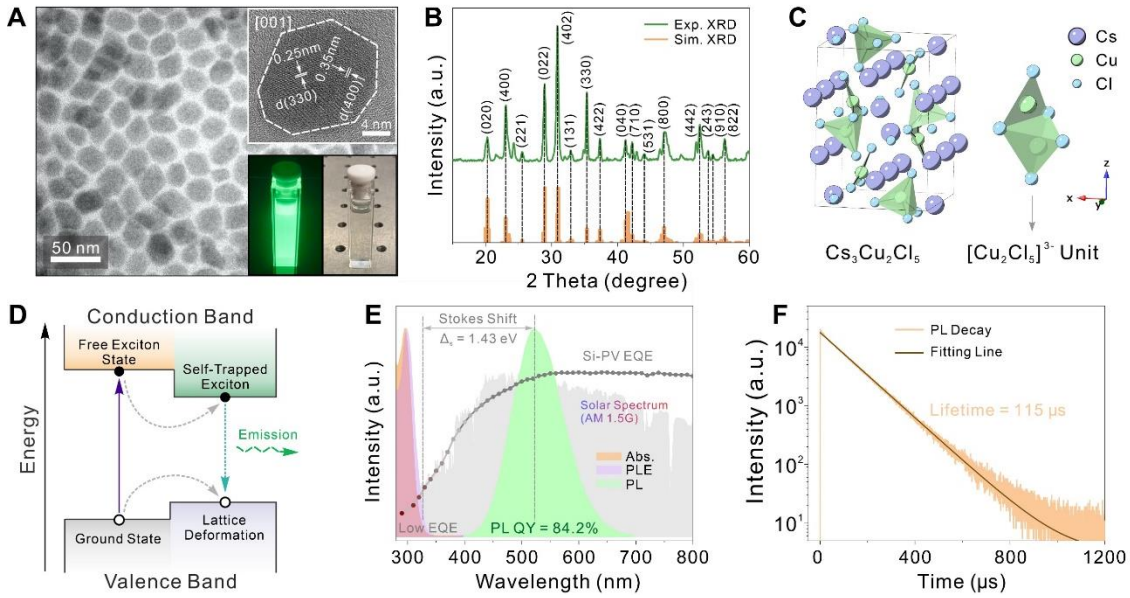

Figure 4.1. (a) Typical TEM image of the $Cs_3Cu_2Cl_5$ NDs. Inset: HR-TEM image of one representative $Cs_3Cu_2Cl_5$ ND (top); photographs of $Cs_3Cu_2Cl_5$ NDs hexane solution under UV light illumination and room light (bottom). **(b)** Experimental (Exp.) and simulated (Sim.) XRD patterns of the $Cs_3Cu_2Cl_5$ NDs. **(c)** Unit cell structure and a $[Cu_2Cl_5]^{3-}$ unit of $Cs_3Cu_2Cl_5$ NDs. **(d)** Band structural alignment of $Cs_3Cu_2Cl_5$ perovskite. **(e)** Absorption (Abs.), photoluminescence excitation (PLE), and photoluminescence (PL) spectra of the $Cs_3Cu_2Cl_5$ NDs along with a standard calibrated external quantum efficiency (EQE) plot (grey) of silicon-photovoltaic cell (Si-PV). **(f)** Time-resolved PL decay curve and fitting line of the $Cs_3Cu_2Cl_5$ NDs in a hexane solution.

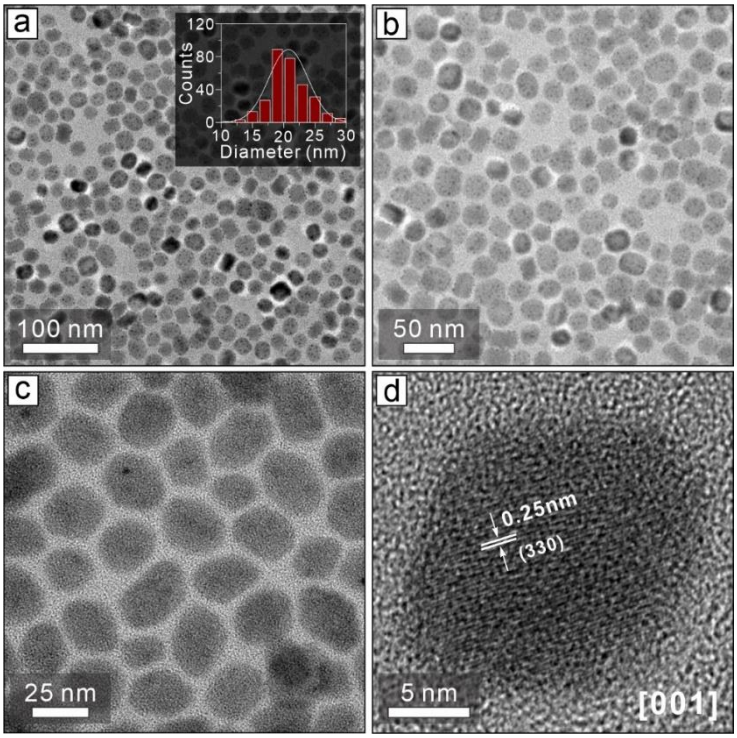

Figure 4.2. Additional TEM images of the $Cs_3Cu_2Cl_5$ perovskite NDs at different magnifications. Inset: Histogram of diameter distribution histogram. The diameter *d* is defined as effective diameter of the $Cs_3Cu_2Cl_5$ perovskite NDs, which is expressed as $d = 2 \times \sqrt{S/\pi}$, where *S* is the surface area of the NDs determined by *ImageJ*.

4.3 $Cs_3Cu_2Cl_5$ perovskite NDs thin film characterization

The obtained $Cs_3Cu_2Cl_5$ perovskite NDs were then used to fabricate LSC/LDS photon-managing devices using our recently developed ultrasonic spray coating method.[20] An ink solution containing $Cs_3Cu_2Cl_5$ perovskite NDs, polydimethylsiloxane (PDMS), and hexane was sprayed onto a pre-heated PDMS substrate using an ultrasonic nebulizer. The ink solution was made up of 8.0 wt% NDs with respect to the PDMS, and the PDMS/hexane volume ratio was 1/10. The ultrasonic vibration generator produced micrometer-scale droplets from the ink solution, forming an even deposition onto the substrate. After hexane evaporation, the resulting NDs/PDMS composite was cured to

form a transparent film. To enhance the device stability and protect the $Cs_3Cu_2Cl_5$ perovskite NDs from oxygen and moisture, a thin layer of PDMS (~ 2.5 μm) was subsequently spray-coated onto the device. Due to its stability to UV radiation, low surface energy (-21 mJ/cm^2), and strong Si-O-Si (siloxane) backbone, PDMS can effectively shield the $Cs_3Cu_2Cl_5$ perovskite NDs from oxygen, moisture, and degradation caused by high-energy photons. Device stability test showed that after 7-day storage in the atmosphere, the emission intensity of the $Cs_3Cu_2Cl_5$-NDs/PDMS composite remained ~96% of the initial value, as compared to only 2.5% remained for the $Cs_3Cu_2Cl_5$ NDs dispersed in a hexane solution (**Figure 4.3a**). Both PL and PLE spectra of the $Cs_3Cu_2Cl_5$ NDs remained intact after being incorporated into the NDs/PDMS composite (**Figure 4.3b**). However, the PL lifetime was slightly shortened to 103 μs comparing to that of a colloidal solution of the $Cs_3Cu_2Cl_5$ NDs (**Figure 4.3c**), indicating minimal non-radiative decay channels were introduced during the device fabrication process.[19, 22] Due to the large Stokes shift with non-reabsorption behavior of the $Cs_3Cu_2Cl_5$ NDs, the emission light-trapping efficiency (defined as: $\eta_{trap} = \sqrt{1 - n^{-2}}$, where n is the refractive index of the polymer matrix) of the NDs/PDMS composite was measured to be 75.2% (**Figure 4.3d**), in good accordance with the theoretically calculated value of 71.5% based on the refractive index of PDMS polymer (n = 1.43), indicating negligible photon scattering and attenuation losses.[20, 23, 47]

We then fabricated a series of NDs/PDMS composite devices by ultrasonic spray coating different volumes of the ND-ink solution with a constant $Cs_3Cu_2Cl_5$ NDs

concentration of 8.0 wt% (with respect to the PDMS): 0.5 mL (Device-1), 1.0 mL (Device-2), 2.0 mL (Device-3), 3.0 mL (Device-4), and 4.0 mL (Device-5). With increasing the volume of coating ink solution while maintaining a low scattering effect, the devices showed a trend of decreasing (increasing) transmission (absorption) in the UV spectral range, which was attributed to the strong UV light absorption of the employed $Cs_3Cu_2Cl_5$ perovskite NDs **(Figure 4.3e)**. Only a slight scattering effect can be visualized when the coating ink solution volume reached 4.0 mL (**Figure 4.3e**, **Figure 4.4, 4.5**). Both the UV-only absorption behavior of the $Cs_3Cu_2Cl_5$ NDs and low light scattering of the NDs/PMDS composite devices warranted a high average visible transmittance (AVT) value of > 85% for all the fabricated devices, demonstrating a superior visible transparency property (**Figure 4.3e**). The PL spectral profiles of all the devices showed a single emission peak centered at 527 nm (**Figure 4.3f**), in good accordance with the emission spectrum of the dilute NDs hexane solution (**Figure 4.1e**). Moreover, the PL peak intensity increased proportionally as increasing the coating volume (*i.e.*, the amount of coated $Cs_3Cu_2Cl_5$ NDs) (**Figure 4.3f**), further confirming a negligible level of emitter aggregation in the fabricated devices.[20, 48]

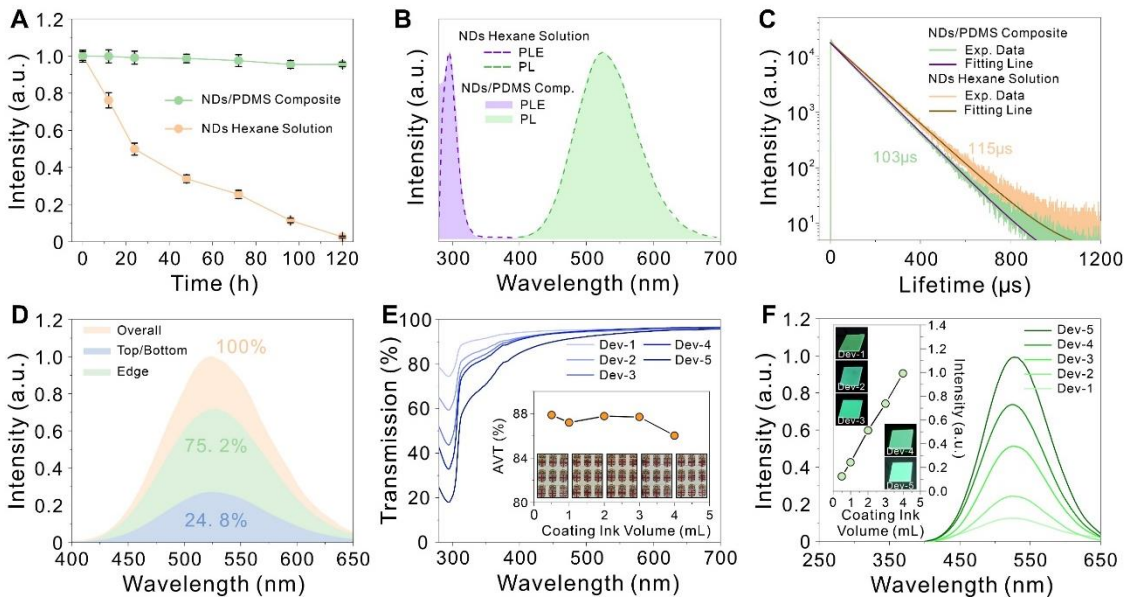

Figure 4.3. (a) Normalized PL intensity evolutions of a $Cs_3Cu_2Cl_5$ NDs hexane solution and a $Cs_3Cu_2Cl_5$ NDs/PDMS composite device as a function of time under ambient conditions. **(b)** Photoluminescence excitation (PLE) and photoluminescence (PL) spectra of $Cs_3Cu_2Cl_5$ NDs hexane solution and $Cs_3Cu_2Cl_5$ NDs/PDMS composite device. **(c)** Time-resolved PL decay curves of a NDs/PDMS composite device and a NDs hexane solution. **(d)** PL spectra collected from the top/bottom surfaces, the edge and the total $Cs_3Cu_2Cl_5$ NDs/PDMS composite device (the device dimension of 4.0 cm × 4.0 cm × 0.1 cm). **(e)** Transmission spectra of a series of $Cs_3Cu_2Cl_5$ NDs/PDMS composite devices with different coating volume of NDs ink solution. Inset: The corresponding average visible transmittance (AVT) and photographs (under ambient light) of the $Cs_3Cu_2Cl_5$ NDs/PDMS devices. **(f)** PL spectra with relative intensity of the series of $Cs_3Cu_2Cl_5$ NDs/PDMS devices. Inset: The PL peak intensity and photographs (under UV light) the corresponding devices coated with different volume of NDs ink solution.

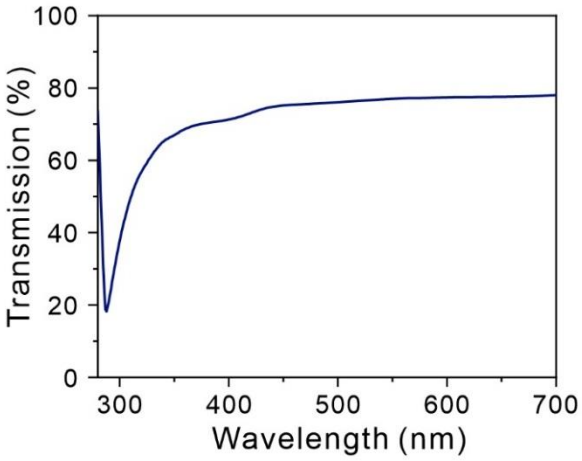

Figure 4.4. Transmission spectrum of the $Cs_3Cu_2Cl_5$ NDs/PDMS composite device ultrasonic spray coated with 6.0 mL NDs coating ink.

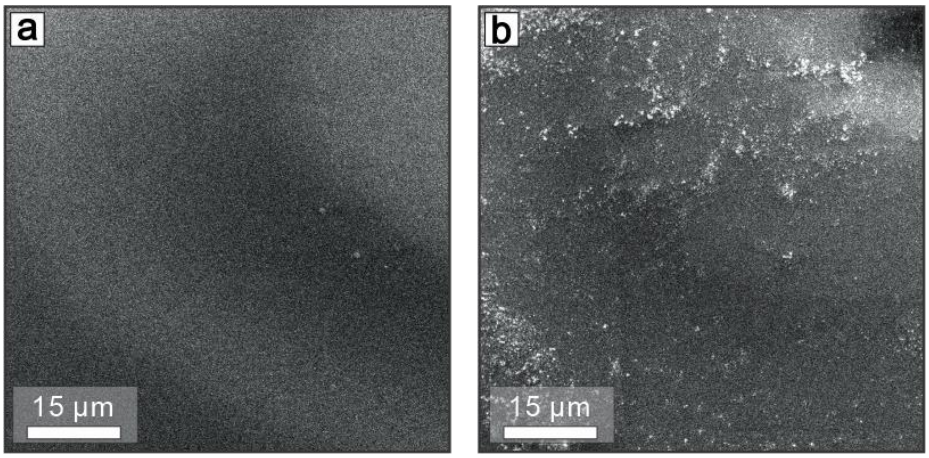

Figure 4.5. SEM images of $Cs_3Cu_2Cl_5$ NDs/PDMS composite film coated with 4.0 mL **(a)** and 6.0 mL **(b)** NDs coating ink solution.

4.4 Luminescent solar concentrators/luminescent down-shifting layer simulation and performance characterization

We used Monte Carlo (MC) ray-tracing simulation to evaluate the photon propagation performance of $Cs_3Cu_2Cl_5$-NDs/PDMS composite devices. A logic flow of the MC simulation for LSC and LDS is presented in **Scheme 4.3, 4.4** in the **Method**. To achieve statistically significant simulation results, we set 12,000 incident photons (wavelength

of 305 nm) to hit the top surface of the devices (cuboid slab dimension: 4.0 cm × 4.0 cm × 0.1 cm; refractive index, n = 1.43, taken from the refractive index of PDMS). A $Cs_3Cu_2Cl_5$-NDs coating layer with a thickness of ~2.5-20.0 μm was considered in the MC simulation. The experimentally measured device absorption spectra were used as the input absorption spectral profiles (**Figure 4.6**). We quantitatively traced incident photons after they hit the device top surface using the photon tracking counters in the MC model. For the MC simulations of LSC devices, when the coating volume increased from 0.5 mL to 4.0 mL, the edge-emitted photons increased from 2.1%, 4.2%, 6.3%, 8.5%, to 10.6% of the total incident photons (**Figure 4.7a**). Meanwhile, the transmitted (absorbed) photons gradually decreased (increased) from 94.0% to 78.3% (from 3.6% to 19.5%). And the fraction of the reflected and scattered photon loss was kept in a low range of 2.1 - 2.4% (**Figure 4.7b**), consistent with the experimental observations with minimal scattering signals (**Figure 4.3e, f**). The fates of ND-processed photons (absorbed and emitted photons by the NDs) were also analyzed and shown in **Figure 4.7c**. While the fractions of escaped (through escape cone of top/bottom surfaces of the devices) and lost photons were maintained at similar levels of ~19% and ~25%, respectively, the collected photons from the edge windows of the devices remained a high fraction of ~56%.

The MC ray-tracing simulation results for the LDS layers are shown in **Figure 4.7d-f**. The portion of collected photons at the bottom surface of the LDS devices increased from 2.7% to 14.2% as the coating volume increased from 0.5 mL to 4.0 mL (**Figure**

4.7d). The statistical result of the first photon contacting process of the LDS layers is similar to the result of the LSC devices. The transmitted (absorbed) photons decreased (increased) from 93.8% to 77.1% (from 3.8% to 20.7%) while increasing the amount of coated $Cs_3Cu_2Cl_5$-NDs (**Figure 4.7e**). At the same time, the statistical result for the fates of the photon behavior for LDS layers is shown in **Figure 4.7f**. For the emitted green photons down-shifted by the $Cs_3Cu_2Cl_5$-NDs, the portion of the escaped photon (from the top and edge windows) maintained at a low level of ~11%, and the fraction of lost photons (through attenuation) kept at ~18% of the total down-shifted photons. The bottom emitted photon kept at a higher level of ~71%. The relatively low level of photon loss can be largely attributed to the re-absorption free characteristic of the $Cs_3Cu_2Cl_5$ NDs. Overall, the MC simulation combined with the experimental results revealed that the ND-based LSC and LDS exhibited a consistent and high light-trapping efficiency, suggesting a superior property of the $Cs_3Cu_2Cl_5$ perovskite ND for UV light harvesting, down-converting, and trapping performance for the subsequent PV-based energy-conversion utilization.

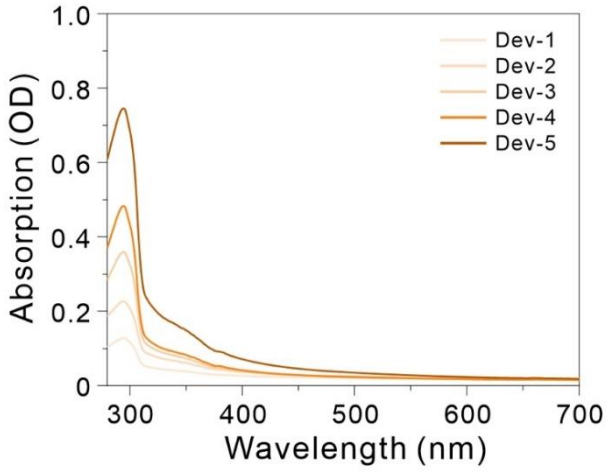

Figure 4.6. Absorption spectra of the five $Cs_3Cu_2Cl_5$ NDs/PDMS composite devices with coated with different volumes of NDs ink solution (8.0 wt%): 0.5 mL (Device-1), 1.0 mL (Device-2), 2.0 mL (Device-3), 3.0 mL (Device-4), and 4.0 mL (Device-5).

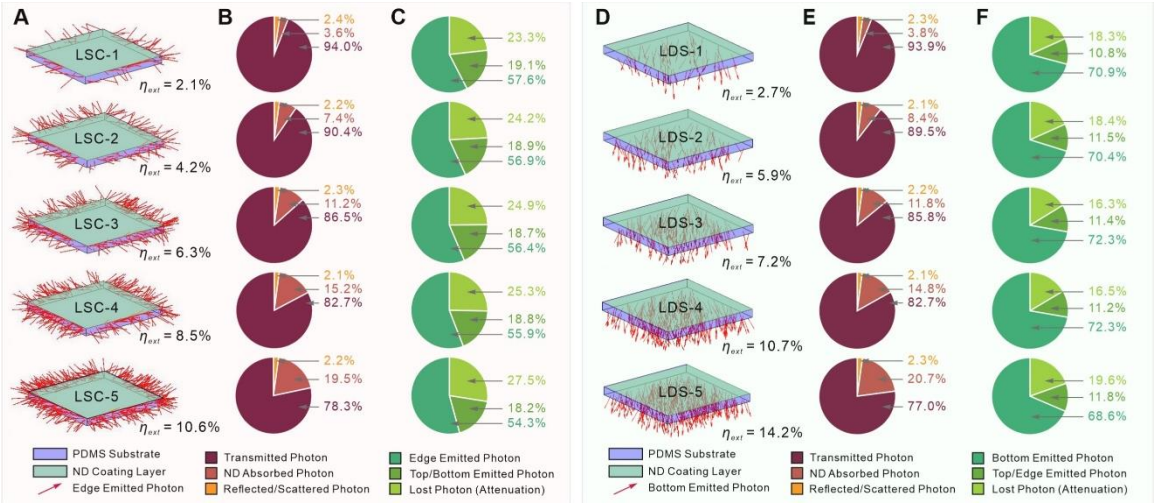

Figure 4.7. (a, d) Visualizations of the Monte-Carlo ray-tracing simulation (MC simulation) for the $Cs_3Cu_2Cl_5$ NDs/PDMS composite devices serving as LSC **(a)** and LDS **(d)** devices. The arrows represent the photon output from the edge (bottom) regions of the LSC (LDS) devices. **(b, e)** Pie charts of incident photon fractions after hitting the surface of the LSC **(b)** and LDS **(e)** devices. **(c, f)** Pie charts of the fates of the absorbed photons for the LSC **(c)** and LDS **(f)** devices.

Next, we carried out electro-optical measurements to evaluate the performances of the $Cs_3Cu_2Cl_5$ NDs/PDMS devices used as either LSC or LDS layer to the attached Si-PV cells (**Figure 4.8**). The working principle of the LSC-PV device is shown in **Figure 4.8a**. The internal optical efficiency (η_{int}, the ratio of the edge-collected photon flux and the total absorbed photon flux) of the five LSC devices were measured to be 58.1% (LSC-1), 56.2% (LSC-2), 56.3% (LSC-3), 55.5% (LSC-4) and 54.1% (LSC-5) under 305 nm light illumination (**Figure 4.9**). The slightly decreasing η_{int} values across all the devices suggests that increasing the coating volume has a minimal impact on the photon scattering effects. These findings are consistent with the device transmission/emission measurements (**Figure 4.3e and f**) and the MC simulation results (**Figure 4.7a-c**). In contrast, the external optical efficiency (η_{ext}, the ratio of the edge-collected photon flux and the total incident photon flux) showed a continuous increase from 2.1±0.4% (LSC-1), 4.2±0.6% (LSC-2), 6.4±0.4% (LSC-3), 8.4±0.5% (LSC-4) to 10.9±0.8% (LSC-5) (**Figure 4.8b**), in line with the MC simulation prediction as well as analytical mode simulation results (**Figure 4.7a** and **Figure 4.8b**, see simulation details in **Method**). Further, we coupled commercial Si-PV cell onto the edge of the LSC devices and measured the current-density (*J*-*V*) plots for each LSC-PV constructs as well as the standalone Si-PV as reference under 305 nm UV light illumination (see the measurement details in **Method**). The short-current densities of the reference Si-PV and LSC-PV systems were obtained to be 0.135 mA/cm^2 (Si-PV), 0.074 mA/cm^2 (LSC-1-PV), 0.138 mA/cm^2 (LSC-2-PV), 0.218 mA/cm^2 (LSC-3-PV), 0.287 mA/cm^2 (LSC-4-PV), and 0.375 mA/cm^2 (LSC-5-PV) (**Figure 4.8c**). The external optical efficiency

(η_{ext}) calculated based on the *J-V* curve measurements were consistent with the values obtained from the optical measurements as well as the MC simulation (**Figure 4.10**). These results showed that the integrated LSC-PV systems can outperform the standalone Si-PV cell for UV light harvesting and conversion when enough $Cs_3Cu_2Cl_5$ NDs was incorporated to the LSC device.

To examine the possibility of applying $Cs_3Cu_2Cl_5$ perovskite NDs for LDS devices, we attached the NDs/PDMS films onto Si-PV cells to construct an LDS-PV system (**Figure 4.8d**). To minimize the total internal reflection, an index matching gel (refractive index of 1.52) was applied at the interface between NDs/PDMS LDS layer and Si-PV cell (**Figure 4.8d**). Under the simulated solar illumination using a sunlight simulator (AM = 1.5), the short current density of the attached Si-PV cell showed a small increase from 16.4 mA/cm^2 (reference Si-PV), 16.5 mA/cm^2 (LDS-1-PV), 16.6 mA/cm^2 (LDS-2-PV), 16.8 mA/cm^2 (LDS-3-PV), 17.0 mA/cm^2 (LDS-4-PV) to 17.3 mA/cm^2 (LDS-5-PV) (**Figure 4.8e**). This limited short-current-density enhancement was mainly due to the small portion of UVB and UVC photons of the total solar spectrum (~0.05% of the total solar photons). However, when the LDS-PV systems were irradiated using a 305 nm UV light source, a maximum of 73% enhancement of the short-current-density can be obtained from 0.137 mA/cm^2 (reference standalone Si-PV), 0.163 mA/cm^2 (LDS-1-PV), 0.178 mA/cm^2 (LDS-2-PV), 0.195 mA/cm^2 (LDS-3-PV), 0.216 mA/cm^2 (LDS-4-PV) to 0.237 mA/cm^2 (LDS-5-PV) (**Figure 4.8f**). Taking together, our results unambiguously revealed that the $Cs_3Cu_2Cl_5$ NDs-based LSC or LDS photon-managing

devices can greatly enhance the high-energy UV photon harvesting and power conversion through effective photon concentrating and/or energy down-shifting processes.

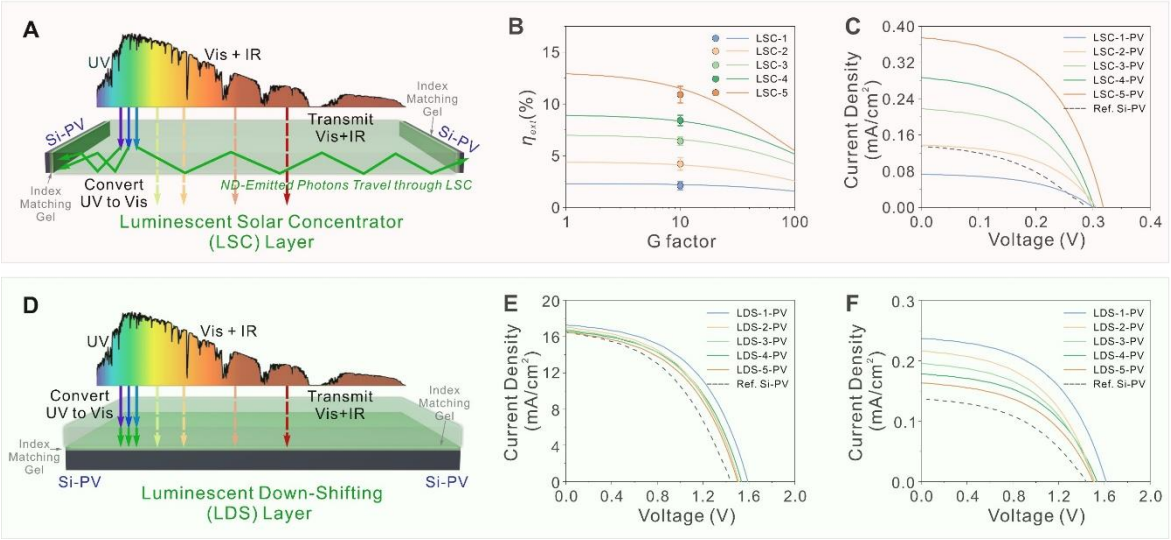

Figure 4.8. (a) Schematic demonstration of the working principle of an LSC device. **(b)** Experimental (spheres) and simulated (lines) η_{ext} for the $Cs_3Cu_2Cl_5$ NDs/PDMS composite LSC devices coated with different amount of $Cs_3Cu_2Cl_5$ NDs coating ink solution. Evolutions of the η_{ext} as a function of G factor under 305 nm light excitation. **(c)** Experimentally measured *J-V* curves of the LSC devices under 305 nm light excitation. **(d)** Schematic demonstration of the working principle of an LDS device. **(e, f)** Experimentally measured *J-V* curves of the $Cs_3Cu_2Cl_5$ NDs/PDMS composite LDS devices coated with different amount of $Cs_3Cu_2Cl_5$ NDs coating ink solution under solar simulator **(e)** and 305 nm light **(f)** excitations.

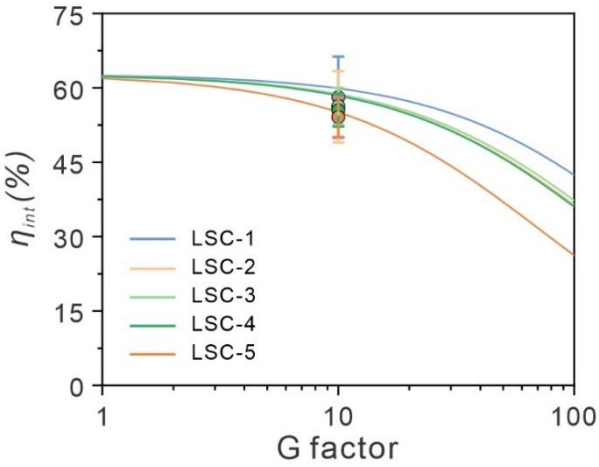

Figure 4.9. Experimental (spheres) and simulated (lines) η_{int} for the $Cs_3Cu_2Cl_5$ NDs/PDMS composite LSC devices coated with different amount of $Cs_3Cu_2Cl_5$ NDs coating ink solution. Evolutions of the η_{int} as a function of G factor.

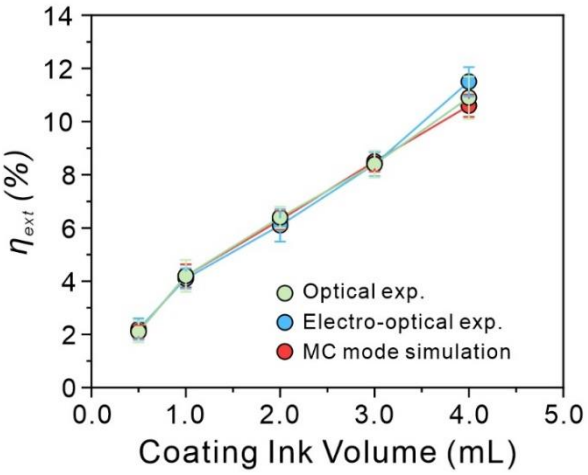

Figure 4.10. η_{ext} (under 305 nm single wavelength excitation) determined by the optical characterizations (based on the PL QYs), electrical-optical measurements (extracted from the corresponding *J-V* curves), and the MC ray-tracing simulations for the $Cs_3Cu_2Cl_5$ NDs/PDMS devices fabricated using different volumes of the $Cs_3Cu_2Cl_5$ coating ink solution (8.0 wt%).

4.5 Luminescent solar concentrators/luminescent down-shifting layer in space applications

Finally, we explored the feasibility of implementing $Cs_3Cu_2Cl_5$ NDs-based photon-managing devices for the space-based solar power station through simulation studies. **Figure 4.11a** shows the comparison of solar spectra in space (AM = 0) and on earth (AM = 1.5). The integrated solar irradiation intensity for the UV portion (*i.e.*, 200-400 nm) of the spectrum is ~ 3.5-fold increase in space as compared to that on the earth surface due to the strong UV absorption and scatting effects by the ozone (**Figure 4.11a**, **insets**).[17, 18] In order to compare the LSC or LDS device performance in space and on earth, we simulated the device performances using incident solar spectra for both cases (see simulation details in **Method**), and introduced an enhancement factor (*EF*), which is represented as follows:

$$EF = \frac{\eta_{ext,\ AM=0} - \eta_{ext,\ AM=1.5}}{\eta_{ext,\ AM=1.5}} \quad (1)$$

Where $\eta_{ext,\ AM=0}$ and $\eta_{ext,\ AM=1.5}$ represented the external optical efficiencies of the device (either applied as LSC or LDS) under AM = 0 and AM = 1.5 solar radiation, respectively. As shown in **Figure 4.11b**, the *EF* for the LSC devices increased from 4.3 to 31.9 as increasing the length of the device (with a cuboidal geometry) from 1.0 cm to 100 cm or decreasing the volume of $Cs_3Cu_2Cl_5$ NDs coating ink solution from 4.0 mL to 0.04 mL. For the LDS device simulation, a universal enhancement in device performance with the $EF > 2.4$ was obtained regardless of the dimensions of the LDS device simulated in this study (**Figure 4.11c**). A maximal *EF* value of over 6.0 can be obtained when coating a thin layer of the $Cs_3Cu_2Cl_5$ NDs/PDMS film (coating solution

volume of < 0.1 mL) on the LDS device substrate. Our simulation results show that $Cs_3Cu_2Cl_5$ NDs-based LSC/LDS devices are ideal for space-based solar power systems and offer enhanced UV photon harvesting/utilization compared to conventional use on earth.

We developed high-performance $Cs_3Cu_2Cl_5$ perovskite NDs-based photon-managing devices that can serve as LSC or LDS layers for PV cells. These perovskite NDs offer strong UV- absorption, high PL QYs of > 80%, and a large Stokes shift with re-absorption-free behaviors, making them ideal for high-energy UV photon harvesting and conversion in space-based solar power applications. The $Cs_3Cu_2Cl_5$-NDs/PDMS composite devices showed low photon scattering and high visible light transparency. Both experimental results and simulations demonstrated that when attached to Si-PV cells, the LSC or LDS devices outperformed standalone Si-PV systems for high-energy UV photon harvesting and power conversion. Our study suggests that using lead-free Cu-based perovskite nanomaterials for energy harvesting in space is a promising direction to explore.

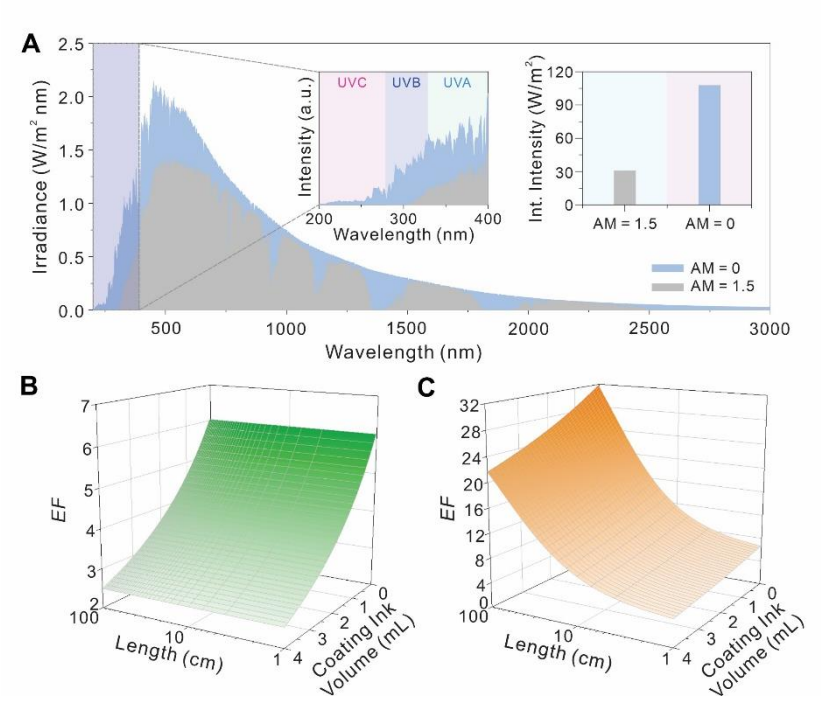

Figure 4.11. (a) The solar radiation spectra with AM = 0 (blue) and AM = 1.5 (grey). Insets: zoom-in spectra for the UV spectral region (left), and the integrated (Int.) solar radiation intensity in the UV wavelength range from 200 nm to 400 nm. **(b, c)** 3D plots of the enhancement factor (*EF*) evolutions as functions of the device length and the volume of the $Cs_3Cu_2Cl_5$ NDs coating ink solution for LSC **(b)** and LDS **(c)** devices.

Method

Chemicals

Cesium carbonate (Cs_2CO_3, 99.9%), copper(II) acetate (99.99%), hydrochloric acid (HCl, 37%), 1-octadecene (ODE, 90%), oleylamine (OAm, 70%), oleic acid (OA, 90%), and hexane (anhydrous, 95%) were purchased from Sigma-Aldrich. Norland Optical Adhesive (NOA) 68 polymer adhesive was purchased by Norland Products Inc. Sygrad 184 Polydimethylsiloxane (PDMS) was purchased by Gelest Inc. All chemicals were used without further purification.

Preparation of OAm-HCl precursors

The OAm-HCl precursors were prepared following a reported procedure.[41] For the preparation of OAm-HCl, 1.5mL of HCl was mixed with 15mL of OAm in a glass vial. The vial was placed on a hot plate at 120 °C, and stirred for 2 hours under nitrogen (N_2) flow. Then the solution was heated up to 150 °C and maintained at this temperature for another one hour. Finally, the solution was cooled down to room temperature (RT) and stored under N_2.

Preparation of $Cs_3Cu_2Cl_5$ perovskite nanodisks (NDs)

0.1 mmol of $Cu(OAc)_2$, 0.05 mmol of Cs_2CO_3, 0.5mL of OAm, and 5 mL of ODE were added into a 25 mL three-necked flask and heated to 200 °C for 30 minutes under N_2 protection. The yellow transparent solution was obtained. Then, the temperature was cooled down to 120 °C, and 0.5 mL of OAm-HCl precursor was swiftly injected into the

mixture. The reaction was kept for 10 seconds before a cold water bath was used to cool down the reaction to RT. Finally, the obtained $Cs_3Cu_2Cl_5$ NDs were purified by two rounds of centrifugation at 6000 rpm for 5 minutes. The precipitates were collected and redispersed into hexane solution.

Fabrication of $Cs_3Cu_2Cl_5$ NDs/PDMS composite devices:

The purified $Cs_3Cu_2Cl_5$ NDs hexane solution was added into a mixture of Sygrad 184 PDMS viscus oligomer and Sygrad 184 curing agent. The weight ratio of the oligomer and curing agent was 1:1. The mixture was degassed by stirring and vacuuming for 1 h to form a clear and homogeneous solution. Hexane was added to the NDs/PDMS mixture solution with a volume ratio of 10:1. The NDs concentration in the final mixture was adjusted to 8.0 wt% (the weight ratio between NDs and PDMS). The NDs ink solution with different volumes (0.5 mL, 1.0 mL, 2.0 mL, 3.0 mL, and 4.0 mL) were ultrasonic spray coated onto the preheated PDMS substrate (preheating temperature: 70°C). The distance between the ultrasonic spray nozzle and substrate was set to 10 cm. After that, another 1 mL of PDMS/hexane ink solution (volume ratio of 1:10) was ultrasonic spary coated onto the substrates. Five mins after spary coating, the fabricated device was annealed at 60 °C for 30 min. The obtained NDs/PDMS composite devices were cut into a desired dimension for the characterizations as descibed in the maintext.

UV-Vis absorption and transmission measurements

UV-Vis absorption spectra and transmission spectra were performed using an Agilent

Technologies Cary 5000 UV-Vis-NIR Spectrophotometer. The NDs/PDMS composite devices were placed onto the solid film holder and a pure PDMS film with the same dimension was used as reference for the absorption measurements. For the transmission measurements, atmosphere was used as the referenece.

Photoluminescence (PL) and PL quantum yield (PL QY) measurements

The PL spectra and PL QYs were measured using an Edinburgh Instruments Fluorescence Spectrometer FS5. The FS5 spectrometer integrated with a built-in integrating sphere was used to measure the sample PL QYs.

X-ray Diffraction (XRD) measurements

XRD pattern was acquired using a Bruker D8 Discovery 2D X-ray Diffractometer equipped with a Vantec 500 2D area detector operating with Cu Kα radiation (λ = 1.541 Å). The $Cs_3Cu_2Cl_5$ NDs sample in a hexane solution was drop-casted on glass slides and evaporated at ambient conditions.

Scanning electron microscope (SEM) measurements

SEM measurements were carried out on Thermo Scientific Quattro S ESEM operated at 10kV on a solid-sample holder.

Transmission electron microscopy (TEM) measurements

TEM measurements were performed on a JEOL 2100F operated at 200 kV. The

$Cs_3Cu_2Cl_5$ perovskite NDs sample in a hexane solution (~10 μL) was dropped onto a 300-mesh copper TEM grid and dried at ambient conditions.

Current density-voltage (*J-V*) curve characterizations

The *J-V* characteristics were measured using a 2400 source meter (Keithley, USA) under simulated one-sun illumination (AM = 1.5, 100 Mw/cm^2), which is generated by an Oriel Sol3A Class AAA solar simulator (Newport, USA).

LSC-PV fabrication and characterization: The fabrication procedure of single-junction LSC-PV device followed a literature approach:[48] a polycrystalline silicon photovoltaic mini cell (Si-PV, from Sunnytech Mini Small Solar Panel) was coupled to one of the four edges of the $Cs_3Cu_2Cl_5$ NDs/PDMS LSC device by using the index matching gel of NOA 68 polymer adhesive (refractive index: 1.52). Black tape was applied to cover the other three device edges, bottom of the LSC, and the excess area of the solar cell (**Scheme 4.2a**). The *J–V* curves of the coupled LSC-PV systems and the standalone Si-PV were obtained using a voltage source meter (Keithley 236) in the range of -0.1 V to 1.0 V with a voltage step of 0.02 V.

LDS-PV fabrication and Characterization: The LDS-PV system was fabricated by attaching the $Cs_3Cu_2Cl_5$ NDs/PDMS LSC device to the top surface of the Si-PV cell using the index matching gel of NOA 68 polymer adhesive (refractive index: 1.52). The four edge areas of the LDS were covered by the black tape to absorb the edge emitted photons **(Scheme 4.2b)**. The *J–V* curves of the coupled LDS-PV systems and the

standalone Si-PV were obtained using a voltage source meter (Keithley 236) in the range of -0.1 V to 1.0 V with a voltage step of 0.02 V.

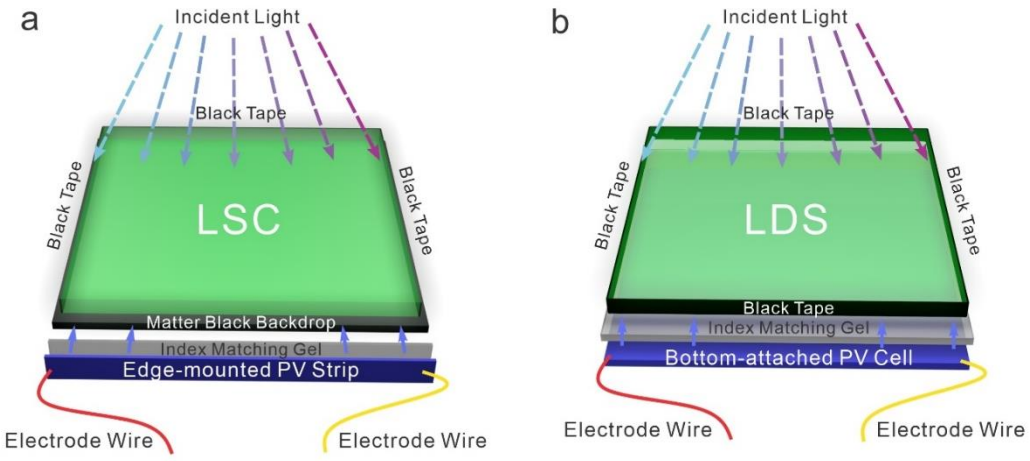

Scheme 4.2: Schematic illustration of the LSC-PV **(a)** and LDS-PV **(b)** systems for *J-V* curve measurements

Internal (η_{int}) and External optical efficiencies (η_{ext}) determined by optical measurements

We applied optical measurements to determine the optical efficiencies of the $Cs_3Cu_2Cl_5$ NDs/PDMS LSC device (4.0 cm × 4.0 cm × 0.1 cm, G = 10). The PL QY of the LSC edge emitted region was first determined by subtracting the total PL QY of the device by the PL QY of the top/bottom emitted region. This value was defined as the internal optical efficiency (η_{int}) of the LSC device, which is the ratio of the edge collected photon flux and the total absorbed incident photon. Further, we calculated the external optical efficiency (η_{ext}) as the ratio of the edge-collected photon flux and the total incident photon flux, which is described by the following equation:[48]

$$\eta_{ext} = \eta_{int} \times \eta_{abs} \quad (2)$$

In this equation, η_{abs} is the absorption ratio of the LSC device, which is the ratio of

the LSC captured photon and the total incident photon, described as:

$$\eta_{abs} = (1-T)(1-R) = (1-R)(1-e^{-\alpha_1 d}) \quad (3)$$

where, T is the transmission of the overall LSC device, α_1 is the absorption coefficient of the LSC device, d is the thickness of the LSC deivce, and R is the reflection coefficient of the air/LSC interface, described as:

$$R = \frac{(n-1)^2}{(n+1)^2} \quad (4)$$

where, n is the refractive index of the PDMS (n = 1.43).

External optical efficiencies (η_{ext}) determined by electro-optical measurements

The electro-optical measurements for the $Cs_3Cu_2Cl_5$ NDs/PDMS LSC devices were carried out based on the previous work.[48] The relationship between the power conversion efficiencies of a standalone PV (η_{PV}) and an LSC-PV device (η_{LSC_PV}) can be expressed as follows:

$$\eta_{LSC-PV} = \frac{\langle Q_{PL} \rangle}{\langle Q_S \rangle} \eta_{s,abs} \eta_{int} \eta_{PV} \quad (5)$$

$\langle Q_S \rangle$ and $\langle Q_{PL} \rangle$ are the averaged external quantum efficiencies (EQEs) of the PV devices over the sunlight incident wavelength range and the LSC emission wavelength range, respectively. $\eta_{s,abs}$ is the absorption ratio under the sunlight radiation. Following this equation, the η_{int} and η_{ext} of the LSC in the LSC-PV coupled devices can be expressed by the following equations:

$$\eta_{ext} = \frac{J_{SC,LSC-PV}\langle Q_S \rangle}{J_{SC} G \langle Q_{PL} \rangle} \quad (6)$$

$$\eta_{int} = \frac{\eta_{LSC-PV}\langle Q_S \rangle}{\eta_{s,abs}\eta_{PV}\langle Q_{PL} \rangle} = \frac{J_{SC,LSC-PV}\langle Q_S \rangle}{J_{SC}\eta_{s,abs} G \langle Q_{PL} \rangle} \quad (7)$$

J_{SC} and $J_{SC,LSC-PV}$ are the short-circuit current densities of the standalone PV and LSC-PV coupled system, respectively.

Average visible transmittance (AVT) calculation

The average visible transmittance (AVT) of a $Cs_3Cu_2Cl_5$ NDs/PDMS device can be calculated based on the following equation:[48]

$$AVT = \frac{\int T(\lambda)P(\lambda)S(\lambda)d\lambda}{\int P(\lambda)S(\lambda)d\lambda} \quad (8)$$

Where λ is the wavelength of the incident light, T(λ) is the transmittance of the device, P(λ) is the photopic response function of the human eye (photonic vision), and S(λ) is the normalized solar spectrum (AM = 1.5).

Monte Carlo ray-tracing simulation (MC simulation)

Firstly, the input parameters for the Monte Carlo ray-tracing simulation mode include:

- the total number of incident photons (*i.e.*, 12,000);
- the dimension of the LSC/LDS device substrate and coating layer (length, width, and thickness);
- the refractive index of the device substrate and the $Cs_3Cu_2Cl_5$ NDs coating layer material;
- the absorption coefficient of $Cs_3Cu_2Cl_5$ NDs, cumulative distribution functions (CDF) plot for PL spectra and PL QY of the $Cs_3Cu_2Cl_5$ NDs.

After that, we assign random x and y coordinates as initial position parameters for each

photon and collect all the position data to generate a photon database. Next, according to Fresnel Law, we randomly delete a certain number of input photons from the database, representing the scattering effect from the device surface. Then, we release a non-scattered photon into the main loop of the coating layer; $Cs_3Cu_2Cl_5$ NDs absorption coefficient spectrum and $Cs_3Cu_2Cl_5$ NDs concentration data can determine if the coating layer absorbs this photon. For the absorbed photon, we determine if this photon will be emitted by the $Cs_3Cu_2Cl_5$ NDs (according to the emission CDF plot and PL QY data). If not, the photon runs through the non-radiative decay channels of the $Cs_3Cu_2Cl_5$ NDs. If the photon can be absorbed and then emitted by the $Cs_3Cu_2Cl_5$ NDs, we further determine if the newly emitted photon will hit any surface (top/bottom/edge surfaces) of the coating layer. If it does not hit any surface, the photon is back to the initial emission determination step. If it hits a surface, the photon will be updated with a new set of location vector parameters to determine which surface it hits (*i.e.*, top/bottom or edge surface of the NDs coating layer). If the photon hits top or edge surface, based on the location vector and refracitve index of the coating layer material, we can determine whether the photon is reflected through the total internal reflection (TIR). If so, the photon moves back to the initial emission determination step. If not, the photon transmits through the top surface or edge surface. The photon tracing loop is closed and the transmitted position is recorded. The photon is counted as an escape cone lost photon. If the photon hits the bottom surface, according to the location vector, refractive index of the coating layer and substrate material, we need to decide if the TIR occurs. If so, the photon goes back to the emission determination step. If not, the photon

transmits into the substrate, and we record the transmitted position and move to the next step.

For LSC devices, when the transmitted photon goes into the substrate, we need to determine which surface the photon will hit. If the photon hits the edge surface, the photon is set to transmit through the edge surface of the substrate. The photon tracing loop is closed and the transmitted position is recorded. The photon is counted as one photon collected by edge-mounted PV strip. If the photon hits the bottom surface of the substrate, we need to consider if TIR occurs. If so, the photon reflects back into the substrate, and loops back to initial determination step for the photons transmitted into the substrate. If no TIR, the photon travels through the bottom surface of the substrate. The photon tracing loop is closed and the transmitted position is recorded. The photon is counted as an escape cone lost photon. If the photon hits the top surface of the substrate, we need to decide if TIR occurs. If so, the photon reflects back into the substrate, and loops back to initial determination step for the photons transmitted into the substrate. If not, the photon travels back into the coating layer and loops back to the initial emission determination step in the NDs coating layer.

For LDS devices, when the transmitted photon travel into the substrate, we need to determin which surface the photon will hit. If the photon hits the bottom surface, the photon is set to transmit through the bottom surface of the substrate. The photon tracing loop is closed and the transmitted position is recorded. The photon is counted as one

photon collected by the bottom-attached PV cell. If the photon hits the edge surface of the substrate, we need to consider if TIR occurs. If so, the photon reflects back into the substrate, and loops back to initial determination step for the photons transmitted into the substrate. If no TIR, the photon travels through the edge surface of the substrate. The photon tracing loop is closed and the transmitted position is recorded. The photon is counted as an escape cone lost photon. If the photon hits the top surface of the substrate, we need to decide if TIR occurs. If so, the photon reflects back into the substrate, and loops back to initial determination step for the photons transmitted into the substrate. If not, the photon travels back into the coating layer and loops back to the initial emission determination step in the NDs coating layer.

The main loop repeats until all the incident photons in the database are traced.

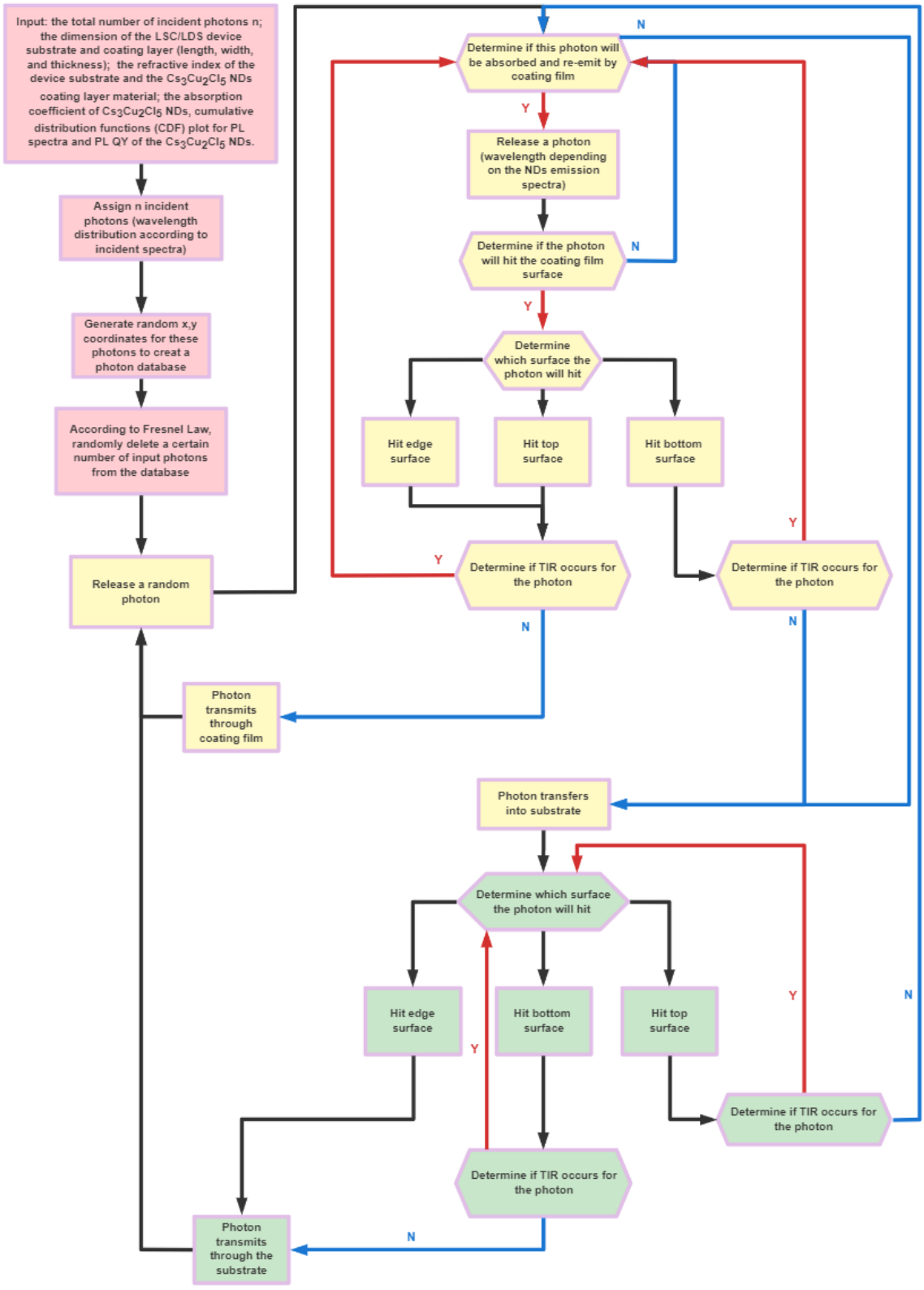

Scheme 4.3: Logic flow chart of the MC ray-tracing simulation for the $Cs_3Cu_2Cl_5$ NDs-based LSC device. The yellow blocks are the main loop region for the NDs coating layer, and the green blocks are the main loop region for the substrate, where individual photons are traced.

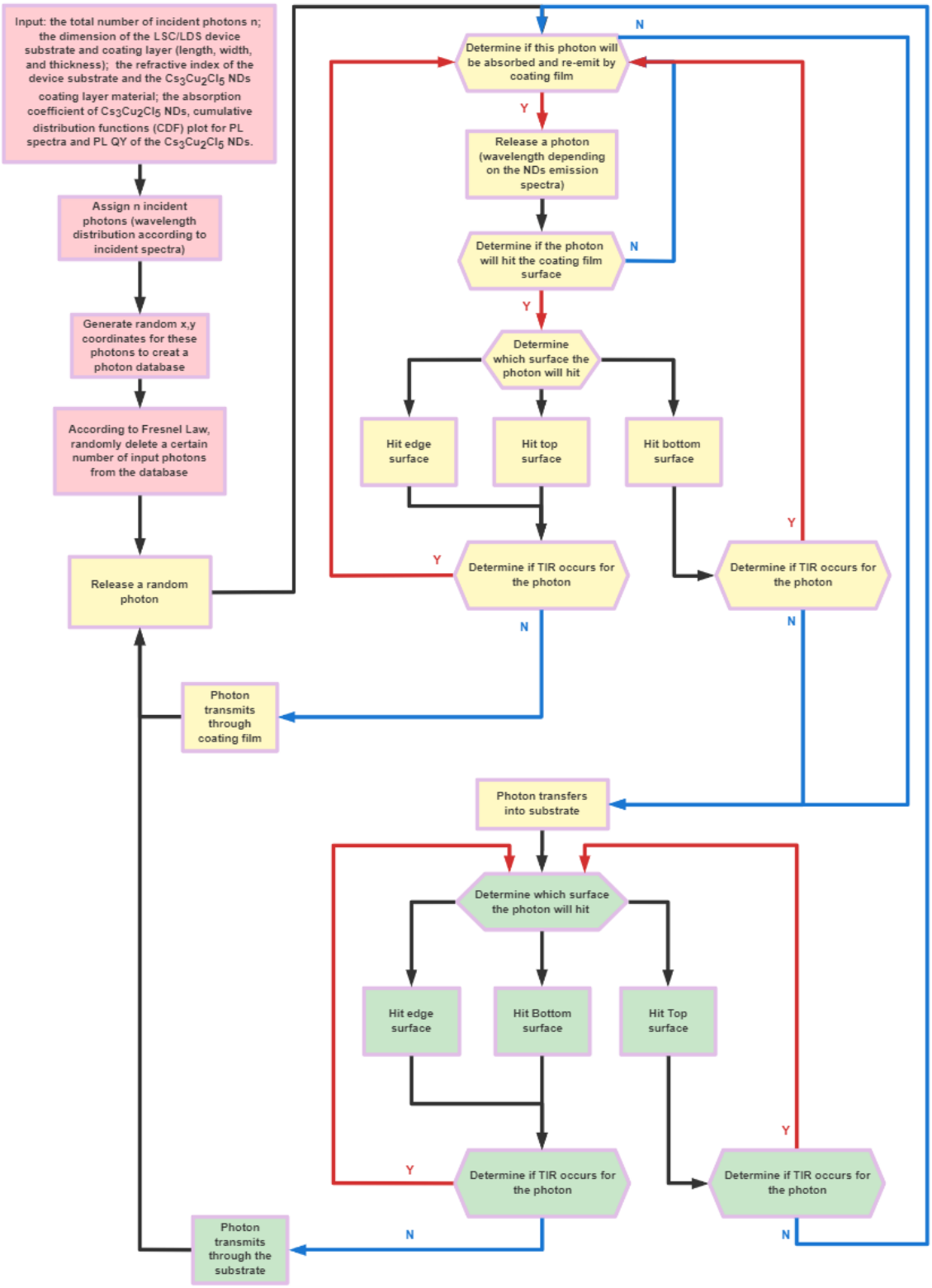

Scheme 4.4: Logic flow chart of the MC ray-tracing simulation for the $Cs_3Cu_2Cl_5$ NDs-based LDS device. The yellow blocks are the main loop region for the NDs coating layer, and the green blocks are the main loop region for the substrate, where individual photons are traced.

Analytical mode simulation

For LSC device simulation: The analytical mode simulation was developed based on previous studies. Following the procedure described in the literature,[20, 24] we determine the following parameters:[48]

$$< \alpha_1 >= -\frac{1}{d} ln\left(\frac{\int_{E_g}^{\infty} S_{in}(\lambda) e^{-\alpha(\lambda)d} d\lambda}{\int_{E_g}^{\infty} S_{in}(\lambda) d\lambda}\right) \quad (9)$$

Where $< \alpha_1 >$ is the average absorption coefficient among the incident light wavelength range, the obtained value can apply the α_1. α is the absorption coefficient of the $Cs_3Cu_2Cl_5$ NDs. λ is the wavelength of light. d is the thickness of the LCS or LDS coating layer. E_g is the bandgap of $Cs_3Cu_2Cl_5$ NDs. S_{in} is the spectral shape of incident light.

α_2 is the absorption coefficient at the wavelength of the emitted light, which can be replaced by the average value of $< \alpha_2 >$, which is defined as:

$$< \alpha_2 > = (d/(d + D)) \frac{\int S_{PL}(\lambda)\alpha(\lambda) d\lambda}{\int S_{PL}(\lambda) d\lambda} \quad (10)$$

Where S_{PL} is the spectral shape of the $Cs_3Cu_2Cl_5$ NDs emission, and α is the absorption coefficient of the $Cs_3Cu_2Cl_5$ NDs. λ is the wavelength of light. D is the thickness of the LCS or LDS substrate.

η_{trap_LSC} is the efficiency of light trapping into the LSC device, which is determined by the refrative index of the LSC matrix, which is:

$$\eta_{trap\_LSC} = \sqrt{1 - n^{-2}} = cos\theta_{esc} \quad (11)$$

Overall, the external optical efficiencies (η_{ext}) of the LSC device can be expressed as:

$$\eta_{ext} = (1-R)(1-T) \times \eta_{int} = \frac{(1-R)\left(1-e^{-\alpha_1 d}\right)\eta_{PL}\eta_{trap\_LSC}}{1+\beta\alpha_2(1-\eta_{PL}\eta_{trap\_LSC})} \quad (12)$$

Where β is geometry correction factor; η_{PL} is the PL QY of the emitters; R is the reflection coefficient of LSC surfaces; T is the transmission of the overall LSC device.

For β value determination, the initial value can be calculated based on the following equation:[7]

$$\beta = 1.4 + 0.5\left(\frac{l}{150}\right)^{0.5} \quad (13)$$

Where l is the edge length for a square-shaped device. This equation is relatively reliable for l = 0-2000 cm.[48]

For LDS device simulation: η_{trap_LDS} is the efficiency of light trapping into the LDS device, which is determined by the refrative index of the LDS matrix as expressed below:[27, 28]

$$\eta_{trap\_LDS} = \frac{1}{2}(1+\sqrt{1-n^{-2}}) \quad (14)$$

According to the previous work,[11] external optical efficiencies (η_{ext}, the ratio of the bottom-collected photon flux and the total incident photon flux) of the LDS layer can be expressed as:

$$\eta_{ext} = (1-R)(1-T) \times \eta_{int} = \frac{(1-R)\left(1-e^{-\alpha_1 d}\right)(1-\alpha_{re\_oc})\eta_{PL}\eta_{trap\_LSC}}{1-\eta_{PL}(\alpha_{re\_IC}\left(1-\eta_{trap_{LSC}}\right)+\alpha_{re\_OC}\eta_{trap\_LSC})} \quad (15)$$

Where, α_{re} is the absorbance at the wavelength of the emitted light, which can be

replaced by the average value $< \alpha_{re} >$ as expressed below:

$$< \alpha_{\mathrm{re}} > = \frac{\int S_{PL}(\lambda) L\alpha(\lambda) d\lambda}{\int S_{PL}(\lambda) d\lambda} \quad (16)$$

Where, L is the a characteristic length of the escape cone. For simplicity, we choose $L = D/2$ and $L = l$ (l is the edge length for a square-shaped device) for the light emitted inside and outside of the escape cone, respectively. And α_{re_IC} and α_{re_oc} are the absorbance at the wavelength of the emitted light inside and outside of the escape cone, respectively.

Reference

1. Kong, M.; Kang, C. H.; Alkhazragi, O.; Sun, X.; Guo, Y.; Sait, M.; Holguin-Lerma, J. A.; Ng, T. K.; Ooi, B. S., Survey of Energy-autonomous Solar Cell Receivers for Satellite–air–ground–ocean Optical Wireless Communication. *Progress in Quantum Electronics* **2020,** *74*.

3. Rahman, M. M.; Selvaraj, J.; Rahim, N. A.; Hasanuzzaman, M., Global Modern Monitoring Systems for PV Based Power Generation: A Review. *Renewable and Sustainable Energy Reviews* **2018,** *82*, 4142-4158.

4. Ahmed, R.; Sreeram, V.; Mishra, Y.; Arif, M. D., A Review and Evaluation of the State-of-the-art in PV Solar Power Forecasting: Techniques and Optimization. *Renewable and Sustainable Energy Reviews* **2020,** *124*.

5. Jordan, D. C.; Kurtz, S. R., Photovoltaic Degradation Rates-an Analytical Review. *Progress in Photovoltaics: Research and Applications* **2013,** *21* (1), 12-29.

6. Vernay, C.; Pitaval, S.; Blanc, P., Review of Satellite-based Surface Solar Irradiation Databases for the Engineering, the Financing and the Operating of Photovoltaic Systems. *Energy Procedia* **2014,** *57*, 1383-1391.

7. Yang, Y.; Zhang, Y.; Duan, B.; Wang, D.; Li, X., A Novel Design Project for Space Solar Power Station (SSPS-OMEGA). *Acta Astronautica* **2016,** *121*, 51-58.

8. Li, W., Overview on Space Solar Power Station. *Advances in Astronautics Science and Technology* **2022,** *5* (1), 1-2.

9. Yermoldina, G. T.; Suimenbayev, B. T.; Sysoev, V. K.; Suimenbayeva, Z. B., Features of Space Solar Power Station Control System. *Acta Astronautica* **2019,** *158*, 111-120.

10. Glaser, P. E., Power From the Sun: Its Future. *Science* **1968,** *162* (3856), 857-61.

11. Li, J.; Aierken, A.; Liu, Y.; Zhuang, Y.; Yang, X.; Mo, J. H.; Fan, R. K.; Chen, Q. Y.; Zhang, S. Y.; Huang, Y. M.; Zhang, Q., A Brief Review of High Efficiency III-V Solar Cells for Space Application. *Frontiers in Physics* **2021,** *8*.

12. Sysoev, V. K.; Pichkhadze, K. M.; Feldman, L. I.; Arapov, E. A.; Luzyanin, A. S., Concept Development for a Space Solar Power Station. *Solar System Research* **2012,** *46* (7), 548-554.

13. Meng, X.-L.; Xia, X.-L.; Sun, C.; Hou, X.-B., Adjustment, Error Analysis and Modular Strategy for Space Solar Power Station. *Energy Conversion and Management* **2014,** *85*, 292-301.

14. Fan, G.; Duan, B.; Zhang, Y.; Li, X.; Ji, X., Full-spectrum Selective Thin Film Based Photonic Cooler for Solar Cells of Space Solar Power Station. *Acta Astronautica* **2021,** *180*, 196-204.

15. Fan, G.; Zhang, Y.; Ji, X.; Yang, Y., Two-Layer Ring Truss-Based Space Solar Power Station. *Energies* **2022,** *15* (8).

16. Cable, T. L.; Sofie, S. W., A Symmetrical, Planar SOFC Design for NASA's High Specific Power Density Requirements. *Journal of Power Sources* **2007,** *174* (1), 221-227.

17. Tu, Y.; Wu, J.; Xu, G.; Yang, X.; Cai, R.; Gong, Q.; Zhu, R.; Huang, W., Perovskite Solar Cells for Space Applications: Progress and Challenges. *Adv Mater* **2021,** *33* (21), e2006545.

18. Fontenla, J. M.; Harder, J.; Livingston, W.; Snow, M.; Woods, T., High-resolution Solar Spectral Irradiance from Extreme Ultraviolet to Far Infrared. *Journal of Geophysical Research* **2011,** *116* (D20).

19. Dobber, M.; Voors, R.; Dirksen, R.; Kleipool, Q.; Levelt, P., The High-Resolution Solar Reference Spectrum between 250 and 550 nm and Its Application to Measurements with the Ozone Monitoring Instrument. *Solar Physics* **2008,** *249* (2), 281-291.

20. Meinardi, F.; Colombo, A.; Velizhanin, K. A.; Simonutti, R.; Lorenzon, M.; Beverina, L.; Viswanatha, R.; Klimov, V. I.; Brovelli, S., Large-area Luminescent Solar Concentrators Based on 'Stokes-shift-engineered' Nanocrystals in a Mass-polymerized PMMA Matrix. *Nature Photonics* **2014,** *8* (5), 392-399.

21. Wang, J.; Yuan, Y.; Schneider, J.; Zhou, W.; Zhu, H.; Cai, T.; Chen, O., Quantum Dot-based Luminescent Solar Concentrators Fabricated through the Ultrasonic Spray-Coating Method. *ACS Appl Mater Interfaces* **2022,** *14* (36), 41013-41021.

22. Klimov, V. I.; Baker, T. A.; Lim, J.; Velizhanin, K. A.; McDaniel, H., Quality Factor of Luminescent Solar Concentrators and Practical Concentration Limits Attainable with Semiconductor Quantum Dots. *ACS Photonics* **2016,** *3* (6), 1138-1148.

23. Zhou, Y.; Benetti, D.; Fan, Z.; Zhao, H.; Ma, D.; Govorov, A. O.; Vomiero, A.; Rosei, F., Near Infrared, Highly Efficient Luminescent Solar Concentrators. *Advanced Energy Materials* **2016,** *6* (11).

24. Cai, T.; Wang, J.; Li, W.; Hills-Kimball, K.; Yang, H.; Nagaoka, Y.; Yuan, Y.; Zia, R.; Chen, O., Mn^{2+}/Yb^{3+} Codoped $CsPbCl_3$ Perovskite Nanocrystals with Triple-Wavelength Emission for Luminescent Solar Concentrators. *Adv Sci (Weinh)* **2020,** *7* (18), 2001317.

25. Wang, J.; Yuan, Y.; Zhu, H.; Cai, T.; Fang, Y.; Chen, O., Three-dimensional Macroporous Photonic Crystal Enhanced Photon Collection for Quantum Dot-based Luminescent Solar Concentrator. *Nano Energy* **2020,** *67*.

26. Kalytchuk, S.; Gupta, S.; Zhovtiuk, O.; Vaneski, A.; Kershaw, S. V.; Fu, H.; Fan, Z.; Kwok, E. C. H.; Wang, C.-F.; Teoh, W. Y.; Rogach, A. L., Semiconductor Nanocrystals as Luminescent Down-Shifting Layers To Enhance the Efficiency of Thin-Film CdTe/CdS and Crystalline Si Solar Cells. *The Journal of Physical Chemistry C* **2014,** *118* (30), 16393-16400.

27. Song, P.; Hase, S.; Zhao, S.; Xu, Z.; Iso, Y.; Isobe, T., Feasibility of Emission-Enhanced CsPbCl3 Quantum Dots Co-Doped with Mn^{2+} and Er^{3+} as Luminescent Downshifting Layers in Crystalline Silicon Solar Modules. *ACS Applied Nano Materials* **2022,** *5* (2), 2522-2531.

28. Yang, D.; Liang, H.; Liu, Y.; Hou, M.; Kan, L.; Yang, Y.; Zang, Z., A Large-area Luminescent Downshifting Layer Containing an Eu^{3+} Complex for Crystalline Silicon Solar Cells. *Dalton Trans* **2020,** *49* (15), 4725-4731.

29. Geyer, S. M.; Scherer, J. M.; Moloto, N.; Jaworski, F. B.; Bawendi, M. G., Efficient Luminescent Down-shifting Detectors Based on Colloidal Quantum Dots for Dual-band Detection Applications. *ACS Nano* **2011,** *5* (7), 5566-71.

30. Nakamura, Y.; Iso, Y.; Isobe, T., Bandgap-Tuned $CuInS_2$/ZnS Core/Shell Quantum Dots for a Luminescent Downshifting Layer in a Crystalline Silicon Solar Module. *ACS Applied Nano Materials* **2020,** *3* (4), 3417-3426.

31. Phelan, M. E.; Needell, D. R.; Potter, M. M.; Bauser, H. C.; Ryczek, C. N.; Nuzzo, R. G.; Atwater, H. A., Photovoltaic Thermal Management in Luminescent Solar Concentrators. In *2022 IEEE 49th Photovoltaics Specialists Conference (PVSC)*, 2022; pp 0820-0825.

32. Brossard, M.; Hong, C.-Y.; Hung, M.; Yu, P.; Charlton, M. D. B.; Savvidis, P. G.; Lagoudakis, P. G., Novel Non-radiative Exciton Harvesting Scheme Yields a 15% Efficiency Improvement in High-Efficiency III-V Solar Cells. *Advanced Optical Materials* **2015,** *3* (2), 263-269.

33. Zondag, S. D. A.; Masson, T. M.; Debije, M. G.; Noel, T., The Development of Luminescent Solar Concentrator-based Photomicroreactors: a Cheap Reactor Enabling Efficient Solar-powered Photochemistry. *Photochem Photobiol Sci* **2022,** *21* (5), 705-717.

34. Alexandre, M.; Chapa, M.; Haque, S.; Mendes, M. J.; Águas, H.; Fortunato, E.; Martins, R., Optimum Luminescent Down-Shifting Properties for High Efficiency

and Stable Perovskite Solar Cells. *ACS Applied Energy Materials* **2019,** *2* (4), 2930-2938.

35. Yang, J.; Bao, Q.; Shen, L.; Ding, L., Potential Applications for Perovskite Solar Cells in Space. *Nano Energy* **2020,** *76*.

36. Kirmani, A. R.; Durant, B. K.; Grandidier, J.; Haegel, N. M.; Kelzenberg, M. D.; Lao, Y. M.; McGehee, M. D.; McMillon-Brown, L.; Ostrowski, D. P.; Peshek, T. J.; Rout, B.; Sellers, I. R.; Steger, M.; Walker, D.; Wilt, D. M.; VanSant, K. T.; Luther, J. M., Countdown to Perovskite Space Launch: Guidelines to Performing Relevant Radiation-Hardness Experiments. *Joule* **2022,** *6* (5), 1015-1031.

37. Kirmani, A. R.; Ostrowski, D. P.; VanSant, K. T.; Byers, T. A.; Bramante, R. C.; Heinselman, K. N.; Tong, J.; Stevens, B.; Nemeth, W.; Zhu, K.; Sellers, I. R.; Rout, B.; Luther, J. M., Metal Oxide Barrier Layers for Terrestrial and Space Perovskite Photovoltaics. *Nature Energy* **2023**.

38. Cai, T.; Dube, L.; Saghy, P.; Yang, H.; Chen, O., Progress in All-inorganic Heterometallic Halide Layered Double Perovskites. *Trends in Chemistry* **2023,** *5* (1), 29-44.

39. Han, L. L.; Sun, B. B.; Guo, C.; Peng, G. Q.; Chen, H. Y.; Yang, Z.; Li, N.; Ci, Z. P.; Jin, Z. W., Photophysics in Zero-Dimensional Potassium-Doped Cesium Copper Chloride $Cs_3Cu_2Cl_5$ Nanosheets and Its Application for High-Performance Flexible X-Ray Detection. *Advanced Optical Materials* **2022,** *10* (6).

40. Liu, C.; Wang, L.; Fang, F.; Zhao, Z.; Pan, J.; Akram, J.; Shafie, S. B.; Talaighil, R. Z.; Li, Q.; Zhao, Z.; Wu, J.; Zhu, Z.; Lei, W.; Zhang, X.; Chen, J., Energy Down-Conversion $Cs_3Cu_2Cl_5$ Nanocrystals for Boosting the Efficiency of UV Photodetector. *Frontiers in Materials* **2021,** *8*.

41. Zhao, S. Y.; Chen, C.; Cai, W. S.; Li, R.; Li, H. Y.; Jiang, S. Q.; Liu, M.; Zang, Z. G., Efficiently Luminescent and Stable Lead-free $Cs_3Cu_2Cl_5$@ Silica

Nanocrystals for White Light-Emitting Diodes and Communication. *Advanced Optical Materials* **2021,** *9* (13).

42. Luo, Z.; Li, Q.; Zhang, L.; Wu, X.; Tan, L.; Zou, C.; Liu, Y.; Quan, Z., 0D $Cs_3Cu_2X_5$ (X = I, Br, and Cl) Nanocrystals: Colloidal Syntheses and Optical Properties. *Small* **2020,** *16* (3), e1905226.

43. Li, Y.; Vashishtha, P.; Zhou, Z.; Li, Z.; Shivarudraiah, S. B.; Ma, C.; Liu, J.; Wong, K. S.; Su, H.; Halpert, J. E., Room Temperature Synthesis of Stable, Printable $Cs_3Cu_2X_5$ (X = I, Br/I, Br, Br/Cl, Cl) Colloidal Nanocrystals with Near-Unity Quantum Yield Green Emitters (X = Cl). *Chemistry of Materials* **2020,** *32* (13), 5515-5524.

44. Zhao, S.; Mo, Q.; Cai, W.; Wang, H.; Zang, Z., Inorganic Lead-free Cesium Copper Chlorine Nanocrystal for Highly Efficient and Stable Warm White Light-emitting Diodes. *Photonics Research* **2021,** *9* (2).

45. Li, C.-X.; Cho, S.-B.; Kim, D.-H.; Park, I.-K., Monodisperse Lead-Free Perovskite $Cs_3Cu_2I_5$ Nanocrystals: Role of the Metal Halide Additive. *Chemistry of Materials* **2022,** *34* (15), 6921-6932.

46. Lian, L.; Zheng, M.; Zhang, P.; Zheng, Z.; Du, K.; Lei, W.; Gao, J.; Niu, G.; Zhang, D.; Zhai, T.; Jin, S.; Tang, J.; Zhang, X.; Zhang, J., Photophysics in $Cs_3Cu_2X_5$ (X = Cl, Br, or I): Highly Luminescent Self-Trapped Excitons from Local Structure Symmetrization. *Chemistry of Materials* **2020,** *32* (8), 3462-3468.

47. Zhou, Z.; Li, Y.; Xing, Z.; Sung, H. H. Y.; Williams, I. D.; Li, Z.; Wong, K. S.; Halpert, J. E., Rapid Synthesis of Bright, Shape-Controlled, Large Single Crystals of $Cs_3Cu_2X_5$for Phase Pure Single (X= Br, Cl) and Mixed Halides (X= Br/Cl) as the Blue and Green Components for Printable White Light-Emitting Devices. *Advanced Materials Interfaces* **2021,** *8* (20).

48. Sumner, R.; Eiselt, S.; Kilburn, T. B.; Erickson, C.; Carlson, B.; Gamelin, D. R.; McDowall, S.; Patrick, D. L., Analysis of Optical Losses in High-Efficiency

$CuInS_2$-Based Nanocrystal Luminescent Solar Concentrators: Balancing Absorption versus Scattering. *The Journal of Physical Chemistry C* **2017,** *121* (6), 3252-3260.

49. Li, H.; Wu, K.; Lim, J.; Song, H.-J.; Klimov, V. I., Doctor-blade Deposition of Quantum Dots onto Standard Window Glass for Low-loss Large-area Luminescent Solar Concentrators. *Nature Energy* **2016,** *1* (12).

Chapter 5

High-Performance Mixing Design Luminescent Solar Concentrators Based on Quantum Dots and Perovskite Nanocrystals

5.1 Introduction

The pursuit of sustainable development necessitates the management of global resources to balance the growing demand for space and energy. Solar energy is a viable substitute for non-renewable fossil fuels[1-3], but its integration into urban architecture poses a challenge due to the excess heat generated by solar irradiation, which results in increased energy consumption required to maintain indoor temperatures.[4] Harnessing and utilizing incident solar irradiation energy would minimize energy consumption needed for temperature regulation, while the excess energy could power the building and reduce reliance on non-renewable energy sources. This vision aligns with the construction of a net zero energy consumption building (NZEB), a self-powered architecture that derives its energy from solar energy.[4-7] Key to this design is the building integrated photovoltaics (PV) system, which serves as a solar energy generator and fundamental building block for the entire construction framework.[8, 9] Luminescent solar concentrators (LSCs) are crucial components in the system, improving solar energy capture and conversion efficiencies. Specifically, LSCs down-convert high-energy solar photons into a narrower wavelength range more suited to PVs, and direct the photons to the PV integrated regions, maximizing energy generation.[10-18]

A typical luminescent solar concentrator (LSC) consists of dopant emitters that focus broadband incident photons to a confined wavelength range and a matrix material, typically one with a high refractive index, that directs the photons to the photovoltaic (PV) region to enhance energy generation.[12, 15, 19-22] Although the original LSC design

dates back to the 1970s, they have yet to find widespread application in the architecture industry.[19, 21, 23] This is due to several limitations, including narrow solar spectral coverage, low photoluminescence (PL) efficiencies, and high re-absorption loss, which constrain the upper limit of the LSC's photon concentration efficiencies. Recent advancements in the use of re-absorption-free semiconductor quantum dots (QDs) and high quantum yield perovskite nanocrystals have substantially improved the energy transfer efficiency of LSCs. These materials overcome the re-absorption loss problem and allow for a more efficient conversion of solar energy.[12, 14, 22, 24-29] Moreover, the tandem design LSC has emerged as an effective strategy for achieving a wider spectral coverage of sunlight. In this approach, each stack of the LSC is optimized to capture a specific wavelength range of incident photons, increasing the overall efficiency of the LSC.[16, 24, 25, 30]

Herein, we present a novel-geometry design for large-area, high-efficiency, and high-visibility luminescent solar concentrators (LSCs) using Yb-doped $CsPbCl_3$ perovskite nanocrystals (Yb-$CsPbCl_3$) and $CuInS_2$/ZnS (CIS) quantum dots as two types of emitters (**Figure 5.1a**). Yb-$CsPbCl_3$ mainly absorbs in the UV-blue range and exhibits high PL emissions in the NIR (PLQY = 160%) and blue light range due to the host-to-dopant energy transfer process and subsequent quantum cutting effect afforded by the Yb dopants.[24, 31-33] An ultra-large Stokes shift (~580 nm) prevents re-absorption and absence of absorption in the visible range, allowing the possibility of forming a co-emitter system with other emitters (**Figure 5.1b**). CIS has broad wavelength range

absorption of solar photons, including the entire visible range and a small portion of the NIR range, with a relatively high NIR emission (PLQY = 70% at peak position = 827 nm) (**Figure 5.1c**). To increase LSC efficiency, one common approach is to stack LSCs containing different emitters into layers to form a tandem design LSC, where different emitters capture solar photons in different wavelength ranges to increase photon absorption ratio and enhance external optical efficiency (η_{ext}). However, tandem LSC emitters typically have relatively small Stokes shifts, which can lead to re-absorption of emitted photons in the top layer by the bottom layer.[16, 30, 34-36]

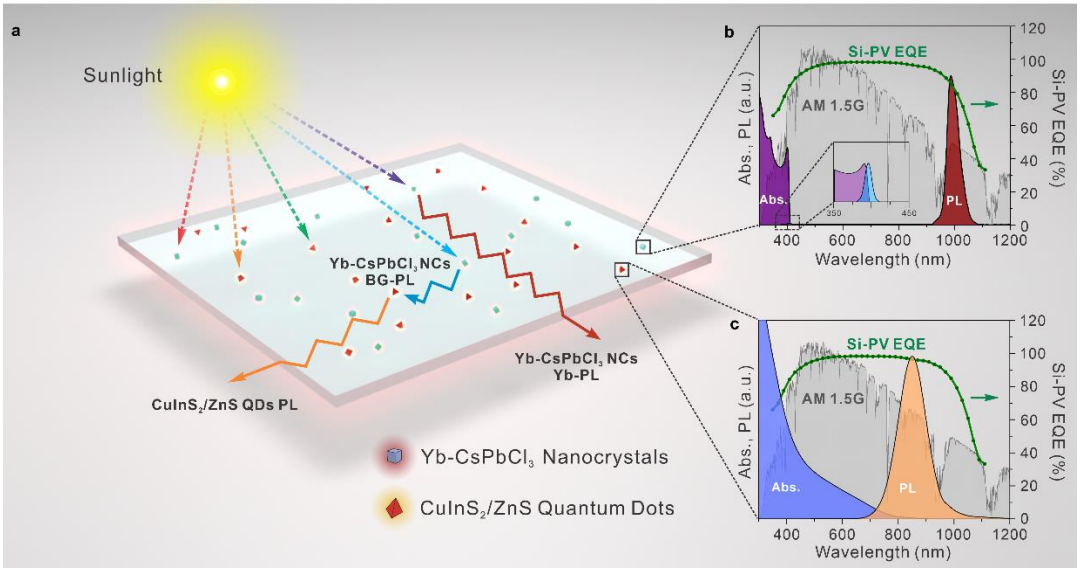

Figure 5.1. (a) Basic principle of mixing design LSC. (b) Absorption (Abs.) and photoluminescent (PL.) spectrum of Yb-$CsPbCl_3$ NCs, insert: zoomed in spectrum of the wavelength range from 350nm to 450nm; (c) Absorption (Abs.) and photoluminescent (PL.) spectrum of $CuInS_2$/ZnS QDs along with the AM 1.5G solar spectrum (grey shades) and a standard calibrated SI-PV EQE plot (green lines).

5.2 $CuInS_2$/ZnS quantum dots and Yb-$CsPbCl_3$ nanocrystals

In this study, we present a new mixing design LSC where CIS and Yb-$CsPbCl_3$ are homogeneously mixed to form a "donor-acceptor"-like LSC. The Stokes shift of Yb-

$CsPbCl_3$ nanocrystals allows the insertion of another emitter, such as CIS, that absorbs light in the Yb-$CsPbCl_3$'s Stokes shift region (visible region) to enhance η_{ext} and extend the LSC's absorption spectral coverage. The mixing LSCs concentrate photons released from two emitters to the same region, reducing scattering and attenuation losses compared to reference tandem LSCs with the same particle doping level and device thickness. The mixing LSC is also easy to fabricate, circumventing the expenses and technical challenges associated with tandem design LSCs. Our experimental and simulation data demonstrate that a specific concentration ratio of the two emitters can nearly double η_{ext}, highlighting the potential for practical integration into solar energy conversion systems with enhanced energy harvesting capabilities.

The structural model of $CuInS_2$ and the tetrahedral shape $CuInS_2$/ZnS core/shell quantum dots model are illustrated in **Figure 5.2a**, left and right, respectively. The X-ray diffraction (XRD) pattern of the sample confirmed the zinc-blended crystal structure with all the major Bragg diffraction peaks assigned to the $CuInS_2$ core simulated peak positions. Meanwhile, the appearance of ZnS shell structure was also observed in the diffraction patterns (**Figure 5.3b**). Due to Cu-related defects, electrons from the conduction band transfer to the native defect position and then drop to localized holes contributed by the defects (**Figure 5.2b**). This intragap energy transfer process causes a large Stokes shift, leading to the PL emission.[23, 37-39] Transmission electron microscopy (TEM) images, as shown in **Figure 5.2c, Figure 5.4b and 5.4d**, demonstrate the quantum dots' tetrahedral structure with an average edge size of 6.30

nm. Overall, $CuInS_2$/ZnS quantum dots possess favorable properties for use in LSC systems, providing a promising solution for enhancing solar photon capture efficiency and enabling efficient energy conversion.

The crystal structure model of Yb-$CsPbCl_3$, depicted in **Figure 5.2d**, demonstrates partial replacement of Pb ions with Yb ions to create a Yb-doping system, yielding cubic-shaped crystal structure perovskite. X-ray diffraction analysis confirmed all major diffraction peaks assigned to Yb-$CsPbCl_3$ simulated peak positions (**Figure 5.3a**). Previous research has shown that Yb-$CsPbCl_3$ nanocrystals exhibit a remarkably high quantum yield due to the quantum cutting effect, which refers to the emission of two low-energy photons following absorption of one high-energy photon, a peculiar optical phenomenon.[24, 33, 40] In the case of Yb-$CsPbCl_3$, a weak band-edge excitonic emission peak at 396 nm and a strong NIR emission peak at 985 nm arose from the *f-f* transition of Yb^{3+} dopants.[40] The quantum cutting effect occurred due to the electron transition from the conduction band of the $CsPbCl_3$ host to the Yb-induced defects, with the released energy being halved and discharged as two lower energy photons due to the Yb *f-f* transition, thereby doubling the PL quantum yield (**Figure 5.2e**).[31, 40] The TEM image of the nanocrystals showed a cubic morphology with an average edge length of 6.87 nm (**Figure 5.2f, Figure 5.4a, 5.4c**). These findings suggest that Yb-$CsPbCl_3$ nanocrystals have significant potential for use in LSC systems due to their high quantum yield and unique optical properties resulting from the quantum cutting effect.

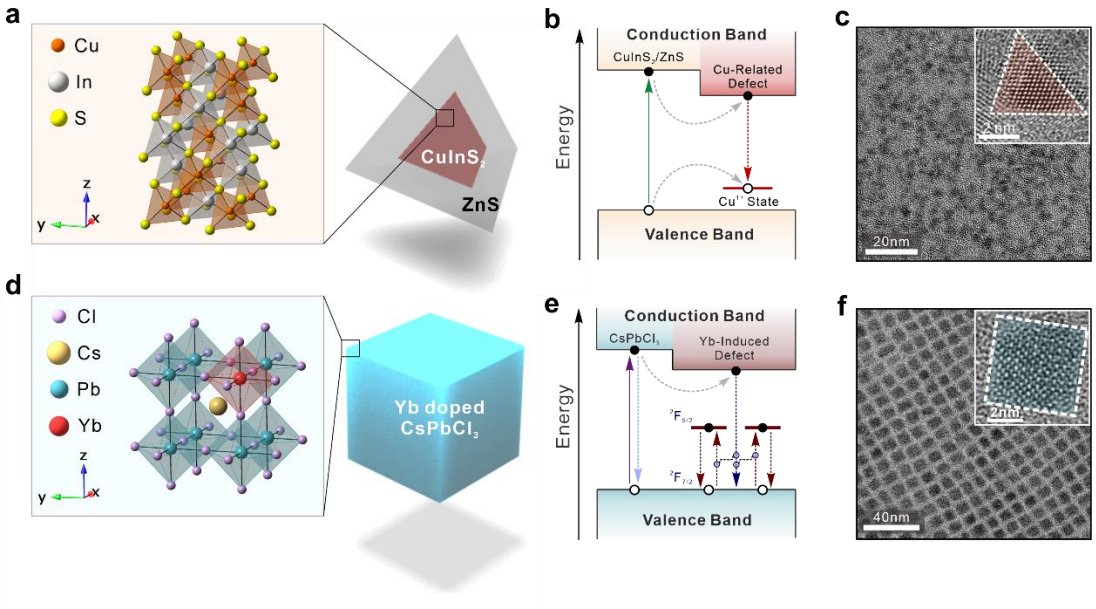

Figure 5.2. (a) Crystal structure of the $CuInS_2$ core (left) and scheme (right) of the $CuInS_2$/ZnS QDs **(b)** Band structural alignment of the $CuInS_2$/ZnS QDs **(c)** Typical TEM image of the $CuInS_2$/ZnS QDs. Inset: HR-TEM image of one of the representative emitters. **(d)** Crystal structure (left) and scheme (right) of the Yb-$CsPbCl_3$ NCs **(e)** Band structural alignment of the Yb-$CsPbCl_3$ NCs **(f)** Typical TEM image of the Yb-$CsPbCl_3$ NCs. Inset: HR-TEM image of one of the representative emitters.

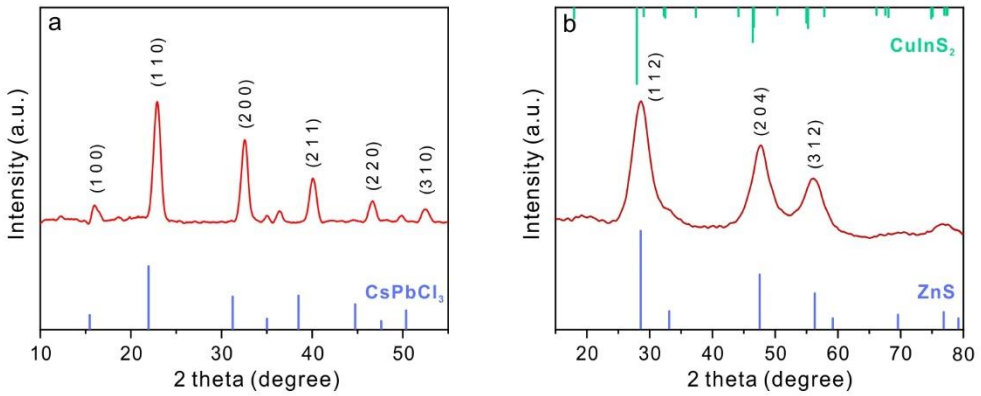

Figure 5.3. (a) X-ray powder diffraction pattern of the Yb-$CsPbCl_3$ NCs. The stick patterns show the standard peak positions of bulk $CsPbCl_3$. (b) X-ray powder diffraction pattern of the $CuInS_2$/ZnS QDs. The stick patterns show the standard peak positions of bulk ZnS. (bottom purple sticks) and $CuInS_2$ (top green sticks).

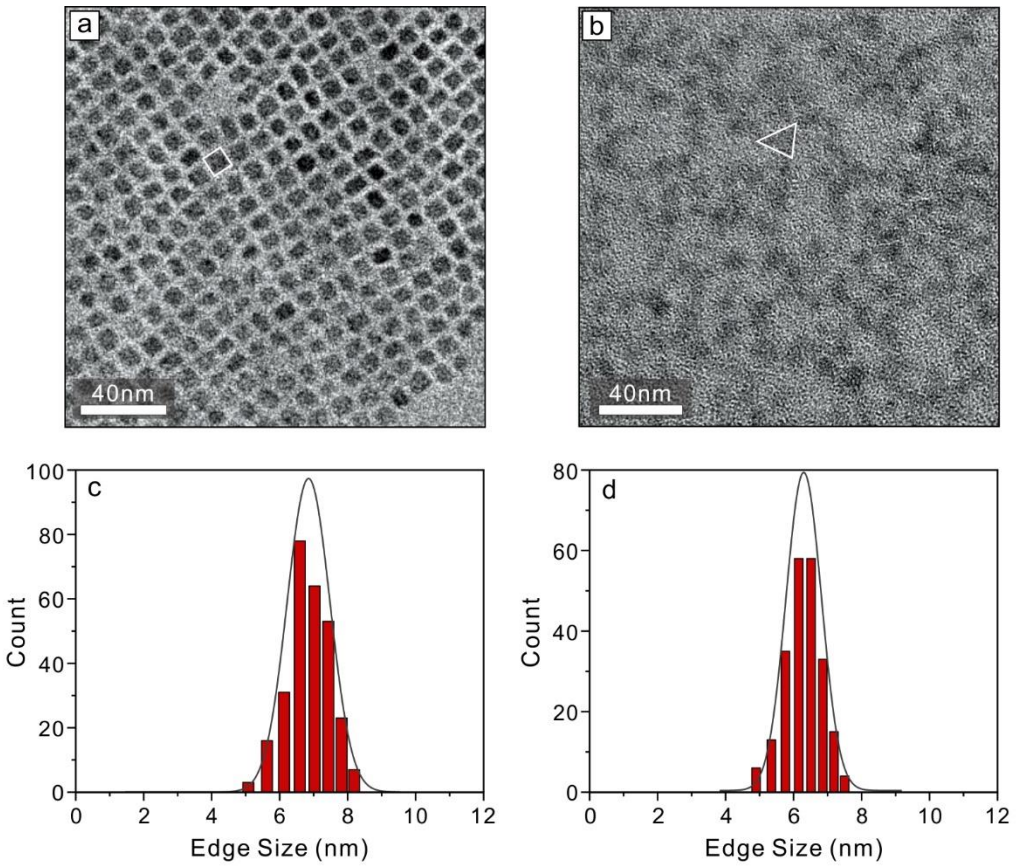

Figure 5.4. TEM images of (a) Yb-$CsPbCl_3$ NCs and (b) $CuInSe_2$/ZnS QDs. (c-d) Histograms of (c) Yb-$CsPbCl_3$ NCs and (d) $CuInSe_2$/ZnS QDs. The average sizes are 6.87 nm and 6.30 nm, respectively.

5.3 Mixing LSC simulation development and characterization

To design a highly efficient luminescent solar concentrator (LSC), it is imperative to identify the major factors that contribute to photon losses. Several mechanisms can significantly impact the performance of LSCs, including: (1) re-absorption of photons resulting from the partial overlap between the absorption and emission spectra of the embedded emitters; (2) reduced emission efficiency caused by non-radiative decay of the emitters, i.e., non-unity photoluminescence quantum yields (PL QYs); (3) photon losses through the escape cone of LSC devices, as defined by Snell's law; (4) a fraction of guided light lost due to scattering effects or photon attenuation; and (5) the fraction

of incident sunlight photons that are not absorbed. Therefore, to design an efficient LSC, it is crucial to mitigate these photon losses by optimizing the properties of the emitters and LSC devices. By applying the mixing emitter into LSC system, the high PL-QY and super large Stokes shift Yb contributes to reduce the losing process (1) and (2) in the mixing LSC system. Meanwhile, the high absorption efficiency CIS contributes to reduce the losing process (5). In order to obtain the enhancement, the concentration of the Yb and CIS in the mixing LSC system needs to be fix in order to balance a high absorption LSC and a low re-absorption high emission efficiency. There's also a competing process of the process (4), for the high concentration inducing scattering lost is another factor to limit the LSC performance.

Considering all relevant factors, we have developed an analytical model based on previous research,[11, 41-43] which incorporates the effects of scattering and balanced emitter systems to guide our experimental design. In the case of a single-emitter LSC, the internal optical efficiency (η_{int}, defined as the ratio of the edge-collected photon flux to the total absorbed solar flux) and external optical efficiency (η_{ext}, defined as the ratio of the edge-collected photon flux to the total incident photon flux) can be represented by the following equations:

$$\eta_{int} = \frac{\eta_{PL}\eta_{trap}}{1+\beta(\alpha_2+s_2)L(1-(\frac{\alpha_2\eta_{PL}+s_2}{\alpha_2+s_2})\eta_{trap})} \quad (1)$$

$$\eta_{ext} = \eta_{abs} \times \eta_{int} \quad (2)$$

Where, η_{PL} is the PL QY of the emitters; η_{trap} is the efficiency of light trapping into the LSC device; η_{abs} is the absorption ratio of the LSC; α_2 is reabsorption coefficient at the

wavelength of the emitted light; s_2 is the scattering factor of the emitter; β is a correction factor for elongation of photon light path in a 3D LSC mode versus a 1D mode. To apply these equations to a mixed-solution system, the interactions between the two emitters must be considered. Initially, the emitters will compete in capturing incident photons. The absorption ratio η_{abs} for a single-emitter LSC can be expressed as follows:

$$\eta_{abs} = (1 - R)(1 - e^{-\alpha_1 d}) \quad (3)$$

Where, R is the reflection coefficient of LSC surfaces; α_1 is the absorption coefficient at the wavelength of incident light; d is the thickness of LSC device. In the investigation of mixed-emitter luminescent solar concentrators (LSCs), it is essential to determine the number of photons absorbed by the LSC device and the proportion of photons captured by Yb and CIS within the LSC. The absorption ratio of the mixed LSC ($\eta_{abs(M)}$) can be expressed as follows:

$$\boldsymbol{\eta_{abs(M)} = (1 - R)\left(1 - e^{-(\alpha_{1(\mathrm{Yb})} + \alpha_{1(\mathrm{CIS})})d}\right)} \quad (4)$$

Where, $\alpha_{1(Yb)}$ and $\alpha_{1(CIS)}$ are the absorption coefficient of Yb and CIS at the wavelength of incident light accordingly. The emitters were systematically examined through absorption and emission spectroscopy to ensure that mutual quenching was not occurring between them (**Figure 5.5**). And the absorption ratio of Yb ($\eta_{abs(Yb)}$) and CIS ($\eta_{abs(Yb)}$) when they serving as an individual emitter in the LSC system should be:

$$\eta_{abs(Yb)} = (1 - R)\left(1 - e^{-\alpha_{1(\mathrm{Yb})} d}\right) \quad (5)$$

$$\eta_{abs(CIS)} = (1 - R)\left(1 - e^{-\alpha_{1(\mathrm{CIS})} d}\right) \quad (6)$$

The proportions of the absorption ratio of Yb ($\eta_{abs(Yb)\_M}$) and CIS ($\eta_{abs(CIS)\_M}$) when they are into a mixing system are:

$$\eta_{abs(Yb)\_M} = \frac{\eta_{abs(M)}\eta_{abs(Yb)}}{\eta_{abs(Yb)}+\eta_{abs(CIS)}} \quad (7)$$

$$\eta_{abs(CIS)\_M} = \frac{\eta_{abs(M)}\eta_{abs(CIS)}}{\eta_{abs(Yb)}+\eta_{abs(CIS)}} \quad (8)$$

Given the minimal reabsorption from the Yb bandgap emission to CIS, we do not consider this loss and assume the photon interaction between Yb and CIS can be disregarded. When a photon is captured by one emitter, its behavior is similar to the photon's travel process in a standard single-emitter LSC. Thus, the internal quantum efficiencies of Yb ($\eta_{int(Yb)}$) and CIS ($\eta_{int(CIS)}$) can be expressed as:

$$\eta_{int(Yb)} = \frac{\eta_{PL\_Yb}\eta_{trap}}{1+\beta(\alpha_{2(\mathrm{Yb})}+s_{2(\mathrm{M})})L(1-(\frac{\alpha_2\eta_{PL(Yb)/2}+s_{2(\mathrm{M})}}{\alpha_{2\_\mathrm{CIS}}+s_{2(\mathrm{M})}})\eta_{trap})} \quad (9)$$

$$\eta_{int(CIS)} = \frac{\eta_{PL\_CIS}\eta_{trap}}{1+\beta(\alpha_{2}(\mathrm{CIS})+s_{2(\mathrm{M})})L(1-(\frac{\alpha_2\eta_{PL(CIS)}+s_{2(\mathrm{M})}}{\alpha_{2(\mathrm{CIS})}+s_{2(\mathrm{M})}})\eta_{trap})} \quad (10)$$

In these equations $\alpha_{2(Yb)}$ and $\alpha_{2(CIS)}$ are reabsorption coefficient of Yb and CIS accordingly. $\eta_{PL(Yb)}$ and $\eta_{PL(CIS)}$ are the PL QY of the Yb and CIS; $s_{2(M)}$ is the scattering factor of the mixing emitters (refer to the **Method** section for details). Further, the η_{ext} of the Yb ($\eta_{ext(Yb)}$) and CIS ($\eta_{ext(CIS)}$) can be expressed as follows:

$$\eta_{ext\_Yb} = \eta_{abs\_Yb\_M} \times \eta_{int\_Yb} \quad (11)$$

$$\eta_{ext\_CIS} = \eta_{abs\_CIS\_M} \times \eta_{int\_CIS} \quad (12)$$

The overall η_{ext} for the mixing LSC ($\eta_{ext(M)}$) is:

$$\eta_{ext(M)} = \eta_{ext(Yb)} + \eta_{ext(CIS)} \quad (13)$$

In this simulation, we can modulate the performance of the mixing LSC by adjusting the concentrations of both Yb and CIS emitters. We also consider the primary interactions between the emitters, including absorption competition and scattering effects. The optimized simulation is detailed in the Methods section. Based on the

mixed LSC simulation, we can determine the optimal LSC performance at specific Yb and CIS concentrations.

To validate the simulation results, we first fabricate small-dimension mixed LSCs (4.0 cm × 4.0 cm × 0.2 cm) with varying Yb and CIS absorption ratios, based on the η_{ext} contour map obtained from the model (**Figure 5.6a**). We also fabricate reference tandem design LSCs with identical amounts of emitters (double the concentration) corresponding to the mixed group (each LSC layer dimension: 4.0 cm × 4.0 cm × 0.1 cm). According to the map, the best-performing LSC (LSC-BP) in this dimension is achieved when the absorption ratios of Yb ($\eta_{abs(Yb)}$) and CIS ($\eta_{abs(CIS)}$) reach 1.27% and 20.38%, respectively, when they serve as individual emitters in the LSC system. To test the simulation's accuracy, we include several reference LSC groups alongside the LSC-BP. We set $\eta_{abs(\mathrm{CIS})}$ to 20.38%, and the reference LSC groups are LSC-Yb1 ($\eta_{abs(Yb)}$ = 0.24%), LSC-Yb2 ($\eta_{abs(Yb)}$ = 0.87%), and LSC-Yb3 ($\eta_{abs(Yb)}$ = 1.56%). Simultaneously, we set $\eta_{abs(Yb)}$ to 1.27%, and the reference LSC groups are LSC-CIS1 ($\eta_{abs(CIS)}$ = 5.40%), LSC-CIS2 ($\eta_{abs(CIS)}$ = 17.78%), and LSC-CIS3 ($\eta_{abs(Yb)}$ = 21.82%) (Figure 3a). **Figure 5.6b** displays photographs of the LSC-BP and reference LSC groups under ambient and UV light, showing a significant concentration effect in all devices. The absorption and emission spectra of the blended solution, comprising Yb group and CIS group solutes dissolved in a PDMS monomer, substantiated the absence of any quenching effects between the emitting species (**Figure 5.7, 5.8**).

To investigate the performance of mixing LSCs, we coupled silicon photovoltaic (Si-PV) cells to the edges of the LSC devices, creating an LSC-PV system. We applied an index-matching gel (refractive index of 1.52) at the interface between the LSC edge and the Si-PV cell to minimize total internal reflection. For comparison, we measured a set of tandem design LSCs with equal amounts of Yb and CIS. Under a sunlight simulator (AM = 1.5), the short-circuit current densities of the attached Si-PV cells are presented in **Figures 5.6c** and **5.6e**.

For the Yb group, the short-circuit current density of the mixed LSC design ranged from 10.69 mA/cm² (LSC-Yb1) to 10.34 mA/cm² (LSC-Yb2), 10.83 mA/cm² (LSC-BP), and 9.39 mA/cm² (LSC-Yb3), while the tandem design LSC ranged from 6.16 mA/cm² (LSC-Yb1) to 6.70 mA/cm² (LSC-Yb2), 6.85 mA/cm² (LSC-BP), and 6.60 mA/cm² (LSC-Yb3) (Figure 3c). Based on the current-voltage (J-V) measurements, the external quantum efficiency (η_{ext}) for the mixed LSC devices varied from 13.25±0.88% (LSC-Yb1) to 13.64±0.72% (LSC-Yb2), 13.92±1.02% (LSC-BP), and 12.43±0.35% (LSC-Yb3), while the tandem LSC devices ranged from 7.67±1.09% (LSC-Yb1) to 8.93±0.66% (LSC-Yb2), 8.74±0.89% (LSC-BP), and 8.73±0.75% (LSC-Yb3). For the CIS group, the short-circuit current density of the mixing LSCs ranged from 3.18 mA/cm² (LSC-CIS1) to 9.40 mA/cm² (LSC-CIS2), 10.83 mA/cm² (LSC-BP), and 9.47 mA/cm² (LSC-CIS3). In comparison, the tandem LSCs exhibited short-circuit current densities of 3.00 mA/cm² (LSC-CIS1), 6.70 mA/cm² (LSC-CIS2), 6.82 mA/cm² (LSC-BP), and 6.55 mA/cm² (LSC-CIS3) (Figure 3e). Based on the J-V measurements, the η_{ext} for the mixed

LSC devices in the CIS group changed from 4.35±0.93% (LSC-CIS1) to 12.4±0.51% (LSC-CIS2), 13.92±1.02% (LSC-BP), and 12.48±0.78% (LSC-CIS3). Meanwhile, the tandem LSC devices exhibited η_{ext} values of 4.10±0.61% (LSC-Yb1), 8.85±1.02% (LSC-Yb2), 8.99±0.84% (LSC-BP), and 8.64±1.02% (LSC-Yb3). The external quantum efficiency **(**EQE) of the LSC-PV devices was evaluated for all mixed configurations. The observed EQE trends were consistent with the absorption patterns depicted in Figures S4 and S5, corroborating the LSC concentrating effect. Furthermore, it was confirmed that the majority of the edge-collected photons originated from the emitters, as illustrated in **Figures 5.9** and **5.10**. The simulation curves correlated well with the experimental data, indicating that the developed analytical model can effectively predict the performance of mixed-emitter LSCs and identify the optimal performance parameters across all dimensions.

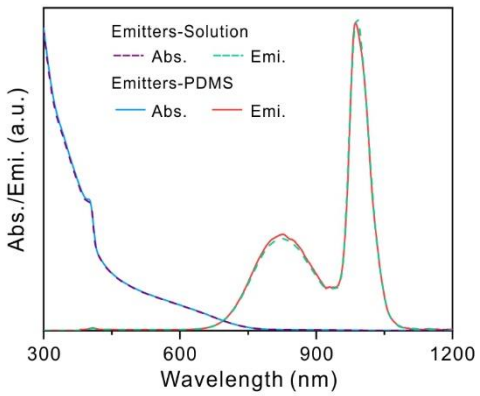

Figure 5.5. Absorption and emission spectra of the mixing emitters solution (Yb: CIS = 8: 1) in toluene solution (solid lines) and in PDMS polymer matrix (dashed lines).

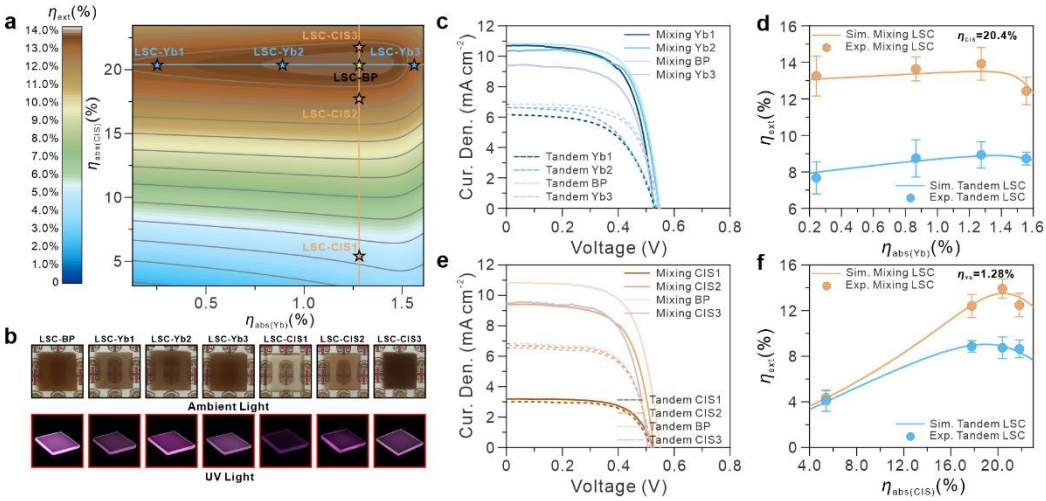

Figure 5.6. (a) Simulated η_{ext} of the mixing design LSC (the device dimension of 4.0 cm × 4.0 cm × 0.1 cm) with different Yb and CIS absorption ratio. The yellow star (LSC-BP) represents the data point for best performance LSC; the blue stars (LSC-Yb1, LSC-Yb2 and LSC-Yb3) represent the data point for reference group of different Yb and same CIS absorption ratio corresponding to LSC-BP; the orange stars (LSC-CIS1, LSC-CIS2 and LSC-CIS3) represent the data point for reference group of different CIS and same Yb absorption ratio corresponding to LSC-BP. **(b)** Photograph of the mixing LSCs based on the simulation. **(c, e)** Experimentally measured J-V curves of the mixing LSCs (solid line) and tandem LSCs (dash line) of **(c)** Yb group and **(e)** CIS group under solar simulator. **(d, f)** Experimental (spheres) and simulated (lines) η_{ext} for the mixing LSCs and tandem LSCs of **(d)** Yb group and **(f)** CIS group. Evolutions of the η_{ext} as a function of η_{abs} under solar simulator.

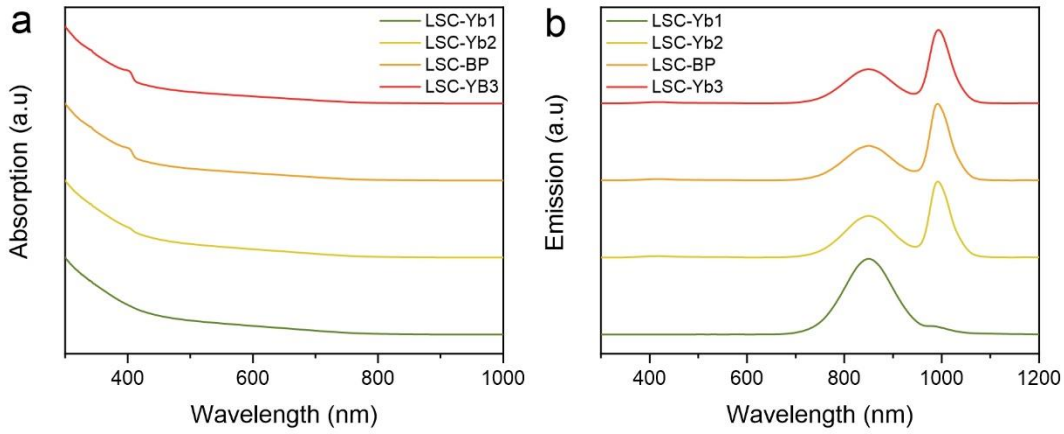

Figure 5.7. (a) Absorption and **(b)** emission spectra of the different mixing solution dissolved in PDMS monomer. (Yb group)

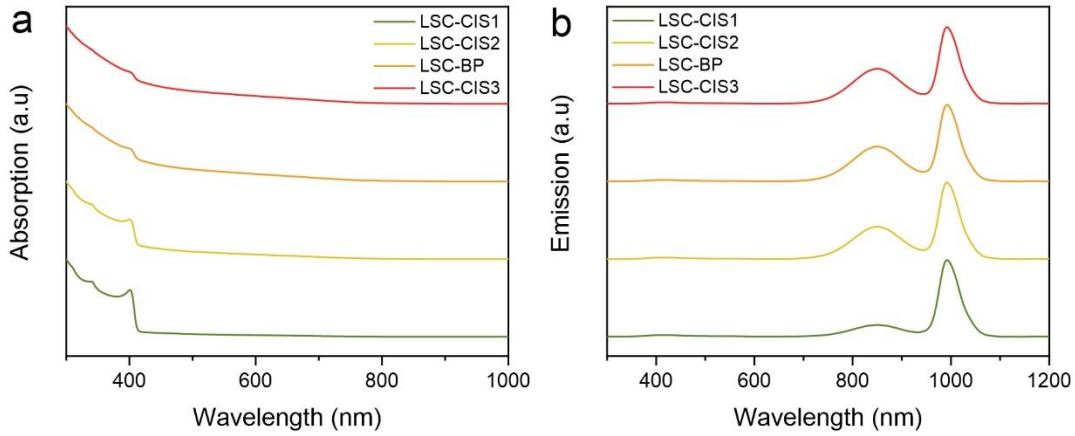

Figure 5.8. (a) Absorption and (b) emission spectra of the different mixing solution dissolved in PDMS monomer. (CIS group)

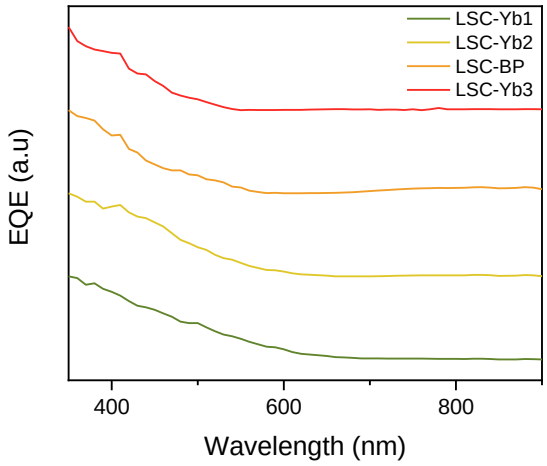

Figure 5.9. EQE spectra of Yb group.

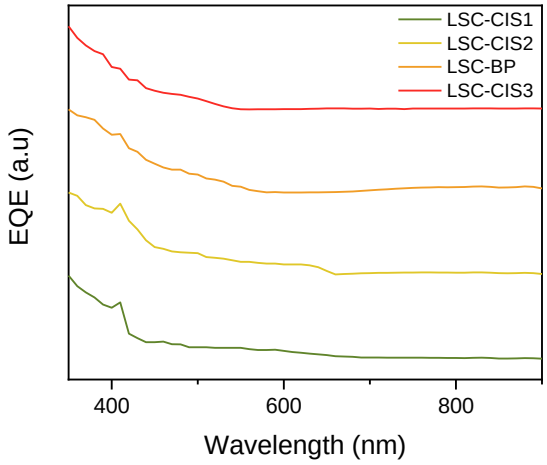

Figure 5.10. EQE spectra of CIS group.

Subsequently, the developed analytical model was employed to simulate the performance of a large-scale LSC. The simulated η_{ext} results revealed that optimal LSC-BP performance in this dimension was achieved when $\eta_{abs(Yb)}$ reached 0.61% and $\eta_{abs(CIS)}$ reached 14.77% (**Figure 5.11a**). Based on the simulation parameters, we fabricated a mixed-emitter LSC device (15.2 cm × 15.2 cm × 0.318 cm) and a reference tandem LSC device with the same emitter quantity (15.2 cm × 15.2 cm × 0.159 cm for each

slab). *J-V* characterization was conducted to measure the LSC energy conversion efficiency. A standard silicon photovoltaic (Si-PV) cell was attached to the LSC device to measure current density data (**Figure 5.11b**; see **Method** for details). Under 1.5 AM Global sunlight illumination, the short-circuit current densities of the standard Si-PV (15.2 cm × 0.318 cm) increased from 11.37 mA cm^{-2} to 17.47 mA cm^{-2} (11.40 mA cm^{-2}) when coupled with the mixed-emitter LSC (tandem LSC) (**Figure 5.11b**). The relationship between short-circuit current densities and η_{ext} showed η_{ext} values of 7.37±0.89% and 4.79±0.59% for the mixed-emitter LSC and tandem LSC under sunlight, respectively. These values were consistent with the developed analytical model simulation results. The simulation curves illustrated the evolution of η_{ext} for the mixed-emitter LSC and tandem LSC as a function of $\eta_{abs(Yb)}$ when $\eta_{abs(CIS)}$ = 14.77% (solid line) and as a function of $\eta_{abs(CIS)}$ when $\eta_{abs(Yb)}$ = 0.61% (dashed line). This demonstrated that the mixed-emitter LSC with $\eta_{abs(Yb)}$ = 0.61% and $\eta_{abs(CIS)}$ = 14.77% exhibited the best performance (**Figure 5.11c**). **Figure 5.11d** presents a photograph of the fabricated large-scale LSC under ambient light taken by a standard camera, which displayed a relatively high visible light transmittance (VLT) of 56.1% and a low scattering effect. **Figure 5.11e** shows a photograph of the same device under 365 nm UV light excitation captured by a near-infrared (NIR) camera, demonstrating strong NIR emission with a light concentration effect in the LSC.

To further investigate photon propagation mechanisms in luminescent solar concentrators (LSCs), we employed the Monte Carlo (MC) ray-tracing model to

simulate photon behavior in large-scale mixing LSCs and tandem LSCs. For meaningful comparisons, we set 30,000 photons (following the sunlight spectral distribution) to strike the LSC device perpendicularly to the top surface. In the simulation, we configured the cuboid mixing LSC to have the same dimensions as the fabricated large-scale LSC (15.2 cm × 15.2 cm × 0.318 cm), a PDMS polymer matrix with a refractive index (n) of 1.4, and 0.4 wt% CIS and 0.6 wt% Yb emitters introduced into the system to achieve the optimal LSC performance (**Figure 5.11f**). Concurrently, two tandem LSC slabs with dimensions of 15.2 cm × 15.2 cm × 0.159 cm were stacked together with a 0.2 cm air gap in the middle. The first layer contained 0.8 wt% CIS, and the second layer incorporated 1.2 wt% Yb (**Figure 5.11g**). In both configurations, blue arrows represented Yb-emitted photons, while red arrows represented CIS-emitted photons. The right insets display edge-side views of the simulations. For clearer visualization, we reduced the input photon quantity to 3,000 for capturing the images. In these configurations, we observed a significant increase in the number of edge-escaped photons in the mixed-emitter LSC. The η_{ext} values obtained from the embedded photon counter were 7.42% and 4.20% for the mixed-emitter and tandem LSCs, respectively, closely aligning with the experimental results (7.37% and 4.79%, respectively) (**Figure 5.11f, 5.11g**).

We conducted a quantitative analysis of incident photon behavior using photon tracking counters in the MC model for both LSC devices. For the mixed-emitter LSC (tandem LSC), 81.7% (78.4%) of incident photons were transmitted through the LSC, 3.1%

(7.0%) were reflected by the LSC surface, 14.7% (13.5%) were absorbed by the CIS emitters, and 0.5% (1.1%) were absorbed by the Yb emitters. The fraction of reflected photons in the tandem LSC doubled due to reflection losses caused by photon transfer at the inter-layer region. The difference in photon absorption between tandem and mixed-emitter LSCs resulted from competing effects in the mixed-emitter design, as both CIS and Yb can absorb photons in the UV and blue range. This competition is avoided in the tandem design, as CIS only absorbs photons after passing through the Yb layer filter (**Figure 5.11h**). We subsequently quantified the performance of the photons' final positions, as shown in **Figure 5.11i**. In the mixed-emitter (tandem) design LSCs, 49.5% (68.2%) of the photons were lost during the re-absorption process and scattering attenuation; 16.0% (9.4%) of the CIS-emitted photons were lost from the escape cone; 0.6% (0.8%) of the Yb-emitted photons were lost from the escape cone; 32.8% (19.4%) of the CIS-emitted photons reached the LSC edge, and 1.1% (1.9%) of the Yb-emitted photons reached the edge.

The differences in re-absorption and attenuation between the mixed-emitter and tandem design LSCs are significant, primarily due to the variations in the G factor and emitter concentrations in the two designs. Notably, the scattering factor s_2 experiences a dramatic increase, leading to nearly twice the photon loss due to scattering attenuation in the tandem LSC compared to the mixed-emitter LSC. In the mixed-emitter LSC, lower emitter concentrations minimize the scattering effect, while a reduced G factor contributes to enhanced edge-capture efficiency. The escape cone loss ratios for CIS

and Yb-CsPbCl3 in both designs are similar, as they employ the same polymer matrix, resulting in an identical refractive index.

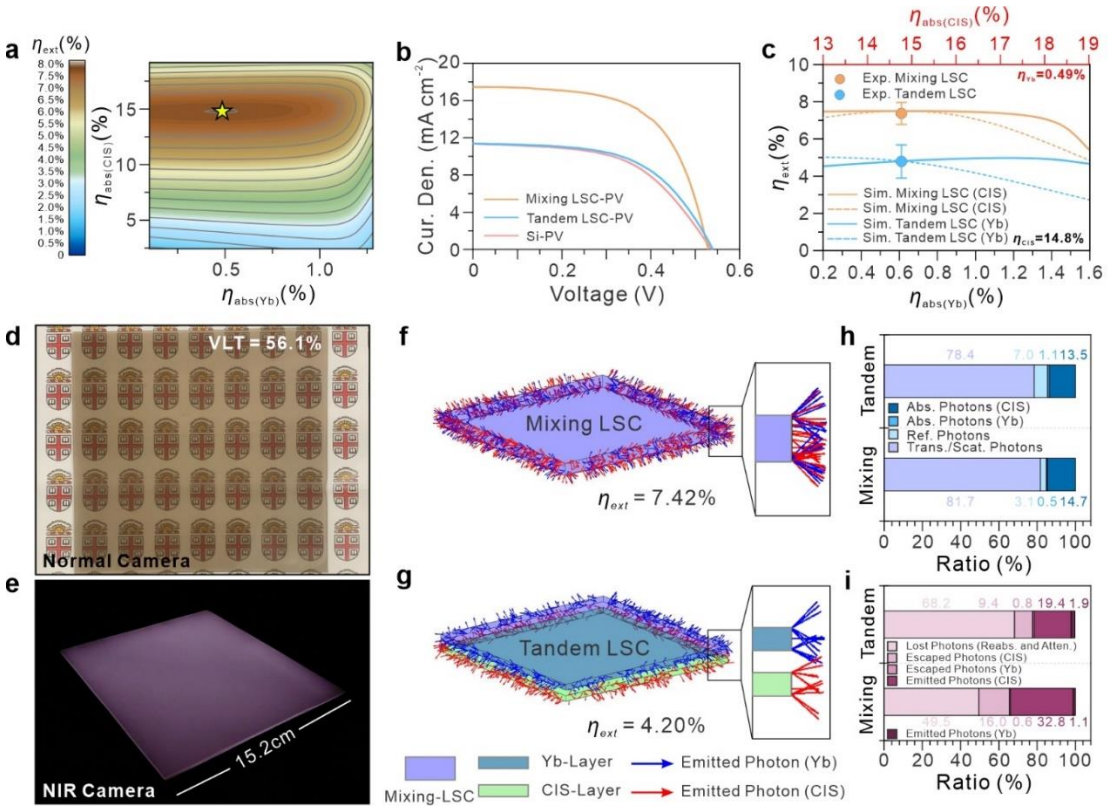

Figure 5.11. (a) Simulated η_{ext} of the mixing design LSC (the device dimension of 15.2 cm × 15.2 cm × 0.318 cm) with different Yb and CIS absorption ratio (η_{abs}). The yellow star (LSC-BP) represents the data point for best performance LSC. **(b)** Experimentally measured J-V curves of the mixing LSCs, tandem LSCs and reference Si-PV under solar simulator. **(c)** Experimental (spheres) and simulated (lines) η_{ext} for the mixing LSCs and tandem LSCs. Evolutions of the η_{ext} as a function of η_{abs} under solar simulator. **(d)** Photograph of the LSC device under normal light illumination. **(e)** Photograph of the LSC device taken by a normal camera under ambient light illumination. **(f)** Visualization of the Monte-Carlo ray-tracing simulation (MC mode) for the mixing design LSC and **(g)** the tandem design LSC. The arrows represent the photon output from the edge region of the LSC devices, where blue arrows represent Yb-$CsPbCl_3$ emitted photons and red arrows represent CIS emitted photons. **(h, i)** Photon statistics for the **(h)** first absorption process and **(i)** the final emission of the attenuation process for the mixing LSC and tandem LSC **(f, h)** and the tandem design LSC. The statistics

data is gathered by the MC mode counter.

5.4 Mixing LSC cost-efficiency calculation

A primary motivation for developing LSC-PV systems is the potential reduction in solar electricity consumption. In this study, we introduce a cost-efficiency factor (η_{cost}) for the mixed-emitter LSC device, defined by the following equation:[16]

$$\boldsymbol{\eta_{cost} = \frac{C_{LSC-PV}}{\chi_\theta q \eta_{ext} C_{PV}}} \quad (14)$$

Here, $C_{LSC\text{-}PV}$ represents the fabrication cost of the LSC-PV system to generate 1 Watt of electricity, while C_{PV} denotes the fabrication cost of Si-PV to generate 1 Watt of electricity. χ_θ is the angular correction factor which is 1.36 after correction (**Figure 5.12**), and q is the spectral re-shaping factor of the LSC (see Method for calculation details). We first calculated η_{cost} for the optimal performance LSC recipe as a function of the geometry gain factor (G factor, defined as G = l/4d, where l and d represent the length and thickness of the LSC, respectively) and device thickness d, based on the actual experimental results of the emitters (**Figure 5.13a**). The red dashed line represents the data where η_{cost} = 1, indicating that the fabrication cost for the LSC-PV system to collect energy is equivalent to that of PV only. Thus, the data within the red dashed circle signifies that LSC-PV systems with these dimensions are more cost-effective than PV only. In this study, the large-scale mixed-emitter LSC has an η_{cost} value of 0.77, suggesting that compared to PV alone, the LSC-PV system could reduce fabrication costs by 23% to produce the same amount of energy. Furthermore, we incorporated ideal emitters into the system, with Yb having 200% PLQY and CIS having 100% PLQY. As shown in **Figure 5.13b**, the area of the red circle substantially

expands, indicating that our experimental prototype still has significant potential to reach the theoretical highest value. In this scenario, the large-scale mixing LSC has an η_{cost} value of 0.40, potentially reducing fabrication costs by 60%. This cost-efficiency calculation can assist in further LSC geometry design, particularly for commercial applications.

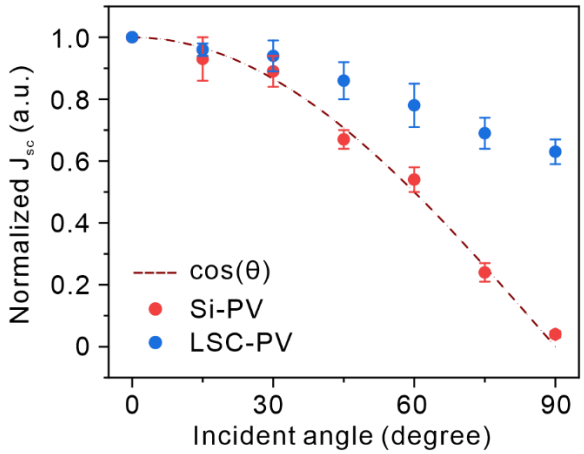

Figure 5.12. The relationship of normalized short-circuit currents (J_{SC}) and solar incident angle (θ) for a polycrystalline Si-PV cell (blue sphere) and the same solar cell coupled to a mixing design LSC (red sphere). The dark red dashed line is an ideal cos(θ) dependence.

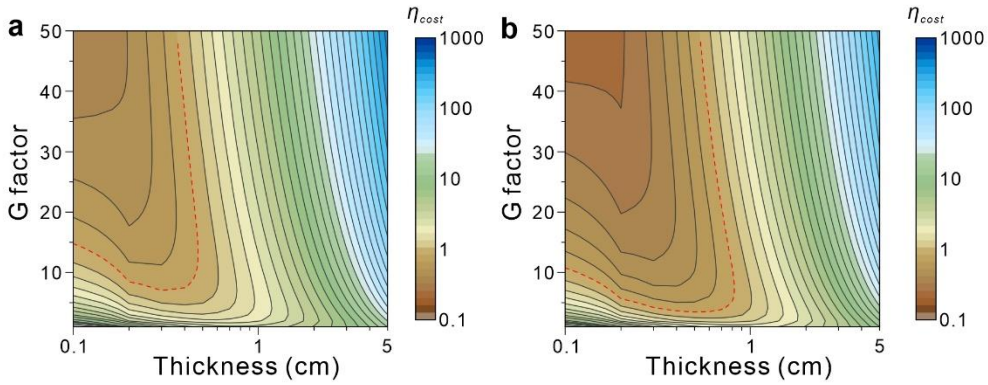

Figure 5.13. Cost-efficiency factor (η_{cost}) based on G factor and thickness of the optimized mixing LSC coupled with PV with the **(a)** real emitter conditions and **(b)** ideal emitter conditions.

5.5 Mixing LSC Building Integrated Photovoltaic Simulation

We further investigated the potential enhancement in power gain by integrating LSC-coupled building-integrated PV systems into skyscrapers to achieve a Net Zero Energy Building (NZEB) objective.[44-47] The working principle of an NZEB is depicted in **Figure 5.14a**: PV systems are typically installed on a building's roof to convert global horizontal irradiance (GHI) into energy. GHI is the total amount of shortwave radiation received by a surface horizontal to the ground, encompassing both direct normal irradiance (DNI) and diffuse horizontal irradiance (DHI).[48, 49] However, for skyscrapers, the radiation received from the edge side is also substantial. Consequently, we modeled the high visible light transmittance (VLT) LSC-PV system as a replacement for glass wall windows, functioning as an edge energy collector. The incident global irradiance (IGI), which includes DNI, DHI, and ground reflected irradiance (GRI), serves as the incident light source for the edge-coupled LSC-PV system. The dimensional setup for a skyscraper (70m × 70m × 420m) features concentration ratio-optimized mixed-emitter LSC-PVs (0.6m × 0.6m × 0.03m). **Figure 5.14b** illustrates the monthly solar radiation of GHI and IGI in four directions during a typical meteorological year in Providence, RI (USA). Correspondingly, we calculated the power gain from the skyscraper when equipped with standalone PVs on the roof or an LSC-PV system on the curtain walls of the building facing south, east, west, and north. The power gain increased in the summer and decreased in the winter. The edge-mounted LSC-PV system exhibited a ~350% energy gain enhancement from solar irradiation compared to roof-mounted PVs in the summer, increasing to ~630% in the winter due to the solar

incident angle (**Figure 5.14c**).

To thoroughly investigate the LSC-PV applications in NZEB buildings, we employed EnergyPlus to simulate the net source energy consumption of a building equipped with an LSC-PV system on its side walls (simulation details are described in the Methods section). In general, we calculated the annual net source energy of a representative building with different PV mounting strategies in the United States. Initially, we assumed the representative building would only mount PVs on the roof. None of the states exhibited a net source energy below 0, indicating that the building would still require energy from the grid to balance its annual energy consumption, regardless of its location. The highest value was obtained in Vermont at 352.25 MJ/m², and the lowest in Arizona at 22.61 MJ/m² (**Figure 5.14d**). By mounting an LSC-PV system on the glass curtain wall and PVs on the roof, net source energy consumption was significantly reduced, as shown in **Figure 5.14e**. More than half of the states exhibited a negative net source energy value, indicating that the energy produced by the building exceeded its consumption. In other words, the building became an NZEB. In the simulation, the highest data point was Arizona at -283.3 MJ/m², and the lowest was Vermont at 154.06 MJ/m². We also calculated the enhancement factor (EF) of the representative building with and without the LSC-PV system, expressed as follows:

$$\boldsymbol{EF} = \frac{\boldsymbol{E}_{\mathbf{LSC-PV}}}{\boldsymbol{E}_{\boldsymbol{PV}}} \tag{15}$$

Where, $E_{LSC\text{-}PV}$ represents the energy produced by LSC-PV system on the walls and the E_{PV} represents the energy produced by PV on the roof. A latitude-related tendency was

observed, indicating that the LSC could assist high-latitude regions in gaining additional solar energy due to lower direct normal irradiance (DNI) angles (**Figure 5.14f**). To confirm this trend, we calculated the *EF* in different cities along the east coast. As illustrated in **Figure 5.14g**, the *EF* increased from 0.36 to 0.43 as the latitude rose from 24.5° N to 45.5° N, further supporting our conclusion.

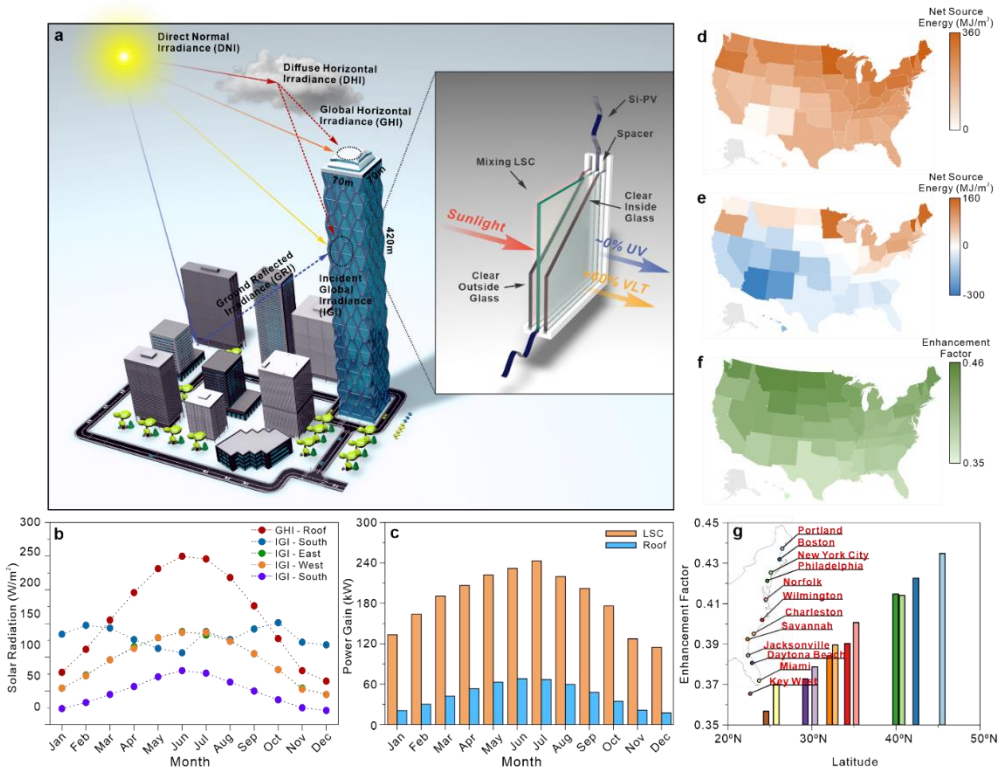

Figure 5.14. (a) Working principle of a skyscraper with solar harvesting window, inset: the structure of the LSC coupled solar window. **(b)** The average Providence solar radiation intensity in 12 months of incident global irradiance on four directions and the global horizonal irradiance on the roof. **(c)** The average power gain obtained over the course of 12 months from a simulated NZEB building by utilizing a solar window on a glass curtain wall (orange) and a PV array installed on the roof (blue). **(d, e)** Simulated total source energy usage for the representative buildings with **(d)** PV array installed on the roof only and **(e)** PV array installed on the roof and LSC integrated solar window based on the solar irradiance data in the United State. **(f)** Enhancement factor for the representative buildings based on the solar irradiance data in the United State.

In conclusion, we have demonstrated a mixed design LSC incorporating high PLQY quantum cutting perovskite Yb-doped $CsPbCl_3$ nanocrystals and Stokes-shift engineered $CuInS_2$/ZnS quantum dots, achieving high η_{ext} performance for large-scale LSC devices through both experimental studies and computational simulations. Our results indicate that the mixed design LSC reduces re-absorption losses and scattering attenuation effects compared to a tandem design LSC. Furthermore, our simulation study reveals that the mixed design LSC-PV system can significantly lower the energy generation costs associated with PV panels. By integrating our findings with the concept of NZEB buildings, we show the potential for energy gain enhancement using mixed LSC-PV mounting compared to stand-alone roof-mounted PV panels. Our study paves the way for the future design and fabrication of LSCs and building-integrated solar windows.

Method

Chemicals

Cesium acetate (Cs(OAc), 99.9%), Lead(II) acetate trihydrate ($Pb(OAc)_2 \cdot 3H_2O$, 99.99%), Ytterbium(III) acetate tetrahydrate ($Yb(OAc)_3 \cdot 4H_2O$, 99.9%), Copper iodide (CuI, 99.9%), Indium acetate (In(OAc)3, 99.9%), Zink acetate (Zn(OAc)2, 99.9%), 1-dodecanethiol (DDT, 98%), oleic acid (OA, 99%), Oleylamine (OAm, 70%), 1-octadecene (ODE, 90%), ethanol and toluene were purchased from Sigma-Aldrich Corporation. Polydimethylsiloxane (PDMS) was purchased by Gelest Inc. All chemicals were used as received without further purification.

Synthesis of Yb-$CsPbCl_3$ perovskite nanocrystals (NCs)

Yb-$CsPbCl_3$ NCs were synthesized using a modified hot-injection method. Briefly, Cs(OAc) (26.9 mg, 0.14 mmol), $Pb(OAc)_2 \cdot 3H_2O$ (37.9 mg, 0.10 mmol), and $Yb(OAc)_3 \cdot 4H_2O$ (16.9 mg, 0.03 mmol) were firstly added to a 50 mL three-neck flask, together with OA (0.25 mL), OAm (0.5 mL) and ODE (5.0 mL) to form a precursor solution. The mixture was degassed for 1 hr at 120 ℃ and then heated to 200 ℃ under N_2 flow. Upon reaching this temperature, 0.10 mL TMS-Cl was injected quickly, and the solution turned turbid immediately. After 5 s, the solution was cooled down to room temperature by an ice bath.[40]

Purification of Yb-$CsPbCl_3$ perovskite nanocrystals (NCs)

The as-prepared Yb-$CsPbCl_3$ solution was firstly centrifugated for 10 min at 7,000 rpm.

The resulting supernatant was discarded, and the precipitate was dispersed in 10 mL toluene. Then, the NC solution was centrifuged again for 5 min at 4,000 rpm and the clear supernatant was kept for further characterization.[40]

Preparation of Zink stock solution

$Zn(OAc)_2$ (734.0 mg, 4 mmol) were mixed with OA (8 mL) and DDT (2 mL) in a 50 mL flask. After being purged with N_2 flow for 10 min, the solution was heated up to 200 ℃ under N_2 flow protection.[50]

Synthesis of $CuInS_2$/ZnS quantum dots (QDs)

CuI (190.5 mg, 1 mmol), $In(OAc)_3$ (292.0 mg, 1 mmol) and DDT (5 ml) were loaded into a 25 mL 3-necked flask and purged with N_2 gas for 10 min. Next, the solution was heated up to 230 ℃ and maintain at this temperature for 30 min. After that, 5 mL as-prepared Zink stock solution were quickly injected into the reaction solution. After 30 min, remove the heating mental to cool down the solution to room temperature. Add ethanol (10 mL) and centrifuged at 8000 rpm for 5 min to form the precipitated, Collect the solid sample and then dispersed in toluene to form a dark solution for purification.[50]

Purification of $CuInS_2$/ZnS quantum dots (QDs)

Add ethanol (10 mL) into the solution to re-precipitate the products and centrifuged at 8000 rpm for 5 min (same as further step). This purification procedure was repeated three times. Finally, the as-obtained products were dispersed in toluene to form a clear

dark solution for further characterization.[50]

Fabrication of Yb-$CsPbCl_3$ NCs and $CuInS_2$/ZnS QDs luminescent solar concentrators (LSCs).

The prurified Yb-$CsPbCl_3$ NCs and CuInS2/ZnS QDs solution were desolved in toluene solution and added into a mixture with Sygrad 184 PDMS viscus oligomer and Sygrad 184 curing agent with a weight ratio of 7: 1, the NCs and QDs concentration were adjusted according to experiment requirement. The degased mixture was stirred and vacumme for 1h to form a clear and homugenius solution, then transferred into different dimension curing moulds (G = 5 thickness d = 0.2 cm, and G = 24 thickness d = 0.16) made by teflon. The curing process was completed by heating samples in the oven at 75 ℃ for 12h. The LSC slab were detached from the mould after the whole procedure.

Fabrication of Yb-$CsPbCl_3$ NCs and $CuInS_2$/ZnS QDs mixing design luminescent solar concentrators (LSCs).

The purified toluene desolved Yb-$CsPbCl_3$ NCs and CuInS2/ZnS QDs solution were firstly mixed in different ratio and sonicate for 10 min to form a clean and homogenous solution. The stock solutions were placed in the dark for 12h and then transfer into Sygrad 184 PDMS viscus oligomer and Sygrad 184 curing agent mixture with a weight ratio of 7: 1, the NCs and QDs concentration were set according to experiment requirement. The mixture firstly degased and then stirred and vacumme for 1h to removed bubbled in the viscus mixture to form a clear and homugenius solution. The

different dimersion aluminum foil moulds (G = 10 and G = 25, thickness d = 0.4 cm)

UV-Vis absorption and transmission measurements

UV-Vis absorption spectra and transmission spectra were performed using an Agilent Technologies Cary 5000 UV-Vis-NIR Spectrophotometer. The Yb-$CsPbCl_3$ NCs ,$CuInS_2$/ZnS QDs and the two component mixing samples were dissolved in anhydrous toluene, and the LSC devices were cut into small pieces (1 cm × 1 cm) and placed onto the solid film holder for the measurement.

Photoluminescence (PL) and PL quantum yield (PL QY) measurements

The PL spectra and PL QY measurements were measured using an Edinburgh Instruments Fluorescence Spectrometer FS5. The Yb-$CsPbCl_3$ NCs and $CuInS_2$/ZnS QDs samples were dissolved in anhydrous toluene for both measurements. The PL QYs were measured by FS5 Spectrometers with a built-in integrating sphere.

J-V characteristics of the tandem design LSC and mixing design LSC samples

The J-V characterization procedure of single junction LSC devices is from previous researchers‘ approach[4]: We used monoscrystalline silicon (c-Si) mini cell (SUNYIMA Mini Small Solar Panel 50mm × 50mm) coupled with the edge regions of LSC devices by using Porcelain index matching gel. The black tape was applied to cover the excess area of the solar cell. The J–V curves of the coupled LSC-PVs and the standalone PV were obtained using a voltage source meter (Keithley 236) in the range of −0.1 V to 0.8

V with a voltage step of 0.01 V. In all LSC-PV measurements, after attaching solar cells to the LSC, the excess edge areas were masked with total absorbing black tape to stabilize the set-up. The J-V characteristics were measured using a 2400 source meter (Keithley, USA) under simulated 1-sun illumination (AM1.5G, 100 mW·cm-2) which is generated by an Oriel Sol3A Class AAA solar simulator (Newport, USA) in air.

Transmission electron microscopy (TEM) measurements

TEM measurements were performed on a JEOL 2100F operated at 200 kV. The Yb-$CsPbCl_3$ NCs and $CuInS_2$/ZnS QDs samples were dissolved in anhydrous toluene. Approximately 10 μL of the prepared solution was dropped cast onto a 300-mesh copper TEM grid and dried at ambient conditions.

X-ray Diffraction (XRD) measurements

XRD pattern was acquired using a Bruker D8 Discovery 2D X-ray Diffractometer equipped with a Vantec 500 2D area detector operating with Cu Kα radiation (λ = 1.541 Å). The Yb-$CsPbCl_3$ NCs in toluene solution and $CuInS_2$/ZnS QDs sample in a hexane solution was drop-casted on glass slides and evaporated at ambient conditions for the XRD measurement.

External optical efficiency (η_{ext}) of LSCs from electro-optical measurements

The electro-optical measurement for the large scale LSCs (each layer of tandem design LSC, 20cm × 20cm × 0.2cm, G = 50; mixing design LSC, 20cm × 20cm × 0.4cm, G =

25) are applied based on the previous work.[4-9] The relationship between the power conversion efficiencies (PCEs) of a single photovoltaic (η_{PV}) and a LSC coupled LSC-PV junction device ($\eta_{LSC\text{-}PV}$) can be expressed as fellow:

$$\eta_{LSC-PV} = \frac{\langle Q_{PL} \rangle}{\langle Q_s \rangle} \eta_{s,abs} \eta_{int} \eta_{PV} \tag{16}$$

$\langle Q_s \rangle$ and $\langle Q_{PL} \rangle$ are the averaged external quantum efficiencies (EQEs) of the PV devices over the sunlight incident spectrum and the LSC emission spectrum, respectively. Fellow by this equation, the η_{int} and η_{ext} of the LSC in LSC-PV junction device can be expressed by the following equations:

$$\eta_{int} = \frac{\eta_{LSC-PV}\langle Q_s \rangle}{\eta_{s,abs}\eta_{PV}\langle Q_{PL} \rangle} = \frac{J_{SC,LSC-PV}\langle Q_s \rangle}{J_{SC}\eta_{s,abs}G\langle Q_{PL} \rangle} \tag{17}$$

$$\eta_{ext} = \frac{J_{SC,LSC-PV}\langle Q_s \rangle}{J_{SC}\eta_{s,abs}G\langle Q_{PL} \rangle} \tag{18}$$

J_{SC} and $J_{SC,LSC-PV}$ are the short-circuit current densities of the standalone PV and LSC-PV, respectively.

Visible light transmittance (VLT) calculation

The visible light transmittance (VLT) of an LSC device is expressed by the following equations:[16]

$$VLT = \frac{\int T(\lambda)P(\lambda)S(\lambda)d\lambda}{\int P(\lambda)S(\lambda)d\lambda} \tag{19}$$

Where λ is the light wavelength, T(λ) is the transmittance of the LSC, P(λ) is the photopic response function of the human eye (photonic vision), S(λ) is the normalized AM1.5 solar spectrum. The VLT is calculated by taking the ratio of the integrated area

of the convoluted curve with the integrated area of the photopic response of the eye.

Analytical mode simulation

The analytical mode simulation was developed based on previous studies. Following the procedure described in the literature,[16] the following parameters were determined:

$$< \alpha_1 >= -\frac{1}{d} ln \left(\frac{\int_{E_g}^{\infty} S_{in}(\lambda) e^{-\alpha(\lambda) d} d\lambda}{\int_{E_g}^{\infty} S_{in}(\lambda) d\lambda} \right) \quad (20)$$

Where $< \alpha_1 >$ is the average absorption coefficient among the incident light wavelength range, the obtained value can apply the α_1. α is the absorption coefficient of the Yb or CIS emitters. λ is the wavelength of light. d is the thickness of the LCS. E_g is the bandgap of emitters. S_{in} is the spectral shape of incident light.

α_2 is the absorption coefficient at the wavelength of the emitted light, which can be replaced by the average value of $< \alpha_2 >$, which is defined as:

$$< \alpha_2 >= (d/(d + D)) \frac{\int S_{PL}(\lambda) \alpha(\lambda) d\lambda}{\int S_{PL}(\lambda) d\lambda} \quad (21)$$

Where S_{PL} is the spectral shape of the emitters emission, and α is the absorption coefficient of the $Cs_3Cu_2Cl_5$ NDs. λ is the wavelength of light. D is the thickness of the LCS or LDS substrate.

η_{trap_LSC} is the efficiency of light trapping into the LSC device, which is determined by the refrative index of the LSC matrix, which is:

$$\eta_{trap\_LSC} = \sqrt{1 - n^{-2}} = cos\theta_{esc} \quad (22)$$

β is geometry correction factor; η_{PL} is the PL QY of the emitters; R is the reflection

coefficient of LSC surfaces; T is the transmission of the overall LSC device.

For β value determination, the initial value can be calculated based on the following equation:[7]

$$\beta = 1.4 + 0.5\left(\frac{l}{150}\right)^{0.5} \quad (23)$$

Where l is the edge length for a square-shaped device. This equation is relatively reliable for l = 0-2000 cm.[28]

S_2 denotes the scattering factor of the LSC, which is defined by the concentration of the emitters. For Yb, the scattering factor $S_{2(Yb)} = 0.005 \times C_{Yb}$, where C_{Yb} represents the Yb concentration in the LSC (unit: wt%); for CIS, the scattering factor $S_{2(CIS)} = 0.0025 \times C_{CIS}$, where C_{CIS} represents the CIS concentration in the LSC (unit: wt%). The scattering factor is confirmed through MC mode and optical measurement. The scattering factor of the mixing LSC, $S_{2(M)}$, is expressed as follows:

$$S_{2(M)} = S_{2(Yb)} + S_{2(CIS)} \quad (24)$$

Equation 24 can be applied to well-dispersed, low-concentration solution systems.

Monte Carlo ray-tracing simulation (MC simulation) of tandem/mixing design LSC

The energy efficiency performance and the input/output photon quantification analysis of the tandem and mixing design LSC were performed via MC ray-tracing simulation. The movement trace of the photons traveling through the LSCs can be described by a

set of vector and location coordinates, according to Fresnel Law (describe the refraction and reflection behaviors at air/LSC polymer matrix interfaces). By tracking the number of photons, we can predict an overall trend of photon propagation and evaluate the photon-concentrating performances of LSC devices. Furthermore, it quantified the photon propagation trend. The logic flow of the tandem design LSC and mixing design LSC are described in the following paragraph and shown in the logic flow chart below (**Caption 1, 2**).

Firstly, the input parameter for the MC simulation mode include the total number of the input photon (i.e., 30,000); the geometry parameter of the LSC (length, width, height LSC, 20cm × 20cm × 0.2cm for each layer of tandem design LSC and 20cm × 20cm × 0.4cm for mixing design LSC, we also set 0.1 cm airgap for tandem design LSC); refractive index of the LSC's polymer matrix material; the absorption coefficient, cumulative distribution functions (CDF) plot for emission spectra and PL QY of the Yb-$CsPbCl_3$ NCs (Yb), $CuInS_2$/ZnS QDs (CIS). The concentration of tandem or mixing LSC-doped Yb and CIS.

For tandem design LSC, we assign random x and y coordinates as its initial position parameters for each photon and collect all the position data to generate a photon database (database 1). Next, according to Fresnel Law, we calculate how many of the input photons are scattered by the LSC surface. Then, we release a non-scattered photon into the main loop of the top layer; Yb absorption coefficient spectra and Yb

concentration value are used to determine if the tandem LSC top layer absorbs this photon. For the photon that Yb does not capture, we record the photon coordinate data into a photon database (database 2) and release another photon. For the absorbed photon, we determine if this photon will be absorbed and emitted by the Yb (according to the Yb CDF plot and PL QY of the applied Yb). If not, the photon is lost through the non-radiative decay channels of the Yb. Two photons are released if the Yb emits the photon based on the quantum cutting effect. We further determine if the new release photons will hit the surface of the top layer LSC. If not hitting the surface, the photons are considered back to the initial emission determination step. If hitting the surface, the photons will be updated with a new set of location vector parameters and proceed to the next step. According to the new photon location data, we can determine which surface the photons hit (top/bottom or edge of the top layer LSC).

If the photons hit the edge and top surface of the LSC, according to the location vector and refractive index of the polymer materials, we can determine whether the photons are reflected back through the total internal reflection (TIR). If so, the simulation procedure moves back to the initial emission determination step. If not, these photons are transmitted through the edge and close one photon tracing loop; the transmitted positions (edge/top region of the LSC) are recorded. After that, another photon in database 1 can be released into the main loop.

If the photons hit the bottom surface of the LSC, again, we can determine if the TIR

occurs. If so, the simulation returns to the initial emission determination step. If not, the photons‘ coordinates are recorded in database 2.

The main loop for the top layer LSC is repeated until all the photons in database 1 are traced.

Then, the Fresnel Law is applied to determine if the photons in database 2 are scattered by the second layer LSC. Next, we released a non-scattered photon into the main loop of the bottom layer. CIS absorption coefficient spectra and Yb concentration value are used to determine if the released photon is captured by the bottom layer LSC. If not, the photon is transmitted through the LSC, and another photon is released into the loop. If so, we determine if the photon will be absorbed and emitted by the CIS based on the CIS CDF plot and PL QY of the applied CIS. If not, the photon is lost through the non-radiative decay channels of the CIS. Further, we check if the new release photon will reach the surface of the bottom layer LSC. If not, the photon is reabsorbed by the CIS. Then the photon is checked by the initial CIS emission determination step. If so, a new set of location vector parameters of the photon will be updated and moved to the next step. Based on the updated photon location data, we can determine the photon reach which faces (top/bottom or edge of the top layer LSC). Then we determine if the TIR occurs. If so, the photon is again checked with the CIS emission determination step. If not, the photon travels through the LSC (transmitted positions are recorded in this step), closing this photon loop. Further, another photon in database 2 is introduced into the

main loop of the bottom layer.

The main loop for the bottom layer LSC is repeated until all the photons in database 2 are traced. After that, the process is finished.

For the mixing design LSC, we first set random x and y coordinates as the initial position parameters for every photon and summarize the position data into the photon database. Next, based on Fresnel Law, we randomly kick out a certain amount of photons (Fresnel Law calculates the kick-out value) in the database to simulate the scattering effect caused by the LSC surface. Then, we release a photon into the main loop. The absorption spectra and concentration data of the CIS and Yb are applied to determine whether the mixing LSC can absorb the photon and which emitter captures the photon. If so, we further determine if the emitter will emit another one (if captured by CIS) or two (if captured by Yb) photons, according to the CIS and Yb CDF plot and PL QY of the applied Yb. If not, the photon is lost through the non-radiative decay channels of the CIS or Yb. If the emitters emit the photon, we further determine if the new release photon will hit the surface of LSC. If not hitting the surface, the photons are considered back to the initial photon captured and emission determination step. If hitting the surface, the photon will be updated with a new set of location vector parameters and proceed to the next step. According to the new photon location data, we can determine which surface the photons hit (top/bottom or edge of the top layer LSC).

The main loop of mixing LSC keeps repeating until all the input photons are traced.

The main uncertainty of the parameters that are input in the model are concluded as follows: The scattering photons from the bottom layer of tandem LSC may scatter back into the first layer of tandem LSC. The total scatters amount of the bottom LSC is ~3.5%. This may lead to an internal/external optical efficiency decrease due to this uncertainty. Compared with the experimental data, the IOE and EOE decrease is hard to observe, which means that this uncertainty can be ignored. The standard deviation of ± 2.5% for the PL QY of Yb-$CsPbCl_3$ NCs and ± 1% of $CuInS_2$/ZnS QDs (CIS). The MC mode itself induced a 0.4% uncertainty for the total amount of traced photons. Overall, the upper limit of our simulation's internal/external optical efficiency uncertainties is within 5%, which is a tolerable error.

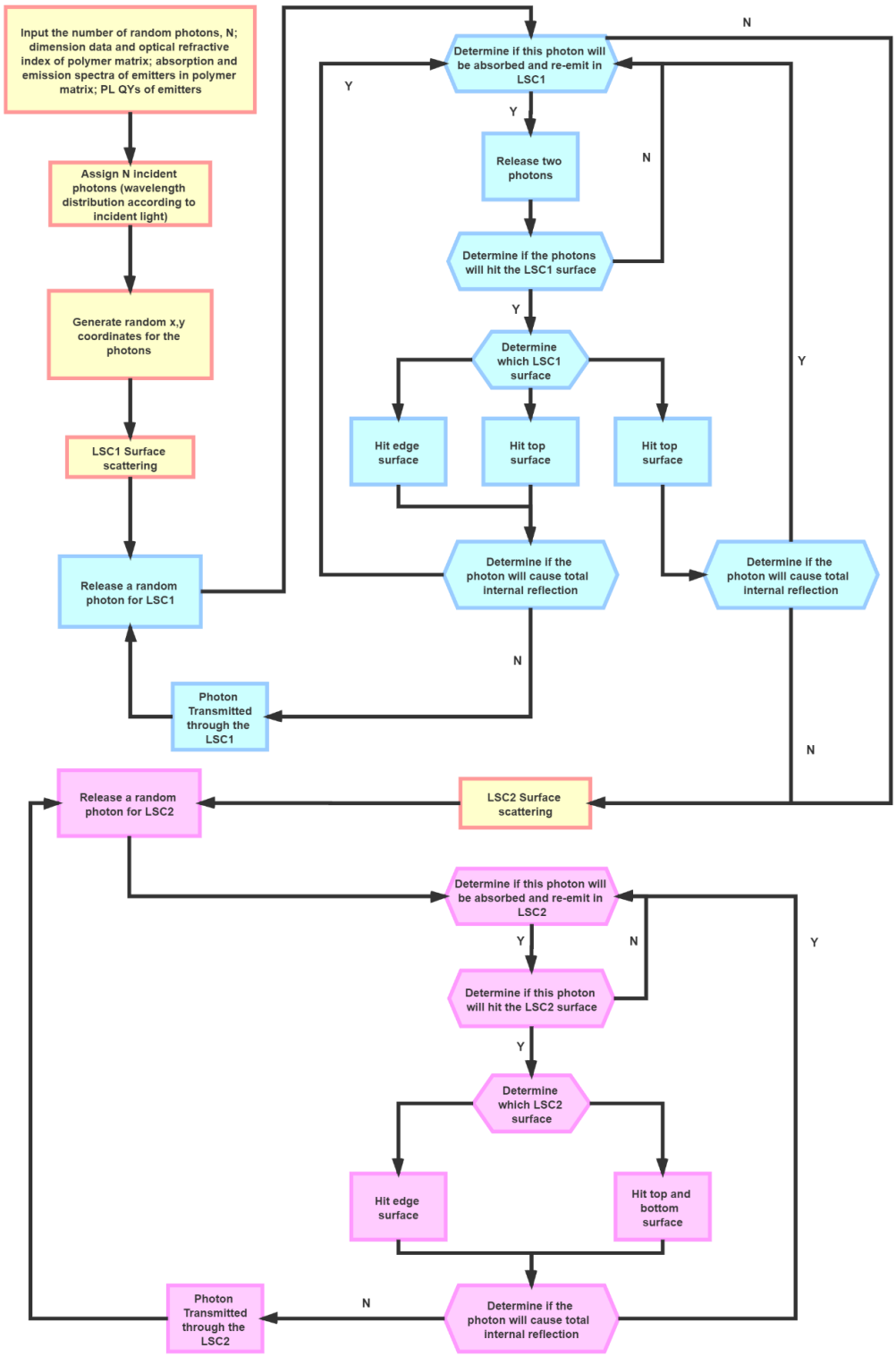

Scheme 5.1. Logic flow chart of the MC ray-tracing simulation for the tandem LSC device. The blue blocks are the main loop region for top LSC device, and the purple blocks are the main loop region for bottom LSC device. In the main loop region, individual photons are traced.

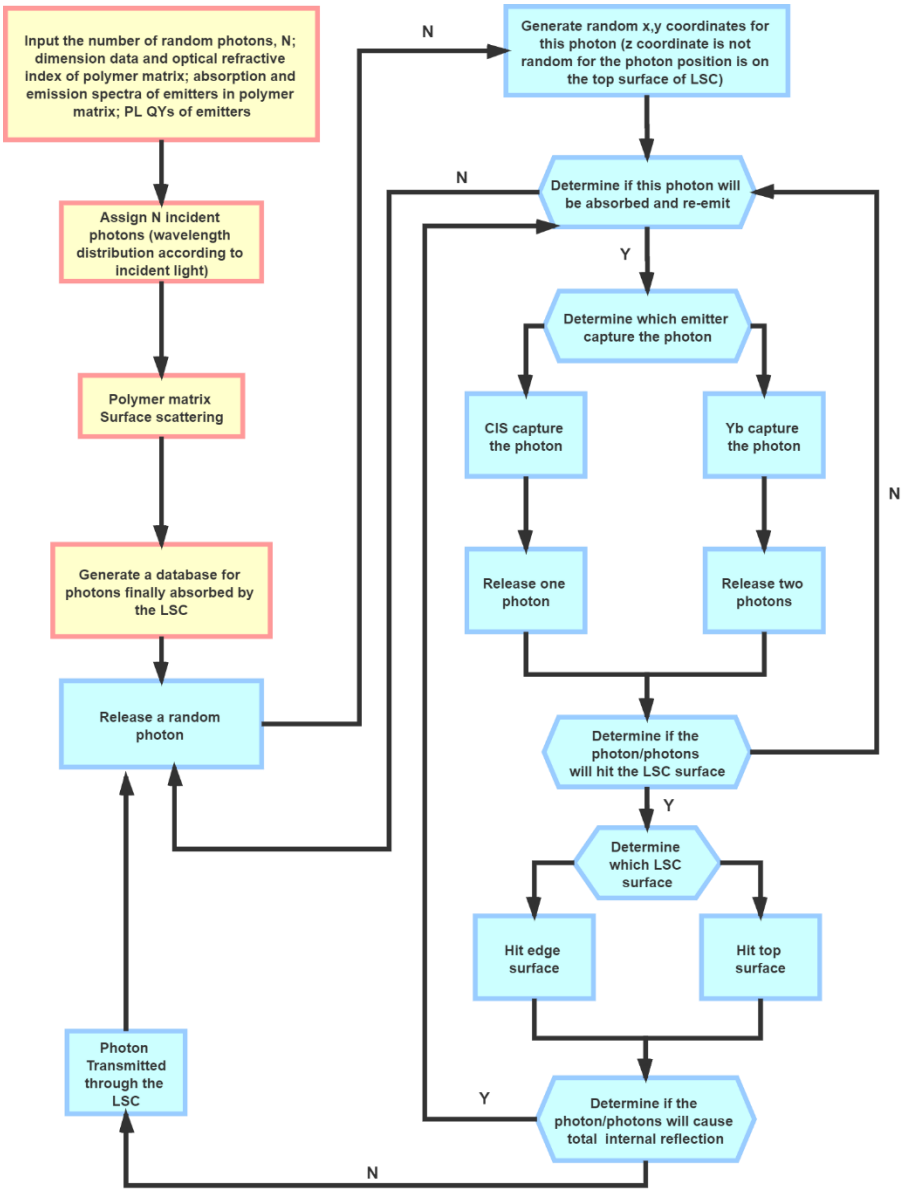

Scheme 5.2. Logic flow chart of the MC ray-tracing simulation for the mixing LSC device. The blue blocks are the main loop region for the LSC device, where individual photons are traced.

Comparing the costs of solar electricity between a standalone PV, a coupled tandem design LSC-PV system and a coupled mixing design LSC-PV system

We here introduced a cost-efficiency factor of LSC (γ) which is defined as the ratio of the per-watt cost of LSC-PV system and standalone PV under normal solar irradiation (1.5 AM). The expression was shown in equation (14) The chemical cost of lab scale production data is summarized from Sigma-Aldrich and the cost of industrial-scale prodction is summarized from Alibaba Group. The data source of silicon PV cost in industry is summaried from EnergyTrend offical site (http:// pv.energytrend.com /pricequotes.html). Accoding to the price of different PV walfers. We choose M12 (area dimension: 210 mm^2) as a reference. The polycrystalline silicon materal price is $31.52 per m^2.

Furthermore, under real outdoor conditions, the incident solar energy is keep changing while the incident angle changing during the day time. We also need to consider the anglar dependence of PCE in the case of a PV stand alone system and LSC-PV system. Based on the data shown in **Figure S12**, the PV-LSC system shows a more angular independent properties than PV standalone system. Based on Klimov's work, we introduce an angular correction factor (χ_θ) to discribe the property different, which is discribed below:[16]

$$\chi_\theta = (< \eta_{LSC-PV,\theta} > / \eta_{LSC-PV,0}) / (< \eta_{PV,\theta} > / \eta_{PV,0}) \quad (25)$$

Where $< \eta_{LSC-PV,\theta} >$ and $< \eta_{PV,\theta} >$ are the average PCE under solar incident which shining angle from 0° to 90° of LSC-PV system and standalone PV system, respectively. The $\eta_{LSC-PV,0}$ and $\eta_{PV,0}$ are the PCE values of normal incident case. According to equation S3, equation S8 can be further expressed as:

$$\chi_\theta = < J_{n,LSC-PV,\theta} > / < J_{n,PV,\theta} > \quad (26)$$

In this work, χ_θ = 1.36. The derivation of standalone PV and PV-LSC system facrication cost per m^2 are shown from **Table 5.1** to **5.5**. The LSC dimension in this simualtion is 15.2cm × 15.2cm × 0.318 for for mixing design LSC. The summaried cost-efficient (γ) contour map based on the expeimental case is shown in the maintext **Figuer 5.13a**. Futher, the cost-efficiency factor contour map of an ideal case (CIS PL QY = 100% and

Yb PL QY = 200%) mixing design LSCs are shown in **Figure 5.13b**.

Chemical	Batch size	Price per batch	Price per g or mL	Source link
CuI	1000g	$273	$0.27/g	https://www.sigmaaldrich.com/US/en/product/sial/03140?gclid=Cj0KCQjwsrWZBhC4ARIsAGGUJurmTw4IOjrnFOW0a8vwabSvy3Y6NslTvIaAfQVmGynyWVX8Sv8JCGoaAv7AEALw_wcB&gclsrc=aw.ds
In(OAc)3	50g	$461	$9.22/g	https://www.sigmaaldrich.com/US/en/product/aldrich/510270
Zn(OAc)2	500g	$875	$1.75/g	https://www.sigmaaldrich.com/US/en/substance/zincacetate18348557346
CsOAc	25g	$176	$7.04/g	https://www.sigmaaldrich.com/US/en/product/aldrich/450154?gclid=Cj0KCQjwsrWZBhC4ARIsAGGUJupeTKZ6ZbYksyTIuCLEK6PRWXxwTjG52Uh12yhpOzXD9eP4U2Gc-bsaAluzEALw_wcB&gclsrc=aw.ds
Yb(OAc)3	25g	$257	$10.28/g	https://www.sigmaaldrich.com/US/en/product/aldrich/326011
Pb(OAc)2	100g	$187	$1.87/g	https://www.sigmaaldrich.com/US/en/product/aldrich/316512?gclid=Cj0KCQjwsrWZBhC4ARIsAGGUJupwhMbcFwpyiyZNrgWZEFyBtu_BzitRGP3NQB6_8NIUE8E35U4dyM0aAsNxEALw_wcB&gclsrc=aw.ds
DDT	18L	$566	$0.03/mL	https://www.sigmaaldrich.com/US/en/pro

				duct/aldrich/471364 S
OA	4000mL	$174	$0.04/mL	https://www.sigmaaldrich.com/US/en/product/aldrich/364525
OAm	615mL	$158	$0.26/mL	https://www.sigmaaldrich.com/US/en/product/aldrich/o7805
ODE	1000mL	$43.6	$0.04/mL	https://www.sigmaaldrich.com/US/en/product/aldrich/o806 S

Table 5.1. Cost of chemicals for lab-scale production.

Chemical	Batch size	Price per batch	Price per g or mL	Source link
CuI	1000g	$2	$0.002/g	https://www.alibaba.com/product-detail/Copper-Iodide-CAS-NO-7681-65_1600551320762.html?spm=a2700.galleryofferlist.normal_offer.d_image.2b3f5383oHW3ai&s=p
In(OAc)3	1000g	$10	$0.01/g	https://www.alibaba.com/product-detail/Factory-supply-Indium-acetate-CAS-25114_1600429689743.html?spm=a2700.galleryofferlist.normal_offer.d_image.28dd5006XNJiDO
Zn(OAc)2	1000kg	$9.99	$0.0099/g	https://www.alibaba.com/product-detail/Zinc-Acetate-Factory-High-Quality-Zinc_1600620072839.html?spm=a2700.galleryofferlist.normal_offer.d_image.41d13

				5f03kt82L&s=p
CsOAc	1000g	$120	$0.12/g	https://www.alibaba.com/product-detail/99-Cesium-Acetate-for-Pharma-Industry_913971117.html
Yb(OAc)3	1000g	$22	$0.022/g	https://www.alibaba.com/product-detail/Rare-rare-earth-price-99-9_1600290846504.html?spm=a2700.galleryofferlist.normal_offer.d_image.6ea52f18UsrvVw&s=p
Pb(OAc)2	1000g	$46	$0.046/g	https://www.alibaba.com/product-detail/High-quality-Lead-acetate-trihydrate-CAS_1600581415344.html?spm=a2700.galleryofferlist.normal_offer.d_image.16246ea8odafqD&s=p
DDT	1000g	$5	$0.005/g	https://www.alibaba.com/product-detail/High-quality-n-dodecyl-mercaptan-1_1600387263901.html?spm=a2700.galleryofferlist.normal_offer.d_title.469f103d4uhI9R
OA	1000g	$9.99	$0.0099/g	https://www.alibaba.com/product-detail/Acid-Oleic-Monomer-Fatty-Acid-Oleic_1600617082178.html?spm=a2700.galleryofferlist.normal_offer.d_image.6c601517FREJ92&s=p
OAm	1000g	$3	$0.003/g	https://www.alibaba.com/product-detail/Oleylamine-Good-Price-Hot-Sales-Liquid_1600613512287.html?spm=a2700.galleryofferlist.normal_offer.d_title.398c2

				7a83cFmdm&s=p
ODE	1000g	$1.5	$0.0015/g	https://www.alibaba.com/product-detail/1-Octadecene-CAS-112-88-9_1600610578736.html?spm=a2700.galleryofferlist.normal_offer.d_title.7a4e7f91j9ZjTo

Table 5.2. Cost of chemicals for industrial-scale production.

Chemical	Amount	Price for lab-scale	Price for industry
CsOAc	53.7 mg	$0.378	$0.00005
$Yb(OAc)_3$	50.8 mg	$0.522	$0.00112
$Pb(OAc)_2$	76 mg	$0.142	$0.0035
OA	1 mL	$0.040	$0.0089
OAm	0.5 mL	$0.130	$0.0012
ODE	5 mL	$0.200	$0.0059
Solvent cost for cleaning (hexane)		$0.16	$0.0016
Total cost of Yb		$1.572	$0.0223
Yb yield		0.12g	
Fabrication cost		$13.100/g	$0.1858/g

Table 5.3. Cost calculation of fabrication Yb-$CsPbCl_3$ NCs (Yb).

Chemical	Amount	Price for lab-scale	Price for industry
CuI	190.5 mg	$0.051	$0.0004
$In(OAc)_3$	292.0 mg	$2.692	$0.0029
$Zn(OAc)_2$	333.8 mg	$0.584	$0.0033
DDT	6 mL	$0.189	$0.0297
OA	4 mL	$0.160	$0.0356
Solvent cost for cleaning		$1.6	$0.1
Total cost of CIS		$6.876	$0.2719
CIS yield		0.3g	
Fabrication cost		$22.921/g	$0.9063/g

Table 5.4. Cost calculation of fabrication $CuInS_2$/ZnS QDs (CIS).

Materials	Mixing/Tandem LSC		Si-PV
	Lab scale	Industrial scale	
PDMS	$0.043/g	$0.0005/mL	
CIS	$22.921/g	$0.9063/g	
Yb	$6.550/g	$0.0929/g	
PV	$2.80/$m^2$		$31.52/$m^2$

Table S5. LSC device fabrication cost

Building energy consumption mode by using EnergyPlus

A local sensitivity analysis was made in EnergyPlus to evaluate the anual building energy consuptions and energy generated by the PV and PV-LSC system. The building to be simulated is a modern four-story hous with a dimension (length×width×height) of 10m×10m×18m. The height of each floor is 4.5m and the window dimension on each side of the wall is 9m×4m. To simulate the installation of PV-LSC system, we tranfer the window into a semi-transparent PV system which PCE is 1.9% according to the PCE of PV-LSC system. he house's geometry was created with Google SketchUp 2019 based on the house plan and then converted to an EnergyPlus input file using the Legacy OpenStudio plugin. he house is equipped with a water-based constant flow floor heating system and a ventilation system. The ventilation system is constant and is made up of intake and exhaust fans that bring fresh air into the house. An undergr ound device (EnergyPlus Earth Tube object) is used to pre-heat/pre-cool the air that enters the house. It works by exchanging heat with the nearly constant temperature of the earth. In the winter the incoming air is a little warmer and in the summer the incoming air is a little cooler than the outside temperature, ther efore the system provides air quality with decreased costs for heating or cooling systems.

In this study, the model is readily applicable for control and fault detection experiments, with a specific focus on a time window during which the heating system is deactivated. This approach facilitates a more rigorous assessment of the model's validity without interference from the heating system. The validation process primarily concerns

material properties and the influence of weather on the interior temperature of the living room, for which real sensor data were available.

EnergyPlus, a highly robust building energy analysis and thermal load simulation tool, was employed to simulate the building model. The OpenStuidio, an open-source software environment, was utilized to establish the simulation framework. OpenStuidio enables the coupling of EnergyPlus with MATLAB and SketchUp, and other software tools, permitting the integration of control logic, such as the heating control of an EnergyPlus building model, using SketchUp for implementation.

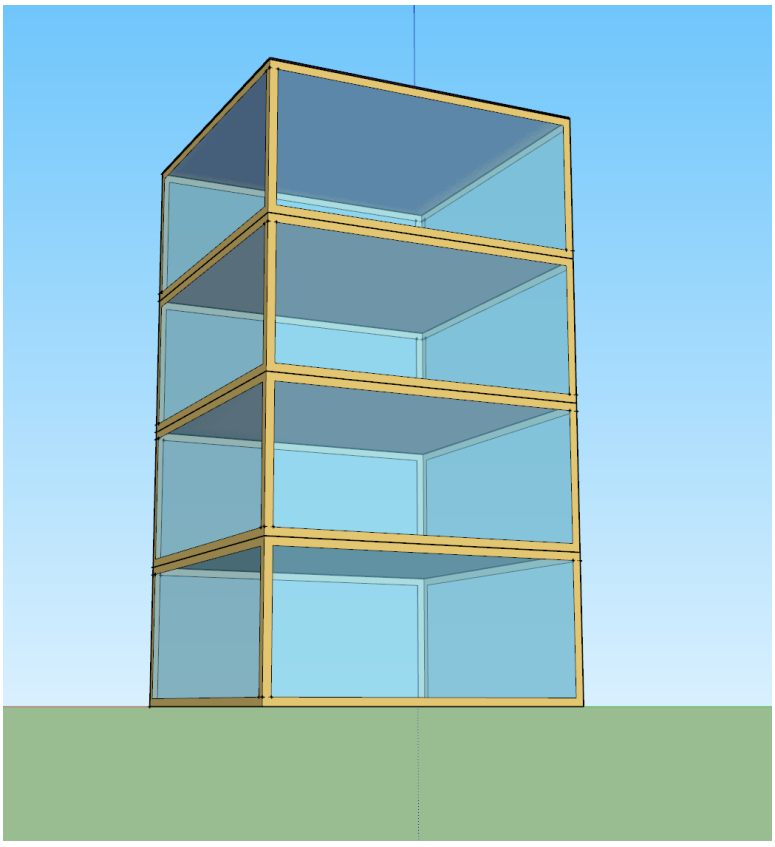

Scheme 5.3. Geometry of the building created for EnergyPlus (built in SketchUp).

Topic	Length (cm)	Width (cm)	Height (cm)	G factor	Volume (cm^3)	EOE (%)
Nat. Photonics 2018, *12(2)*, 105-110.	15.20	15.20	0.32	11.88	73.93	6.40% (tandem LSC)
	15.20	15.20	0.16	23.75	36.97	5.50% (bottom LSC)
Small 2016, *12(38)*, 5354-5365	7.00	1.50	0.30	2.06	3.15	1.40%
Nat. Photonics 2014, *8(5)*, 392-399.	21.50	1.35	0.50	1.27	14.51	0.60%
Nat. Energy 2016, *1(12)*, 16157.	10.20	10.20	0.16	15.94	16.65	1.90%
Adv. Mater 2017, *29(30)*, 1700821.	10.00	10.00	0.10	25.00	10.00	1.65%
Nat. Energy 2019, *4(3)*, 197-205.	10.00	10.00	0.20	12.25	20.00	0.87%
Nano Lett. 2019, *19(1)*, 338-341.	5.00	5.00	0.20	6.25	5.00	3.70%
J. Phys. Chem. C 2017, *121(6)*, 3252−3260	7.50	7.50	0.14	13.40	7.88	5.70%
Nat. Nanotechnol 2015, *10(10)*, 878-885.	12.00	12.00	0.30	10.00	43.20	3.30%
Nat. Energy 2017, *11(3)*, 177-185.	12.00	12.00	0.26	11.54	37.44	2.90%
Adv. Energy Mater 2016, *6(11)*, 1501913.	10.00	1.50	0.20	3.26	3.00	1.10%
ACS Energy Lett. 2018, *3*	10.00	10.00	0.14	17.86	14.00	8.10%

***(3)*, 520-525**						
ACS Energy Lett. 2022, 7, 5, 1741–1749	9.5	9.5	0.77	3.08	69.49	11.8%
Mater. Adv., 2020, 1, 119--138	10	10	0.2	12.5	20	5.02%
ACS Appl. Nano Mater. 2020, 3, 6489−6496	10	10	1	2.5	100	0.53%
Joule. 2020, 4(3), 631-643	10	10	0.2	12.5	20	2.0%
This work	15.2	15.2	0.318	11.95	73.47	**7.37%** (mixing LSC)

Table 5.6. Overview of literature results for large scale high-efficiency nanocrystal based LSCs.

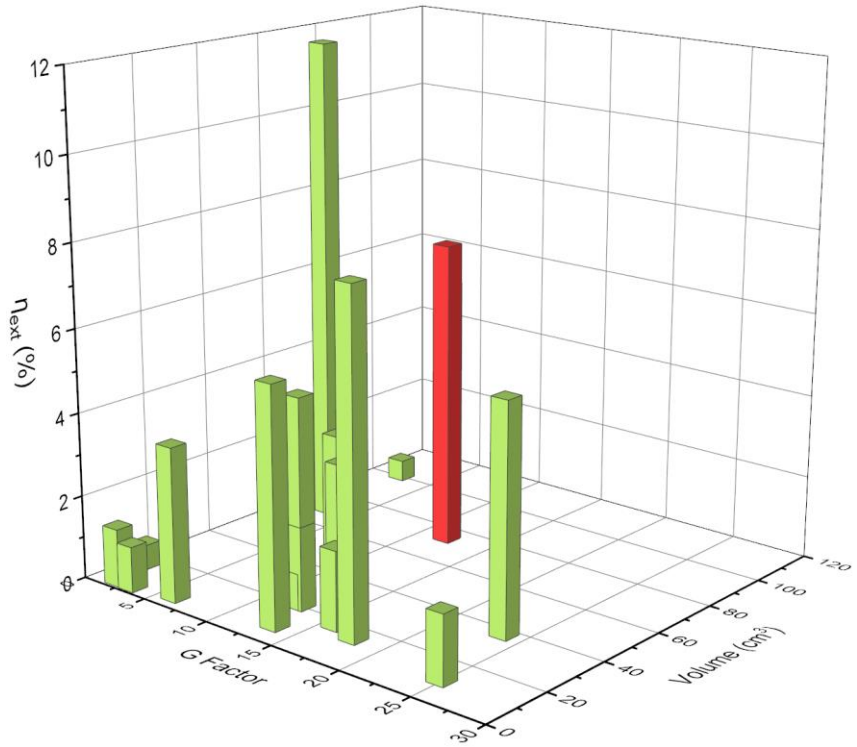

Scheme 5.4. The overall comparison of the LSC performance. The green cuboids are the η_{ext} of other reported LSC devices; the red cuboid is the mixing design LSC's η_{ext} in this work.

Reference

1. Kannan, N.; Vakeesan, D., Solar energy for future world: - A review. *Renewable and Sustainable Energy Reviews* **2016,** *62*, 1092-1105.
2. Sebestyén, V., Renewable and Sustainable Energy Reviews: Environmental impact networks of renewable energy power plants. *Renewable and Sustainable Energy Reviews* **2021,** *151*.
3. Creutzig, F.; Agoston, P.; Goldschmidt, J. C.; Luderer, G.; Nemet, G.; Pietzcker, R. C., The underestimated potential of solar energy to mitigate climate change. *Nature Energy* **2017,** *2* (9).
4. Fankhauser, S.; Smith, S. M.; Allen, M.; Axelsson, K.; Hale, T.; Hepburn, C.; Kendall, J. M.; Khosla, R.; Lezaun, J.; Mitchell-Larson, E.; Obersteiner, M.; Rajamani, L.; Rickaby, R.; Seddon, N.; Wetzer, T., The meaning of net zero and how to get it right. *Nature Climate Change* **2021,** *12* (1), 15-21.
5. Svetozarevic, B.; Begle, M.; Jayathissa, P.; Caranovic, S.; Shepherd, R. F.; Nagy, Z.; Hischier, I.; Hofer, J.; Schlueter, A., Dynamic photovoltaic building envelopes for adaptive energy and comfort management. *Nature Energy* **2019,** *4* (8), 671-682.
6. Fares, R. L.; Webber, M. E., The impacts of storing solar energy in the home to reduce reliance on the utility. *Nature Energy* **2017,** *2* (2).
7. Brockway, P. E.; Owen, A.; Brand-Correa, L. I.; Hardt, L., Estimation of global final-stage energy-return-on-investment for fossil fuels with comparison to renewable energy sources. *Nature Energy* **2019,** *4* (7), 612-621.
8. Traverse, C. J.; Pandey, R.; Barr, M. C.; Lunt, R. R., Emergence of highly transparent photovoltaics for distributed applications. *Nature Energy* **2017,** *2* (11), 849-860.
9. Lee, K.; Lee, J.; Mazor, B. A.; Forrest, S. R., Transforming the cost of solar-to-electrical energy conversion: Integrating thin-film GaAs solar cells with non-tracking mini-concentrators. *Light: Science & Applications* **2015,** *4* (5), e288-e288.

10. Meinardi, F.; Bruni, F.; Brovelli, S., Luminescent solar concentrators for building-integrated photovoltaics. *Nature Reviews Materials* **2017,** *2* (12).
11. Li, H.; Wu, K.; Lim, J.; Song, H.-J.; Klimov, V. I., Doctor-blade deposition of quantum dots onto standard window glass for low-loss large-area luminescent solar concentrators. *Nature Energy* **2016,** *1* (12).
12. Bradshaw, L. R.; Knowles, K. E.; McDowall, S.; Gamelin, D. R., Nanocrystals for luminescent solar concentrators. *Nano Lett* **2015,** *15* (2), 1315-23.
13. Zhou, Y.; Benetti, D.; Tong, X.; Jin, L.; Wang, Z. M.; Ma, D.; Zhao, H.; Rosei, F., Colloidal carbon dots based highly stable luminescent solar concentrators. *Nano Energy* **2018,** *44*, 378-387.
14. Zhao, H.; Zhou, Y.; Benetti, D.; Ma, D.; Rosei, F., Perovskite quantum dots integrated in large-area luminescent solar concentrators. *Nano Energy* **2017,** *37*, 214-223.
15. Meinardi, F.; McDaniel, H.; Carulli, F.; Colombo, A.; Velizhanin, K. A.; Makarov, N. S.; Simonutti, R.; Klimov, V. I.; Brovelli, S., Highly efficient large-area colourless luminescent solar concentrators using heavy-metal-free colloidal quantum dots. *Nat Nanotechnol* **2015,** *10* (10), 878-85.
16. Wu, K.; Li, H.; Klimov, V. I., Tandem luminescent solar concentrators based on engineered quantum dots. *Nature Photonics* **2018,** *12* (2), 105-110.
17. Coropceanu, I.; Bawendi, M. G., Core/shell quantum dot based luminescent solar concentrators with reduced reabsorption and enhanced efficiency. *Nano Lett* **2014,** *14* (7), 4097-101.
18. Erickson, C. S.; Bradshaw, L. R.; McDowall, S.; Gilbertson, J. D.; Gamelin, D. R.; Patrick, D. L., Zero-reabsorption doped-nanocrystal luminescent solar concentrators. *ACS Nano* **2014,** *8* (4), 3461-7.
19. Batchelder, J. S.; Zewail, A. H.; Cole, T., Luminescent solar concentrators. 1: Theory of operation and techniques for performance evaluation. *Appl Opt* **1979,** *18* (18), 3090-110.

20. Aste, N.; Tagliabue, L. C.; Del Pero, C.; Testa, D.; Fusco, R., Performance analysis of a large-area luminescent solar concentrator module. *Renewable Energy* **2015,** *76*, 330-337.
21. van Sark, W. G.; Barnham, K. W.; Slooff, L. H.; Chatten, A. J.; Buchtemann, A.; Meyer, A.; McCormack, S. J.; Koole, R.; Farrell, D. J.; Bose, R.; Bende, E. E.; Burgers, A. R.; Budel, T.; Quilitz, J.; Kennedy, M.; Meyer, T.; Donega Cde, M.; Meijerink, A.; Vanmaekelbergh, D., Luminescent Solar Concentrators--a review of recent results. *Opt Express* **2008,** *16* (26), 21773-92.
22. Meinardi, F.; Colombo, A.; Velizhanin, K. A.; Simonutti, R.; Lorenzon, M.; Beverina, L.; Viswanatha, R.; Klimov, V. I.; Brovelli, S., Large-area luminescent solar concentrators based on 'Stokes-shift-engineered' nanocrystals in a mass-polymerized PMMA matrix. *Nature Photonics* **2014,** *8* (5), 392-399.
23. Sumner, R.; Eiselt, S.; Kilburn, T. B.; Erickson, C.; Carlson, B.; Gamelin, D. R.; McDowall, S.; Patrick, D. L., Analysis of Optical Losses in High-Efficiency CuInS2-Based Nanocrystal Luminescent Solar Concentrators: Balancing Absorption versus Scattering. *The Journal of Physical Chemistry C* **2017,** *121* (6), 3252-3260.
24. Cohen, T. A.; Milstein, T. J.; Kroupa, D. M.; MacKenzie, J. D.; Luscombe, C. K.; Gamelin, D. R., Quantum-cutting Yb3+-doped perovskite nanocrystals for monolithic bilayer luminescent solar concentrators. *Journal of Materials Chemistry A* **2019,** *7* (15), 9279-9288.
25. Nikolaidou, K.; Sarang, S.; Hoffman, C.; Mendewala, B.; Ishihara, H.; Lu, J. Q.; Ilan, B.; Tung, V.; Ghosh, S., Hybrid Perovskite Thin Films as Highly Efficient Luminescent Solar Concentrators. *Advanced Optical Materials* **2016,** *4* (12), 2126-2132.
26. Luo, X.; Ding, T.; Liu, X.; Liu, Y.; Wu, K. F., Quantum-Cutting Luminescent Solar Concentrators Using Ytterbium-Doped Perovskite Nanocrystals. *Nano Letters* **2019,** *19* (1), 338-341.

27. Zhao, H.; Sun, R.; Wang, Z.; Fu, K.; Hu, X.; Zhang, Y., Zero-Dimensional Perovskite Nanocrystals for Efficient Luminescent Solar Concentrators. *Advanced Functional Materials* **2019,** *29* (30).
28. Zhao, Y.; Meek, G. A.; Levine, B. G.; Lunt, R. R., Near-Infrared Harvesting Transparent Luminescent Solar Concentrators. *Advanced Optical Materials* **2014,** *2* (7), 606-611.
29. Meinardi, F.; Akkerman, Q. A.; Bruni, F.; Park, S.; Mauri, M.; Dang, Z.; Manna, L.; Brovelli, S., Doped Halide Perovskite Nanocrystals for Reabsorption-Free Luminescent Solar Concentrators. *ACS Energy Lett* **2017,** *2* (10), 2368-2377.
30. Zhao, H.; Benetti, D.; Tong, X.; Zhang, H.; Zhou, Y.; Liu, G.; Ma, D.; Sun, S.; Wang, Z. M.; Wang, Y.; Rosei, F., Efficient and stable tandem luminescent solar concentrators based on carbon dots and perovskite quantum dots. *Nano Energy* **2018,** *50*, 756-765.
31. Cai, T.; Wang, J.; Li, W.; Hills-Kimball, K.; Yang, H.; Nagaoka, Y.; Yuan, Y.; Zia, R.; Chen, O., Mn(2+)/Yb(3+) Codoped CsPbCl(3) Perovskite Nanocrystals with Triple-Wavelength Emission for Luminescent Solar Concentrators. *Adv Sci (Weinh)* **2020,** *7* (18), 2001317.
32. Mir, W. J.; Mahor, Y.; Lohar, A.; Jagadeeswararao, M.; Das, S.; Mahamuni, S.; Nag, A., Postsynthesis Doping of Mn and Yb into CsPbX3 (X = Cl, Br, or I) Perovskite Nanocrystals for Downconversion Emission. *Chemistry of Materials* **2018,** *30* (22), 8170-8178.
33. Sommer, D. E.; Gamelin, D. R.; Dunham, S. T., Defect formation in Yb-doped CsPbCl3 from first principles with implications for quantum cutting. *Physical Review Materials* **2022,** *6* (2).
34. ZdraZil, L.; Kalytchuk, S.; Hola, K.; Petr, M.; Zmeskal, O.; Kment, S.; Rogach, A. L.; Zboril, R., A carbon dot-based tandem luminescent solar concentrator. *Nanoscale* **2020,** *12* (12), 6664-6672.
35. Li, J.; Zhao, H.; Zhao, X.; Gong, X., Red and yellow emissive carbon dots integrated tandem luminescent solar concentrators with significantly improved efficiency. *Nanoscale* **2021,** *13* (21), 9561-9569.

36. Lunardi, M. M.; Needell, D. R.; Bauser, H.; Phelan, M.; Atwater, H. A.; Corkish, R., Life Cycle Assessment of tandem LSC-Si devices. *Energy* **2019,** *181*, 1-10.
37. Nakamura, Y.; Iso, Y.; Isobe, T., Bandgap-Tuned CuInS2/ZnS Core/Shell Quantum Dots for a Luminescent Downshifting Layer in a Crystalline Silicon Solar Module. *ACS Applied Nano Materials* **2020,** *3* (4), 3417-3426.
38. Li, H.; Jiao, J.; Luo, D.; Xiong, D.; Gao, L., Controllable synthesis of Cu-based quantum dots/nanocrystals and application in white light-emitting diodes. *Dalton Trans* **2022,** *51* (46), 17883-17894.
39. Park, J.; Kim, S.-W., CuInS2/ZnS core/shell quantum dots by cation exchange and their blue-shifted photoluminescence. *Journal of Materials Chemistry* **2011,** *21* (11).
40. Milstein, T. J.; Kroupa, D. M.; Gamelin, D. R., Picosecond Quantum Cutting Generates Photoluminescence Quantum Yields Over 100% in Ytterbium-Doped CsPbCl(3) Nanocrystals. *Nano Lett* **2018,** *18* (6), 3792-3799.
41. Klimov, V. I.; Baker, T. A.; Lim, J.; Velizhanin, K. A.; McDaniel, H., Quality Factor of Luminescent Solar Concentrators and Practical Concentration Limits Attainable with Semiconductor Quantum Dots. *ACS Photonics* **2016,** *3* (6), 1138-1148.
42. Song, H. J.; Jeong, B. G.; Lim, J.; Lee, D. C.; Bae, W. K.; Klimov, V. I., Performance Limits of Luminescent Solar Concentrators Tested with Seed/Quantum-Well Quantum Dots in a Selective-Reflector-Based Optical Cavity. *Nano Lett* **2018,** *18* (1), 395-404.
43. Gungor, K.; Du, J.; Klimov, V. I., General Trends in the Performance of Quantum Dot Luminescent Solar Concentrators (LSCs) Revealed Using the "Effective LSC Quality Factor". *ACS Energy Letters* **2022,** *7* (5), 1741-1749.
44. Crawley, D. B.; Lawrie, L. K.; Winkelmann, F. C.; Buhl, W. F.; Huang, Y. J.; Pedersen, C. O.; Strand, R. K.; Liesen, R. J.; Fisher, D. E.; Witte, M. J.; Glazer, J., EnergyPlus: creating a new-generation building energy simulation program. *Energ Buildings* **2001,** *33* (4), 319-331.

45. Fumo, N.; Mago, P.; Luck, R., Methodology to estimate building energy consumption using EnergyPlus Benchmark Models. *Energ Buildings* **2010,** *42* (12), 2331-2337.
46. Dahanayake, K. W. D. K. C.; Chow, C. L., Studying the potential of energy saving through vertical greenery systems: Using EnergyPlus simulation program. *Energ Buildings* **2017,** *138*, 47-59.
47. Boyano, A.; Hernandez, P.; Wolf, O., Energy demands and potential savings in European office buildings: Case studies based on EnergyPlus simulations. *Energ Buildings* **2013,** *65*, 19-28.
48. Karlessi, T.; Kampelis, N.; Kolokotsa, D.; Santamouris, M.; Standardi, L.; Isidori, D.; Cristalli, C., The Concept of Smart and NZEB Buildings and the Integrated Design Approach. *Procedia Engineering* **2017,** *180*, 1316-1325.
49. Attia, S.; Eleftheriou, P.; Xeni, F.; Morlot, R.; Ménézo, C.; Kostopoulos, V.; Betsi, M.; Kalaitzoglou, I.; Pagliano, L.; Cellura, M.; Almeida, M.; Ferreira, M.; Baracu, T.; Badescu, V.; Crutescu, R.; Hidalgo-Betanzos, J. M., Overview and future challenges of nearly zero energy buildings (nZEB) design in Southern Europe. *Energ Buildings* **2017,** *155*, 439-458.
50. Liu, Z.; Guan, Z.; Li, X.; Tang, A.; Teng, F., Rational Design and Synthesis of Highly Luminescent Multinary Cu-In-Zn-S Semiconductor Nanocrystals with Tailored Nanostructures. *Advanced Optical Materials* **2020**, 8 (6).

Chapter 6

Conclusions and Future Directions

In conclusion, my PhD study mainly focus on explores the optimization method of LSCs from various perspective, including coating techniques, photonic surface modification, emitter development, and innovative geometries. Despite being in the preliminary stages of development, LSCs hold great potential for enhancing solar cell efficiency and reducing solar power generation costs. Through a combination of experimental and computational methods, this research delves into the intricacies of LSCs and provides innovative solutions to improve their performance. By addressing the challenges and limitations in the field, my projects try to make the contribution to the advancement of LSC technology and paves the way for future developments in solar energy applications.

More specifically, the optimization of the LSCs can be divided in 4 parts: the fabrication method development, the LSC mechanism losses reduction, the emitter efficiency enhancement and the composite component optimization. In my research, I introduced an ultrasonic spray coating technique for the device fabrication, which creates high-quality QD-LSCs with smooth, customizable layers, reduces QD aggregation, and works with various substrates. By adjusting the QD-ink solution, photon capture, transparency, and solar energy harvesting for QD-LSC devices can be fine-tuned, marking a significant step toward integrating programmable, high-performance LSC devices in diverse applications. I also developed a 3D macroporous-structured photonic crystal (PC) coated QD-based LSC (PC-LSC) device, which effectively reduces escape cone photon loss and increases light-trapping efficiency by ~30% compared to

conventional LSCs. This highlights the potential of PC-LSC devices in practical solar energy conversion systems with enhanced energy harvesting capabilities. Moreover, I introduced a Lead-free $Cs_3Cu_2Cl_5$ NDs, which exhibit high PL QY and a large Stoke shift. Incorporating these NDs into LSC and LDS devices results in high visible light transmission, low photon scattering, and superior UV photon harvesting, paving the way for lead-free perovskite nanomaterials in space-based solar power systems. Lastly, I claimed a mixed-design LSC is demonstrated, incorporating high PLQY quantum cutting perovskite Yb-doped $CsPbCl_3$ nanocrystals and Stokes-shift engineered $CuInS_2$/ZnS quantum dots. This design reduces re-absorption losses and scattering attenuation, achieving high η_{ext} performance for large-scale LSC devices. Simulations indicate that the mixed LSC-PV system can significantly reduce energy generation costs and enhance energy gain in NZEB buildings compared to stand-alone roof-mounted PV panels.

Overall, this works contributed to advancing LSC technology and offered perspectives on future directions for LSC developments, including potential avenues to improve performance limitations and exploring novel LSC applications within the solar energy field.

In the future development of LSCs, a critical aspect to explore is the development of highly efficient, polymer-friendly, and stable emitters. Experimenting with new luminescent semiconductor nanomaterials such as doping system perovskite[1-3] and

carbon quantum dots[4-8] can lead to the development of emitters with high absorption properties (covering most of the solar irradiation range) and suitable emission properties (emitting photons that can be effectively absorbed by PV cells), ultimately enhancing LSC solar energy conversion. Quenching effects are common in emitter/polymer films, so it is essential to develop polymer-friendly properties that enable emitters to be well-dispersed into LSCs at higher concentrations.[9, 10] Additionally, considering the potential real-world applications, LSCs may be subjected to challenging working conditions.[11] As a result, the stability of emitters is another crucial consideration for LSC devices. Protective coating layers or protective shell may be applied to enhance the durability of LSCs, ensuring high performance over extended periods. This approach can help address the stability issue and maintain the efficiency of LSCs, paving the way for their successful implementation in various applications.

Another promising approach for the development of LSCs involves the integration of anisotropic emission materials. These unique materials display direction-dependent emission properties due to the non-uniform distribution and preferential alignment of their emitting molecules or particles. Anisotropic emission materials have potential applications in various fields, such as optical devices, photovoltaics, and light-emitting diodes (LEDs), because of their distinct advantages.[12-14]

Incorporating anisotropic emission materials in LSCs can lead to improved light-trapping capabilities and reduced losses associated with re-absorption, ultimately

enhancing the overall efficiency. However, there are still some challenges in introducing these materials into LSCs. One of the main obstacles is achieving the proper alignment of the materials within the polymer matrix, as the anisotropic emission materials should preferentially direct the emitted light towards the solar cells. This requires employing self-assembly methods to guide the emitters.

During my PhD study, I attempted to use PDMS polymer wrinkle patterns to direct the CdSe nanorods and subsequently fabricate LSC devices. However, due to the mismatch in scale between the microscale wrinkle patterns and the nanoscale nanorods, the self-assembly pattern did not result in a clear alignment, and the device did not exhibit the desired anisotropic emission. Despite these challenges, the potential application of anisotropic emission materials in LSCs remains promising, and I am eager to explore this field further in my future research.

Moreover, expanding the application of LSCs beyond solar energy systems to include photoreactors presents an exciting avenue for further exploration in the field. By attaching the LSC to a transparent reaction chamber or flow cell, it creates an environment for photochemical reactions to occur. The reaction chamber should be made of a material resistant to the reactants and products involved in the process while allowing the transmission of concentrated light from the LSC.[15-17]

LSC-based photoreactors offer localized light sources, which provide precise control over reaction zones. This feature enables the optimization of reaction conditions and the possibility of conducting multiple reactions simultaneously. This approach has numerous potential applications, such as assisting in the degradation of pollutants through photocatalytic processes, driving sustainable chemical reactions like hydrogen production from water or synthesizing fine chemicals using solar energy.

Furthermore, LSC-based photoreactors can be integrated with artificial photosynthesis systems to convert sunlight, water, and carbon dioxide into valuable chemicals or fuels, mimicking natural photosynthesis. They can also be combined with photobioreactors to cultivate photosynthetic microorganisms like algae for various applications, including biofuel production, wastewater treatment, or CO_2 sequestration. Overall, using LSCs as photoreactors offers a versatile and promising approach to harness solar energy for diverse applications across various fields.

In conclusion, the continued advancement of LSCs necessitates a sustained focus on research and development. Key areas for exploration include the development of new materials with improved performance characteristics, the optimization of device structures, and the integration of LSCs with various solar energy applications. By addressing the current limitations and challenges in the field, it is possible to unlock the full potential of LSCs, thereby contributing to the broader goals of enhancing solar cell efficiency and reducing solar power generation costs.

Reference

1. Gu, G.; Zheng, Z.; Zhang, H.; Zhang, Y.; Gan, Z.; Huang, R.; Zhang, X., Re-absorption-free perovskite quantum dots for boosting the efficiency of luminescent solar concentrator. *Journal of Luminescence* **2022,** *248*.

2. Cohen, T. A.; Milstein, T. J.; Kroupa, D. M.; MacKenzie, J. D.; Luscombe, C. K.; Gamelin, D. R., Quantum-cutting Yb3+-doped perovskite nanocrystals for monolithic bilayer luminescent solar concentrators. *Journal of Materials Chemistry A* **2019,** *7* (15), 9279-9288.

3. Cai, T.; Wang, J.; Li, W.; Hills-Kimball, K.; Yang, H.; Nagaoka, Y.; Yuan, Y.; Zia, R.; Chen, O., Mn(2+)/Yb(3+) Codoped CsPbCl(3) Perovskite Nanocrystals with Triple-Wavelength Emission for Luminescent Solar Concentrators. *Adv Sci (Weinh)* **2020,** *7* (18), 2001317.

4. Li, J.; Zhao, H.; Zhao, X.; Gong, X., Red and yellow emissive carbon dots integrated tandem luminescent solar concentrators with significantly improved efficiency. *Nanoscale* **2021,** *13* (21), 9561-9569.

5. ZdraZil, L.; Kalytchuk, S.; Hola, K.; Petr, M.; Zmeskal, O.; Kment, S.; Rogach, A. L.; Zboril, R., A carbon dot-based tandem luminescent solar concentrator. *Nanoscale* **2020,** *12* (12), 6664-6672.

6. Mateen, F.; Ali, M.; Lee, S. Y.; Jeong, S. H.; Ko, M. J.; Hong, S.-K., Tandem structured luminescent solar concentrator based on inorganic carbon quantum dots and organic dyes. *Solar Energy* **2019,** *190*, 488-494.

7. Zhao, H.; Liu, G.; You, S.; Camargo, F. V. A.; Zavelani-Rossi, M.; Wang, X.; Sun, C.; Liu, B.; Zhang, Y.; Han, G.; Vomiero, A.; Gong, X., Gram-scale synthesis of carbon quantum dots with a large Stokes shift for the fabrication of eco-friendly and high-efficiency luminescent solar concentrators. *Energy & Environmental Science* **2021,** *14* (1), 396-406.

8. Han, Y.; Zhao, X.; Vomiero, A.; Gong, X.; Zhao, H., Red and green-emitting biocompatible carbon quantum dots for efficient tandem luminescent solar concentrators. *Journal of Materials Chemistry C* **2021,** *9* (36), 12255-12262.

9. Talite, M. J.; Huang, H. Y.; Wu, Y. H.; Sena, P. G.; Cai, K. B.; Lin, T. N.; Shen, J. L.; Chou, W. C.; Yuan, C. T., Greener Luminescent Solar Concentrators with High Loading Contents Based on in Situ Cross-Linked Carbon Nanodots for Enhancing Solar Energy Harvesting and Resisting Concentration-Induced Quenching. *ACS Appl Mater Interfaces* **2018,** *10* (40), 34184-34192.

10. Banal, J. L.; Zhang, B.; Jones, D. J.; Ghiggino, K. P.; Wong, W. W., Emissive Molecular Aggregates and Energy Migration in Luminescent Solar Concentrators. *Acc Chem Res* **2017,** *50* (1), 49-57.

11. Delgado-Sanchez, J.-M., Luminescent solar concentrators: Photo-stability analysis and long-term perspectives. *Solar Energy Materials and Solar Cells* **2019,** *202*.

12. Nam, S.; Oh, N.; Zhai, Y.; Shim, M., High efficiency and optical anisotropy in double-heterojunction nanorod light-emitting diodes. *ACS Nano* **2015,** *9* (1), 878-85.

13. Bai, X.; Purcell-Milton, F.; Gun'ko, Y. K., Optical Properties, Synthesis, and Potential Applications of Cu-Based Ternary or Quaternary Anisotropic Quantum Dots, Polytypic Nanocrystals, and Core/Shell Heterostructures. *Nanomaterials (Basel)* **2019,** *9* (1).

14. Castelli, A.; Meinardi, F.; Pasini, M.; Galeotti, F.; Pinchetti, V.; Lorenzon, M.; Manna, L.; Moreels, I.; Giovanella, U.; Brovelli, S., High-Efficiency All-Solution-Processed Light-Emitting Diodes Based on Anisotropic Colloidal Heterostructures with Polar Polymer Injecting Layers. *Nano Lett* **2015,** *15* (8), 5455-64.

15. Cambie, D.; Zhao, F.; Hessel, V.; Debije, M. G.; Noel, T., A Leaf-Inspired Luminescent Solar Concentrator for Energy-Efficient Continuous-Flow Photochemistry. *Angew Chem Int Ed Engl* **2017,** *56* (4), 1050-1054.

16. Zhao, F.; Chen, Z.; Fan, W.; Dou, J.; Li, L.; Guo, X., Reactor optimization and process intensification of photocatalysis for capillary-based PMMA LSC-photomicroreactors. *Chemical Engineering Journal* **2020,** *389*.

17. Cambie, D.; Dobbelaar, J.; Riente, P.; Vanderspikken, J.; Shen, C.; Seeberger, P. H.; Gilmore, K.; Debije, M. G.; Noel, T., Energy-Efficient Solar

Photochemistry with Luminescent Solar Concentrator Based Photomicroreactors. *Angew Chem Int Ed Engl* **2019,** *58* (40), 14374-14378.